UNIVERSITY OF PRETORIA

FACULTY OF ENGINEERING, BUILT ENVIRONMENT AND INFORMATION TECHNOLOGY

DEPARTMENT OF MECHANICAL AND AERONAUTICAL ENGINEERING

Blade tip timing to determine turbine blade fatigue in high backpressure conditions

Student:

Willem Johannes Visagie

Supervisor:

Professor P.S. Heyns

Submitted in partial fulfilment of the requirements for the degree

Masters of Engineering

(Mechanical Engineering)

2020

UNIVERSITEIT VAN PRETORIA
UNIVERSITY OF PRETORIA
YUNIBESITHI YA PRETORIA

Summary

In service, blade failure in turbines is a known problem and with a significant safety risk, high repair cost, non-operational revenue loss and even retiring of the unit. Therefore, the reliability of these blades, especially the low pressure (LP) blades, is of utmost importance for the successful operation of a steam turbine. To aggravate the matter, low load and/or high backpressure conditions can lead to stall flutter, high cycle fatigue and failure of last stage blades (LSB). Although the mechanism is well known, the conditions under which this may occur in a specific unit are not well defined. Recommended minimum load levels and maximum backpressure (poor vacuum) are typically defined by the original equipment manufacturer (OEM). However, it is not always easy to consistently adhere to these requirements and conditions do arise where some units operate out of these specifications for varying timespans.

This dissertation focuses on an investigation of blade tip timing (BTT) data together with finite element analysis (FEA) as a possible procedure for calculating the fatigue life of a steam turbine LSB running under FSNL, or low load at high backpressure conditions in the condenser. The investigation concentrates on the non-synchronous vibration of the LSB while vibrating at a blade resonance frequency. The procedure makes use of BTT data and a method, which assumes that a dominant resonance frequency is present in the BTT signal, and that only the mode excited by the dominant frequency contributes to the fatigue damage. The procedure does not include the participation of other modes with the dominant mode, in terms of establishing life estimations.

The FEA was conducted on the complete LSB through a cyclic symmetric analysis of a single blade and rotor sector with two half damping pins connected to either side of the blade. Plasticity is applied where the blade root deforms plastically due to initial overspeed testing. Damping was added to the model by means friction and Raleigh damping coefficients. The modal analysis and correct extraction of natural frequencies and modes are important factors to consider. Two tests were conducted to verify the FEA. The first verification is a static impact test conducted by a modal hammer, to verify stationary blade natural frequencies. The second verification test is a balance pit test with strain gauges, to verify natural frequencies at operating speed.

The fatigue life calculated for the dominant frequency for mode two, nodal diameter seven was 4.24 years in operation, for which deflection was measured during low load conditions. A significant change in results can be expected if a higher stress is present or, the duration of exposure at peak stress is higher than what the test data has shown. At high load conditions, the blade life calculations presented not to be an area of concern and fatigue life was calculated to be twelve orders higher than during low load conditions. The locations of the lowest fatigue life, which are the top two serrations on the inlet side, corresponds to the location of failures were cracks initiated.

Key terms: Steam turbine, low pressure, loose damping pins, high cycle fatigue, finite element analysis, modal analysis, BTT, non-synchronous, last stage blade.

Acknowledgements

I would like to thank Eskom Rotek Industries for providing me the opportunity to further develop my skills and knowledge by pursuing my master's degree in Mechanical Engineering.

I would like to thank the following people for their assistance and contribution to this project:

Table of contents

Nomenclature

Acronym	Description
1D	One-dimensional
2D	Two-dimensional
3D	Three-dimensional
BPF	Blade passing frequency
BTT	Blade tip timing
BVM	Blade vibration monitoring
CAD	Computer aided design
CFD	Computational fluid dynamics
DOF	Degree of freedom
EPRI	The Electric Power Research Institute
FEA	Finite element analysis
FFT	Fast Fourier transform
FM	Frequency modulated
FRF	Frequency response function
FSNL	Full speed no load
HCF	High cycle fatigue
LCF	Low cycle fatigue
LP	Low pressure
LSB	Last stage blade
MPC	Multi point constraint
NDT	Non-destructive testing
OEM	Original equipment manufacturer
rms	Root mean square
RPM	Revolutions per minute
RUL	Remaining useful life
SCC	Stress corrosion cracking
SIMO	Single input multiple output
STL	Standard triangle language
SWT	Smith-Watson-Topper
TOA	Time of arrival
UHCF	Ultra high cycle fatigue
UML	Universal material law
VHCF	Very high cycle fatigue

Symbols

Symbol	Description	Units
A	Amplitude	
A_c	Area	m^2
b	Fatigue strength exponent	
C	Damping matrix	
c	Fatigue ductility exponent	
c^*	Damping	N s/m
c_c	Critical damping	N s/m
D	Dynamic stress response	MPa
E	Modulus of elasticity	GPa
F	Applied force	N
F_r	Frequency response factor	
f_{max}	Maximum frequency	Hz
f_n	Natural frequency	Hz
f_s	Sampling frequency	Hz
H'	Cyclic strength coefficient	Pa
K	Stiffness matrix	N/m
k	Stiffness	N/m
L	Length	m
M	Mass matrix	kg
m	Mass	kg
n'	Cyclic strain hardening exponent	
N_{FL}	Fatigue limit reversal / cycles	
N_f	Nyquist frequency	Hz
N_s	Number of sensors	
R	Stress ratio	
S	Stimulus	mm
S_{FL}	Stress fatigue limit	Pa
T_0	Original time period	s
t	Time	s
u	Displacement	m
$\dot{u}$	Velocity	m/s
$\ddot{u}$	Acceleration	m/s^2
x	Displacement	m

Greek symbols

Symbol	Description	Units
α	Mass Rayleigh damping coefficient	
β	Stiffness Rayleigh damping coefficient	
δ	Damping	
$\Delta\sigma$	Stress range	MPa
ε_e	Elastic strain	
ε_f'	Fatigue ductile coefficient	
ε_p	Plastic strain	
ζ	Damping ratio	
ρ	Density	kg/m^3
σ_0	Yield stress	MPa
σ_a	Stress amplitude or alternating stress	MPa
σ_E	Endurance limit	MPa
σ_f'	Fatigue strength coefficient	Pa
σ_m	Stress mean	MPa
σ_{max}	Maximum stress	MPa
σ_{min}	Minimum stress	MPa
σ_u	Ultimate tensile strength	MPa
ω	Angular frequency	rad/s
ω_n	Natural angular frequency	rad/s
θ	Phase angle	degrees
ψ	Eigenvector or modal shape	

Chapter 1

Introduction and literature review

In service, blade failure in turbines is a known problem with a significant safety risk, high repair cost, non-operational revenue loss and even retiring of the unit. In a turbine train, the low pressure (LP) blades are the most likely to fail, especially the last stage blade (LSB). Therefor the reliability of these blades, especially the low pressure (LP) blades, are of utmost importance for the successful operation of a steam turbine. To increase the importance of the matter, low load and or high backpressure conditions can lead to stall flutter, high cycle fatigue and failure of last stage blades (LSB). Failure of these blades can be catastrophic with significant safety risks, unavailability of a unit for a long period as well as possible retiring of the unit. Although the mechanism is well known, the conditions under which this may occur in a specific unit are not well defined. Recommended minimum load levels and maximum backpressure (poor vacuum) are typically defined by the original equipment manufacturer (OEM) and operation within these parameters are required by plant procedures. However, conditions do arise where some units operate out of these specifications for varying timespans. The risk and possible accumulated fatigue damage due to this intermittent out of normal operation have as yet not been quantified.

1.1   Problem statement

During low flow conditions in a steam turbine, the LP and in particular the LSB will see a range of conditions which it will not see during normal operations. These conditions are referred to as off-design conditions. Some of these conditions entail wetter steam, stall flutter (cf. section 1.2.1.1) and high cycle vibration. When a unit is run under these conditions it could result in damage to the blade, but the damage in these conditions is not well defined and OEMs usually only stipulate that the turbine should not be run under these conditions.

Unfortunately, in practice it is not always easy to consistently adhere to these requirements. For example, a particular unit might have been designed to run as a base load unit, which means it would be running at full load or near full load for most of its life. But due to changes in the demand of electricity or availability of units, it can result in a unit running as a peaking station or load following station. This might result in the unit running at no load or low load during non-peak hours and only be running full load or near full load during peak hours. This can induce additional forces on the machine, since it is running for long periods under off-design conditions, which may not have been well explored, since the machine was not designed for these conditions.

Other possible reasons for low vacuum or high backpressure can be associated with:
- Leaks in the condenser vacuum boundary.
- Scaling build up in the condenser heat exchanger tubes.
- Plugging of leaking condenser heat exchanger tubes.
- Unavailability of feed heating plant or poor performance of the cooling system.

The immediate and costly consequence of operating under conditions of poor condenser backpressure, is the reduction in cycle efficiency and the increases in the associated fuel, water and auxiliary power costs. In extreme cases it can also result in the reduction of rated machine output. Low vacuum or high backpressure also cause high condenser temperature, which cause additional heat build-up on LSB and heat recirculation, especially under low load or no load conditions. Thermal growth of the steam path components under these conditions will also occur. This can lead to vibrations as a result of running clearances between the rotating and stationary components being compromised and consequent rubbing developing. The reaction to this is to switch on hood or exhaust sprays to cool down LSB, which can then lead to erosion, adding damaging effects to the blade. All of this then have an end effect on the effective life of the blade and cause pre-mature failing of the blade.

Blade vibration in high backpressure conditions are normally excited due to flow separation on the LSB. The wet steam and recirculation can add energy to the blade enhancing the vibration. Other environmental conditions like wet steam, salt causing stress corrosion cracking (SCC) and recirculation, should also not be ignored.

The specific blade used in this dissertation investigation has experienced several cases of SCC and high cycle fatigue (HCF). HCF was seen on the top serration of the blade root at the convex side of the blade, which was on the inlet side. This is represented in Figure 1-1. SCC was seen on the top serration of the concave side, running into or near the scallops of both the inlet and the outlet sides of the blade as shown in Figure 1-2. Recently a small number of occurrences of lower aerofoil cracking has been seen, due to HCF, which is located on the trailing edge of the blade, approximately 20mm above the root platform (cf. Figure 1-3).

Figure 1-1: Top serration convex cracking

Figure 1-2: Cracks shown on the concave side of the blade

Figure 1-3: Lower aerofoil cracking (Alstom, 2016)

The aim of this dissertation is to investigate the fatigue damage that can be a result of operating a unit under off-design conditions. It focuses in particular on the effect on LSB at low vacuum or high backpressure and no load or low load conditions. The investigation was done for a specific unit, which is currently experiencing premature failure of the last stage blade and cracks are usually present in the top serration, which is the highest stress region. The investigation of vibration of LSB running in off-design conditions, due to low load and low vacuum, can be one of many reasons for blade failure. The dissertation is not seen an exhaustive investigation of why the blade has failed, but rather an in depth investigation of a possible method and the effect of running in off-design conditions, on the blade life.

Other possible reasons for failure are SCC caused poor steam chemistry control, wrong temper conditions of blade material, insufficient shot peening or residual stress in high stress regions, HCF due to excessive starts with high backpressure, excessive erosion on blade and possible human error while assembling. Possible human errors can be physical damage to the blade and incorrect clearance installation of damping pins. All of this can cause unnecessary movement or constraints, which can result in excessive vibration or high stress regions.

1.2 Literature review

1.2.1 Off-design conditions

Off-design conditions relate mainly to the difference of load and backpressure to the specification that the blade was designed for (EPRI, 2017). The different combinations of the flow angle, steam density, exhaust velocity and unsteadiness in the exhaust flow can cause fluctuation or vibrating loads on a blade. The backpressure is primarily dependent upon the heat rejection capability of the condenser cooling water. The low flow conditions cause a lower exhaust velocity that causes the steam inlet angle on the blade to be larger, meaning that the direction of flow is pointing away from the blade, causing separation of flow. This is illustrated in Figure 1-4 (Rama Rao and Dutta, 2014). The LP blades, specifically the LSB is more prone to damage due to off-design conditions. This is mainly due to the long length of the LSB, which result in a relatively low natural frequency and can get excited by the fluctuations. In EPRI, (2017) it is reported that blade vibration results in HCF, which lead to initiation and propagation of cracks. The location of the LSB near to the exhaust hood also result in low aerodynamic damping due to low steam density.
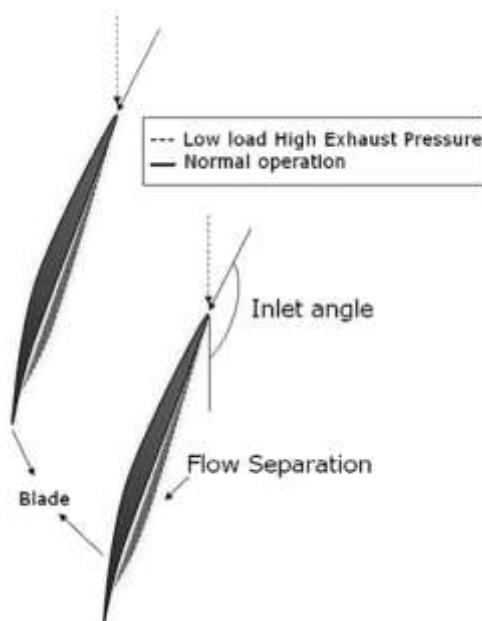

Figure 1-4: Illustration showing angle of steam incidence on the blade (Rama Rao and Dutta, 2014)

Some LP turbines, specifically the LSB can experience high levels of moisture content or condensate as the blade will see two phases of saturated steam and liquid condensate. This is normally when the turbine's exhaust pressure is lower than atmosphere, where the exhaust flow exits in the condenser. Also during low load conditions the moisture content that the blade experience can increase significantly (EPRI, 2017). During this conditions, the condensate moves at a lower velocity than the steam, causing the leading edge of the blade to collide with the liquid condensate, effectively initiating high erosion on the blade. The moisture droplets cause erosion damage on the blade, due to mechanical interaction between the droplet and the blade. This is mostly located on the tip of the blade leading edge, due to the velocities that are greater at the tip (Singh and Lucas, 2011). Trailing edge erosion can also take place and is normally due to droplets that are caught in the recirculation

loop, causing damage near the root of the trailing edge. A common activator for droplet recirculation is the hood spray system, which is activated to manage LSB heat build-up, which is prominent in low load applications.

The moisture content, causing LSB erosion, is dependent on the amount of moisture in the stage and is not a function of the exhaust pressure in the condenser. This is due to the moisture at the inlet of the blade is causing the erosion on the blade (Sanders, 1996). The exhaust pressure in the condenser however effects the trailing edge erosion on LSB.

Bad steam chemistry or steam impurity becomes more significant at low load conditions. Superheated steam have a lower salt solubility and can cause higher salt deposition on the blade (EPRI, 2018). This phenomenon can create pitting which then can lead to crack initiation in the pits, ultimately leading to fatigue and failure. This mechanism is known as stress corrosion cracking. According to (EPRI, 2017) this is commonly located around shrouds, as well as tenon and blade attachment areas. The pitting mechanism normally initiates at high oxygen levels, typically when the unit is off line.

The term exhaust loss is associated to the energy lost to the condenser, due to the steam velocity going into the condenser, causing backpressure on the LSB. The higher the steam velocity leaving the blade, the bigger is the loss. The best way to increase efficiency is to increase the area and ultimately increasing the length of the LSB (Rama Rao and Dutta, 2014).

When blades vibrate due to running at off-design conditions, mainly high backpressure, the blade is self-excited in nature. During this condition, the amplitude of blade passing frequencies (BPF) reduces, mainly due to the self-excited nature of the vibration. The amplitude of BPF increases again as soon as the vacuum in the condenser is restored and self-excitation is limited again (Rama Rao and Dutta, 2014).

Many units do not have online blade vibration monitoring systems and therefore the result of running a unit at off-design conditions cannot be determined (EPRI, 2017).

Typical sources of excitation may be summarised as (EPRI, 2017):
- Blade vibration modes and nodal diameters
- Harmonic blade vibration
- Non-harmonic blade vibration (broad frequency spectrum)
    - Stall flutter instability
    - Unstalled flutter instability
    - Condensation shock
    - Vibration at low volumetric flow
    - Exhaust flow induced vibration
- Shaft lateral vibration influence
- Shaft torsional vibration influences

To summarise, low load conditions can have the following effects on a LP turbine and thus, LSB will have a higher risk of exposure:

- Blade vibration, due to flow separation
- Higher moisture content due to steam conditions, pressure and load
- Higher temperature on LSB due to heat build-up and recirculation
- Higher moisture content due to activation of hood or exhaust sprays, where recirculation can take place
- Bad steam chemicals or steam impurity, causing salt deposits which can initiating pitting

1.2.1.1 Flutter

Flutter is an aerodynamic instability caused by the fluid structure interaction in a manner that it creates a self-excitation. Flutter is resisted only by the material and structural damping in the blade. Two types of flutter are known, namely stall flutter or unstalled flutter (Mccloskey, Dooley and McNaughton, 1999b).

- Stall flutter is the same phenomenon observed when airplane wings "stall". This is usually present in a steam turbine in the last stage blade at low load and high backpressure, normally where the upper part of the blade experiences a negative angle of attack. Stall flutter can also be a consequence of operating at high backpressure, as the result of higher temperatures, typically in the summer months (EPRI, 2017). With the increase of backpressure, the exhaust velocity also drops, increasing exhaust loss and reducing efficiency of the unit (Rama Rao and Dutta, 2014). According to EPRI, (2017) the frequencies exited by stall flutter is normally distributed over a broad frequency, due to the random nature of the vortex shedding and eddies associated with flow separation. The energy supplied to the blade will typically then excite the blade at one of its natural frequencies. Stall flutter is therefore present at non-synchronous or non-engine orders of the operating speed.
- Unstalled flutter is experienced at high flow rates, the flow is fully attached to the blade and generally no separation is present. There is also no backpressure that obstructs the flow. It is more prevalent in freestanding blades, which do not have any frictional damping. Unstalled flutter is normally associated with engine orders of the rotational speed.

Inlet conditions contribute significantly to flutter and an increase in pressure produces an increase in the steady work and consequently the aerodynamic damping. Therefore the systems can be stabilized with an increased inlet pressure, if the system has a positive aerodynamic damping and can be destabilized if the system has a negative aerodynamic damping. During instability the aerodynamic forces induced due to blade vibration feed energy into the structure, which is why flutter is so destructive (Srinivasan, 1997).

The minimization of stress due to flutter can be done only if there is sufficient damping. Mechanical or aerodynamic damping can come from material or any rubbing interaction at interfaces (Srinivasan, 1997).

1.2.1.2 Aerodynamic analysis

Zhang, He and Stüer, (2011) reported that at low mass flow and off-design conditions the unsteady flow phenomenon known as rotating instability occurs, which is mostly present in the LP turbine LSB. This instability can cause high stress levels in the LP blades. The investigations showed high unsteady pressure instabilities at the tip of the blade at frequencies that do not coincide with BPF. These instabilities are not present during high mass flow conditions, but only become apparent as the mass flow becomes lower. The instabilities are also higher in magnitude compared to the BPF. As the mass flow rate drops, the frequency associated with the rotating instability changes, becoming higher and the magnitude becomes more significant. The nodal pattern of the instabilities was also investigated showing a special nodal number of 16. The nodes are running in the same direction as the rotor, but at about half the rotor speed. Near the hub location no instabilities could be detected and is seems like the blade is not affected by rotating instabilities at the root of the blade.

According to EPRI (2008), in the case where LP blades are normally tapered and twisted, this condition will start at the tip of the blade and continue down the aerofoil as the condition of the blade becomes worse.

To effectively estimate stress levels on a blade the following information is required (Srinivasan, 1997):
- Aerodynamic analysis capable of calculating the magnitude and phase of forcing functions.
- Aerodynamic damping.
- Magnitude of non-aerodynamic damping.
- Structural analysis calculating the force vibration response.

Due to low load or no load and low vacuum, the steam flow or velocity flow is entering the stage with a negative incidence angle causing the flow to strike the suction side of the blade aerofoil. This will result in the blade vibrating, together with the pressure fluctuations; flow recirculation and counter flows (Mazur, García-Illescas and Porcayo-Calderón, 2009) (Mazur *et al.*, 2006).

According to Megerle, (2014), the "ventilation" phenomenon occur at low flow operating conditions, when the LSB do not extract energy from the stream, but return energy to the fluid. This causes non-synchronous vibrations or aerodynamic excitation. His investigation showed that it is not an aero-elastic phenomena where inertial, elastic, and aerodynamic forces interact with one another, and normal computational fluid dynamics (CFD) can be used to investigate the matter without considering full structural fluid coupling. The CFD analysis is also very dependent on the exhaust geometry, which needs to be very accurately modelled. The leakage flow over the tip however does not have much effect on the low frequency vibrations, but plays a part in higher frequency unsteady fluctuations. The suction side of the blade generate two regions of unsteady fluctuations and the casing vortex plays a key role in reversed flow. From his research he also showed that the frequency of the excitation caused by this phenomenon ranges from 4 to 9 times the rotor frequencies. The magnitude of these excitations however is fairly low, with a maximum of just below 100 Pascal at 95% of the blade span. The pressure fluctuations are present in two regions with the 90% to 100% blade span being present

in a wide variety of flow conditions and the second region between 60% to 90% of blade span for low volume flow conditions.

High condenser pressures or backpressure is a function of cooling water temperature and the steam mass flow (EPRI, 2017) and is typically caused by one, or a combination of the following conditions:

- Load decrease should always decrease the condenser pressure.
- Inefficacy of condenser for example due to aging, plugged tubes and scaling in tubes.
- Air ingress in condenser due to leaks.

1.2.2 Turbine blade vibrations and measurement techniques

Vibration is one of the primary concerns when considering blade design and only a short period of exposure can lead to large damages. The vibration can be divided into two types, synchronous and non-synchronous. Synchronous vibration usually occur at multiples or harmonics of the operating speed, resulting from the same dynamic force with every revolution. Non-synchronous vibration is normally caused by unsteady flow causing excitation and is not related to the operating speed (Mccloskey, Dooley and McNaughton, 1999b).

The most common type of vibration problems in turbines are resonances that occur at integral orders (multiples of rotational speed) and stall flutter which is an aero-elastic instability occurring generally as a non-integral order. In the event of failure the mechanism is HCF. Resonance is categorized by frequencies that are multiples of operating speed and a Campbell diagram can be used to track it. Resonance is also identified by a rapid rise in amplitude if moving towards a resonant speed and rapid drop after passing through the speed. To estimate the unsteady aerodynamics the following two types are required; first the aerodynamic damping and second the pressures that acts on the blade due to flow variations in the stream (Srinivasan, 1997). To ensure that a rotor is safe during resonance, there needs to be sufficient damping in the aero elastic system. This is not always easily achievable for low order resonances (Srinivasan, 1997). Grid instability can also cause resonance of a seemingly well detuned blades, in the sense that a small drift in the rotational speed can cause blade frequencies to be excited at the higher harmonics of the operating speed (EPRI, 2008).

According to Siewert *et al.*, (2017) damping elements can reduce the vibration response by an order of magnitude compared to freestanding blades. The structural improvement and increased natural frequencies of the blade are the main reasons for adding damping elements.

1.2.2.1 Dynamic analysis

According to Logan and Roy, (2003) blades are generally designed to be tuned for the synchronous vibration frequencies to avoid HCF.

According to Mccloskey, Dooley and McNaughton (1999) dynamic response can be simplistically formulated as:

$$D = \sigma_a cos\omega t \qquad\qquad (1.1)$$

where ω is the angular frequency of the dynamic response. The dynamic response can be caused by many different factors, but can be further defined by the stimulus (<u>S</u>), damping (δ) and a resonance response factor F_R as:

$$\sigma_a = \left(\frac{\pi}{\delta}\right) F_R \underline{S} \sigma_{bo} \tag{1.2}$$

Non-uniform flows causing non-synchronous vibration for per-revolution diaphragm harmonics can be calculated by analysing the Fourier spectrum of the nozzle throat dimensions to identify principal harmonics. This method may not give exact magnitudes. Another method will be to use CFD to calculate the magnitudes in relation to the geometry and flow conditions (Mccloskey, Dooley and McNaughton, 1999b).

According to EPRI, (2017), blades which are linked with one another have higher damping which tend to minimize the aerodynamic vibration.

In order to do a numerical study of turbine blade life the excitation forces are normally calculated by CFD analysis (Zhang and Xie, 2008) and advanced CFD analysis. This requires substantial experience and validation (EPRI, 2017). A CFD analysis also have many variables that need to be considered and need to be included in order to get an accurate model. Some of the variables are listed below:

- Influence of upstream flow on LSB excitation
- Finite element analysis (FEA) model updating to include the deflection of the blade under centrifugal and load conditions
- Aerodynamic damping
- Exhaust hood and diffusor configuration (Megerle, 2014)
- Recirculation of flow and spray water system

Condensation shock is another mechanism that can excite a blade. The mechanism produces non-harmonic excitations to the blade causing non-synchronous blade vibration. This however is a very rare phenomenon (EPRI, 2017).

1.2.2.2 Blade vibration monitoring

Various different methods are used to monitor blade vibration. Some are more traditional while other methods are more recent. The monitoring techniques are also divided in direct and indirect methods. Some of the most common direct methods are listed below:

1. **Strain gauge** approach is where a strain gauge is attached to the blade and the dynamic conditions of the blade can be monitored. The key disadvantage of this method is that it only measures the instrumented blades, it has a limited life due to steam wear and operating conditions and it also requires a slip ring or telemetry system to measure (Russhard, 2014).
2. **Frequency modulated (FM) grid** method, where a magnet mounted on the blade tip is used and a conductive wire grid in the rotor casing or external. A frequency modulation, which is directly proportional to the amplitude and frequency of the blade, is generated with a combination of the grid shape, magnet and rotor speed (Sabbatini *et al.*, 2012; Russhard,

2014). Again, this can only measure the blades, which are fitted with a magnet, which generally is a modification of the blade.

3. **Eulerian Laser Doppler Vibrometry (ELDV)**, works on the principle of laser light reflected back to the source, classifying this technique as a non-contact measurement technique. It need to have a fix reference, with a stationary transducer and measuring a moving target. The laser is pointing to a fixed point in space and measure the displacement as the blade passed through the measuring point location. Disadvantages are speckle noise in the measurements and practical issues with measuring in a steam environment (Oberholster and Heyns, 2009)

4. **Casing Pressure Signal Methods (CPSM)** is a non-contact method, measuring internal pressure fluctuations to estimate blade natural frequencies. This can be done by only looking at a single engine operating speed. The spectrum contains sidebands at multiples of shaft operating speed to estimate blade natural frequencies. This is the same spectrum which is found in casing vibration measurements (Forbes and Randall, 2013).

5. **Blade tip timing (BTT) or blade vibration monitoring (BVM)**, is a modern technique of the FM (Russhard, 2014) which is used to estimate blade vibration in normal operating conditions. It is using a set of non-contact, stationary, proximity sensors: either an eddy-current, optical sensor or a micro-wave sensor, which is mounted in the casing and monitors the blade tip. From a shaft speed measurement, the expected and actual time of arrival is recorded and from the difference, the blade displacement can be calculated. Due to this system measuring expected and actual time of arrival (TOA), which is linked to the rotating speed of the shaft, it is very difficult to measure resonant vibration which is close to shaft speed. Generally it is simpler to measure non-synchronous vibration (EPRI, 2008). This method can provide data about an individual blade for the full life during installation and the sensor can be replaced for well-designed installations while the unit is online. For this method knowledge of the expected frequencies of vibration is required (EPRI, 2002).

6. **Casing vibration** is a method that is used where the casing is seen as a pressure vessel and responds to dynamics, which is exerted on the casing with the movement of the rotor. Every stage generates its own distinctive frequency and amplitudes of pulsating pressures. The method aims at measuring spectrum and spectrum changes, together with BPF and the changes thereof (Rama Rao and Dutta, 2014).

The effective frequency that a BTT system can capture is dependent on the amount of sensor which is installed. By adding more sensors, the effective bandwidth is increased. The bandwidth is calculated by the number of sensors (N_s) times the rotational frequency, times the Nyquist frequency (N_f). The equation is shown in equation (1.3).

$$\text{Bandwidth} = N_s \cdot N_f \cdot \frac{RPM}{60} \tag{1.3}$$

The ability of the BTT to capture the vibration response of the blade is largely driven by the measured signal being aliased or sub-sampled. Many different algorithms have been developed to overcome this difficulty (Sabbatini *et al.*, 2012).

A BTT system normally records an apparent vibration or deflection, this is a combination tangential, axial and torsional blade deflections components. These components are specific to a blade design as well as the mode shape which the blade undergoes during the vibration. The BTT systems normally records the tangential displacement of the blade very accurately and this needs to be converted to modal vibration. This however is a purely geometric transformation and as an industry standard the tangential displacement is typically about three times the axial displacement, but it will be highly dependent on the blade shape and vibration mode of the blade. More detail on the conversion method is shown in Appendix C and how this is applied in section 4.1.

Running a BTT with synchronous vibration will show the blade always in the same position and therefore more than one sensor is needed to effectively capture the vibration. However the opposite is true in the case of non-synchronous vibration, the blade will technically be in a different position every time and the sinusoidal signal can be captured with only one sensor (Bachschmid, Pesatori and Bistolfi, 2015).

Blade vibration changes are commonly linked to two changes; first the changes of operational conditions and secondly the initiation of cracks on the blade. Blade cracking results in changes in the blade stiffness, which ultimately changes the natural frequency of the blade. Various techniques can be used to inspect or identify crack in blades (EPRI, 2012):

1. Non-destructive testing (NDT) testing by means of **magnetic particle inspection**. This technique requires the unit to be stopped to gain access to the rotor. Usually the rotor and the blades need to be removed and parts cleaned using an aluminium oxide grit blasting process.

2. NDT testing by means of **eddy current** probe. This technique entails the same amount of work on the rotor as mentioned above, but with the exception of grit blasting.

3. In-situ offline NDT testing by means of **phased array ultrasonic** rig inspection and natural frequency impact testing. This technique requires the unit to be open, but no need to remove the unit. This method has a high initial cost to develop the technique as well as requires a specialised scarce skill to execute the work.

4. **In-situ natural frequency impact testing**. This technique features a large scatter of data, due to blade to rotor root variance. The variance is usually due to steeple fit as well as oxidation. FEA proved that because of a relative large blade root section, the fatigue cracks has to be relatively big in order to create a significant shift in natural frequency. The standard deviation of the scatter frequency results is very close to the critical crack length therefore this approach was not pursued further.

5. Blade root **strain gauge**. This method make use of natural frequency and mode changes on blade to detect cracks. This however required a reference condition of the blade when there were no crack. This technique can be an online vibration measurement technique.

6. **Torsional vibration monitoring**, by means of a shaft strain gauge. This uses the same methodology as the blade root strain gauges, where a change in natural frequency is detected. This technique can also be done online, but is not guaranteed to detect blade excitation or flutter.

7. Blade vibration measurement by means of **blade tip timing**. This also uses the same methodology of change in natural frequency detection. This technique is also an online monitoring technique.
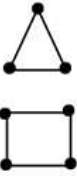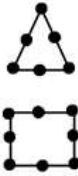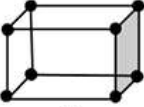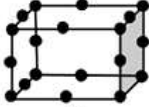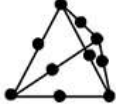
1.2.3 Turbine blade analysis

The power of today's computers as well as the advancement of FEA technology, make it a preferred method to analyse turbines via simulation. Simulation is a fast cost effective approach eliminating the need to build prototypes and perform extensive testing. Simulation however does not replace the need for testing, but reduces the elaborated prototype testing and updating process. This generally results in quicker design initiations from concepts to implementation. FEA is used to achieve this and many different scenarios can be investigated in a shorter time than building prototypes.

1.2.3.1 Element selection and convergence

Correct element selection in a FEA is very important, This is to ensure that the solution converges to the correct answer. First order or single order elements are elements with only one node at the corners of the element where second order or higher order elements have a mid-node or mid-nodes between the corner nodes. An example is shown in Table 1-1 for 1D (one-dimensional), 2D (two-dimensional) and 3D (three-dimensional) elements. According Harish, (2016) higher order elements allow for precise geometric modelling, with the same size of element as a single order element, but is not always the best element to use. A second order element in general performs better in bending and incompressible analysis, due to its ability to deform easily and accurately, but it tends to be less stiff. On the other hand a single order element performs better in contact analysis. In computational terms the second order element takes longer to solve due to more nodes, relating to more degrees of freedom (DOF's) that need to be solved. Studies done by both Fondjo and Dzogbewu, (2019) and Deshpande *et al.*, (2016), that looked at FEA methods to accurately calculate stress concentration areas, showed that higher order elements results are closer to empirical result than first order elements. For fatigue calculation, it is extremely important to capture stress concentration accurately, due to the exponential effect of fatigue life.

Table 1-1: Example of first and second order elements (Quijano, 2018)

With ANSYS software, it selects the element to be used based on the geometric shape and analysis type. In the case of the blade analysis ANSYS selected the second order 20 node 3D element (Solid186), which is shown in Figure 1-5 and have 3 degrees of freedom per node, being x, y and z translations.

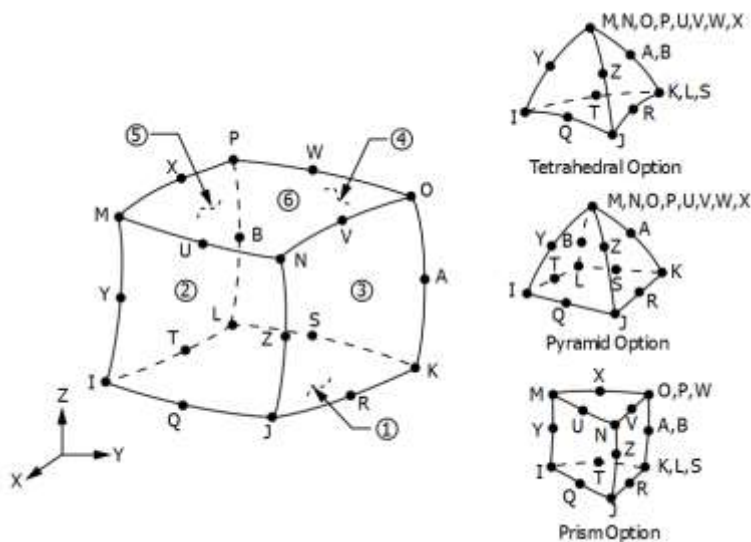**Figure 1-5:** ANSYS Solid186 element formulation

Generally, FEA mesh is stiffer than the object in reality and the smaller the mesh gets the more stiff the results become (Wheel, Frame and Riches, 2015).

The natural frequency is a function of mass and stiffness as shown in (1.4) and stiffness is a function of cross-sectional area and length as shown in equation (1.5). The length of the blade stays constant

through all the mesh sizes, but the cross-sectional area varies depending on how well the elements match the area. The smaller the mesh size, the better the area approximation, but the analysis takes longer to solve. The same argument can be used for the mass, since the mass is calculated as shown in (1.6) and also dependent on the area (Logan, 2007).

$$\omega = \sqrt{\frac{k}{m}} \tag{1.4}$$

$$k = \frac{A_c E}{L} \tag{1.5}$$

$$m = \frac{\rho A_c L}{2} \tag{1.6}$$

1.2.3.2 Blade loading

The major contributor to blade loading is the centrifugal force on the blade. This is dependent on the speed of the rotor and can be accurately determined to 1%. The aerodynamic (steam) loads are much less and are usually dependent on power output, these are normally known to 2-5% (Mccloskey, Dooley and McNaughton, 1999b). The steam bending forces on the aerofoil of the blade contribute to a lesser amount to the steady stress in a blade. Thermal stresses below 400-450˚C can be ignored (EPRI, 2008).

Blade roots need to be designed to be able to withstand the centrifugal loading and transfer the moment to the rotor to spin the shaft. Rim bending or deflection is where the rim opens up and the blade can slip out. Typical application where this is of utmost concern is high-speed compressors, LSB running in condensing conditions and highly loaded first stage blades. The fir tree root design is one of the designs that can resist rim bending and withstand higher centrifugal and radial tensile loads (Singh and Lucas, 2011).

Blades are generally made from martensitic stainless steel alloys, with high tensile strength, high fatigue strength, corrosion and erosion resistance and high ductility. Bigger LP stages are normally manufactured form titanium due to the lower density and therefore lower centrifugal loading for large blades. It is however very important that the elastic modulus to density (E/ρ) ratios are close to that of the martensitic stainless steel. This results in frequencies and mode shapes in close proximity, no matter which material is used.

1.2.3.3 Damping

Three types of damping are present in LP blades, material, mechanical and aerodynamic:
- **Material damping** is an integral part of the material properties, where temperature and frequency do not have that much influence.
- **Mechanical or Coulomb damping** occurs with the movement of parts in the mechanism of friction and slip. The damping generally exist between contact surfaces.

- **Aerodynamic damping** is the result of the steam passing over the blade and can either be negative or positive (Mccloskey, Dooley and McNaughton, 1999b).

Of these three types of damping, mechanical damping dominates (Logan and Roy, 2003) and aerodynamic damping generally is low (Hamidipoor *et al.*, 2015). Small differences in tolerances and clearances are largely influenced by damping in blade root attachments. Damping pins add mechanical damping due to relative motion and friction (Logan and Roy, 2003).

Damping is a very important parameter in vibration; it is the mechanism, which dissipates the vibrating energy, caused by resonant stresses. The damping logarithmic decrement increases with increases in stress, with material damping being the dominant factor (Hamidipoor *et al.*, 2015). However, as speed increases the frictional effect becomes less. This is due to the high friction force, preventing slip, resulting in an increase in the material damping, influence by the strain amplitude. (Logan and Roy, 2003; Hamidipoor *et al.*, 2015). Coulomb damping is significant in the contact model during micro slip conditions (Rao, 2013).

Studies done by Vyas and Rao, (1994) showed that frictional damping becomes less dominant after 400 rpm for the first and the second mode and above 500 rpm for the third and fourth mode due to the increased centrifugal force. With higher speeds of about 1000 rpm the damping is dominated by hysteresis and is totally interlocked.

According to Ostrovskii (1969) who investigated the damping of chromium turbine blades, a remarkable increase in decrement is also observed with increased stress.

The Rayleigh damping ratio is proportional to the natural frequencies of a system (Chowdhury and Dasgupta, 2003).

Material damping can be introduced in ANSYS in two ways; first via the constant damping coefficient and secondly by the Rayleigh damping. Material damping literature has better reference to constant material damping which is introduced as the damping ratio. The damping ratio is represented as a ratio of the actual damping to critical damping as shown below.

$$\zeta = \frac{c^*}{c_c} = \frac{c^*}{2\sqrt{km}}$$

(1.7)

During modal analysis in ANSYS damping can be introduced in two ways. The first is in the form of Rayleigh damping constants α and β and the second method is with the constant damping ratio ζ. This however is not possible in ANSYS for the cyclic symmetry analysis. The α coefficient is multiplied by the mass matrix and the β coefficient is multiplied by the stiffness matrix to form a new damping matrix [C] as shown in equation (1.8), where [M] and [K] is the mass and stiffness matrix respectively.

$$[C] = \alpha[M] + \beta[K]$$

<div align="right">(1.8)</div>

The constants α and β for a large system with many DOF's can be estimated with the method by Chowdhury and Dasgupta (2003). This method makes use of the natural frequencies of the pre-stress condition and is as follows:

The orthogonal transformation of the damping matrix reduces the damping matrix to the following

$$2\zeta_i \omega_i = \alpha + \beta \omega_i^2$$

<div align="right">(1.9)</div>

with i being the ith mode.

If equation (1.9) is further simplified in respect of the damping ratio, equation (1.10) is obtained.

$$\zeta_i = \frac{\alpha}{2\omega_i} + \frac{\beta \omega_i}{2}$$

<div align="right">(1.10)</div>

If equation (1.10) is plotted, the lower natural frequencies are non-linear, but thereafter the higher natural frequencies become linear as shown in Figure 1-6.
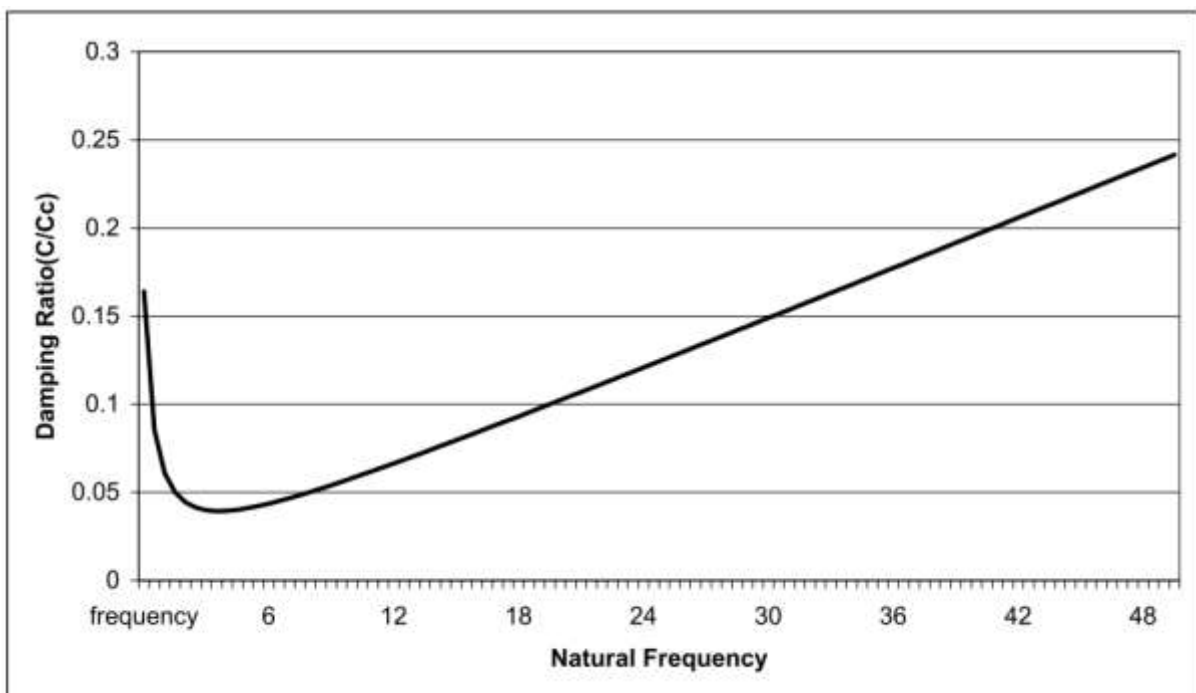

Figure 1-6: Damping ratio vs natural frequency (Chowdhury and Dasgupta, 2003)

For large structures, only the first few modes, which have a significant mass participation, have an influence on the damping ratio. Therefore, only these modes will be considered and instead of applying a constant damping ratio to all modes, a minimum damping ration will be applied to mode one and a maximum damping ratio to the highest significant mode. The rest of the modes are interpolated or extrapolated, for the full range.

As shown in Figure 1-6 the linear section can be estimated using a linear line equation as

$$\zeta_i = \frac{\zeta_m - \zeta_1}{\omega_m - \omega_1}(\omega_i - \omega_1) + \zeta_1 \qquad (1.11)$$

where i is for the ith mode, 1 is for the first mode and m is for the mth significant mode.

Based on the 1st and the mth mode, β can be obtain from

$$\beta = \frac{2\zeta_1\omega_1 - 2\zeta_m\omega_m}{\omega_1^2 - \omega_m^2} \qquad (1.12)$$

and back-substituting β in equation (1.9) α one be calcualted.

Now one set of data is obtained for α and β. A second set can then be obtained by using ζ_1, $\zeta_{2.5m}$, ω_1, $\omega_{2.5m}$. A third set can be obtained by using the average of the values above. And the fourth set is the interpolated or extrapolated data.

The respective damping ratio can be calculated by using equation (1.10). These datasets then need to be plotted on a single graph. From the three generated plots, the dataset which is present in the centre of all the data, should be used. This is seen as the average set, representing the data.

1.2.3.4   Modal analysis

Natural frequencies and mode shapes are important in turbine equipment. Since steam turbines usually operate at very high rotational speeds, it is expected that the blade will go through one or two of the natural frequencies of a blade, during start-up. It is critical that the blade does not operate for too long at or near a natural frequency during the start-up and warm up cycles.

In turbines that have discs, which are flexible interaction between the blades and the disc can be expected. The disc vibration generate a sinusoidal wave, with a certain amount of nodes and travels around the circumference of the disc as it rotates, representing the mode shapes of the disc (Hultman and Groth, 2015). In a one nodal (N) diameter, there are 2xN nodal or zero points where the displacement of the disc is zero. In between the nodal points, there is a local maximum displacement on the one side and a local minimum displacement towards the other side. This is shown in a schematic in Figure 1-7. An interference diagram can be used to plot the disc mode shapes to frequency (Mccloskey, Dooley and McNaughton, 1999b). Interference or SHAPE diagrams (see Figure 1-8) are the natural frequencies of each natural mode at a specific rotational speed against the corresponding number of nodal diameters.
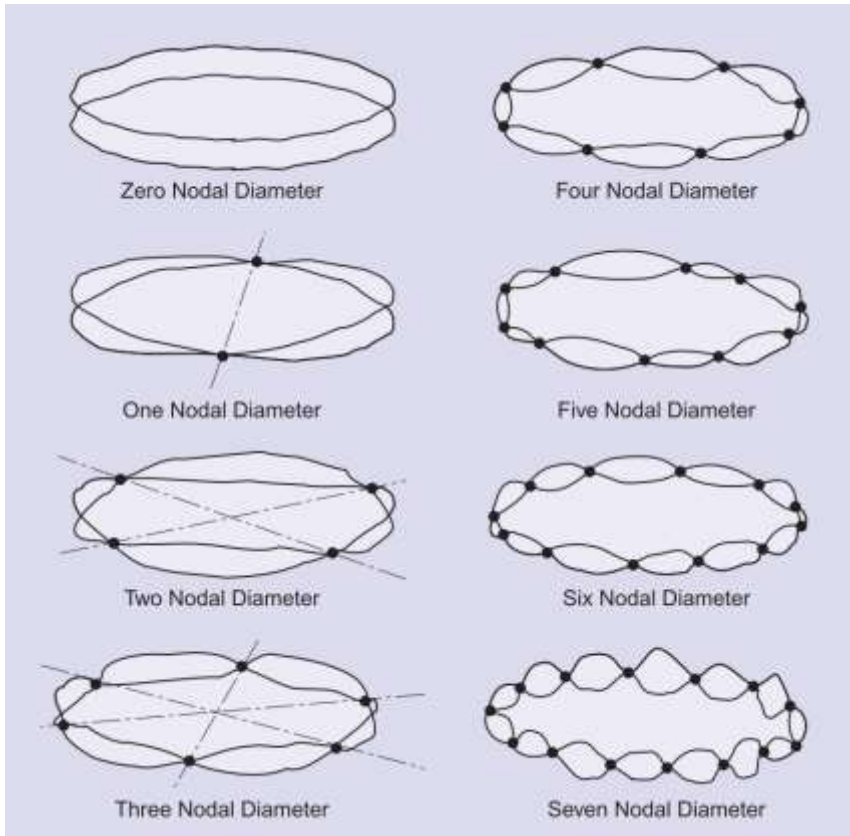
Figure 1-7: Schematic representing nodal diameters or disc mode shapes (Mccloskey, Dooley and McNaughton, 1999b)
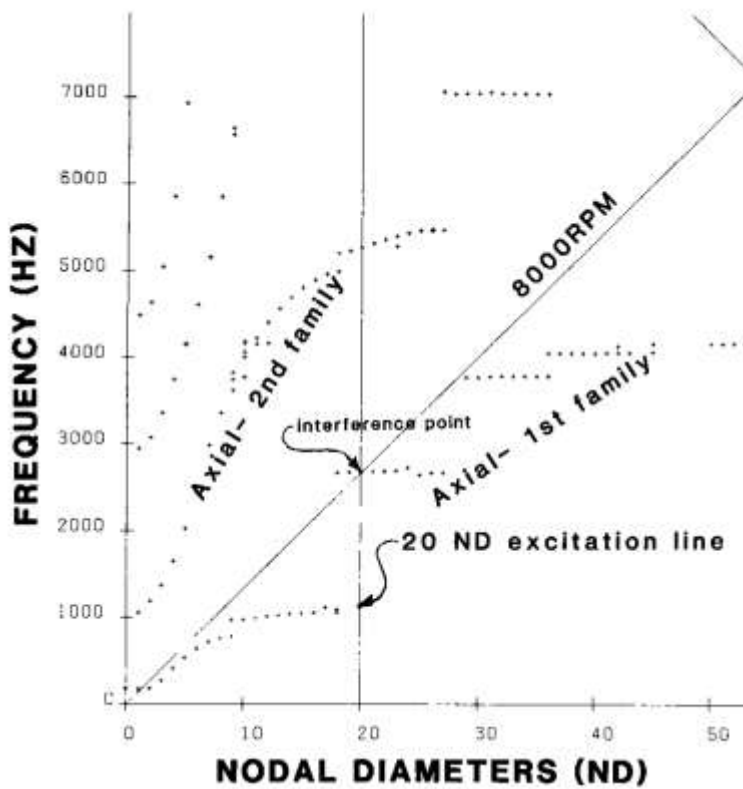

Figure 1-8: Example of a SAFE diagram (Singh *et al.*, 1988)

Natural frequencies for LP blades should usually be at least four times the operating speed (Singh and Lucas, 2011). Also blade natural frequencies which are 10% away from the operating speed or multiples thereof, is considered as well de-tuned and would not cause resonance. On LSB the natural frequency can be closer to operating conditions and a frequency range of 3 to 5% is considered (EPRI, 2008).

Du Toit, (2017), reported that usually the natural frequency of a blade will drop as the temperature increases and this was detected with the BTT tests, which were conducted.

Pre-stress modal analysis is when the static analysis is run to capture any effect which will alter the stiffness or geometry of the model. This ultimately will change the natural frequency of a model (Fung, E.H.K., Yau, 1999).

1.2.4 Turbine blade life estimation based on fatigue

Fatigue is the mechanism where material experience microscopic damage while it is experiencing a varying and repetitive load. This is even possible while the stress in the component is well below the yield stress of the material. It usually starts with a small crack that develops and then grows from there onwards.

The most common LP turbine failures can be allocated to fatigue. This is mainly due to the length of the blade resulting in higher stresses. The last two rows on a LP turbine get drastically affected by its environment, which can speed up failure of the blades.

There are currently three major fatigue analysis methods, which are used for analysing and designing against fatigue:

- First is the **stress-based** method, which usually operates under the elastic range of materials and relates to cases of HCF. This is the oldest and most widely used method and was also the first to be developed. This type of fatigue is normally related to synchronous vibration.
- The second is the **strain based** fatigue method, which relates to conditions where the strain is plastic. The strain-based approach incorporates localized yielding which may be present at stress concentrations and the stress distribution becomes non-linear. This is normally for cases of low cycle fatigue (LCF). This type is normally related to stop and start conditions.
- The final method is the **fracture mechanics** method, which relates to predicting the life of a component after a crack has initiated (Dowling, 2013).

Fatigue analysis is fairly sensitive to the stress range and therefore large safety factors are used when designing turbine component. Safety factors of 5 to 20 or even more are common (Dowling, 2013). LCF is evident where mechanical deformation or plastic deformation is present at the failure surface and normally occurs in areas near the blade roots (Mccloskey, Dooley and McNaughton, 1999b). Since very large numbers of cycles are applied in service, the concept of safe stress or fatigue limit may not be valid.

According to Mccloskey, Dooley and McNaughton (1999b) stall flutter can be classified as a HCF mechanism. The aerodynamic instability usually causes a group of adjacent blades to fail.

According to Perkins and Bache (2005) the long service of power generating equipment, though well designed, will result in failure some time or other. The component with the highest risk of failure is usually the LP and the common failures occur due to fatigue or environmental assisted fatigue.

Well designed blades generally have vibratory or dynamic stresses of 6-20 MPa, but as soon as stresses of 55-62 MPa are observed it critical to the integrity of the blade. This can easily be achieved in resonance conditions where the stress can increase to as much as $10 - 20$ times (EPRI, 2008).

1.2.4.1   Mean stress effect

Fatigue tests are generally conducted on materials by means of a rotating bending fatigue assessment, where the test sample experiences a fully reversible load. This is mainly done due to the simplicity of the test and high cycles can be achieved within a reasonably short time. However, in practice equipment very rarely see loads with a zero mean (fully reversible). Therefore, many studies were done in the past to consider the effect of mean stress on the stress or strain-life of materials. Some of the most common approaches are the Gerber, Goodman, Morrow, Smith-Watson-Topper (SWT) and Walker. According to Dowling (2010) the modified Goodman is highly inaccurate, with Morrow having introduced substantial improvement. Nevertheless, Morrow's work that employs the fatigue strength coefficient may not be accurate at all for metals other than steel.

The fatigue life of any component is influenced by the presence of a static mean stress. In turbines, the centrifugal force generates this mean stress, by spinning of the blade. Previous studies have shown that components with an increased mean stress had a decreasing endurance limit.

The mean stress effect is classified in three sections:
1. A **completely reverse cycle** is classified, where the mean stress is zero and the stress ratio is one.
2. The **zero-to-tension cycle**, refers to applications where the minimum stress or stress ratio is equal to zero.
3. The **tension-tension cycle** is where the mean stress is greater than the amplitude. Such applications are more damaging where the tensile mean stress has shown to have a noteworthy effect on lowering the life of a component (Bader and Kadum, 2014).

Mean stress correction was investigated to eliminate having fatigue testing being done at various mean values and could be related or corrected to the completely reversed cycle. Mean stress correction with Goodman modification, show to be more accurate and mostly used in practise (Bader and Kadum, 2014).

1.2.4.2   Rainflow cycle counting

Many different cycle counting methods can be used to count a random time signal. However, the rainflow cycle counting algorithm is widely used. It makes use of half cycles and full cycles counting, which can be added to each other. It also counts cycles based on amplitudes and mean values. The rainflow cycle counting is normally displayed in a matrix form. Visually it gives very good information on the cycles and type of loading which is present during the time period (Niesłony, 2009).

The ASTM E1049-85 standard describes rainflow cycle counting in detail, where maximum peaks and minimum valleys are extracted from a time-base signal and counted according to amplitudes and mean values. An example of the algorithm is shown in Figure 1-9 (Niesłony, 2009).
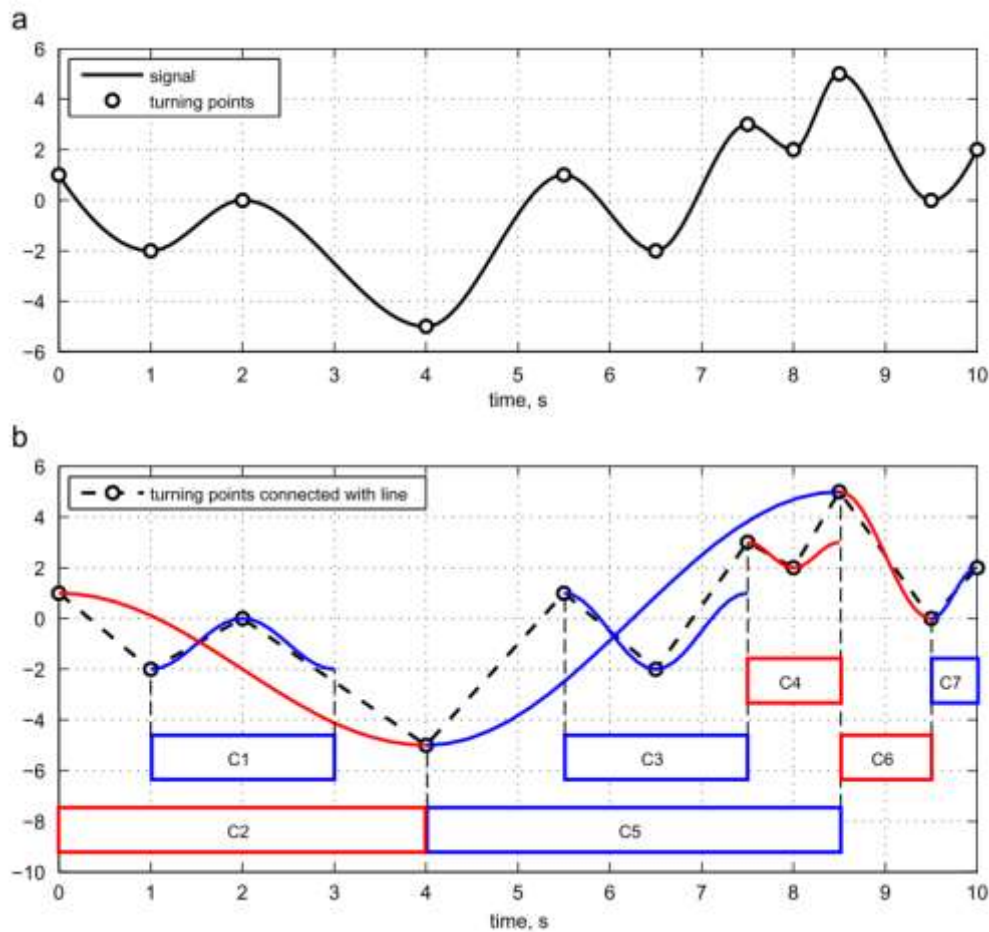

Figure 1-9: Rainflow cycle counting according to ASTM E1049-85 (Niesłony, 2009)

The rainflow cycle counting method however does not take into account the sequence of effect on the data and according to Zakaria et al., (2016), the sequence of loading does have an influence on the fatigue life.

1.2.4.3 Damage or life assessment

With known material properties, the number of reversals could be calculated according to equation (1.13). Where S_{FL} is the stress fatigue limit, σ_f the fatigue strength coefficient and b the fatigue strength exponent.

$$N_{FL} = \left(\frac{S_{FL}}{\sigma_f} \right)^{\frac{1}{b}}$$

(1.13)

In order to incorporate the Morrow mean stress correction, equation (1.13) can be re-written as

---

$$N_{FL} = \left(\frac{\sigma_a}{\sigma_f - \sigma_m} \right)^{\frac{1}{b}} \tag{1.14}$$

The damage can then be calculated per node or element from the FEA results. This is achieved by taking the number of cycles (n) the node or element has experienced at a specific amplitude and mean and divides it by the number of cycles to the fatigue limit (N_{FL}) for that specific amplitude (See equation (1.15) for the Palmgren Miner rule). This is done for all the different amplitudes and cycles the node or element has experienced. When the damage is added and equal to 1 the component has failed.

$$D = \sum \frac{n}{N_{FL}} \tag{1.15}$$

The damage can then be used to calculate the expected life as per equation (1.16) from the amount of damage and time that caused the damage.

$$Life = \frac{1}{D} \tag{1.16}$$

Since the data in use is for a certain time span, the data can be converted to total life or total cycles by multiplying equation (1.16) by the original time period as shown in equation (1.17) (Niesłony, 2009).

$$Total\ Life = \frac{T_0}{D} \tag{1.17}$$

1.2.4.4 Material fatigue properties

In ultra high cycle fatigue (UHCF), with cycles above 10^8 cycles, crack initiation is subsurface, rather than the normal surface crack initiation. These cracks normally originate from internal inclusions (Wang, Khan and Bathias, 2012). The main mechanism of failure for UHCF is hydrogen embrittlement and dispersive decohesion of the spherical carbide. As a result of hydrogen surrounding the inclusions it is believed that hydrogen play an essential role in UHCF failure (Ming *et al.*, 2014).

According to BS 7608:1993 at high cycle fatigue or UHCF of low stress cycles with high numbers of repetitions can start to contribute to fatigue failure and propagate. In order to compensate or allow for this the S-N curve slope is modified at the so called endurance limit of 10^7 cycles, changing the slope from m to (m+2) making the slope shallower. The Haibach S-N curve corrections suggest similar results with the slope being modified by $(2m + 1)$ (Schijve, 2003).

It is known that vibration at frequencies up to 100 Hz has no impact on HCF, but this is not necessarily the case for very high cycle fatigue (VHCF). Research has shown that fatigue strength decreases about 50 to 200 MPa when cycles experienced ranges from 10^6 to 10^9, depending on the material. Crack initiation in the VHCF regime is normally internal and normally starts with internal defects or large grains. Inclusion in high strength steel, will act like stress concentrations and play a critical role in

gigacylce fatigue. Low strength steel with maximum tensile strength of less than 1100 MPa, will normally crack on the surface (Palin-luc and Jeddi, 2018).

FV566 material operated in humid and corrosive environments showed considerable decrease in fatigue strength. The crack will initiate due to oxide inclusion and causes an initial transgranular crack, which is not present in the non-oxygen environment (Perkins and Bache, 2005).

Lee and Song, (2006); investigated and compared various methods to get material properties for strain-life fatigue properties, using material hardness. For steel the modified universal slopes method is the best method to be used is the, but the ultimate tensile strength and fracture ductility data of the material should be known. When this is not available, the uniform material law (UML) or the median method could be utilized.

There are a couple of different models, to get estimates of material fatigue properties. However the method to be used depends on the type of material, alloy and available data. The UML is a common way of estimating fatigue properties of material for when all the fatigue properties are not know. The UML uses only the ultimate tensile strength of a material. This method however is not applicable for high strength steel and high alloy steel. Therefore the UML was extended to high strength and high alloy steel and called the Extended Universal Material Law. The equations for the two laws are compared in Table 1-2.

Table 1-2: Equation comparison between the conventional UML and the extended UML (Sinan Korkmaz, 2008)

	Conventional UML	Extended UML
σ_u	400-2400	400-2400
E	210	210
H'	$1.61 \cdot \sigma_u$	$\dfrac{\sigma_f'}{\left(\varepsilon_f'\right)^n}$
n'	0.15	b/c
σ_f'	$1.5 \cdot \sigma_u$	$\sigma_u \cdot (1 + \psi)$
ε_f'	$0.59 \cdot \psi$	$0.58 \cdot \psi + 0.01$
b	-0.087	$-log\left(\dfrac{\sigma_f'}{\sigma_E}\right) \cdot \dfrac{1}{6}$
σ_E	$0.45 \cdot \sigma_u$	$\sigma_u \cdot \left(0.32 + \dfrac{\psi}{6}\right)$
c	-0.58	-0.58
ψ	$\psi = 1$ for $\frac{\sigma_u}{E} < 0.003$ $\psi = 1.375 - 125 \cdot \left(\frac{\sigma_u}{E}\right)$ for $\frac{\sigma_u}{E} > 0.003$ and $\psi \geq 0$	$0.5 \cdot cos\left(\pi \cdot \dfrac{(\sigma_u - 400)}{2200}\right) + 1$

According to Rieger and Salzman, (2005) who investigated life estimation on turbines, the fatigue life estimation is heavily dependent on the fatigue strength exponent, b. An 6% decrease of the numerical value b, give rise to a 5 times increase in estimated life.

Applying shot peening to a blade root, creates an additional source of residual stress on the blade. This is contrary to just relying on the overspeed plasticity, which is created on some areas of the pull faces. The advantages of shot peening in situation of fatigue are as follows:

1. It lowers the mean stress of the static load, resulting in longer life
2. By adding a compressive stress on the surface it reduces the chances of having a crack on the surface since it first needs to overcome the residual stress.

An illustration of the residual effect of a blade root, at the top serration at various loading conditions is shown in Figure 1-10. The blade used for this test was of the same configuration and material as the blade under investigation (Newby, 2013).
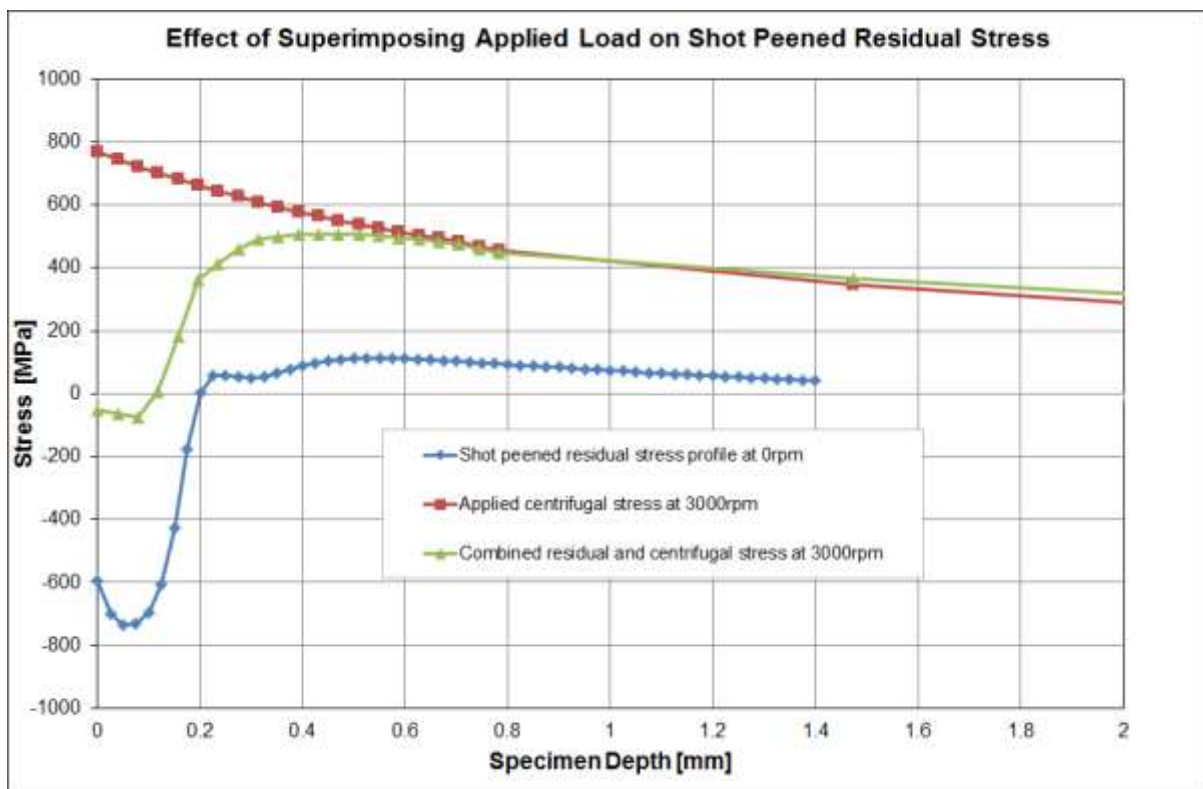

Figure 1-10: Illustration of a shot peened residual stress profile on a turbine blade combined with centrifugal loading and the stress raiser at the top of the fir tree serration (Newby, 2013)

The effect of residual stress in the blade roots gets reduced with increasing cycles near the yield stress of the material. Extrapolated data from test data show that residual stress can reduce by as much as 150MPa for 10^6 cycles at a level of 50 microns below the surface (James *et al.*, 2010).

1.2.4.5   Plasticity

In new blade installations for steam turbine applications, the rotor is run at an overspeed of 20% (EPRI, 2008) of normal operating speed in a balancing pit, to ensure that initial plastic deformation occurs. The plastic deformation is important for the life of the blade. This is due to the strain hardening which

occurs and then also the compressive residual stress which is created on the blade root. A normal overspeed test is done on site at 10% of normal operating speed, which is higher than what the blade will see in normal operation and lower than the initial 20% overspeed.

Plasticity normally occurs at high stress regions due to localized stress concentrations or stress raisers. This is normally used in strain-base fatigue analysis, where there is an elastic and plastic strain region. The stress strain curves for the elastic and plastic regions are combined with the Ramberg–Osgood relationship as shown in Figure 1-11 with equation (1.19). The yield stress is estimated using equation (1.20).

In cases where the stress exceeded the yield stress of the material, the stress needs to be adjusted to incorporate the reduction due to plastic relaxation of the material. This is sometimes called true stress. Local yielding can be handled in two ways during a FEA:

- An elastic plastic analysis could be run, with a number of repeated iterations to converge to the true stress.
- A linear elastic analysis could be run and elastic correction could be done by using Neuber's hyperbola, equation (1.18) and the Ramberg Osgood equation (1.19).

Due to the highly localised stress in turbine blades the second method can be applied with high accuracy (EPRI, 2008).
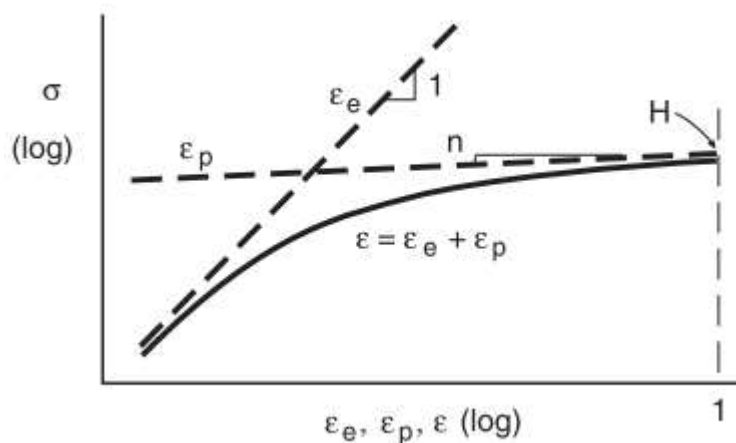

Figure 1-11: Ramberg–Osgood relationship (Dowling, 2013)

$$\sigma_e{}^2 = \sigma \cdot \varepsilon \cdot E \tag{1.18}$$

$$\varepsilon = \frac{\sigma}{E} + \left(\frac{\sigma}{H}\right)^{1/n} \tag{1.19}$$

$$\sigma_0 = H(0.002)^n \tag{1.20}$$

The plastic strain terms of a cyclic stress-strain curve can be estimated by equations (1.21) and (1.22) (Dowling, 2013).

$$n' = \frac{b}{c} \tag{1.21}$$

$$H' = \frac{\sigma_f'}{\left(\varepsilon_f'\right)^{n'}} \tag{1.22}$$

ANSYS has various plasticity models, which could be used under the material model. The most common models are:

- Bilinear Isotropic Hardening
- Multilinear Isotropic Hardening
- Bilinear Kinematic Hardening
- Multilinear Kinematic Hardening

With the Isotopic hardening model it is assumed that the yield surface or value increase due to work hardening and therefore it is assumes that the tension and compression are maintained equally; while the kinematic hardening model assumes that the elastic range stays constant. The result of this is shown in Figure 1-12, where a real material is somewhere in between. The bilinear kinematic hardening rule was implemented since this is more conservative.
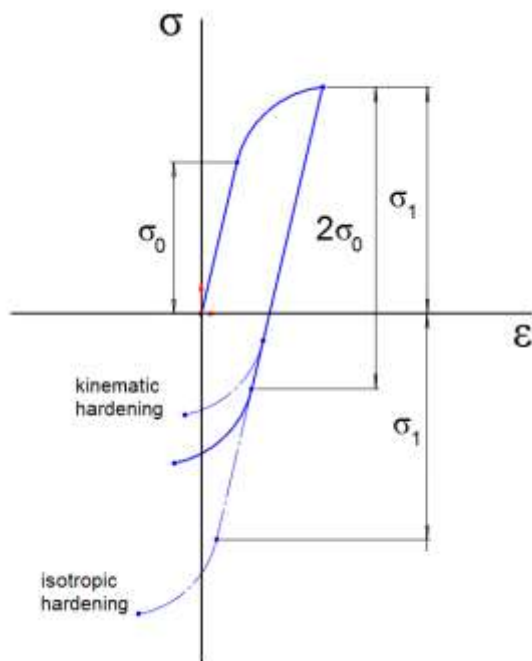

Figure 1-12: Kinematic vs isotropic hardening

1.2.4.6   BTT as a input to fatigue estimation

With the use of a BTT system information can be obtained on the dynamic and vibratory response on all individual blades. This data can then be used to effectively do real time fatigue estimation on each

blade. This method was implemented and visualised by Balda (2018), where data captured by BTT together with material testing and FEA modal analysis give good estimates of the blade remaining useful life (RUL). The method makes use of the stress tensor developed (using FEA modal analysis), the rainflow data (from the BTT analysis) and the initial provided material model to calculate the blade damage using Miner's rule. The residual fatigue life of blades is calculated in real time and the data is superimposed on the history data. Relative damage of all the blades is plotted as shown in Figure 1-13.
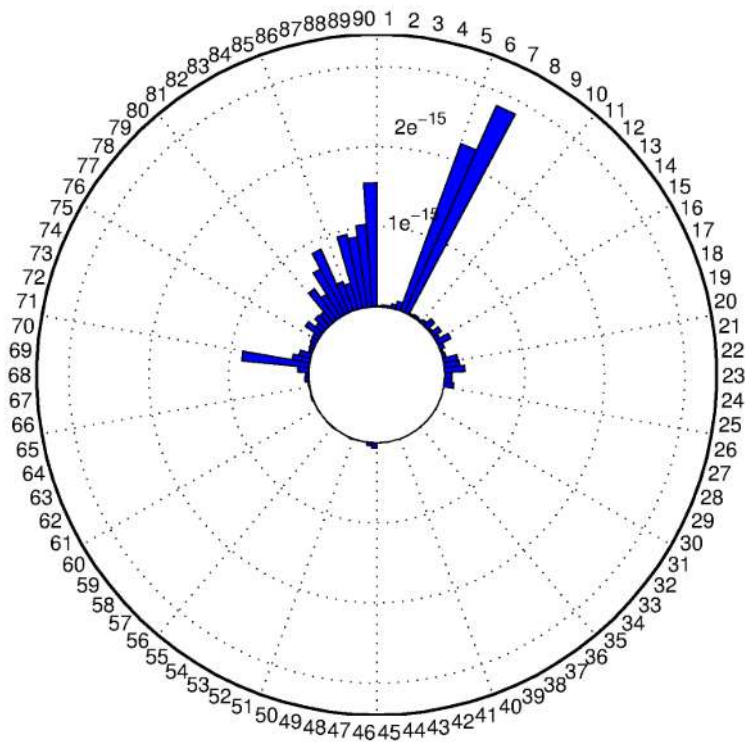
Figure 1-13: Relative damage of all blades (Balda, 2018)

Diamond, (2016), looked at rotor blade probabilistic fatigue damage determination using BTT data and compared this to deterministic approach of fatigue damage. His work stipulate different methods to get from the raw BTT data to some meaningful engineering data, including vibration, tip displacement and frequency content. Typical errors of BTT algorithms are up to ±30%, which can result in estimated cycles being 100 times higher. However if a probabilistic approached is followed it can result in highly accurate results. The method becomes more accurate as more revolutions are used for the calibration process.

When simulations are conducted, two common assumptions are made concerning the response of the blade:

- Blade response are simulated to be perfectly sinusoidal or in the case of multiple engine orders a superposition of perfect sinusoids. In practise, the blade spectrum is composed of multiple frequency components comprehending all the structural dynamics characteristics.
- Blade deflections are calculated based on a simulated zero position, determined through data zeroing in practice, which is very difficult to accurately determine while the blade is in operation.

Knappett and Garcia, (2008), correlated BTT data with strain gauges data and found this to be within their quality checks set and therefore within correlation. Detail considerations were done, which included telemetry roll-off characteristics, strain gauge temperature compensation, BTT zeroing and BTT noise suppression with low pass filters. The BTT results tended to measure higher than the strain gauge, when converted to the amplitude-frequency level via the FEM. A general assumption was made that only one mode was present during measurements. If two modes were present, there was no way to calculate the response of each mode's amplitude.

Witos (2003) used BTT data together with modal analysis to detect changes in compressor blade behaviour. The experimental modal analysis method was used to characterise a defect free blade, which remain continuous under resonance conditions and showed good symmetry around the resonance frequency. When a cracked blade was compared to the resonance curve shape an asymmetric curve was identified with a resonance attractor (S_n) and a non-resonance attractor (S_r) as shown in Figure 1-14. Fatigue data analysis showed material strengthening and material weakening phases as depicted in Figure 1-15 and Figure 1-16 respectively.
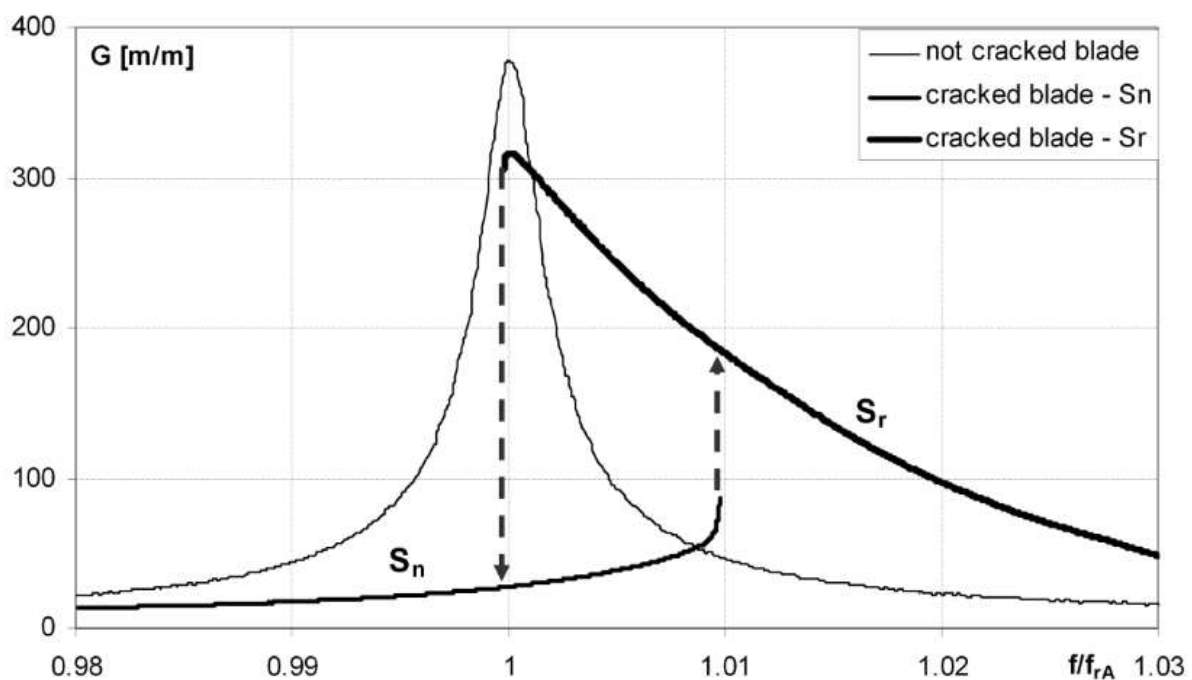

Figure 1-14: The effects of a crack on the firs mode characteristics shape (Witos, 2003)
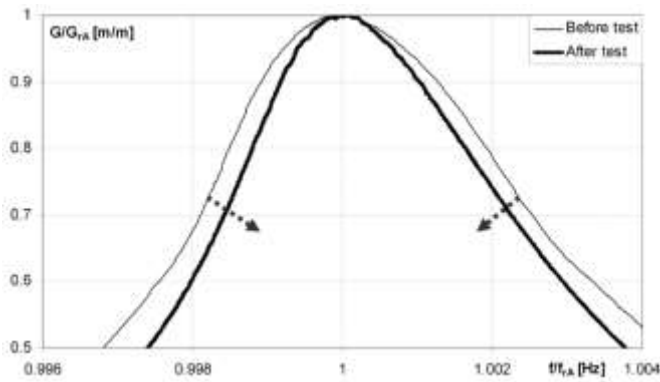
Figure 1-15: Changes in modal parameters during material strengthening phase (Witos, 2003)
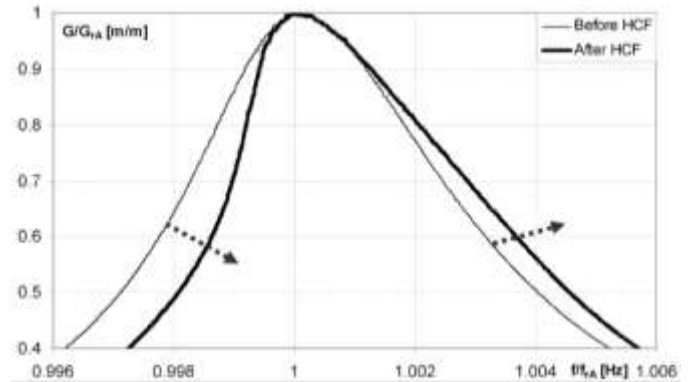

Figure 1-16: Changes in modal parameters during material weakening phase (Witos, 2003)

1.3 Scope of research

The power utility under consideration has a large fleet that uses the specific last stage LP blade design considered in this investigation. On this LP blade, several blade root cracks have been noticed. One of the possible mechanisms identified is non-integral blade vibration, which is included in this investigation. This however is not seen as the only cause, but possibly one of the causes. Various SCC have been identified in the past in the 12% chrome blade material, susceptible to SCC. The 12% chrome material is sensitive to conditions of SCC and therefore blades are currently being replaced by 14% chrome steel, which is more resilient to SCC.

Some units have experience several occurrences of low vacuum and while the reasons for low vacuum are investigated, the unit is still operated with low vacuum condition. It is known from the literature that this can have detrimental effects on the blade, which can cause crack initiation, growth, and eventually failure. A catastrophic failure is something which no utility wants, since it involves high repair or replacement cost as well as long unavailability of the unit. This is also not considering the high safety risk that is involved to the people working near the turbine.

The intention of this study is to better understand what the possible damage or life expectancy of a LSB can be, while running at or near these conditions. These effects are not well described in the literature, even though a lot of research was done to understand the mechanisms that cause blades to fail under these circumstances. It is known that a blade can experience vibration, whether it be due to blade resonance, excitation due to operating frequency or integral orders of it or even flutter. It is however not known is how long or how many times can this occur before this will become a problem.

In order to learn more about the vibration effects of blades under off-design conditions, the data from a BTT system will be utilised. There however is not much known for this specific blade design of which mechanism is present during high backpressure. Therefore, the actual vibration frequency and amplitude will be extracted from BTT data to aid in this analysis. BTT systems in general, are well developed and BTT is becoming more commonly used in practice. BTT can provide relevant information about the vibratory state of all the individual blades and identify abnormal vibration of a single blade. According to Diamond (2016) there is still work being done on BTT systems to overcome aliasing of the data and to accurately capture the exact time when the blades pass the sensor. This

has the result that the actual recorded displacement, deflection, or vibration might not be as accurate as expected to be. Much research time is therefore spend on this topic at the moment, but in the meantime BTT data can be used to investigate the effect of vibration on a blade. The OEM performed a series of tests at low vacuum and low load conditions, causing high backpressure on the LSB and the data was recorded via a BTT system. The data was post-processed and was provided as input for this investigation. The data presented a dominating vibration frequency of one of the modes, which was used in the analysis.

The aim of this study is to look at the structural integrity of the blade, under centrifugal load. The investigation will focus at full speed conditions, while undergoing non-synchronous vibration. The study will include plasticity present in the blade by overspeed, mean stress, dynamic stresses, material fatigue properties and stiffening of the blade from damping pins. The vibration is usually a blade natural mode, which is excited, that cause vibration with minimum energy input. It will assume that only one mode is excited and that no other mode is present to participate in fatigue life analysis. This mode will be presented as a perfect sinusoidal vibration. This will be assumed mainly due to the inability of BTT systems to give more accurate results.

Various other mechanisms are also present during low flow conditions in the LSB, for example erosion, heat rejection, wet steam, recirculation, flow separation, etc. This dissertation only focuses on the vibratory aspects during low flow conditions, causing fatigue and limit of life. The steam load on the blade was neglected due to low influence on the overall load and stress in the blade according to Mccloskey, Dooley and McNaughton, (1999a). Also the blade tip timing (BTT) data will capture the effect of the steam load in the displacement measurement. More detail on the CFD analysis for this particular blade design is documented by Maré (2018). Low load conditions can generally cause wet steam to be present in the LP turbine last couple of stages, which can be detrimental to the life of the blade. The wet steam condition will however not be analysed, but it is acknowledged that it can cause the blade to fail sooner than expected due to these conditions. The dissertation focuses on fatigue based crack initiation and does not include fracture mechanics to establish crack growth principles. This work does further not include life depletion due to start-up conditions and more information about fatigue during start-up is recorded by Booysen (2014).

It is noticed that excessive erosion and SCC can cause changes in the natural frequencies of the blade and can cause structural defects. Both these effects can cause the blade to fail earlier than predicted by fatigue methods, but this is very difficult to quantify and therefore not included in this dissertation.

The main focus of the dissertation is to use the vibratory response at high backpressure conditions and estimate the fatigue life of a blade, while operating in this condition. The work is based on two assumptions: first that the dominant resonant frequency is the only mode, which is excited, and secondly the vibrational response is simulated as a perfect sinusoid. The BTT system measures the tip displacements at a dominant frequency, which is related to a mode shape with an associated stress. This dynamic stress can reduce the life of the blade. Life or damage data can be used to predict the inspection intervals. If significant damage or vibration is calculated using the method developed in this investigation, a unit can be stopped and inspected before accumulative damage is done. At worst

accumulative damage can lead to catastrophic failure, which can result in high financial losses and has critical safety implications.

The analysis was further extended to investigate the fatigue damage if another mode were to be excited, but having the same vibratory response measured by the BTT system. It should be noted that this extension is a very crude way of looking at the results. This is due to the mode shape and vibration patterns which can be vastly different between the different modes and frequencies. This can result in higher or even lower displacements with different vibration patters, than what was recorded from the BTT system and used in the analysis.

1.4   Document overview

The dissertation is divided into five chapters. The first chapter is an introductory overview of the research. The literature study provides a broad overview in the field of turbine dynamics as related to blade vibration. The study mostly highlights the area of the LP steam turbine and effects, which cause or prevent vibration and the effects on the blade. It also covers some of the theoretical and mathematical aspects, which are required for this research.

Chapter 2 focuses on the development of the geometry, critical for setting up of the FEA model, including the selection of boundary conditions, mesh and creating material properties. It also includes assumptions on which the FEA model were based. A modal analysis is conducted to characterise the blade natural frequencies, with the centrifugal force as a pre-stress condition to the modal analysis.

The experimental validations and verification of the FEA setup are covered in Chapter 3. This was done with data from a spin test done in a balancing pit and impact testing of blades. A Campbell diagram is used to show the comparison, to ensure the FEA results are accurate and can be used for the BTT and fatigue analysis.

Chapter 4 covers the fatigue analysis using the BTT data and how FEA is used to get comparative stress for the BTT data in the root of the blade. It explains the relationship between the measured BTT data and the FEA and formulates calculations. It also explores different methods to calculate fatigue properties, used in the analysis. Then it concludes with the process followed to do the fatigue analysis and the fatigue results for both low load and high load conditions in low vacuum, which cause high backpressure on the LSB.

Chapter 5 concludes with the research results and outlines possible areas of further investigation and future work.

Chapter 2

Finite element model and analysis

This chapter focuses on the geometrical setup as well as the boundary conditions, mesh and material properties required to run the FEA model. The chapter also includes assumptions, on which the FEA model is based. The FEA is done with the ANSYS software. A 3D analysis was used, due to the complex geometry of the blade. And the blade used in this investigation goes from an impulse turbine at the root to a reaction blade design at the tip. A 2D analysis would have not accurately capture this blade's behaviour.

2.1 Geometry analysis

The particular LP last stage blade used in the investigation has an aerofoil height of 945mm, has a 5-land curved side entry root with a fir tree profile (see Figure 2-1) and a blade to blade interconnection lacing rods or damping pins at 86% height. The rotor is a double flow turbine with 78 blades per stage and a blade mass of about 24kg. The lacing rods are used as inter-blade connections to add damping. Figure 2-2 shows different types of LP root designs widely used, while Figure 2-3, show different types of inter-blade connection. The blade under investigation was originally designed using configuration (a) for the root and configuration (f) for the inter-blade connections.
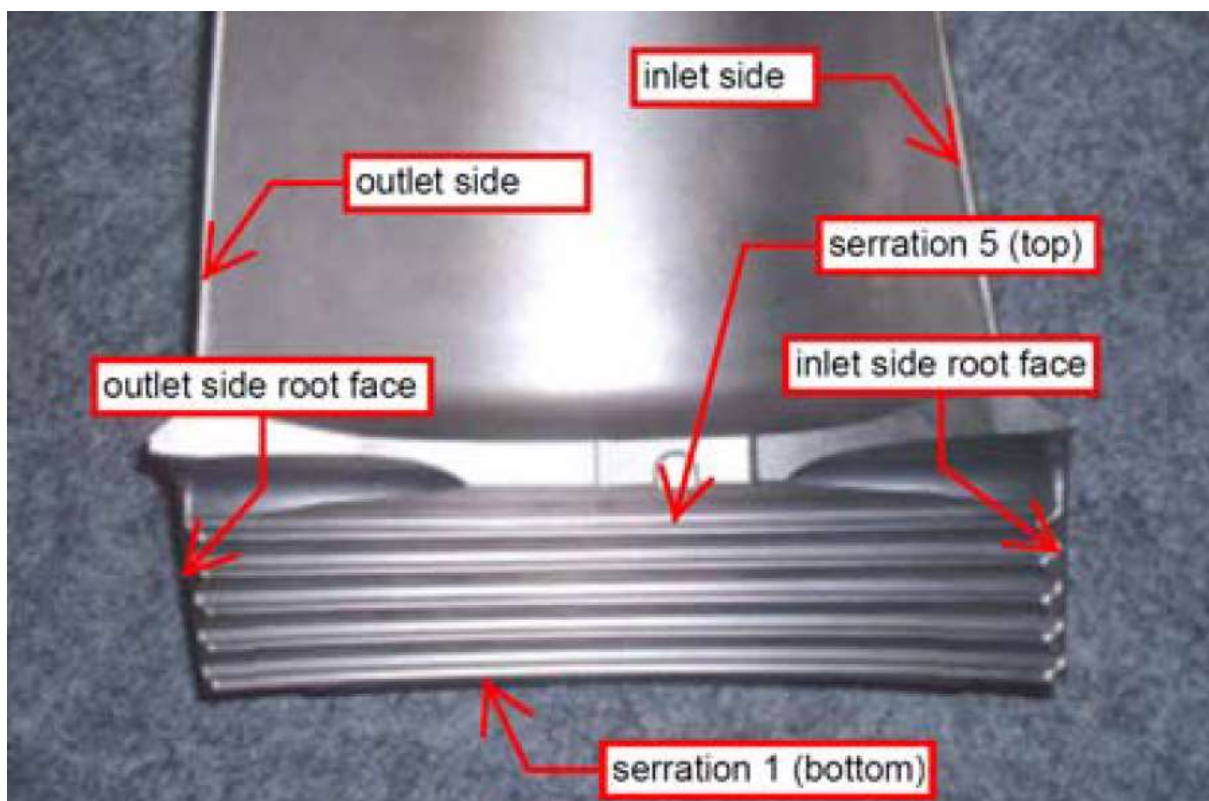

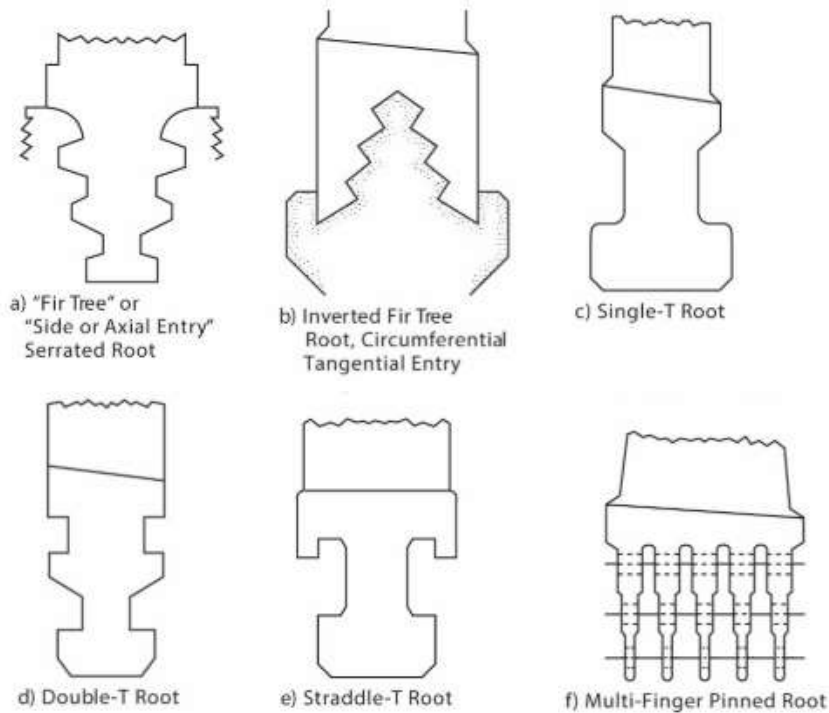**Figure 2-1:** Blade root description (Scheepers and Booysen, 2012)

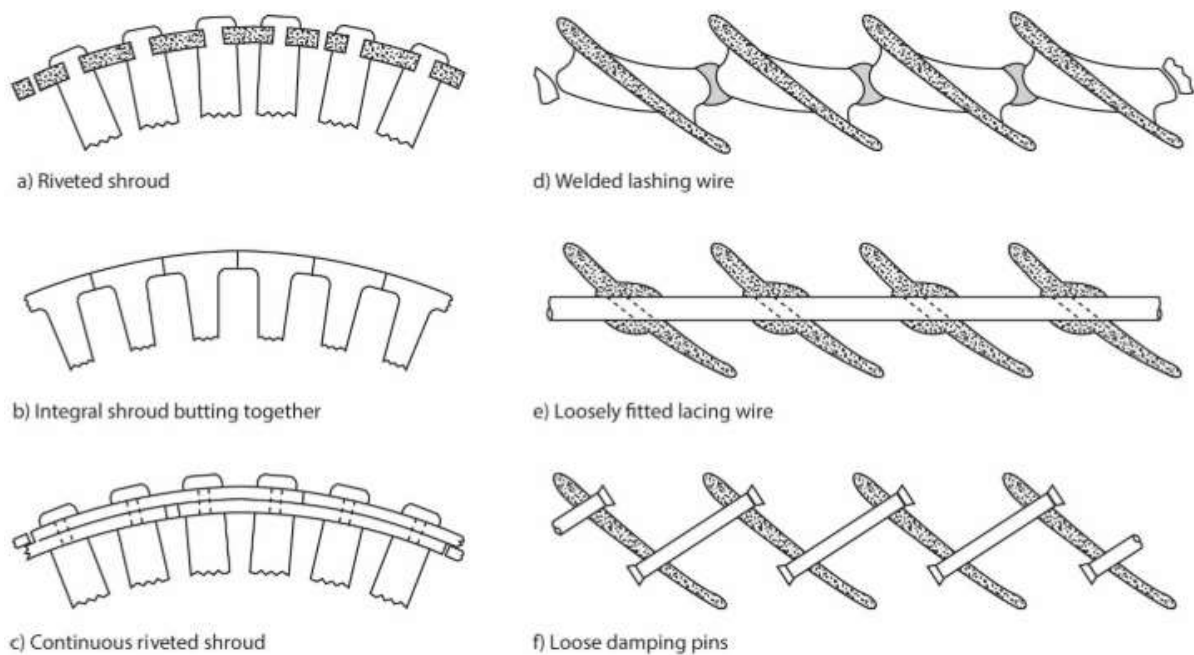**Figure 2-2:** Typical types of LP blade root design (EPRI, 2017)

Figure 2-3: Typical types of inter-blade connections (Mccloskey, Dooley and McNaughton, 1999b)

Due to a high stressed region on the root and potential small changes effecting huge stress pattern changes, an accurate model of the LSB with an understanding of the interfaces with rotor is required. This was achieved using 3D scans to get accurate 3D geometry models of the LSB and rotor.

This was accomplished by using the ATOS Core Scanning System together with ATOS's Professional Software package to perform the 3D scanning of the components as shown in Figure 2-4. The ATOS Core system uses a stereo camera set-up working on the principle of triangulation. The sensor projects different fringe patterns onto the object's surface. These patterns are recorded by the two cameras, forming a phase shift based upon sinusoidal intensity distributions on the camera chips. ATOS Core uses multiple phase shifts based on the heterodyne principle to achieve highest sub-pixel accuracy. Independent 3D coordinates are automatically calculated for each camera pixel, based on the optical transformation equations. The projection technology developed by GOM operates with narrowband blue LED light. As a result, precise measurements can be taken independently of ambient light conditions. The robust blue light technology has an extremely long service life, minimum heat development, and low maintenance costs (*ATOS Core*, no date).
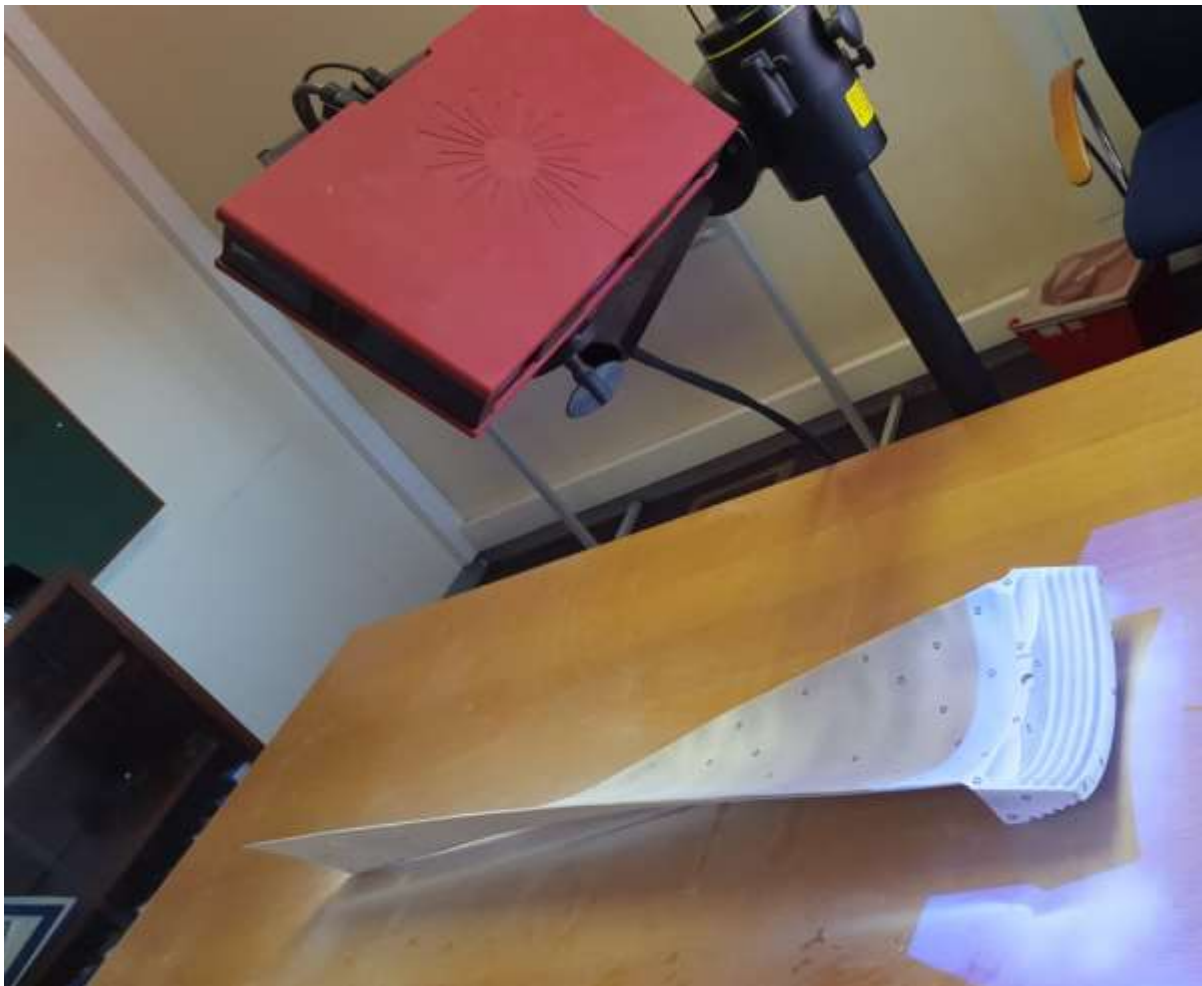

Figure 2-4: Illustration of the ATOS Core 500, capturing the blade

The LSB, shown in Figure 2-5, was prepared for scanning. LD 7 developer was sprayed on the component to reduce reflection and the markers on the blade were used for reference during the scan. It uses the dots to recognise the position of the part in the scan and to overlay or position the images that where taken in a 3D point cloud.

After scanning of the blade, the data was converted to a 3D mesh standard triangle language (STL), which was used for further analysis in GOM Professional. The final scanned blade shown in the GOM professional software can be seen in Figure 2-6.

From the software, various geometric entities, like best fit planes, cylinder circles etc. can be created to aid with constructing the appropriated geometry. These entities are then used to align the scanned geometry in a coordinate system, from where section of the scanned geometry can be exported to a computer aided design (CAD) package. The sections are then used to generate a CAD model and the CAD model can then be compared to the actual scan data to by overlaying it to see how close the CAD compares to the scan. The blade comparison can be seen in Figure 2-7. The hot spots shown in the figure are mostly due to wear or imperfections on the blade, since this scan was a worn blade that was previously in service.

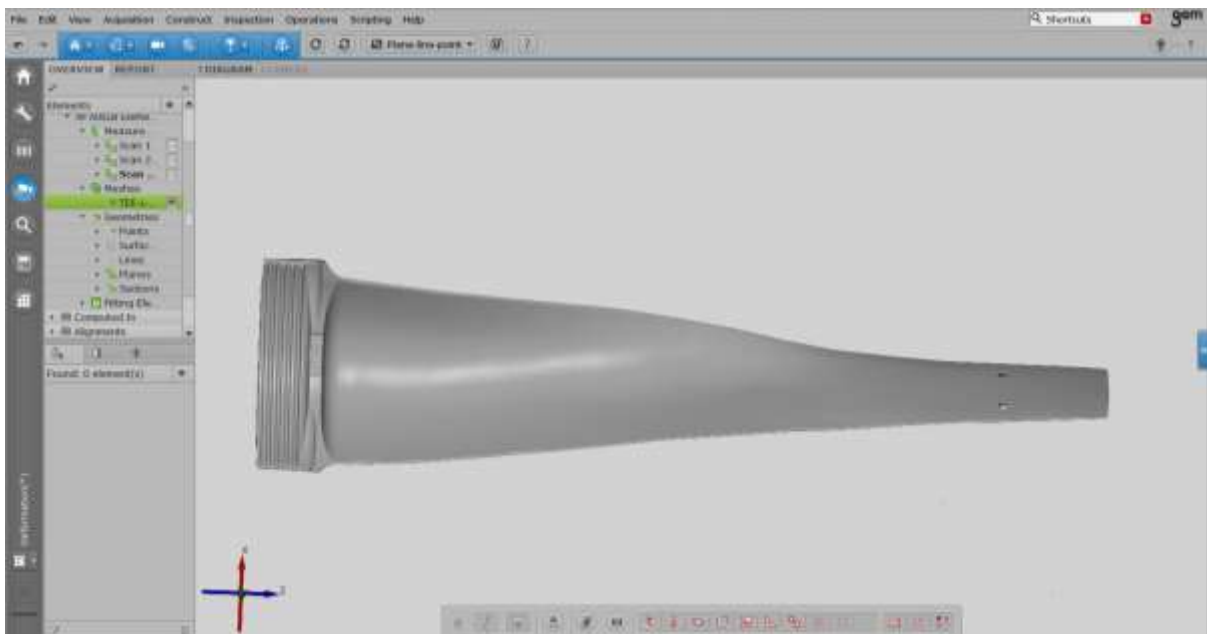**Figure 2-5:** Preparation of blade for 3D scanning

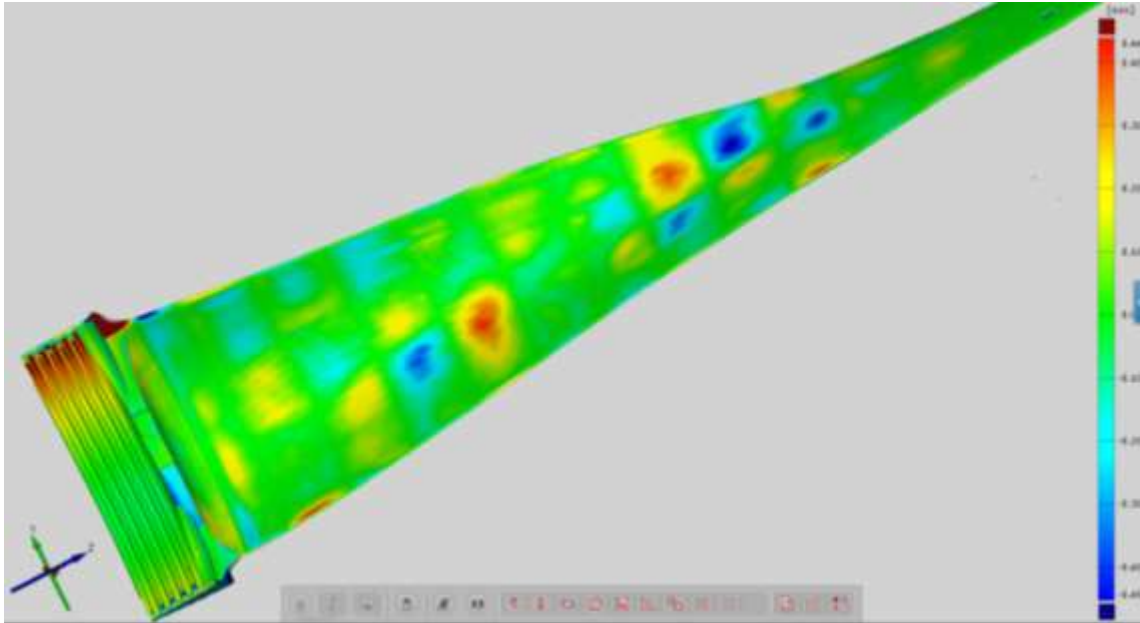**Figure 2-6:** LSB shown in GOM Professional

Figure 2-7: Comparison of CAD geometry to the scan data

2.1.1 Comparison of root fit

In order to create an accurate FEA model a good understanding of the interaction of the blade and the rotor is needed. To do this the rotor and blade 3D scans were superimposed as shown in Figure 2-8. A section was then taken 10 mm from the sides and in the centre of the rotor to check how the two parts fit. Figure 2-9 shows the blade touching at the top face on the serrations and by measuring the gap between the blade and the rotor some conclusions can be made:

- The gap seems fairly constant between all the serrations, with an average of 242 µm
- The difference between the maximum and the minimum gaps compared to the average gap are calculated as 64 µm

Based on the first finding it was assumed that the fit between the blade and rotor is uniform. The CAD model was modelled to represent the uniformity.
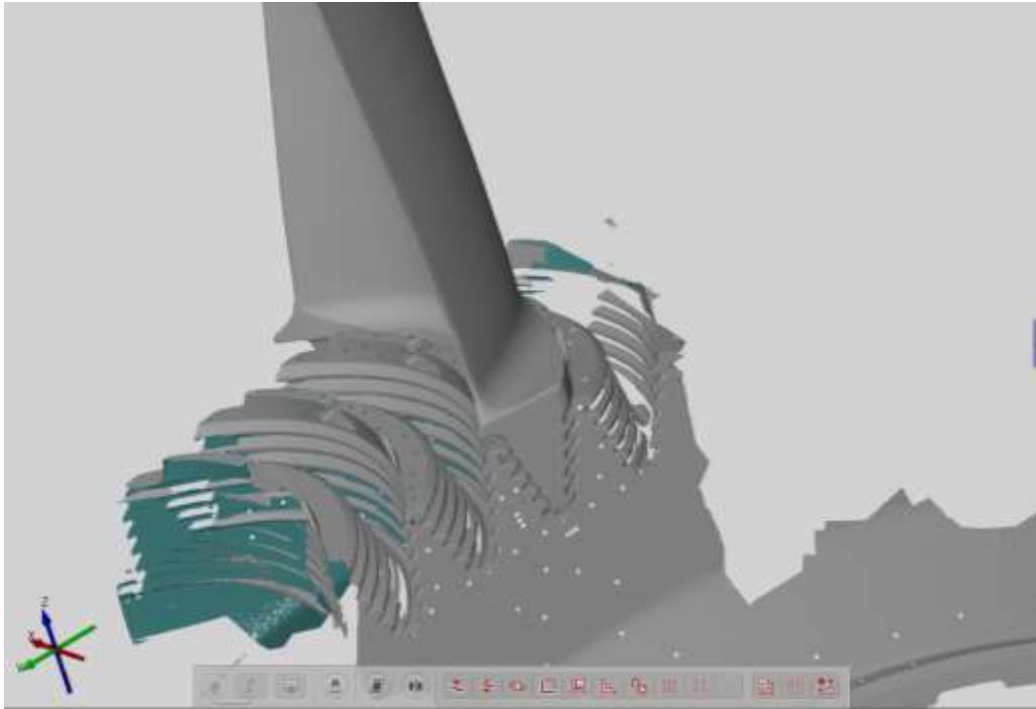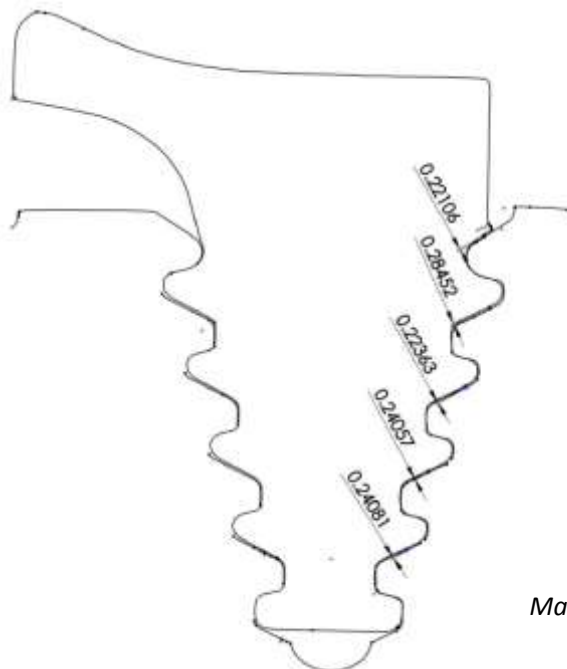
Figure 2-8: Superimposed blade and rotor in GOM Professional

Actual gap [mm]	Difference from average [µm]
0.22106	-21
0.28458	42
0.22363	-19
0.24057	-2
0.24081	-1

	Actual gap [mm]	Difference from average [µm]
Average:	*0.24213*	*17*
Minimum:	*0.22106*	*-21*
Maximum:	*0.28458*	*42*
Maximum difference:	*0.06352*	

Figure 2-9: Section on root interface at RHS 10mm from side

For FEA purposes, most of the corner radiuses were removed as well as the cut section to fit the key, which functions as a locking mechanism. The face of the key however was imprinted in the model to constrain the model to avoid rigid body motions. An overview of the CAD model used for the FEA is shown in Figure 2-10.
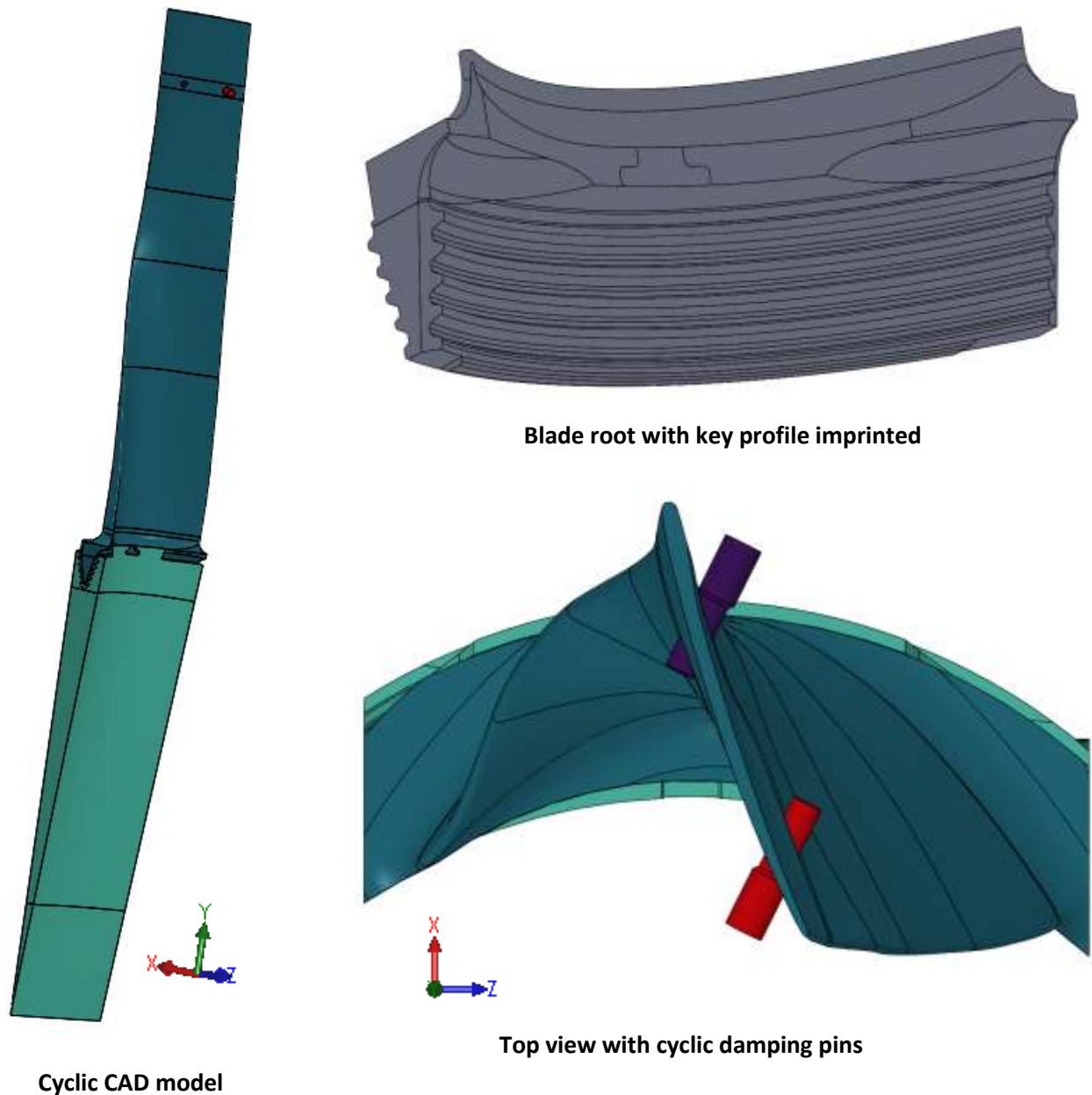
Blade root with key profile imprinted

Top view with cyclic damping pins

Cyclic CAD model

Figure 2-10: Simplified CAD model for FEA

2.1.2 Rotor

The rotor serrations were modelled as a perfect geometry with the contact faces matching the blade. The rotor was cut to the centre line of the rotor and in a section to represent the number of blades on the rotor as shown in Figure 2-11. This was done to be able to run a cyclic symmetric analysis.
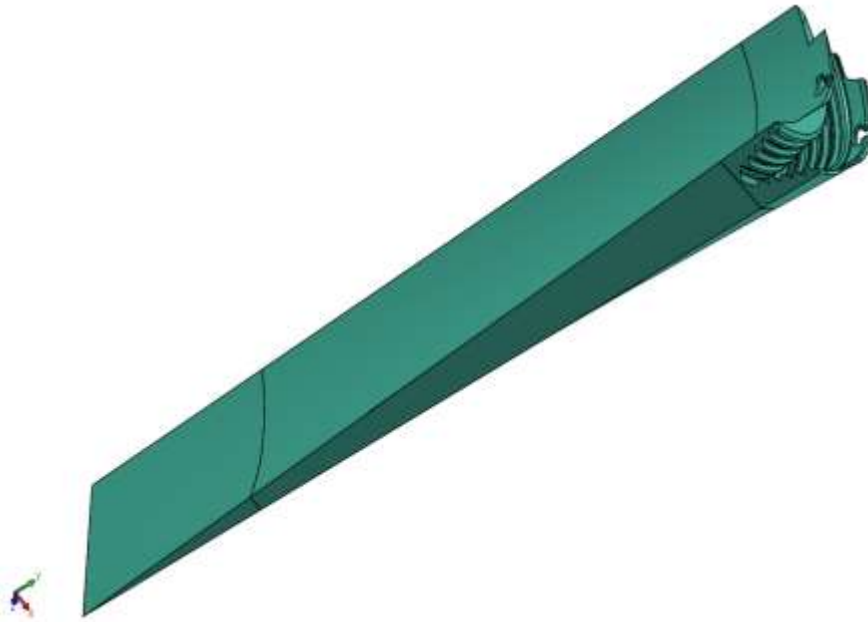
Figure 2-11: CAD geometry of rotor

2.1.3 Damping pins

The damping pins fitted in the blade, consist of a loose fit. They lock, as the blade untwists in operation due to the centrifugal load on the blade. The pins then help to change the stiffness of the tip of the blade. This is mainly done to change the stiffness in the blade and in effect changing the natural frequency of the blade to move away from the operating or run up speeds, which coincide with natural frequencies. During installation the pins should allow for an axial movement of 1.016 to 1.27mm between blades at ambient conditions. This is usually measured during installation by using a clock gauge and checking the travel between the two extremes. Different pins with shoulder widths are installed to achieve this. The pin diameter at the interface of the blade is 10.7mm while the hole in the blade is about 11.5mm.

2.2 Model setup

A 3D cyclic symmetric model of the blade attached to the rotor with non-linear contact was modelled in ANSYS. Different material models were used to evaluate the blade, ranging from linear elastic, to elastic plastic modelling, bi-linear and multilinear hardening. More detail of the plasticity used in the dissertation is available in section 2.2.3. Large deflections were not activated, for the analysis.

2.2.1 Cyclic symmetry

Cyclic symmetry is a tool that can be used in most FEA packages and it is applied when a certain section of an object repeats itself around a common axis. The main advantage of using cyclic symmetry is that it solves faster and uses less CPU resources. For a steam turbine this this method can be used effectively, where the blades and their attachments to the rotor are the same all around the circumference. Therefore, only a single blade with a rotor sector needs to be modelled and with the correct boundary conditions, the same results can be achieved when a full model was analysed. In this approach smaller elements can be used in the high stress regions, which are the regions of interest. One of the disadvantages of cyclic symmetry is that the turbine set is simulated at a perfectly tuned

set, which is not true in practice. This however can still be used as a very good first estimation to gain insight into the turbine blade.

ANSYS makes use of sectors to define the geometry, with the basic sector being one piece of a pattern that get repeated a number of times to create a full profile, as shown in Figure 2-12. This is done in a cylindrical coordinate system with a common axis. ANSYS uses high and low component nodes as with multi-point constraints (MPC's) to constrain the nodes. The final analysis results can be plotted as the full model for better understanding and interpretation.
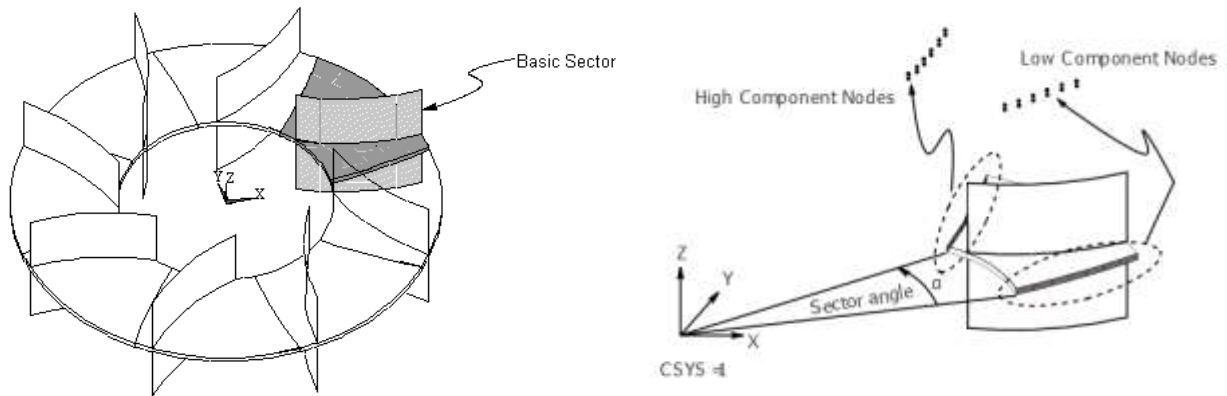

Figure 2-12: Basic sector definition in a cyclic symmetry analysis ('ANSYS Help Viewer, Theory referance', 2017)

Two cyclic symmetric regions are used in the model, one being the rotor and the other being the damping pins as shown in Figure 2-13. The rotor was cut between the blade, starting at the top right through to the centre of the rotor axis. The damping pin was cut in half, with two half pins installed in the two hole in the blade, connecting to the adjacent blade.
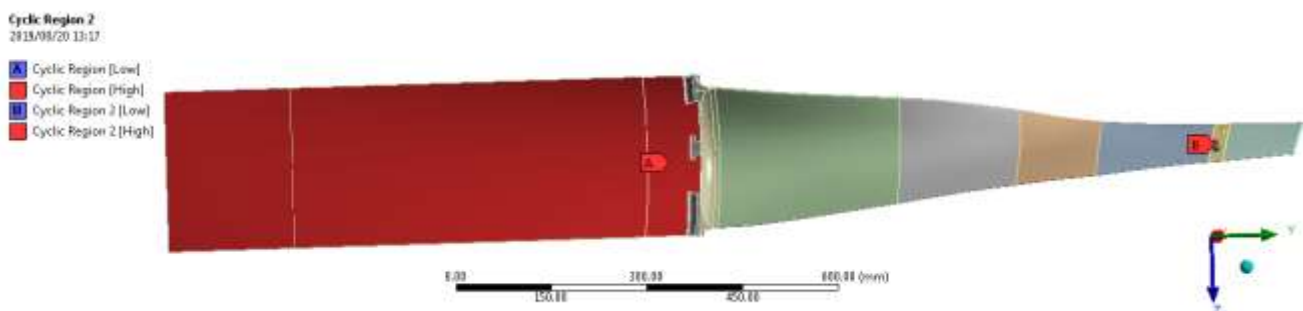

Figure 2-13: Cyclic symmetric regions

2.2.2 Mesh

The mesh of a FEA is the heart of the model and all calculations are done on the individual mesh level. Therefore, a good quality mesh is required to be able to get accurate results. For 3D analysis the hex elements are the most effective element and therefore all bodies that are sweepable were meshed with hex elements. Non-sweepable bodies were modified to reduce the volume of non-sweepable bodies. The non-sweepable bodies were meshed with second order tetrahedral elements.

A mesh summary of the model is represented in Table 2-1, with the mesh shown in Figure 2-14.

Body	Nodes	Elements
Blade aerofoil	10 777	2 951
Blade root	88 893	28 133
Damping pins	10 287	6 375
Rotor	138 854	79 402

Blade root mesh

Cyclic FEA model mesh

Rotor root mesh
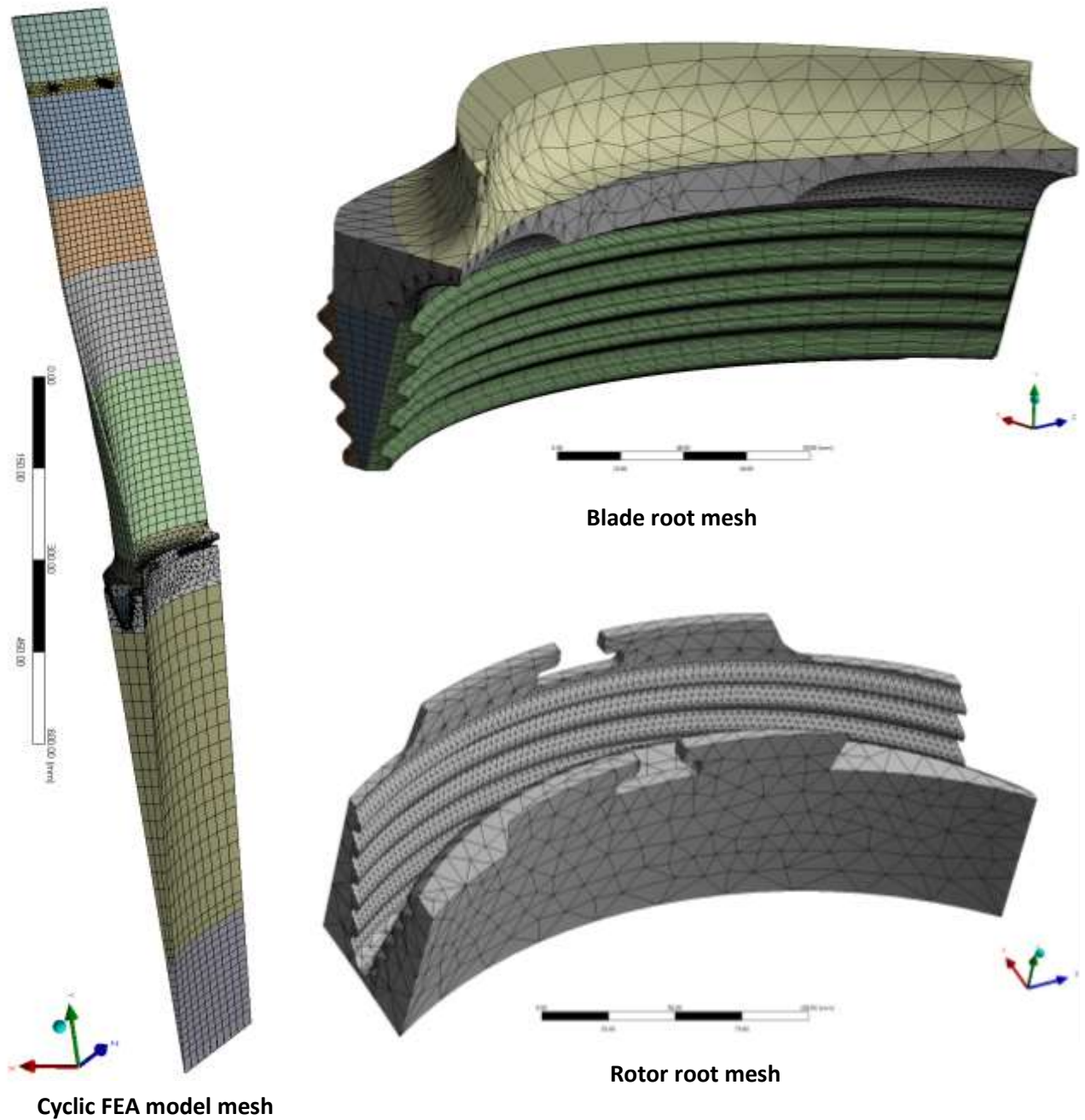
The mesh convergence was checked by doing a model analysis with various mesh sizes and different elements. Figure 2-15 show typical response for the first four modes. Fairly good mesh convergence is seen at 0.1 to 0.15 of 1/(mesh size) between all four modes, which result to 10 mm and 6.6 mm mesh size respectively. This was used as a good initial estimate to be used for mesh size.
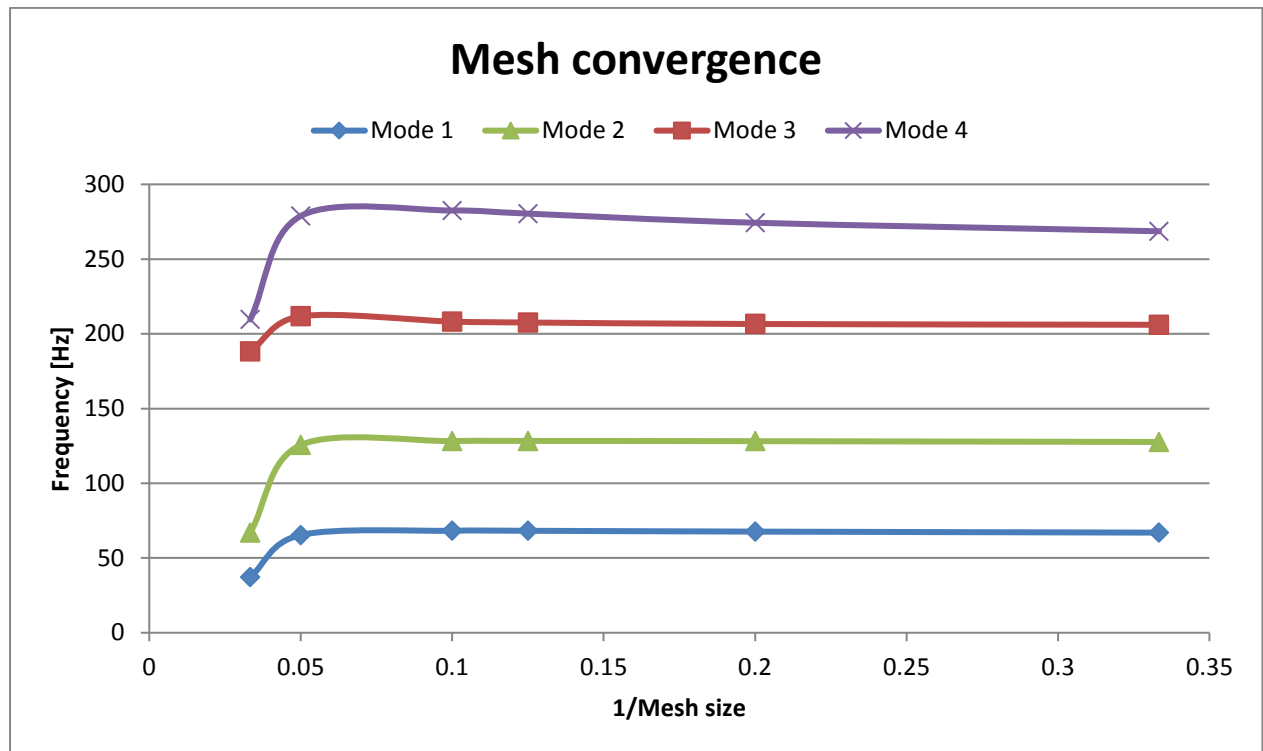

Figure 2-15: Mesh convergence for first four modes

The quality of the elements was also checked in ANSYS. The Jacobian ratio was plotted, which is a shape parameter, showing the deviation from an ideally shaped element. Typically, a zero is a perfect shape ('ANSYS Help Viewer, Theory referance', 2017). The results for the complete model is shown in Figure 2-16, which show that the majority of the model have a very good Jacobian ratio.
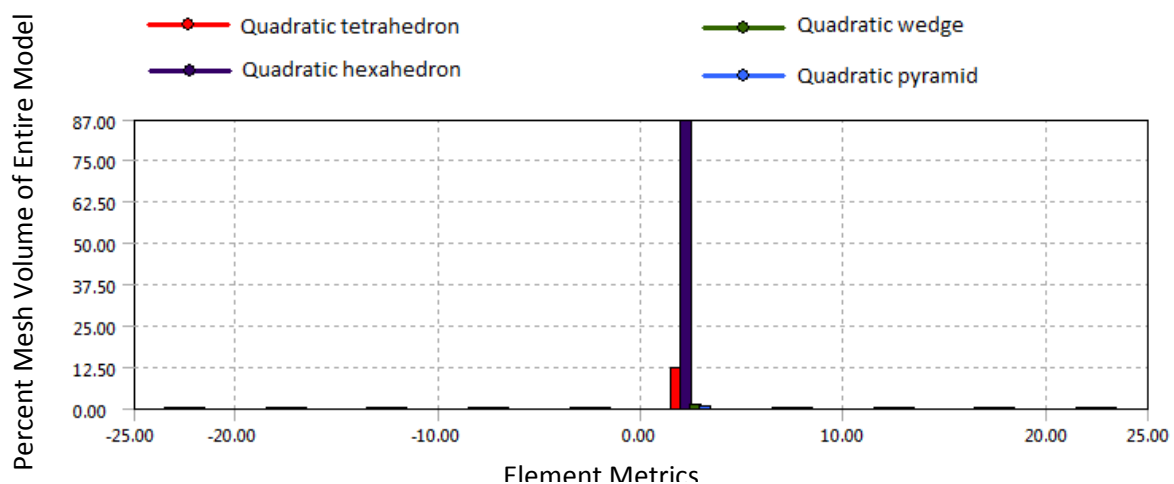

Figure 2-16: Element quality based on Jacobian ratio

The rotor was modelled and included to get the correct stiffness and contact region on the blade and is mainly used to transfer the load to the blade. Therefore the stress distribution on the rotor is not of significant importance, but a good quality element at the contact faces is important.

2.2.3 Material properties

The blade used in the investigation is made of 12%CrNiMoVNb (FV566), a high strength martensitic stainless steel. It has a very good combination of strength, toughness and corrosion resistance. It also has a high inherent damping characteristic (Das *et al.*, 2003). 12% Cr steels are used for the blade due to their superior material damping (*Modern Energetics*, no date). The material also has very good impact properties. The blade material however does not have very good SCC properties and were subsequently updated to a 14% Cr material, FV520B, which has better SCC properties. A consistent mass matrix formulation was used, which takes longer to solve than a lumped mass matrix formulation, but result in more accurate results.

The material properties used in the analysis are shown in Table 2-2. These properties are presented at room temperature.

Table 2-2: Material Properties

Material	Component	Density [kg/m³]	Modulus of Elasticity [GPa]	Poisson's ratio	Ultimate Tensile Strength [MPa]	Yield Strength [MPa]
FV 566 tempered at 250-350°C at room temperature (Bastow and Hosking, 1971)	Blade	7770	213	0.3	1380	1030
FV 566 tempered at 600°C at room temperature (Bezuidenhout and Van Rooyen, 2004)	Blade	7770	213	0.3	1140	1000
FV 566 tempered at 650°C at room temperature (Bastow and Hosking, 1971)	Blade	7770	213	0.3	1015	815
3.5Ni1.5Cr0.5Mo0.1V (ASTM A470 class 5) (EPRI, 2006)	Rotor	7177			620	458
X4CrNiCuMo 14-5 / FV520B (Ming *et al.*, 2014)	Damping Pins	7800			1170	1029

2.2.4 Damping and contact

Material damping in the form of a constant damping coefficient of 0.003 was assumed for the blade material, which were an average damping ration reported by Booysen, (2014). For the modal analysis a Rayleigh damping ratio was calculated as per the procedure stipulated in section 1.2.3.3. The calculation is shown in Appendix B, with the resulting α and β values respectively as 0.00000116 and 2.21826245.

Mechanical damping, between the damping pins and the blades and the root of the blade and the rotor is introduced in the form of frictional contact. The static frictional coefficient for steel on steel in dry conditions varies from 0.5 to 0.8 and in lubricated greasy conditions it is 0.16. The friction coefficient will also reduce dramatically when sliding is initiated. Also with extreme pressure; which is true in this case due to centrifugal force; the friction coefficient will rise and become almost as if bonded (*Friction and Friction Coefficients*, no date).

In practice, the blade root and rotor disc is lubricated on assembly, with a high graphite content lubrication. The lubricant is specified as an anti-seize lubrication for high alloy steels under stress at high temperatures. Also the damping pins are nitro-carburised to allow sliding in service. A friction coefficient for both application of 0.25 was selected. The friction was added to ensure an accurate result for mechanical damping between contact surfaces. The contact regions for the analysis are shown in Figure 2-17; which is the contact between the blade with the damping pins and the contact between the blade root and the rotor root.
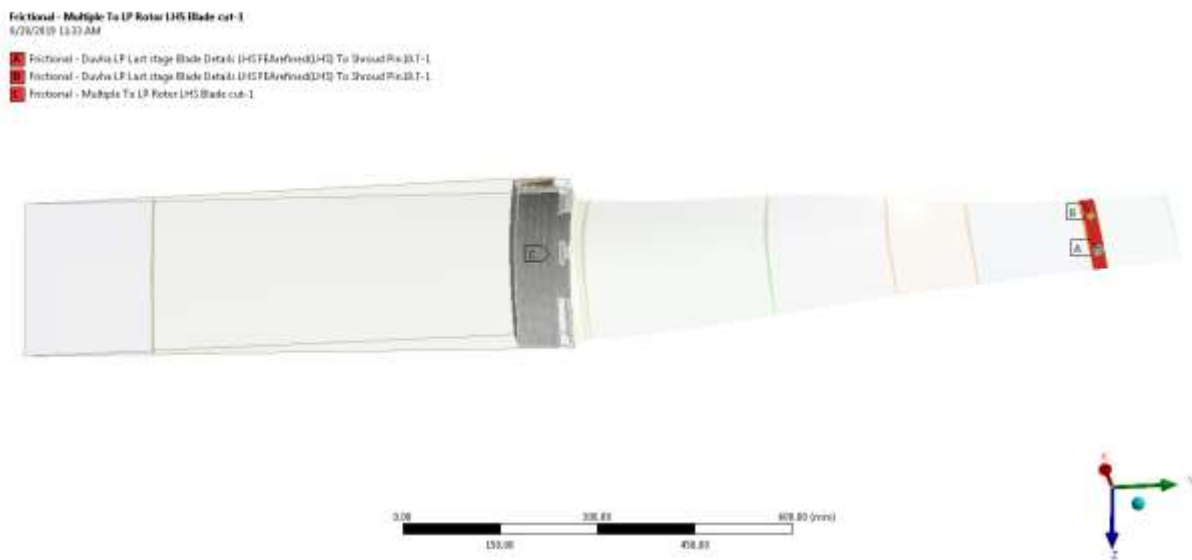

Figure 2-17: Contact regions

2.2.5 Damping pins

A sensitivity analysis was done to determine the effect of having a gap between the diameter of the damping pin and the blade hole. This was achieved by comparing the displacement, stress and natural frequencies, together with the resource usage, by means of analysis time. The results for the case

including a gap and a case excluding a gap are shown in Table 2-3. The maximum displacement, located at the tip of the trailing edge of the blade, was recorded in all directions as well as the stress in the root section of the blade. The results for the analysis with the gap between the pins, show slightly lower displacement in all directions, but the stress is slightly higher. If the natural frequencies is compared, there is very little difference, with the maximum being 1.2% difference. The analysis solves 50% faster for the actual size pin. Based on these results, it will be more conservative to use the pin with actual sizes, due to higher stress on the root section of the blade.

Table 2-3: Damping pin sensitivity study results

File name		Sweepable3600_600		Sweepable3600_600_pin		
Comments		Size for size		Actual pin with gap		% Difference
Displacement res [mm]		21.528		18.03		16.2%
Displacement X [mm]		3.6283		3.4827		4.0%
Displacement Y [mm]		0.45212	-15.464	0.37638	-13.345	16.8%
Displacement Z [mm]		14.537		11.621		20.1%
Von-Mises Stress [MPa]		1244		1272.1		2.3%
Max Principle Stress [MPa]		1433.1		1461.1		2.0%
Min Principle Stress [MPa]		318.08	-1179.5	359.38	-1522.2	13.0%
PresStress Modes	OEM					
1	105	101.26	3.6%	101.69	3.2%	0.4%
2	161.25	164.43	2.0%	164.66	2.1%	0.1%
3	307.5	311.18	1.2%	314.9	2.4%	1.2%
	Average		2.2%		2.6%	0.6%
	Sum		6.7%		7.7%	1.8%
Analysis Time [min]		**64.86667**		**35.61667**		45.1%
Static [min]		37.68333		12.56667		66.7%
Pre-stress Modal [min]		27.18333		23.05		15.2%
Static Modal [min]						

2.2.6 Boundary conditions

The model boundary conditions are as follows:

- A fixed nodal constraint was added in the x and y directions of the rotor as shown in Figure 2-18.
- A displacement constrained in the z direction on the blade was added on the imprint profile of the key, to represent the key locking the blade to the rotor as shown in Figure 2-19.
- A rotational velocity of -3000 rpm was applied on all the elements (blade, rotor and pins) to simulate the rotating turbine, around the centre axis of the rotor (Figure 2-20).
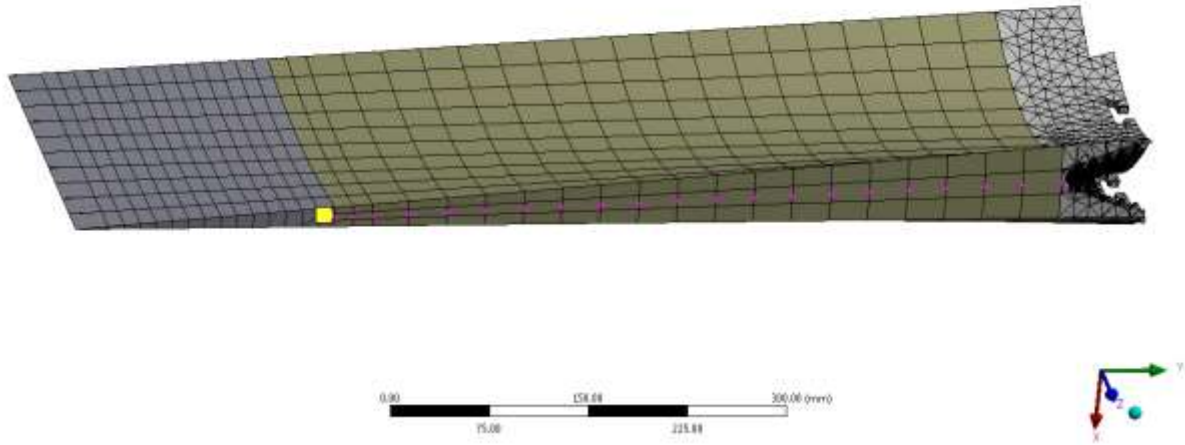
Figure 2-18: Fixed nodal constrained on rotor
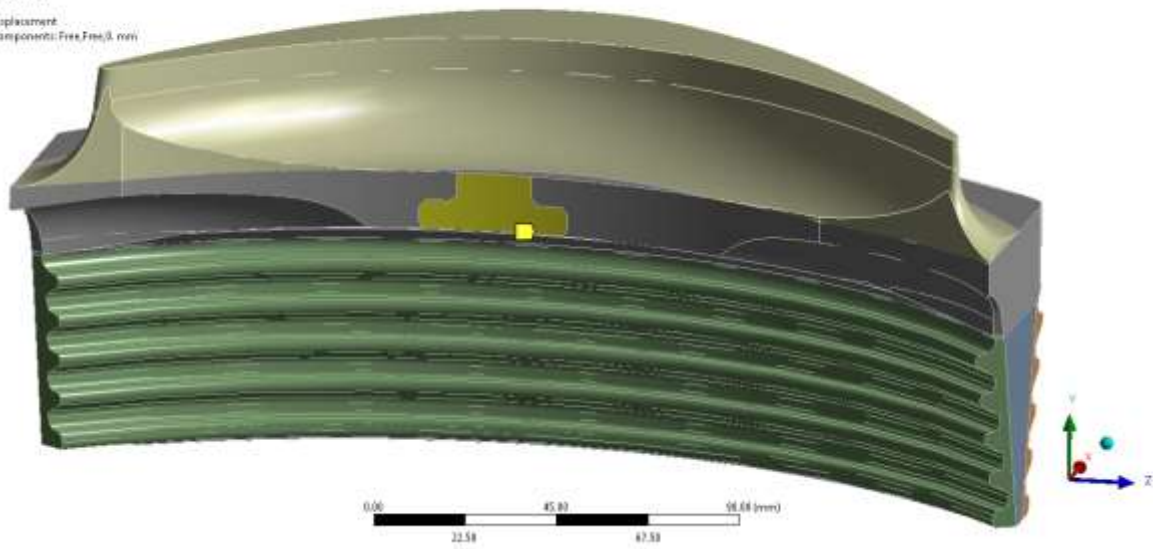

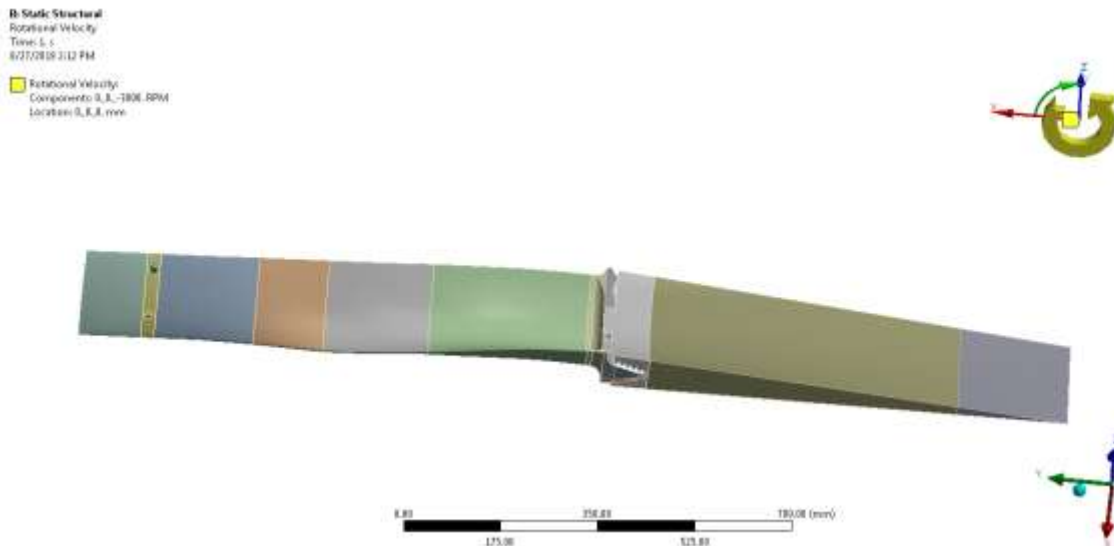**Figure 2-19:** Fixed nodal constrained to represent locking key

Figure 2-20: Rotational velocity

2.3 Modal analysis

A modal analysis was done in order to get the natural frequencies of the blade assembly. It is important to have both the natural frequencies and the mode shape in order to use for the BTT analysis. It is also important to check if a blade is vibrating, that it is not vibrating at or near a natural frequency that can cause resonance. ANSYS can be used to solve for modal analysis using a direct or iterative solver. The direct solver uses the sparse matrix solver method. Generally, the direct solver is more accurate versus the iterative solver, which uses fewer resources. The direct solver was used in this instance.

A pre-stress modal analysis is an analysis, where a static analysis is completed before a model analysis. This is to capture any effect which can alter the stiffness or geometry of the model which ultimately will change the natural frequency of a model (Fung, E.H.K., Yau, 1999). In turbine blade analysis this is represented in the stress stiffening effect, due to centrifugal force and blade locking and stiffening due to the damping pins, lacing wire or snubbers. In ANSYS, just before a pre-stressed modal analysis is solved, the stiffness matrix is updated by the pre-stressed condition and the modal analysis is solved with the only difference being the updated stiffness matrix.

For some natural frequencies all the blades move in phase in the same direction, while for other modes some of the blades move in opposite directions. Where phase shift is encountered between blades, a nodal radius exists where no translation is present. Two of these nodal radiuses on opposite sides of a bladed disc form a nodal diameter. The maximum nodal diameter is equal to half the number of blades, which means every adjacent blade vibrate out of phase. The nodal diameter can also be interpreted as the number of waves that travel along the circumference of rotor. For this investigation a total of ten nodal number were solved.

The model analysis was solved with a pre-stress condition of normal operating speed of 3000 rpm to get the natural frequencies of the blade assembly under operating conditions. Various rotational speeds were analysed in order to create a Campbell diagram, which was compared to the spin pit tests data, which is discussed in more detail in section 3.2.

The natural frequencies of the cyclic symmetry model is shown in Table 2-4, with the mode shapes of the first six modes are shown in Figure 2-21, with initial blade condition shown in wireframe and the contour plot being the displacement.

Table 2-4: Cyclic symmetry model natural frequencies

	Natural Frequency [Hz]										
	Nodal Diameter										
Mode	0	1	2	3	4	5	6	7	8	9	10
1	101.10	101.54	102.85	104.96	107.83	111.37	115.47	120.02	124.93	130.08	135.36
2	164.25	164.32	164.51	164.84	165.30	165.88	166.60	167.44	168.43	169.57	170.89
3	310.17	310.24	310.42	310.68	310.99	311.31	311.62	311.92	312.18	312.41	312.59

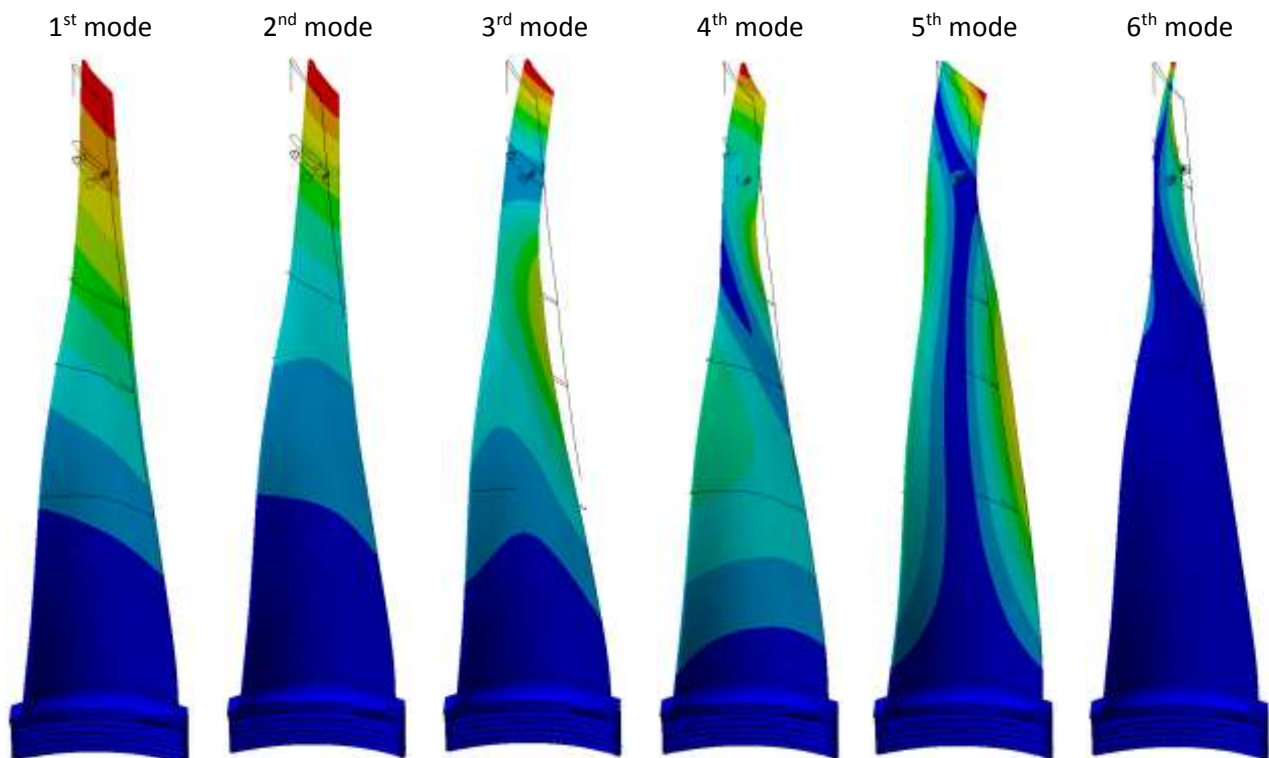1st mode   2nd mode   3rd mode   4th mode   5th mode   6th mode

Figure 2-21: The first six mode shapes

The stress distribution of the first six modes at the root section is shown in Figure 2-22, with the front, convex side of the root on the left hand and the back concave side of the root on the right hand side. The blue arrow shows the location of the minimum stress and the red arrow show the location of the maximum stress. It is important to note that here the magnitude of the stress has no significant meaning, due to this being normalised in the mode extraction process in the analyses. This however gives a very good indication of where the hot spot areas on the blade are, compared for every mode shape.
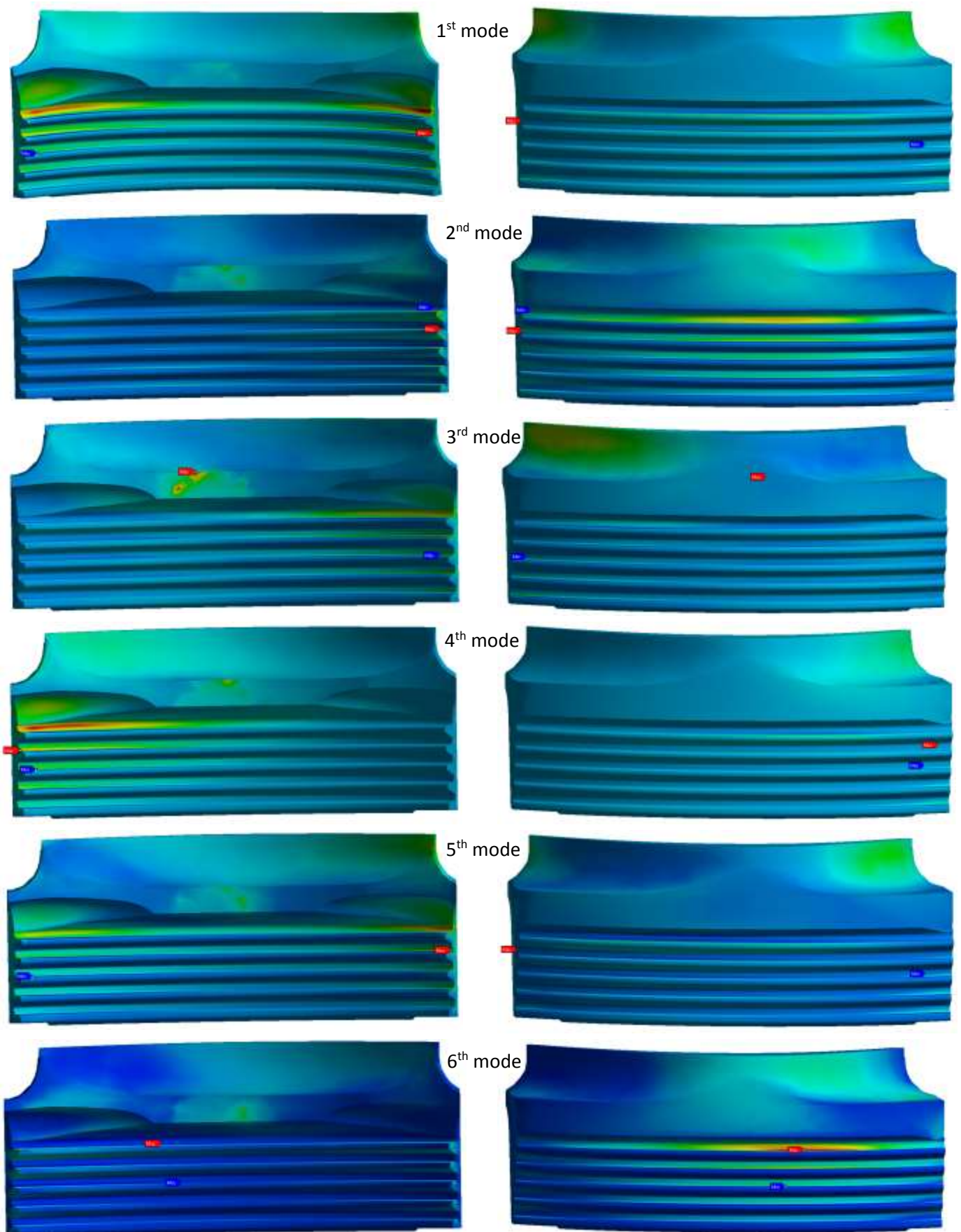
1st mode

2nd mode

3rd mode

4th mode

5th mode

6th mode

Figure 2-22: The first six modal shapes, equivalent Von-Mises stress distribution at the root

2.4 Plasticity model

The normal operating practice for fitting new blades on a steam turbine, is that the turbine gets balanced and is then run up to 20% overspeed (3600 rpm for 50Hz applications). This is to allow for initial plastic deformation in highly stressed areas. This then results in initial residual stress in the highly stressed regions; which usually is in the root attachment section of a turbine blade. This results in a lower average stress on the blade root region due to overcoming of the residual stress first.

The same model, mesh and boundary conditions as described in the model setup in section 2.2 are used. The only difference is the load history and the plasticity material model. A bilinear kinematic hardening model was selected to capture the material behaviour for the analysis. The centrifugal load was applied as shown in the load history plot in Figure 2-23. The maximum and minimum principal stress results for the various load history points are shown in Figure 2-25. The history comparison of the minimum and maximum stress range shown in Figure 2-27. The benefit of the residual stress, which is present after the initial run, can be seen at time step three. This concept is also represented by the hysteresis loop, which is shown in Figure 4-9.
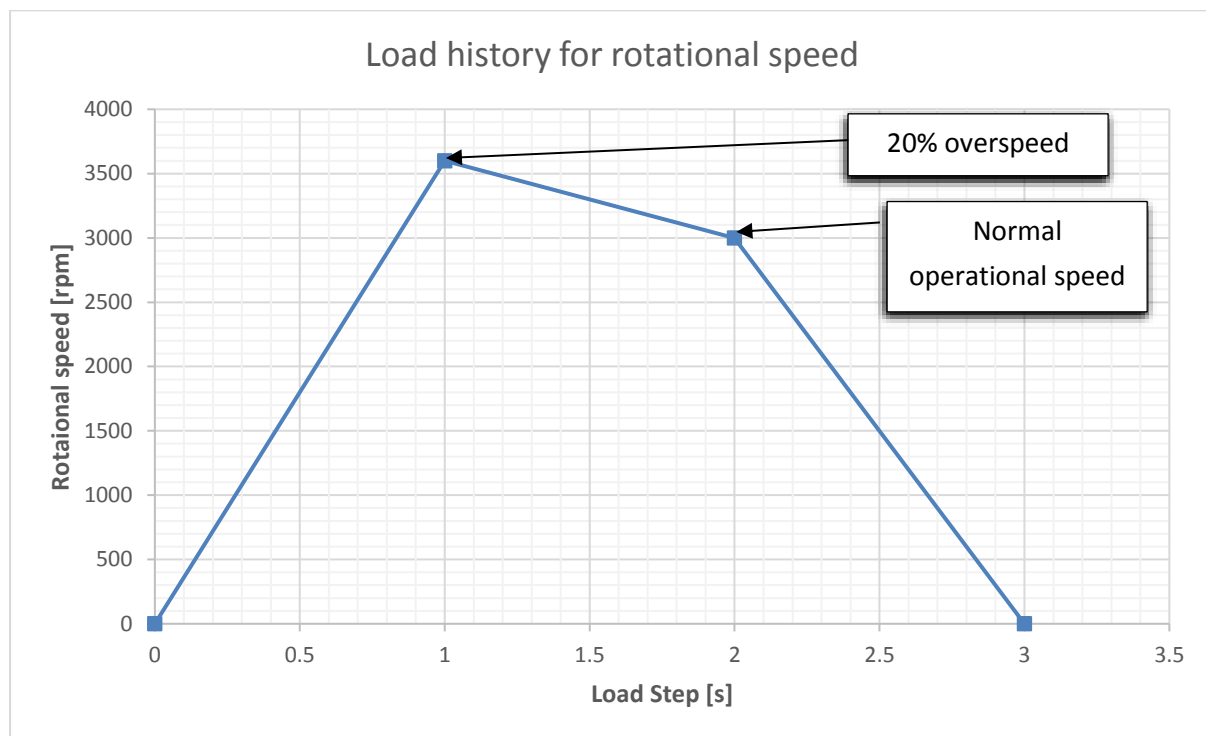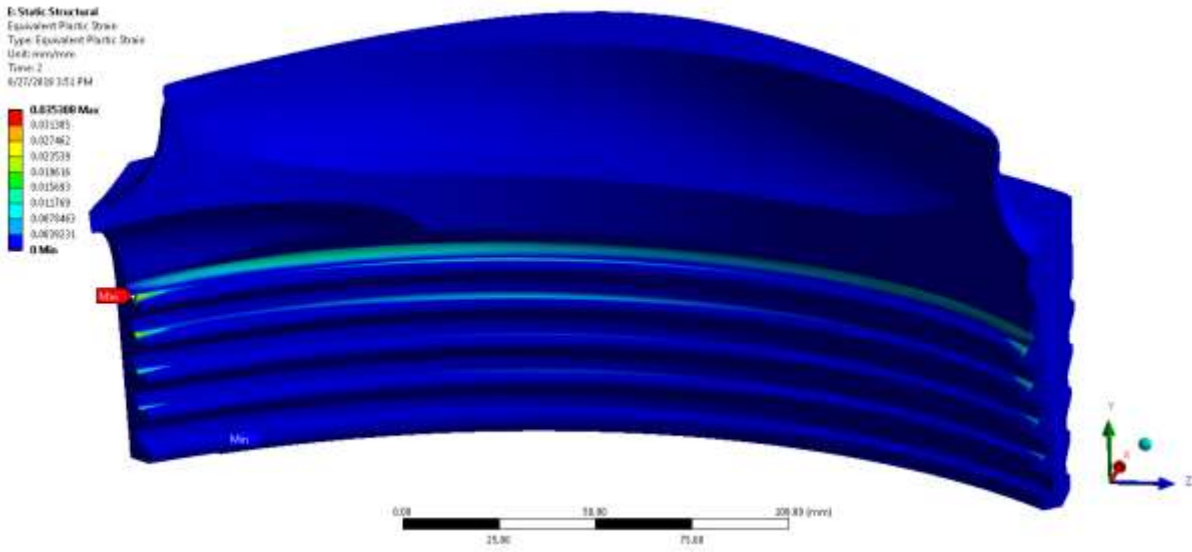

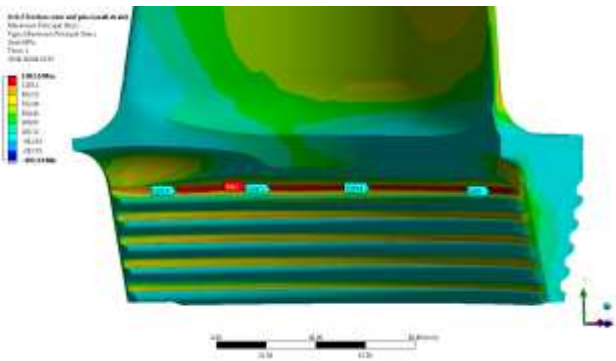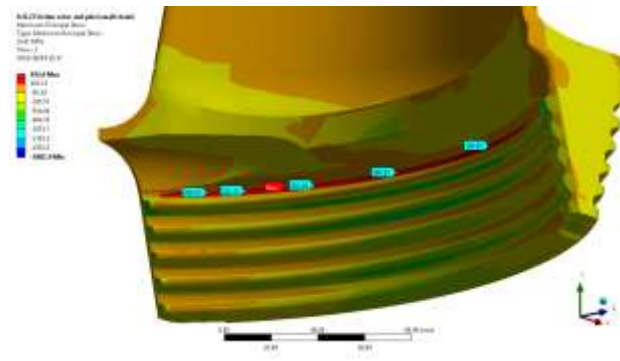**Figure 2-23:** Load history for plasticity model

Figure 2-24: Total equivalent plastic strain in blade root

a) Maximum Principal stress at 3600 rpm

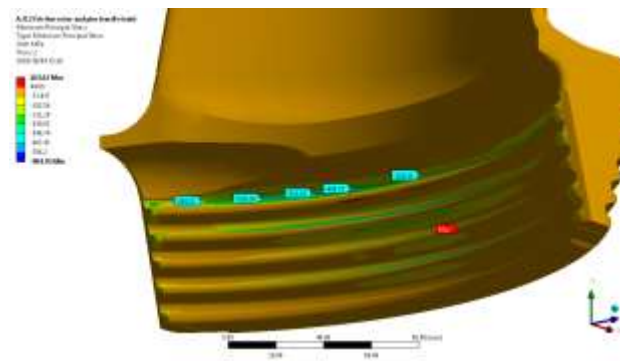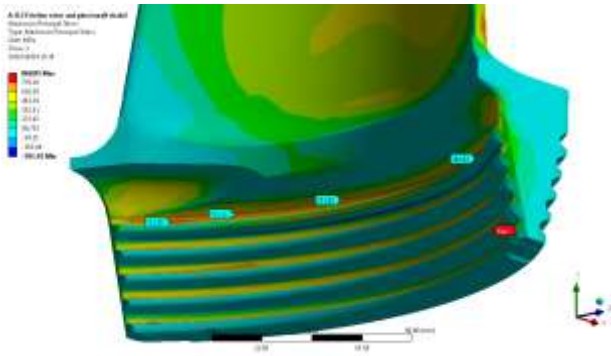b) Minimum Principal stress at 3600 rpm
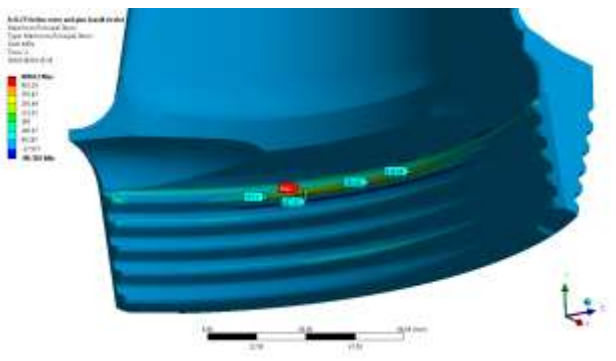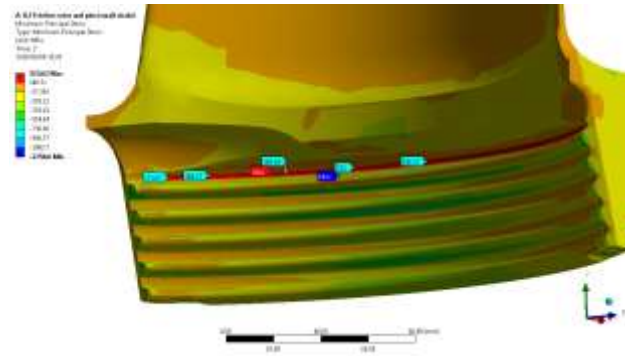

c) Maximum Principal stress at 3000 rpm

d) Minimum Principal stress at 3000 rpm

e) Maximum Principal stress at 0 rpm   f) Minimum Principal stress at 0 rpm

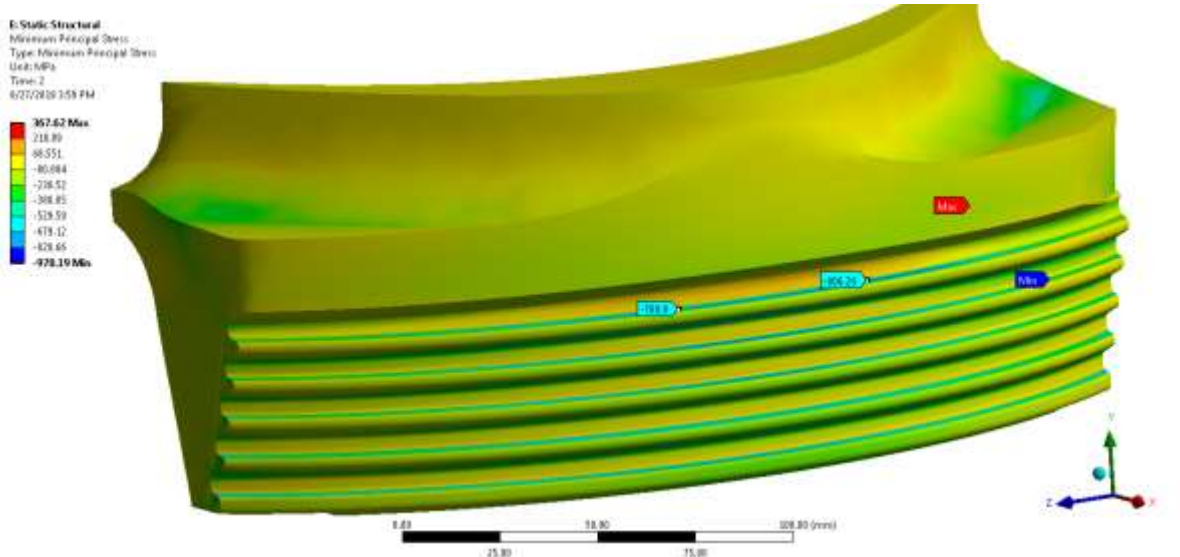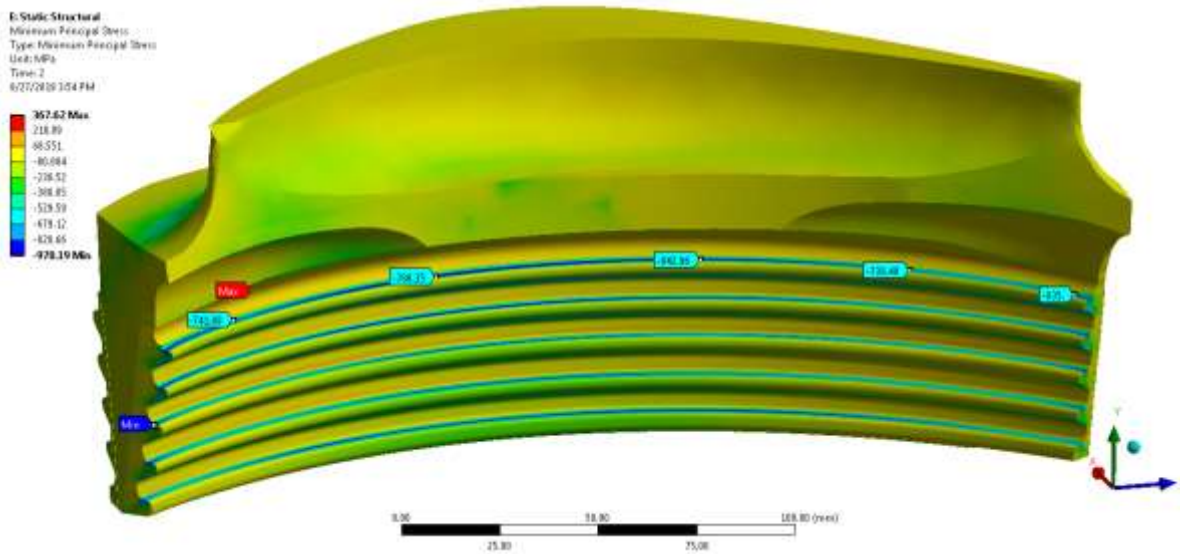**Figure 2-25:** Maximum and minimum principal stress of root during load history

Figure 2-26: Minimum principles stress [MPa] after overspeed
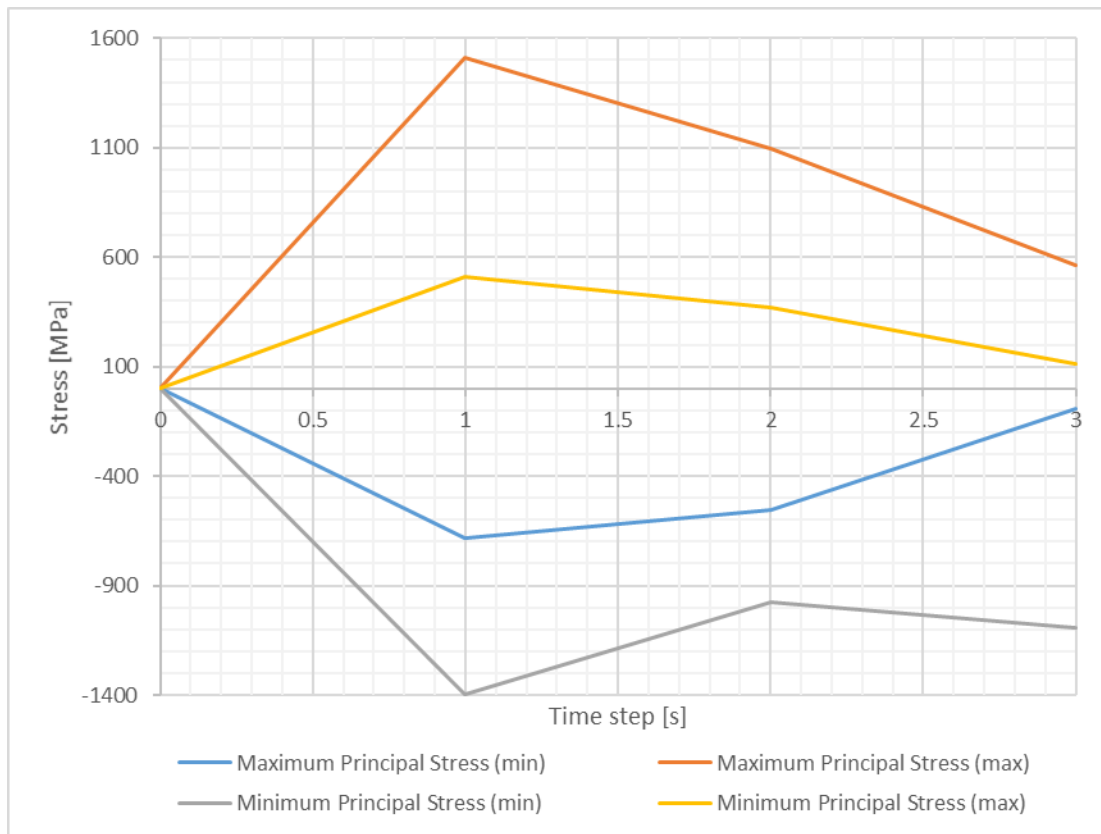
Figure 2-27: History plot of the maximum and minimum principals stress range

2.5 Chapter summary

This chapter focused on the development of the FEA, including the key assumptions and boundary conditions that were used. A cyclic symmetry model setup assumes that all blades are identical, assuming that the blade set is a perfectly tuned system. The geometry was simplified for FEA meshing by removing some of the small features, including the locking key on the blade. The chapter also includes sensitivity studies, on the mesh convergence and damping pin gap. The results for the modal analysis was captured in Table 2-4, showing the natural frequencies for the first three modes and up to the tenth nodal diameter. The stress pattern on the root was investigated and high stress regions corresponding to failure locations were observed. A plasticity model was created to capture the residual stress generated during an overspeed test. This resulted in a lower maximum stress under normal loading conditions, which directly relate to a lower stress range and longer fatigue life. The plasticity analysis was done mainly to achieve more accurate results and due to fatigue results being very sensitive to the stress range.

Chapter 3

Experimental setup and model verification

An experimental setup was done to verify the FEA model, by means of natural frequencies. Two tests were conducted, one being a static tap test on the blade, while the blade situated in the rotor and secondly a telemetry spin pit test of strain gauges attached to the blades. Both these data sets were used to verify the model by means of a Campbell diagram. These verifications are partial verification that were done at different conditions, mainly that it is not at actual steam load conditions in order to validate the FEA model in actual operating conditions. According to section 1.2.3.2, the majority of the load is generated by the centrifugal loading of the blade. By simulating the centrifugal load in the spin test, most of the blade stiffening is accounted for and a good correlation between natural frequencies can be established.

3.1 Experimental modal analysis

Modal testing is a very common way of verifying a FEA due to the signature or characteristics of the blade being captured by its natural frequency and as soon as a crack is present in a blade the natural frequencies will change. In FEA the model is mathematically calculated and the blade is seen as a perfect blade with no deviations between blades. In practice there is a slight difference between blades and the typical deviations or uncertainty in natural frequencies is commonly assumed to be 2 to 3% (EPRI, 2008). The main driver for the differences in natural frequencies are allowable dimensional variations, all within manufacturing tolerance. Other minor drivers may include slight material differences, residual stresses in the blade due to manufacturing processes and cracks or surface defects. For long LSBs, which is the case in this study, the natural frequency accuracy should be within ±3 to 5%, where the first four modes are generally below 500 Hz (EPRI, 2008).

3.1.1 Experimental setup

The vibration impact testing was done with the blade in-situ on the rotor. This was to ensure that the simulated condition is the same as the operating conditions during, which a blade is installed. A single input multiple output (SIMO) setup was done with the HBM QuantumX MX840 data acquisition system, Endevco 45kg modal hammer and three single channel acceleration sensors. Two variable capacitance accelerometers were used. One radially on the tip of the blade and the other one perpendicular to the edge of the blade. And one Integrated Circuit Piezoelectric acceleration sensor, which were positioned normal to the aerofoil of the blade. All the channels were sampled at 19.3 kHz. The acquisition software used to capture the results was a HBM catmanAP 4.1.2.7. The setup is shown in Figure 3-1.

The tip of an impact hammer has a significant influence on the frequency content of the energy transferred to the structure and therefore the response measurements that are excited. For instance a harder tip results in a shorter pulse duration, which excites the higher frequency content (*The Fundamentals of Modal Testing*, 1997). A nylon tip was used in this application, since this usually excite up to a frequency of 1000 Hz, which is the upper limit of the acceleration sensors.

Eight hammer impacts were done per measurement. The acceleration sensor positions comprise of three positions: on the top tip of the blade, at the lacing hole on the side of the blade and just under the lacing hole on the blade. These positions covered all three directions (x, y and z), which were all recorded simultaneously with the hammer impacts. The blade was impacted at two different positions. Both positions were located at the tip of the blade, but the first being perpendicular to the aerofoil of the blade and the second one on the edge of the blade. The setup also involved different blade positions on the rotor. This was mainly done due to the slight change in stiffness due to gravity pulling it down, while positioned in a 3, 6 and 9 o'clock positions as shown in Figure 3-2. Unfortunately, a 12 o'clock position test could not be performed due to restricted access at the top of the rotor. All the sensors and the modal hammer were checked to ensure they have a valid calibration certificate and will give accurate results.
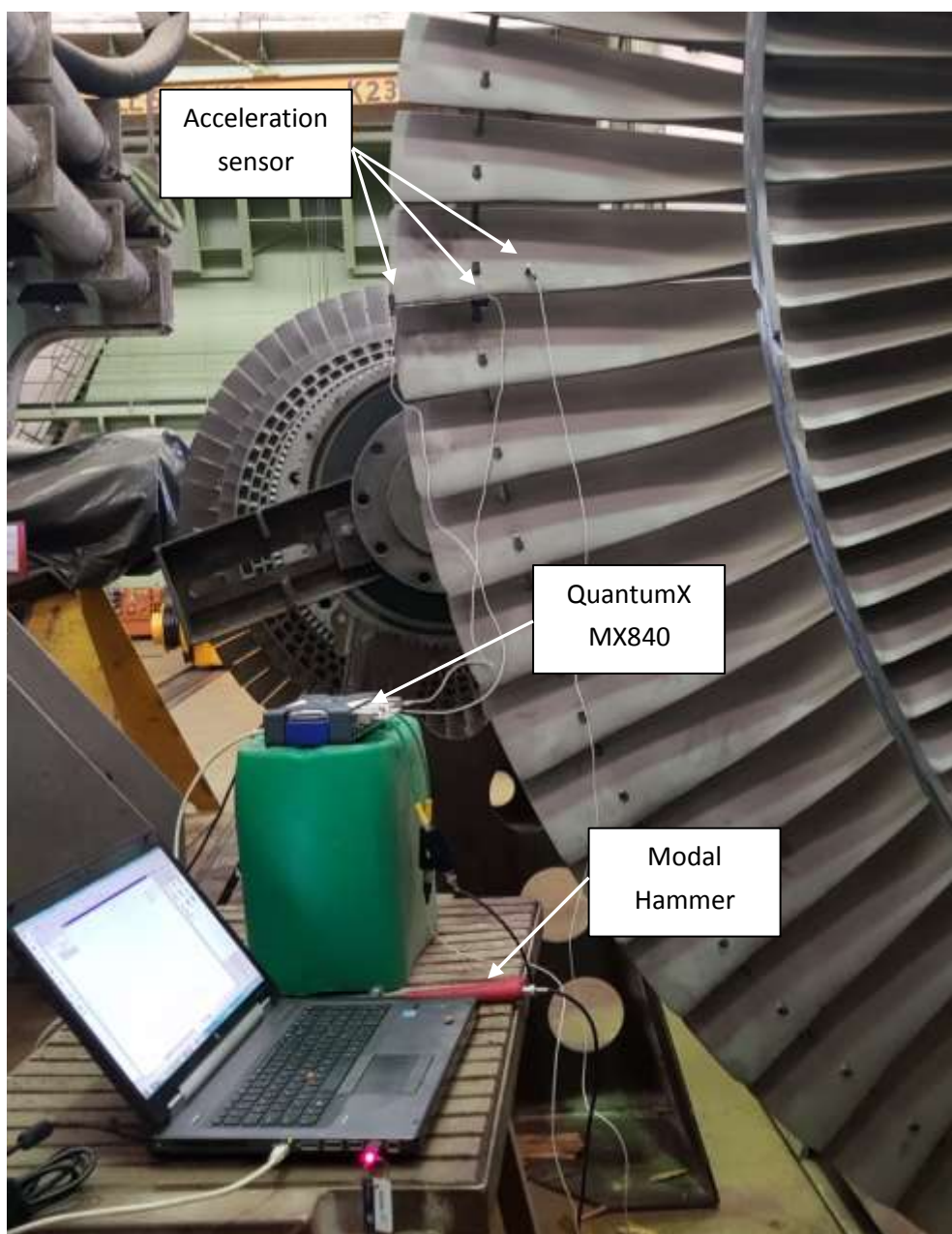

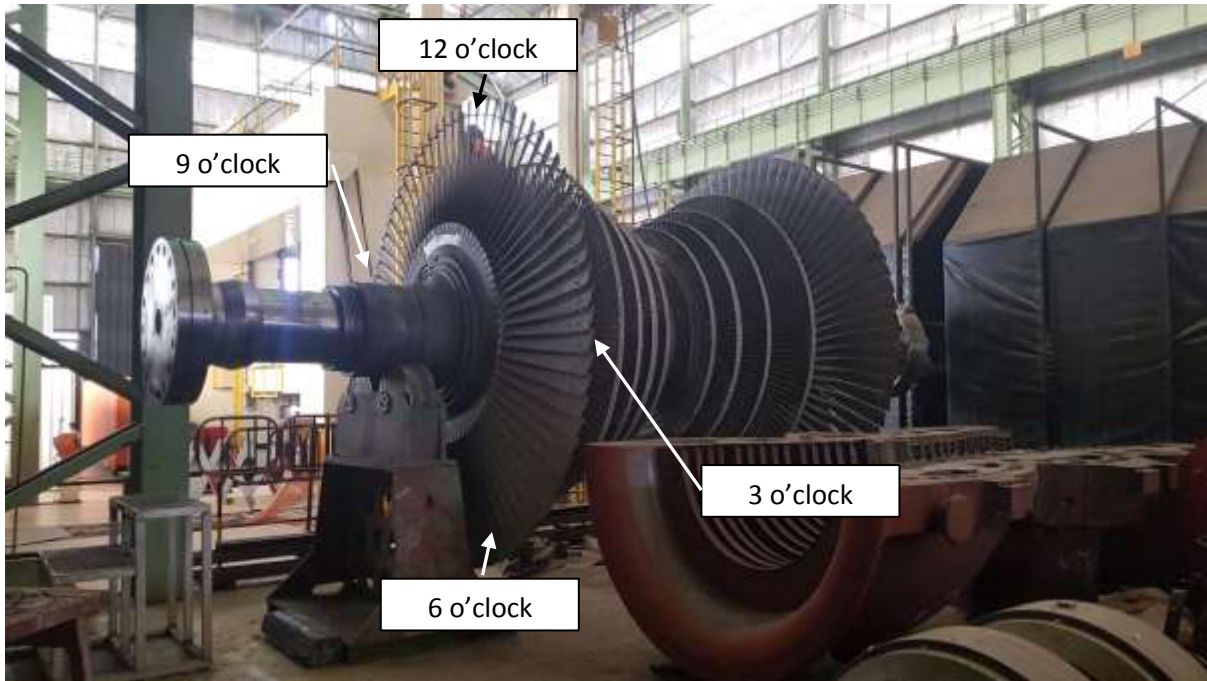**Figure 3-1:** Impact testing performed on a turbine LSB

Figure 3-2: Positions of measurements

3.1.2 Post processing of modal impact testing

The impact test data was post-processed with HBM nCode version V18.0.3, with a typical process flow as shown in Figure 3-3. nCode is a software program which could be used to post-process captured data. It can import various different file formats generated by a wide variety of programs. It works on the basis of "*glyphs*", which is almost like small function blocks with different parameters or setting to be executed. The *glyphs* then are connected in a sequence depending on what is required.

The captured impact test data (cf. section 3.1.1) was imported as raw data. This consisted of about eight impacts with response. The single test of eight impacts was repeated with two different impact regions to ensure all modes has received enough energy to be excited. These test were repeated three times. Then in order to achieve a better average the test results that were repeated were combined with a half sinusoidal wave in a single long signal. Lastly a fast Fourier transform (FFT) (see process flow in Figure 3-3) was done on the data and compared to the previous set. Post-processing was done for every sensor channel at the various sensor positions. Then lastly the impact position data was averaged by appending the data in the time series to get a more accurate response. The data was joined with a half-sinusoidal wave to ensure smooth transition between the data sets and limit the effect of leakage. For the FFT analysis a Hanning window with 8192 buffer size and 67% overlap was used. A window is used to improve the accuracy of the data due to reducing the magnitude of the data at end ends of the bins, avoiding discontinuities at the changeover or appending of bins. The benefit of using a large overlap is to minimizing the leakage at the edges of each window, where a bigger buffer size increase the resolution of the spectrum.

The frequency response function (FRF) was calculated using similar settings as for the FFT and the process flow is shown in Figure 3-4, with the results captured in Figure 3-5. The results for the other positions is shown in Appendix A.
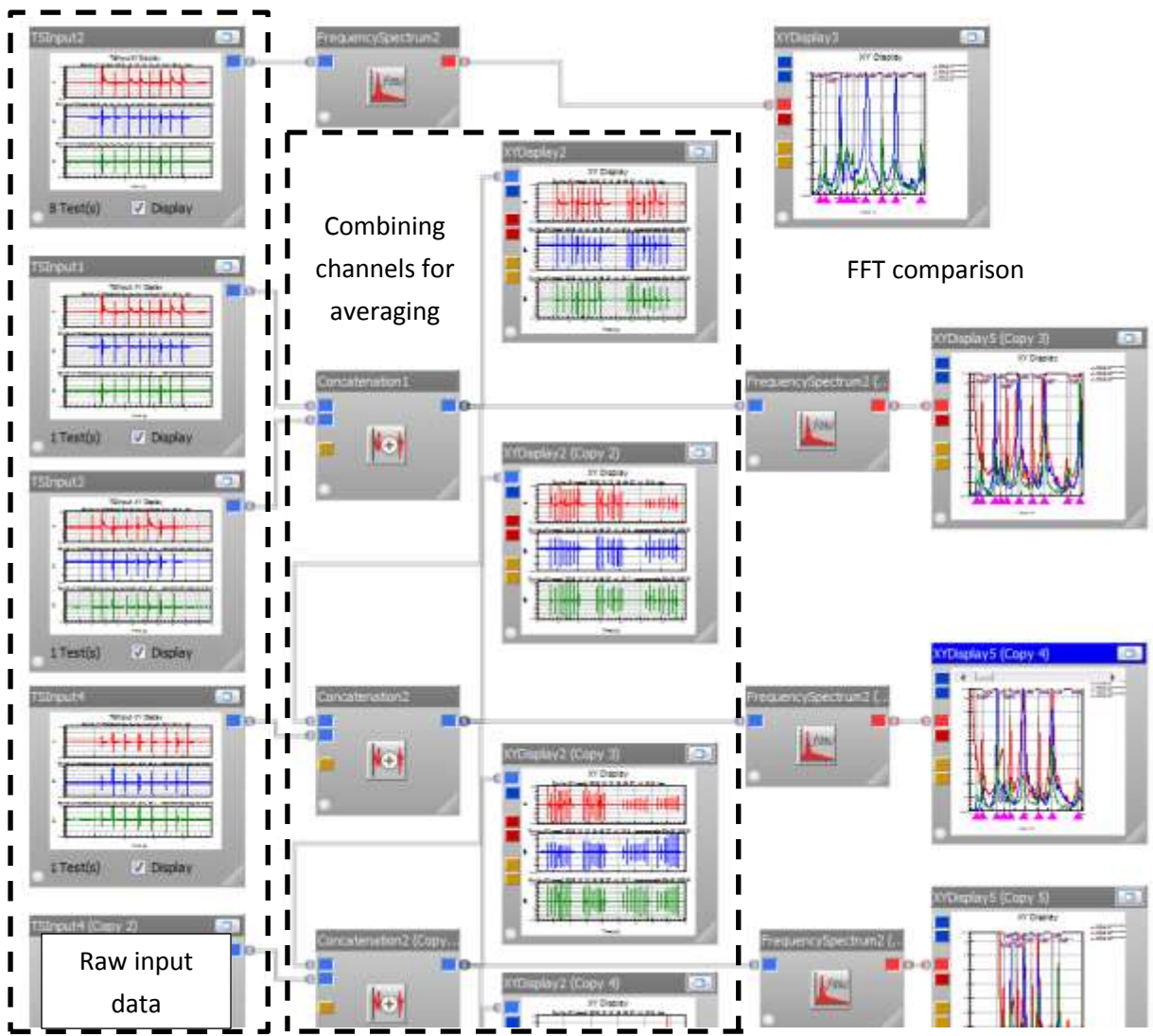
Figure 3-3: Typical nCode process flow for FFT averaging
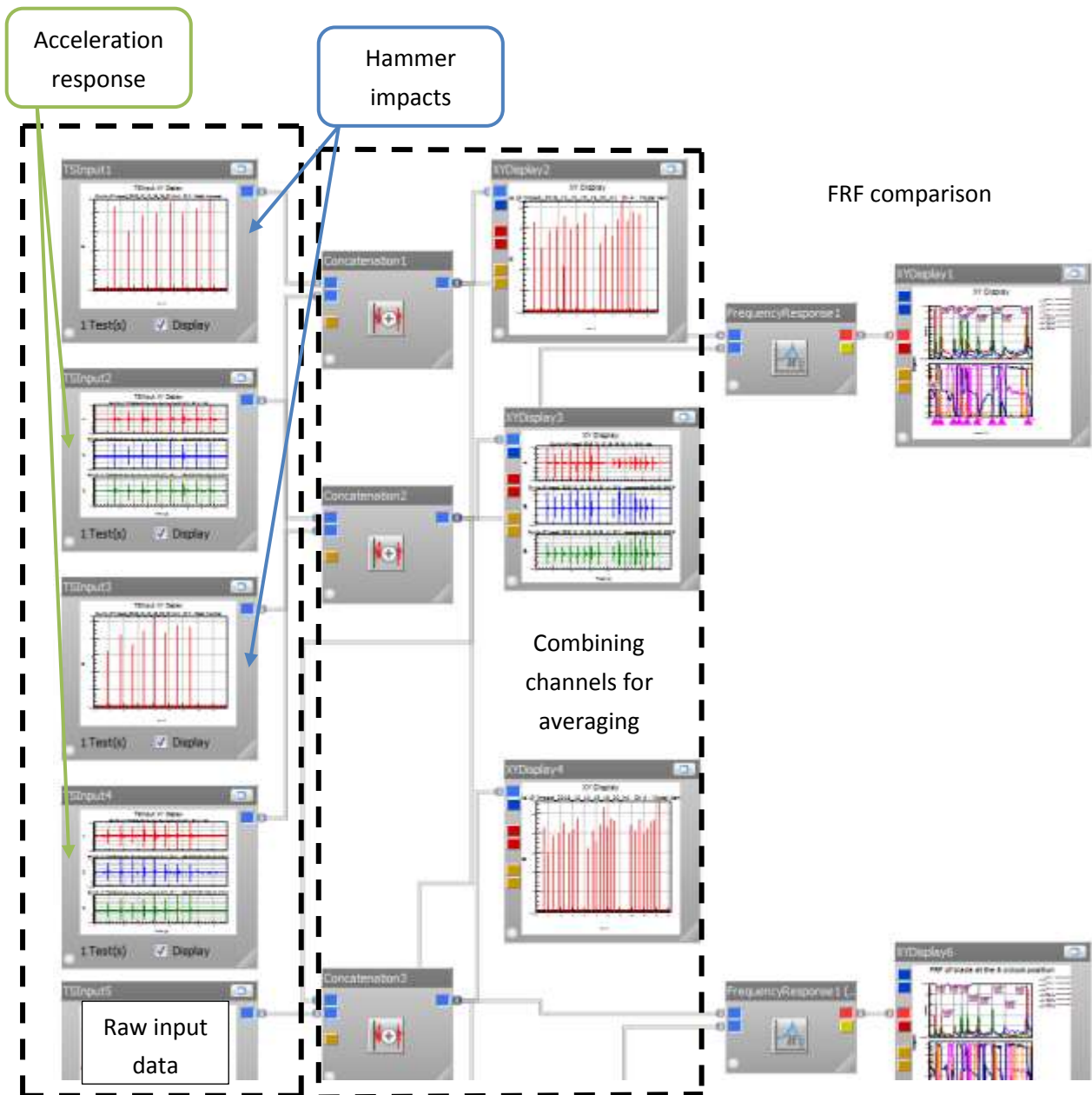
Figure 3-4: Typical nCode process flow for FRF averaging

Figure 3-5, shows the FRF results, measured at the 6 o'clock position. The data was averaged for all six the individual measurements (three per impact position). The figure show the results as per the legend for the three different channels or sensors. The phase angle is also plotted to show the existence of an actual mode where the phase angle shift by 180 degrees. The difference between the measured and computed results are shown in Figure 3-6 and Table 3-1, with green being good (< 3%), yellow moderate (>3% and <5%) and red being fair (>5%). The computed results are from a FEA, with no damping pins in the model. The reason for not having damping pins is that in reality the damping pins are completely loose while the rotor is stationary and does not add any stiffness to the model, while in the FEA the damping pins and holes are an exact match and therefore will add some stiffness and restrictions to the model.

Figure 3-5: FRF results of the blade at the 6 o'clock position

Figure 3-6: FEA compared to impact test results

Table 3-1: Comparison between FEA and FRF results

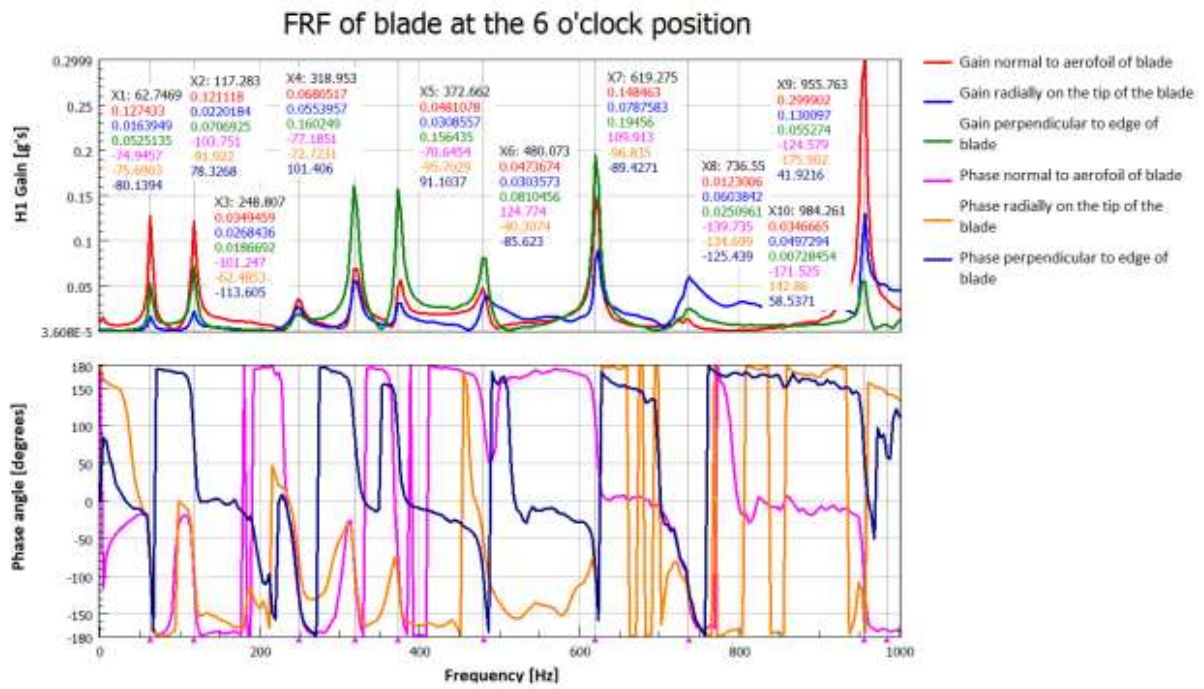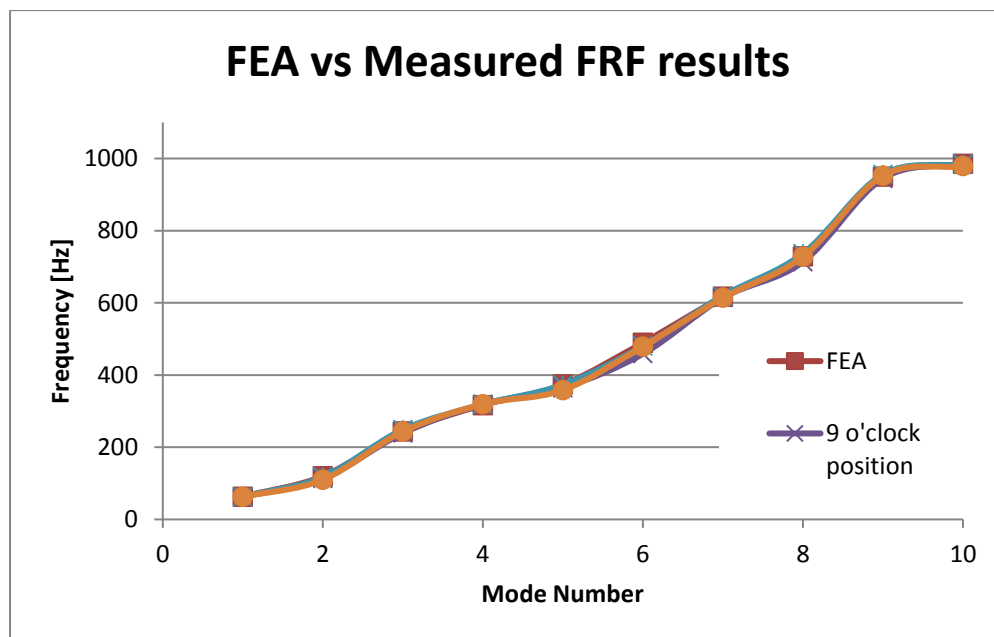| Position in Rotor	FEA	9 o'clock position		6 o'clock position		3 o'clock position	
	f_n [Hz]	f_n [Hz]	%Difference	f_n [Hz]	%Difference	f_n [Hz]	%Difference
Mode 1	63.158	62.7	0.7%	62.7	0.7%	62.5	1.1%
Mode 2	119.65	112.9	5.6%	117.3	2.0%	109.9	8.1%
Mode 3	243.61	238.9	1.9%	248.8	2.1%	243.3	0.1%
Mode 4	316.64	319.4	0.9%	319.0	0.7%	319.4	0.9%
Mode 5	373.65	364.7	2.4%	372.7	0.3%	358.4	4.1%
Mode 6	489.25	458.8	6.2%	480.1	1.9%	479.0	2.1%
Mode 7	617.49	614.1	0.6%	619.3	0.3%	614.1	0.6%
Mode 8	729.13	713.8	2.1%	736.6	1.0%	727.8	0.2%
Mode 9	949.81	944.8	0.5%	955.8	0.6%	952.5	0.3%
Mode 10	984.98	986.5	0.1%	984.3	0.1%	978.8	0.6%

The 6 o'clock position proves to be the most consistent position, between the three positions where measurements were taken, compared to the FEA results. This can be explained due to the slight pre-stress on the blade in the radial direction due to gravity, which is in the same direction as the centrifugal force while in operating condition.

3.1.3   Modal parameter estimation

Modal parameter estimation is a technique, which is used to experimentally calculate the damping associated with each mode. With well-separated modes, the estimation can be done by means of peak-picking method on the FRF. Peak picking does however rely heavily on the maximum-recorded value at the peak. It also has to be noted that the damping is for a stationary blade and that there is no untwisting of the blades to ensure that the damping pins lock the blade. The damping estimates was therefore only seen as an indication of the initial damping in the blade.

The post-processing was executed with nCode, with a typical process as shown in Figure 3-7. The peaks were recorded at the natural frequency and the half power point was calculated from the amplitude at the natural frequency divided by the square root of 2 as shown in equation (3.1).

$$Haft\ power\ point = {|A|}/{\sqrt{2}}$$

(3.1)

The horizontal line at the half power point was then used to identify two frequency points. These values are then used to calculate the damping and the damping ratio at the examining natural frequency. The respective equations are shown in equations (3.2) and (3.3) (Ewins, 1995).

$$n_r = \frac{\omega_1^2 - \omega_2^2}{2\omega_n^2} \cong \frac{\Delta\omega}{\omega_n}$$

(3.2)

$$\zeta_r = \frac{1}{2}r_r$$

(3.3)

From the results above it was shown that the 6 o'clock position provides the most realistic values and therefore only the results from this position were considered. The results for the first four modes at the 6 o'clock position are shown in Table 3-2. These results were further utilised in the Rayleigh damping calculations shown in Appendix B.
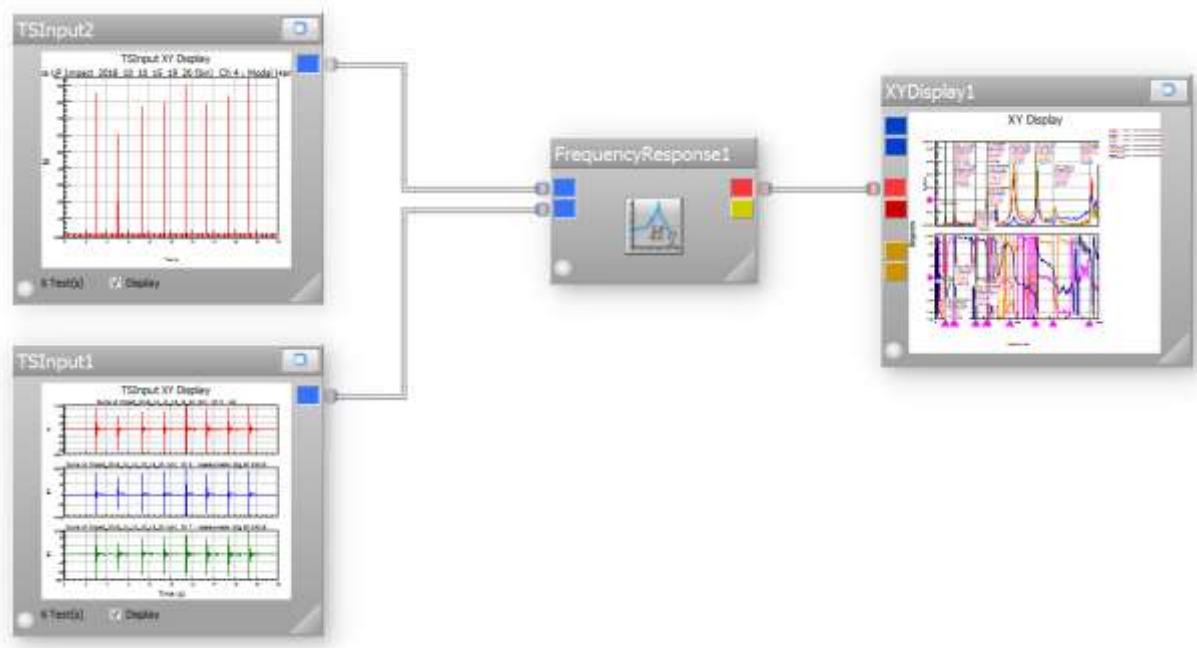
Figure 3-7: Typical FRF process in nCode

Table 3-2: Damping ratios from model measurements for 6 o'clock position

Position in Rotor	6 o'clock position		6 o'clock position		6 o'clock position		6 o'clock position	
Impact	Perpendicular impact		Side impact		All		Average	
	n	ζ	n	ζ	n	ζ	n	ζ
Mode 1	7.641%	3.821%	8.859%	4.430%	9.106%	4.553%	8.535%	4.268%
Mode 2	4.996%	2.498%	4.927%	2.463%	4.979%	2.489%	4.967%	2.484%
Mode 3	4.303%	2.152%	3.307%	1.653%	1.887%	0.944%	3.166%	1.583%
Mode 4	2.940%	1.470%	3.066%	1.533%	3.070%	1.535%	3.025%	1.513%

3.2 Telemetry spin test

A spin test analysis was conducted in a balancing pit to get the natural frequencies of the blades at different speeds. Four blades were instrumented with strain gauges and data was recorded via a

telemetry system. The data was captured on the same typical blade design as in section 3.1, but a different actual rotor (Newby, 2006). When the rotor speed increases, the centrifugal force rises and stress stiffening occurs. The damping pins located between the blades also react to the untwisting of the blades and interlock. All of these effects have a slight influence on the natural frequencies of the blades and cause the natural frequencies to shift.

The setup consisted of four blades, which were instrumented with strain gauges, and the signals were brought from the rotating shaft through a telemetry system, with a slip ring configuration. The blades were then artificially excited with a magnet, which were positioned in the balance pit near the LSB, which were instrumented. The strain gauges subsequently captured the dynamic responses of the blade. The Campbell diagram is showing the result of the first three modes from this test and is shown in Figure 3-8. The second light grey lines, which are shown in the figure, represent the OEM data from various spin tests they conducted through the years on the current LSB under investigation (*Alstom Drawings*, 1993). The data from the measurements and the OEM data seem to correspond reasonable well around 3000 rpm with the exception of mode 3. A combined table of measured and computed results are shown in Table 3-3, with green representing good correspondence (< 3%), yellow moderate (>3% and <5%) and red being poor (>5%) as discussed in section 1.2.3. The light grey block indicate data that were not measured during the test. A negative percentage indicate where the computed FEA results were higher than the measured results.
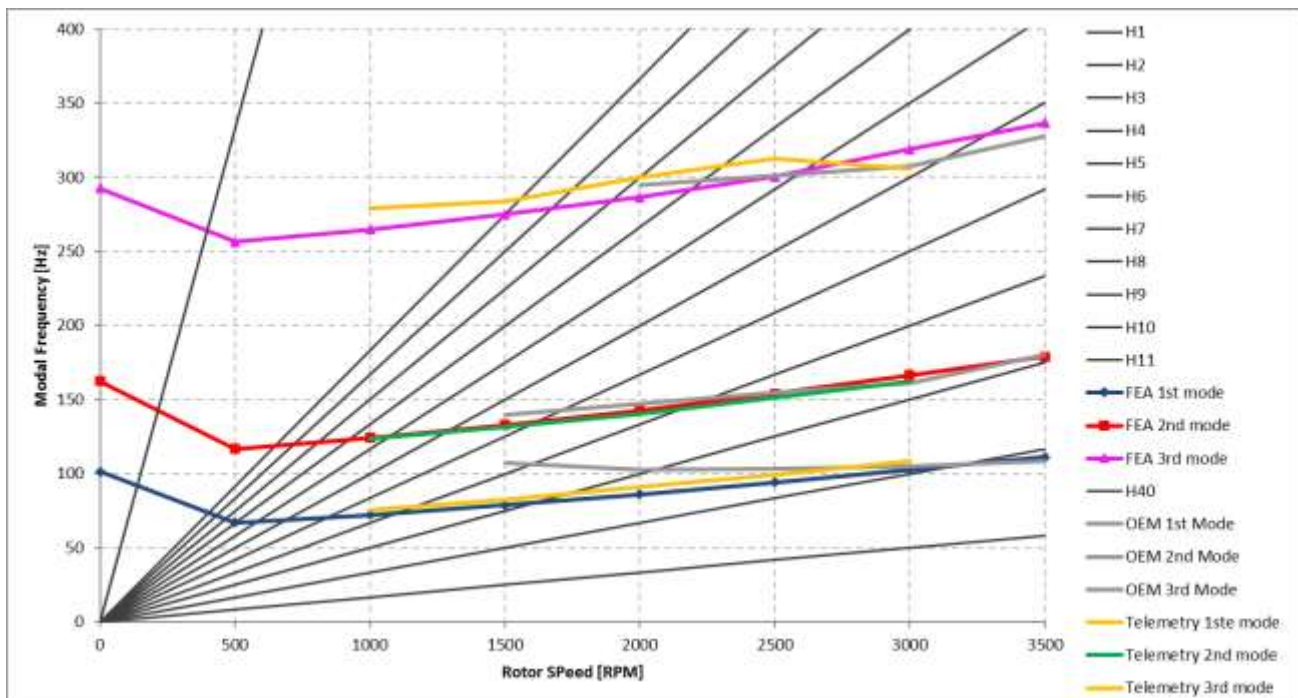

Figure 3-8: Campbell diagram of spin pit testing, comparing OEM, telemetry and FEA results

Rotor Speed (rpm)	1st Mode	2nd Mode	3rd Mode
1500	26.72%	4.93%	
2000	16.15%	3.26%	3.12%
2500	9.27%	1.02%	0.95%
3000	2.99%	-2.35%	-2.09%
3500	-1.43%	1.59%	-0.98%

3.3 Chapter summary

The FEA model shows very good comparison with the blade tap testing or vibration impact testing. The tap test was used to verify the FEA model at stationary conditions. The FEA model used had no damping pins in the model, since they are loose when there is no untwist on the blade and will not add stiffness to the blade.

Model parameter estimation was conducted on the tap test data in order to estimate damping present in the model. Based on the data captured from the tap test, the 6 o'clock position showed the best results and therefore the model parameter estimation was only conducted for the 6 o'clock position.

In order to verify the FEA model at operating speed, a telemetry spin test was done at different speed intervals and the natural frequencies were extracted and compared to the FEA results. Only the first three modes were extracted and used for the comparison. The data showed very good comparison of the first three modes, at the operating speed (3000 rpm) speed and overspeed (3500 rpm) and all modes are within 3%. Most of the FEA analysis showed in Table 3-3 is lower than the measured results, for instance the first mode at 3000 rpm is about 107 Hz, which is far enough from the second harmonic of the shaft, but FEA results show 101 Hz. The data comparison for the lower speeds did not compare that well, but this was neglected, since the dissertation focuses on calculations at operating speed.

Chapter 4
Fatigue life analysis

The fatigue life analysis was done based on non-integral or non-synchronous vibration on the blade. This is when the blade will vibrate randomly and not at integrals of the operating speed. From the BTT data the dominant mode shape which is present during full speed no load (FSNL) conditions with high backpressure on the blade was analysed. The BTT data was used to get an indication of the movement of the blade tip. These values were then applied to scale the model analysis, which was gathered from the FEA. A mean stress was added to the fatigue analysis that is present due to the centrifugal load on the blade. The mean stress applied however is a mean stress after initial plasticity and strain hardening has occurred in localised high stress regions on the blade This resulted in a stationary compressive residual stress in the root section of the blade after the blade was run at 20% (3600 rpm) overspeed.

4.1   BTT data

BTT data of the last stage blade at high backpressure conditions was made available by the OEM and used in this analysis. The unit with the utility has is slightly different from the unit from which the BTT data was obtained. The two units have the same design, but other differences are present, for instance atmospheric conditions, which have an influence on the condenser and outlet conditions. The raw BTT data was analysed by the OEM, by means of FTT and data containing records every second was supplied. Two sets of data was supplied, both running at high backpressure conditions, but one having low steam loading and the other having high steam loading. The tip displacement amplitude is plotted in real time with the exhaust pressure and the estimated load output of the turbine in Figure 4-1 and Figure 4-2 for low load and high load conditions respectively. The LP exhaust pressure have about the same shape, with the maximum exhaust pressure being the same at about 130 mbar for the high backpressure condition. The power is for the full turbine with total power capability of about 550 MW. The higher backpressure causes flow separation, which most likely cause the blade vibration.

Also plotted is a comparison between the blade tip displacements against the exhaust pressure as shown in Figure 4-3 and Figure 4-4 for low load and high load conditions respectively. It needs to be noted that the unit scale for the displacement is not the same for the low load and high load conditions. The displacement is about 13.5 times higher for the low load condition than for the high load condition. This plotted data supports the argument that the backpressure is proportional to the vibration of the blade for low load conditions. Generally for higher backpressures, the displacement is larger. It is also evident that the high load condition does not have a huge increase in displacement with exhaust pressure, as in the case for the low load conditions. The data was sampled at 50 Hz, with a FFT response plotted every second. The sample rate is very low for a fatigue analysis and aliasing of the data is expected due to Nyquist frequency as explained in section 1.2.2.2. The OEM however made use of other techniques in order to extract the data and get higher frequency response. These techniques include measuring the wheel mode frequency by measuring the vibration of all blades,

giving us a sampling frequency of; 78 blades times the 50 Hz sampling frequency resulting in 3900 Hz. The OEM also track the aliased frequency of the vibration mode during run-up and run-down in speed. The relationship between real frequency and aliased frequency changes with a change in rotational speed, so the OEM can distinguish between modes with different real frequencies and the same aliased frequency. In order to limit the effect of aliasing the main vibratory signal were superimposed to the data, which is explained below.
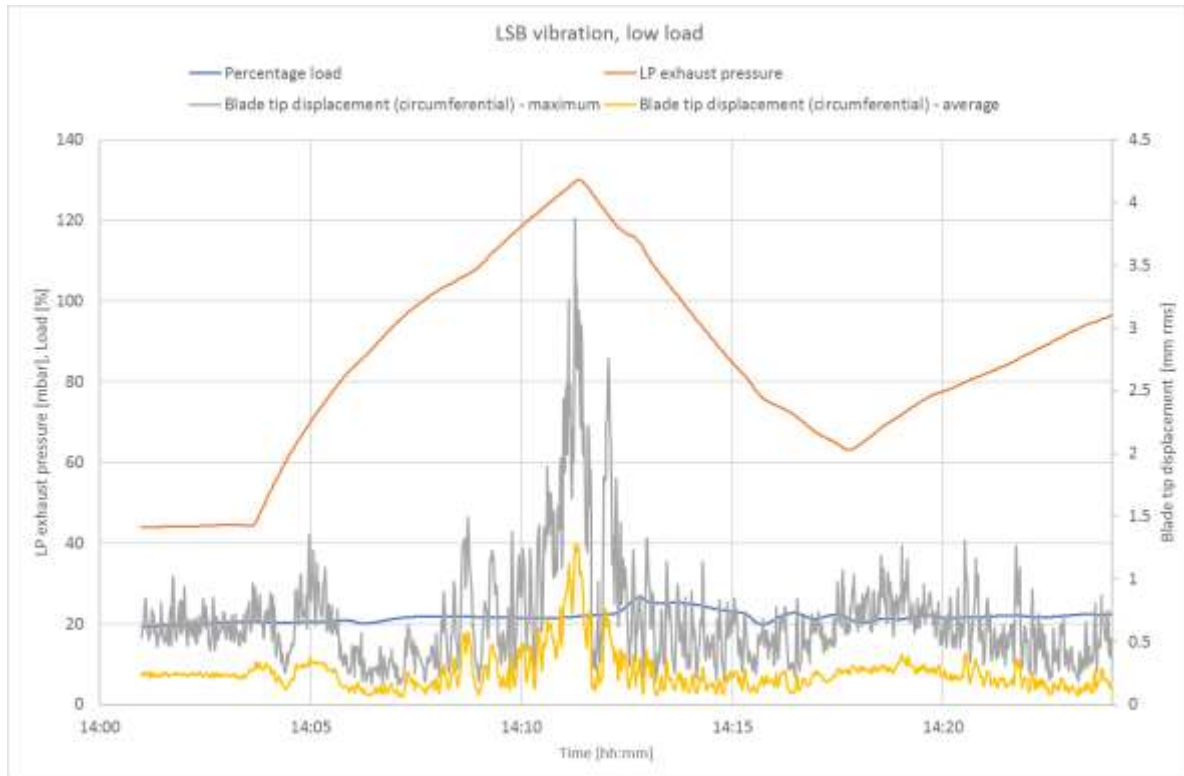

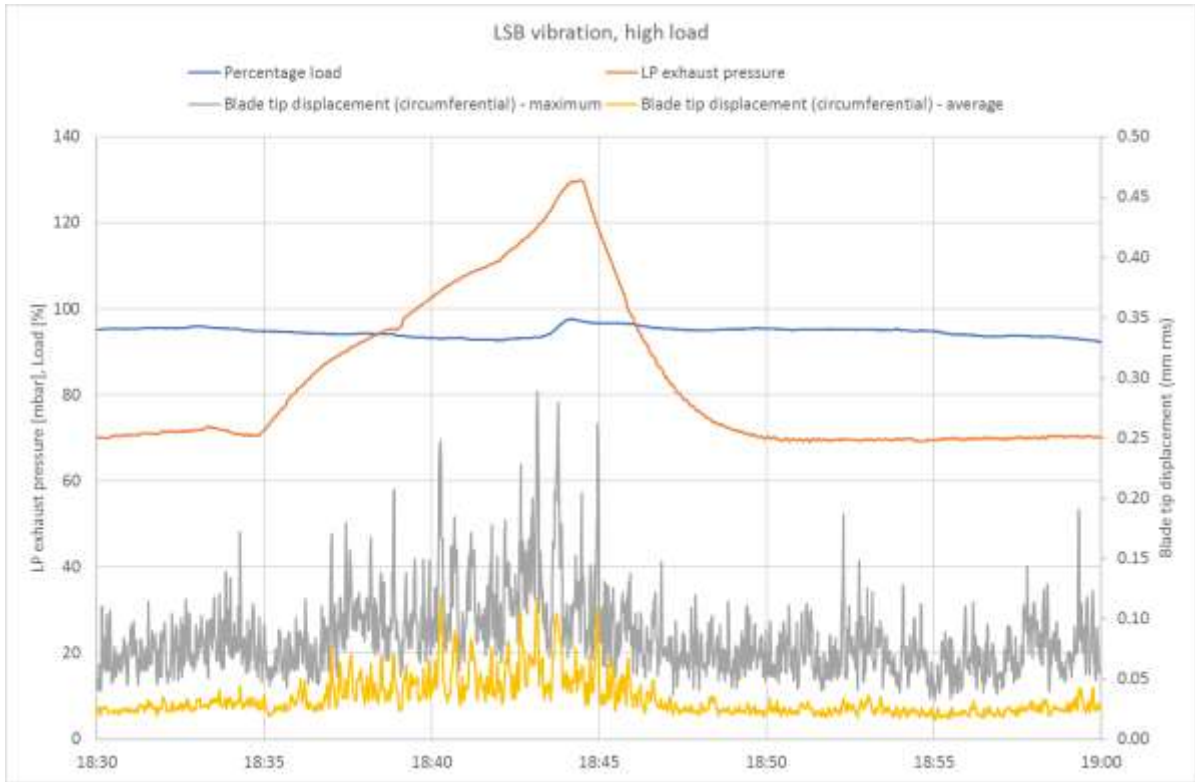**Figure 4-1:** BTT vibration data at low steam load conditions

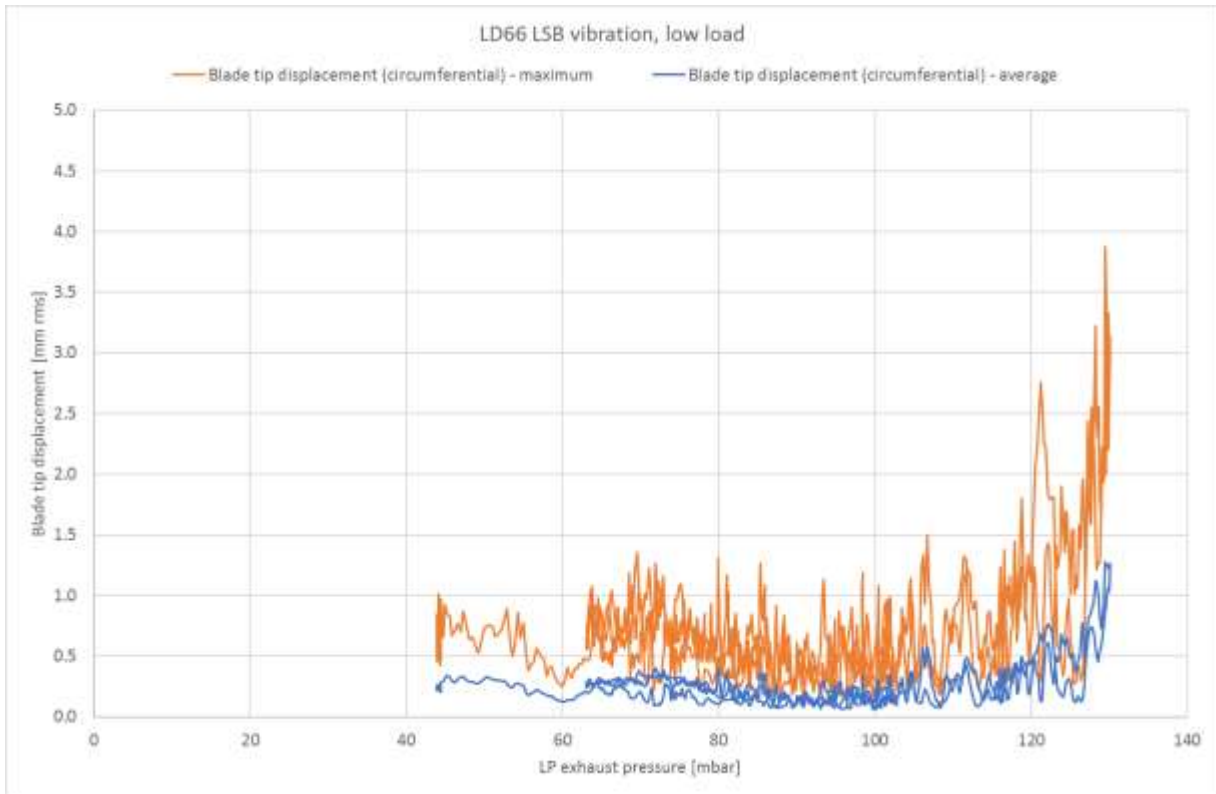**Figure 4-2:** BTT vibration data at high steam load conditions

Figure 4-3: Blade tip displacement vs LP exhaust pressure at low steam load conditions
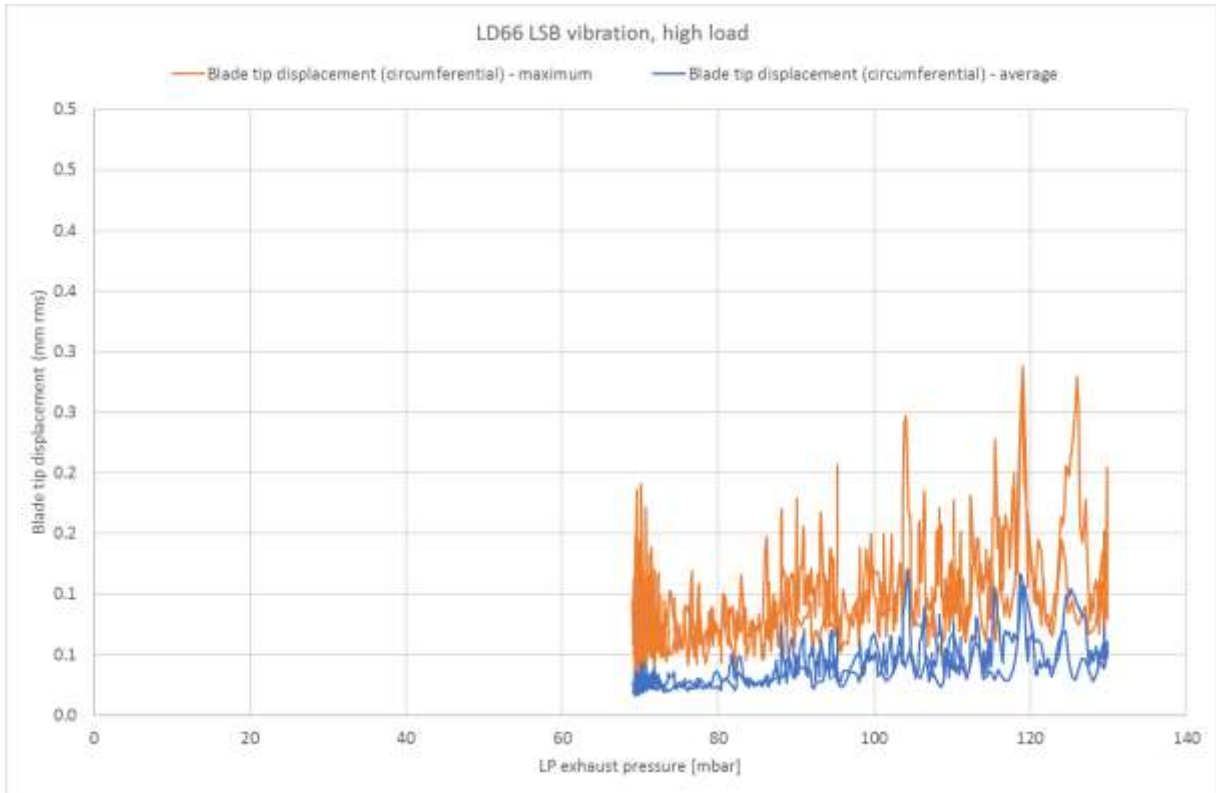
Figure 4-4: Blade tip displacement vs LP exhaust pressure at high steam load conditions

As a conservative approach for fatigue, the maximum data from all the blades per revolution was used. The data were converted from root mean square (rms) values to the peak displacement by means of equation (4.1).

$$x_{peak} = \sqrt{2}x_{rms} \tag{4.1}$$

The post-analysed data from the OEM, shows that the dominant frequency during operation was about 174 Hz in the case for the low load condition, the second mode with seventh nodal diameters was excited. For the high load condition, no mode excitation could be measured. The frequency together with the peak amplitude were used to create the displacement results against time as per equation (4.2). It was assuming that the signal provided by the BTT measurements was a perfect sinusoid, with only the dominant frequency present.

$$Displacement = A_{peak}\sin(\omega t) \tag{4.2}$$

All of the above calculations were done in nCode with the g*lyphs* process shown in Figure 4-5 and the results shown in Figure 4-6. The data was analysed with two conditions. The first condition was where the amplitude was kept constant over a second, causing a step response. The secondly condition was where the amplitude was linearly interpolated between the neighbouring values, which causes a

Blade tip timing to determine turbine blade fatigue in low vacuum conditions   67

continuous connection between values. The results of these respective methods are shown in Figure 4-7 and Figure 4-8, where only a matching zoomed section of a couple of seconds is shown. A sensitivity study was done to see the effect of the interpolated data against the hold value. In all the cases the hold value had a higher life prediction than the interpolated values, which make the interpolated value more conservative to use. The results of the case study is tabulated in Table 4-1 and from the low standard deviation and variance values it can be concluded that the data is fairly close to the median.

Table 4-1: Results for case study of hold vs interpolated data

Description	Value
Maximum percentage difference	37.50%
Minimum percentage difference	0.01%
Average percentage difference	7.49%
Standard deviation	7.51%
Variance	0.56%

Data input

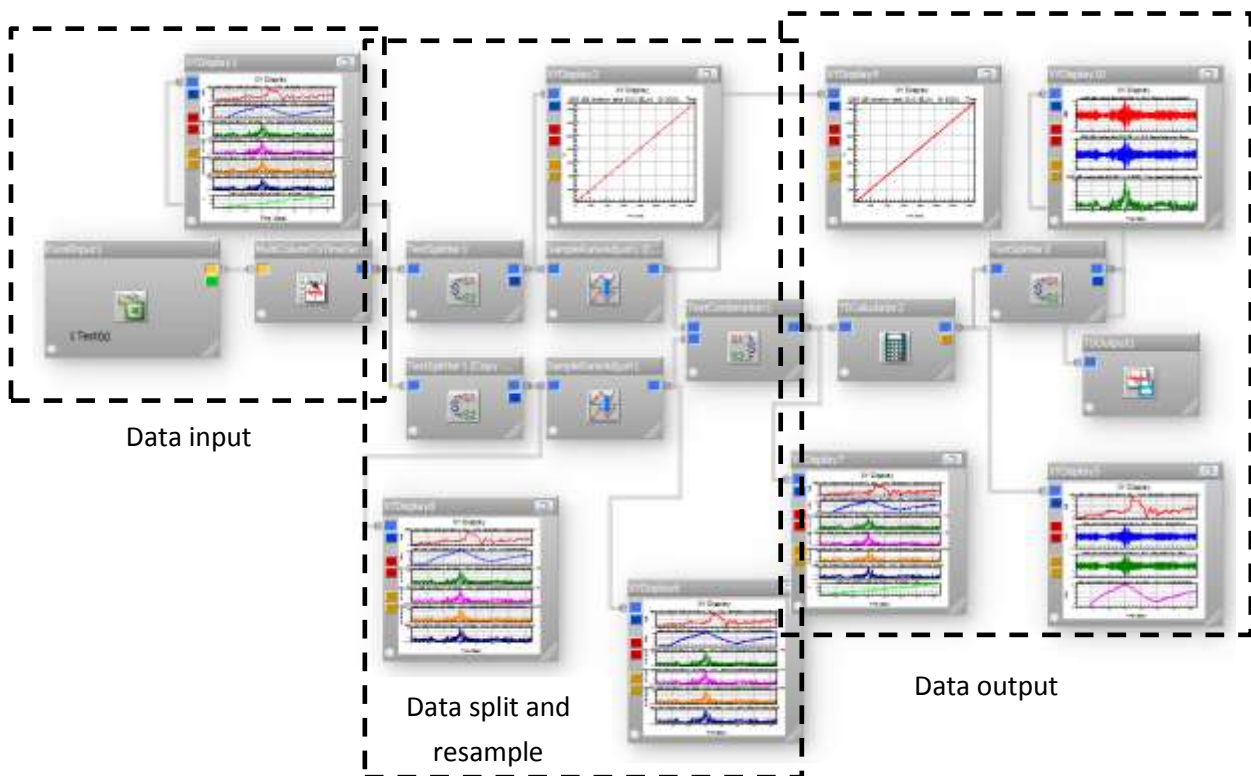Data split and resample

Data output

Figure 4-5: nCode *glyphs* showing post-processing process of BTT data into sinusoidal displacement
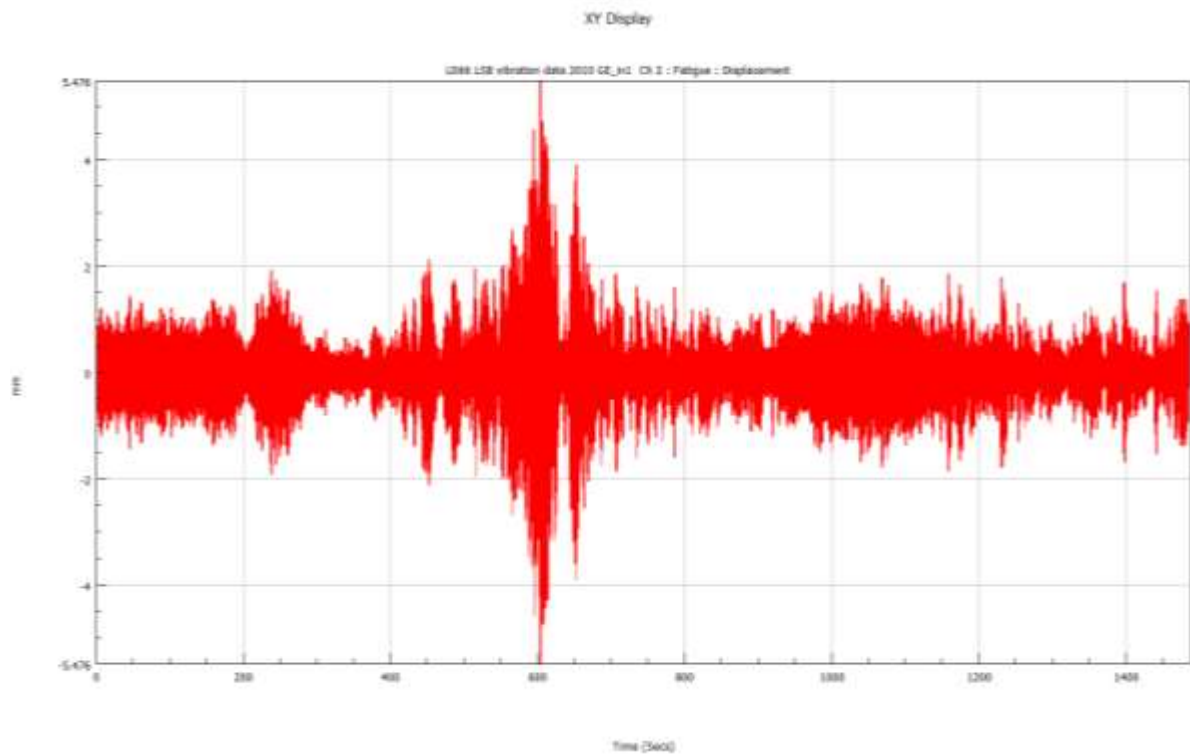
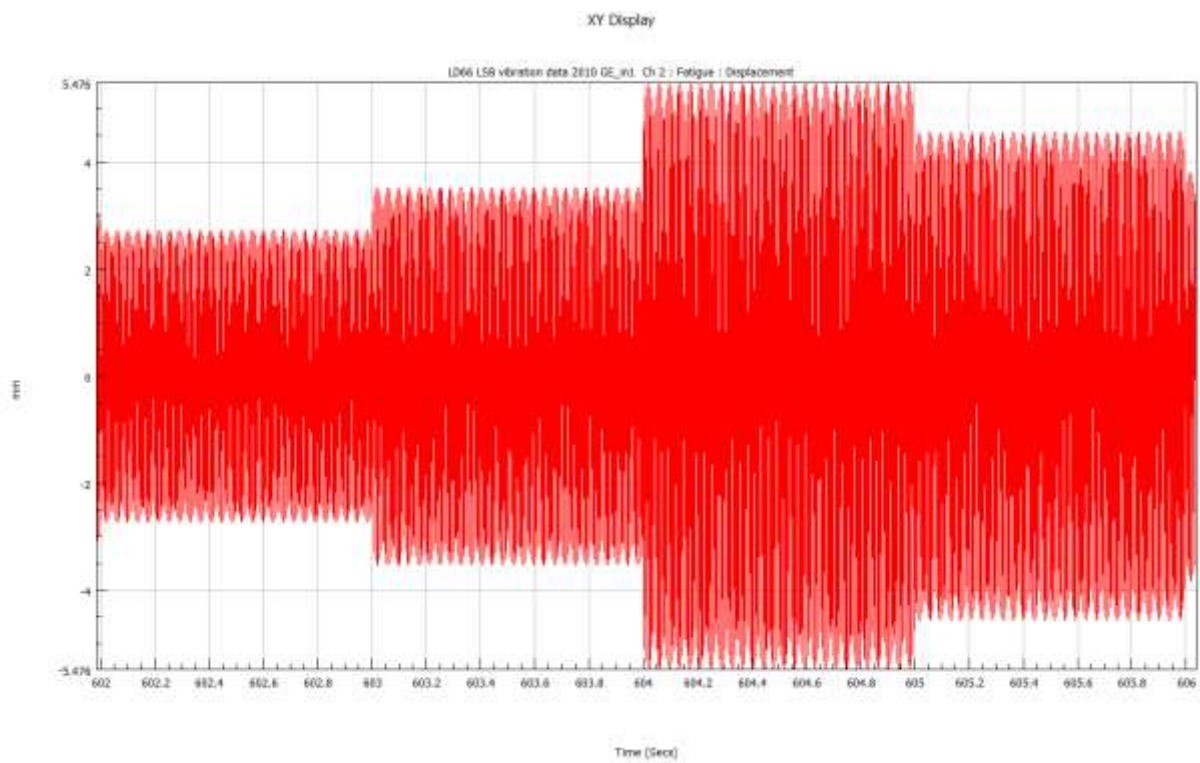**Figure 4-6:** Result of post-processed BTT data

Figure 4-7: Constant amplitude between intervals
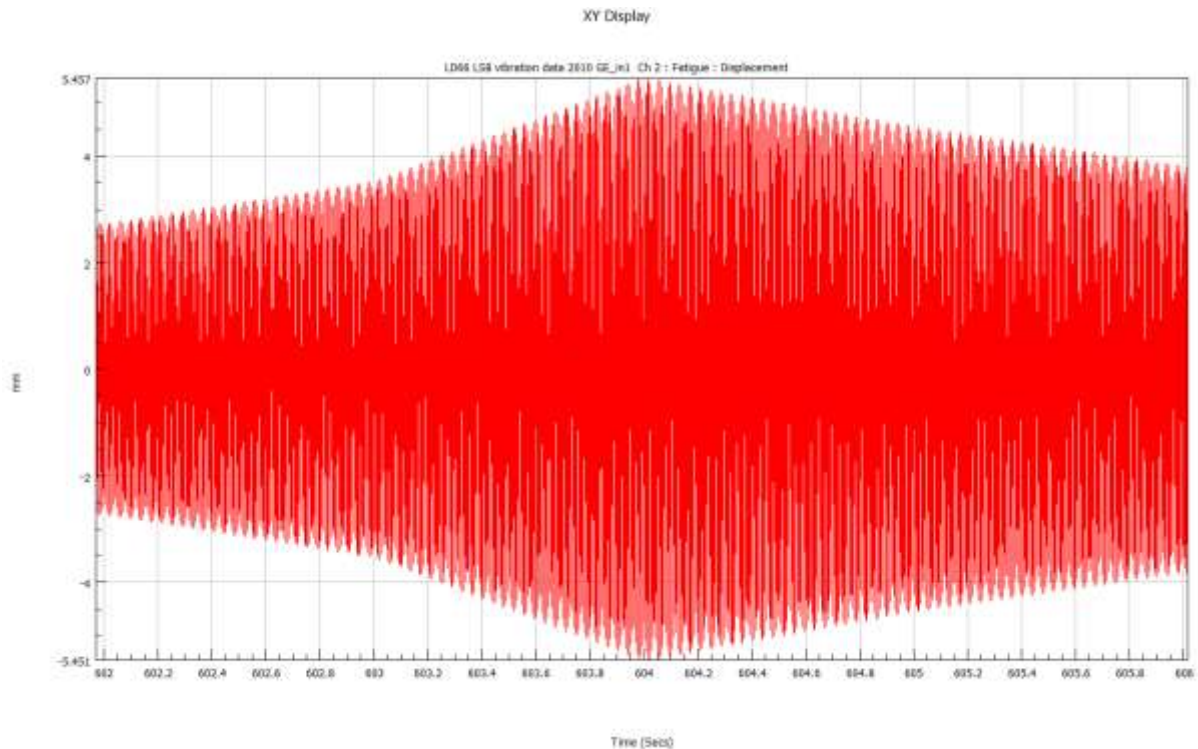
Figure 4-8: Interpolated amplitude between intervals

A key assumption was made during the analysis that the maximum amplitude measured by the BTT systems is the maximum deflection in the mode shape calculated by FEA. This assumption is only true in the following cases:

- When the data is measured over a long enough time period and the peak is captured.
- The data is captured during steady flow.
- If there is only one dominant frequency present during measurements.

None of the above could be definitively confirmed, since the sample rate is only 50Hz and the total measuring time is just 26 minutes, the flow is only constant between 20 -30 kg/s and even though this frequency is dominant there are also other frequencies present in the signal.

The modal displacement needed to be converted to the apparent displacement measured by the BTT system. The method of the conversion to the apparent displacement is explained in Appendix C.

4.2   Material fatigue properties

For the blade material, no materials fatigue properties could be found and the properties had to be estimated from known methods. As per the literature review in section 1.2.4.4 the UML is not accurate for high strength steel and therefore the extended UML was used for the analysis. Due to plasticity being present in the model an ε-N fatigue analysis needed to be used and these properties also needed to be included in the model. The results for the calculations are shown in Table 4-2, including different temper conditions and methods.

Table 4-2: Material fatigue properties of different methods and temper conditions

	Temper temperature of 350 ˚C		Temper temperature of 600 ˚C		Temper temperature of 650 ˚C	
	Extended UML	UML	Extended UML	UML	Extended UML	UML
σ_f [MPa]	2187.7	2070.0	1990.3	1710.0	1847.0	1523.0
ε_f	0.3494514	0.3334330	0.4426025	0.4165317	0.4850000	0.4600000
b	-0.097000	-0.087000	-0.099054	-0.087000	-0.100069	-0.087000
c	-0.58	-0.58	-0.58	-0.58	-0.58	-0.58
n	0.1664940	0.1500000	0.1707827	0.1500000	0.1725324	0.1500000
H [MPa]	2606.2	2440.7	2287.6	1950.1	2092.6	1711.1

In order to show the difference of the various fatigue models on the blade material a hysteresis loop of the various material properties and conditions is plotted, see Figure 4-9. This was executed in MATLAB with the code shown in Appendix E.1, using the Ramberg Osgood equations as explained in section 1.2.4.5. The hysteresis plot is representing the load the blade is experiencing as calculated by the FEA values, but with different material fatigue properties. The ε-N curve using the same material properties as for the hysteresis plot, are also shown in Figure 4-10, with the elastic, plastic and total strain lines plotted. This again was executed with a MATLAB code shown in Appendix E.2.

From the hysteresis plot in Figure 4-9, it can be seen that the UML and the extended UML are close to each other for the lower yield stress at temper conditions of 350˚C. As the yield stress increase the difference in the UML and the extended UML is also increasing.
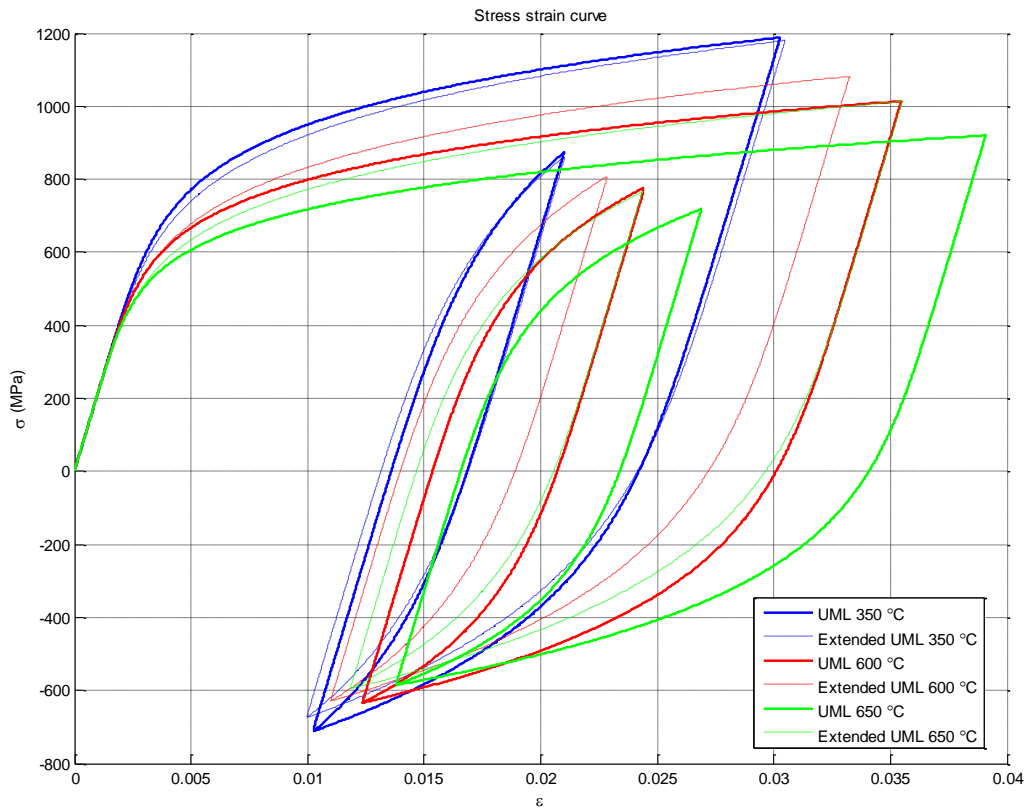
Figure 4-9: Stress strain curve of different material models
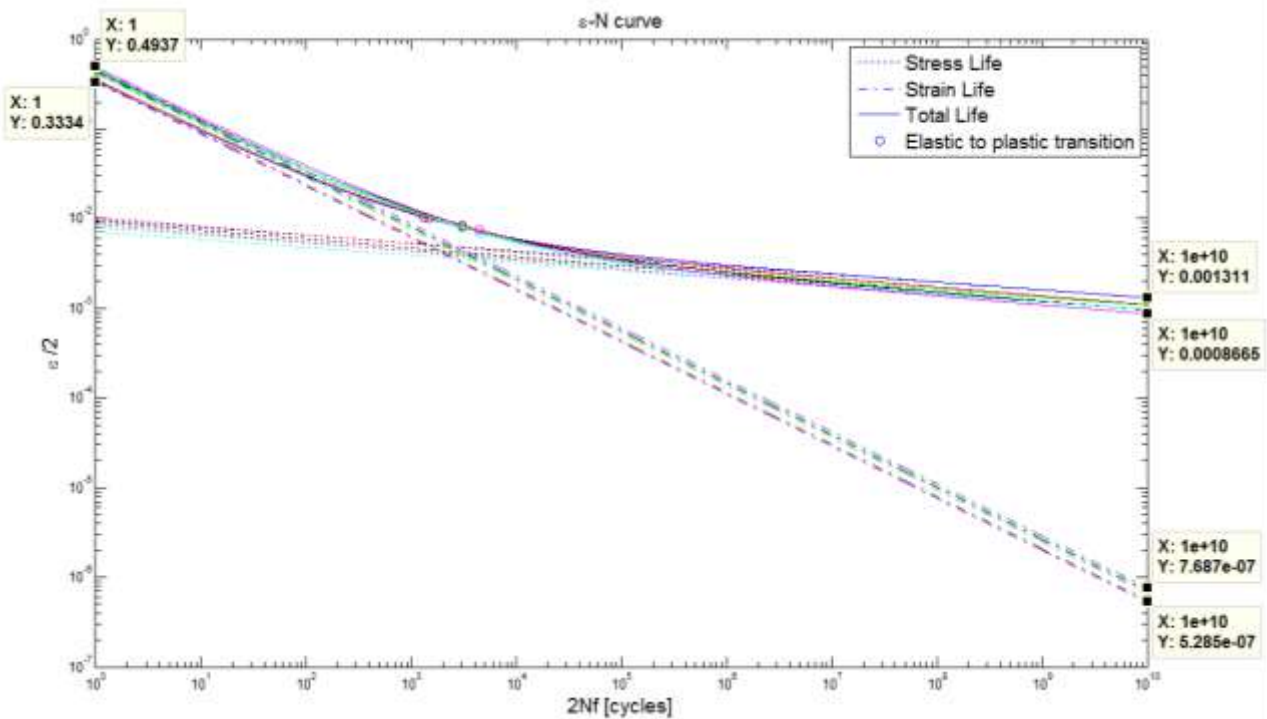
Figure 4-10: ε-N curve for the different material models
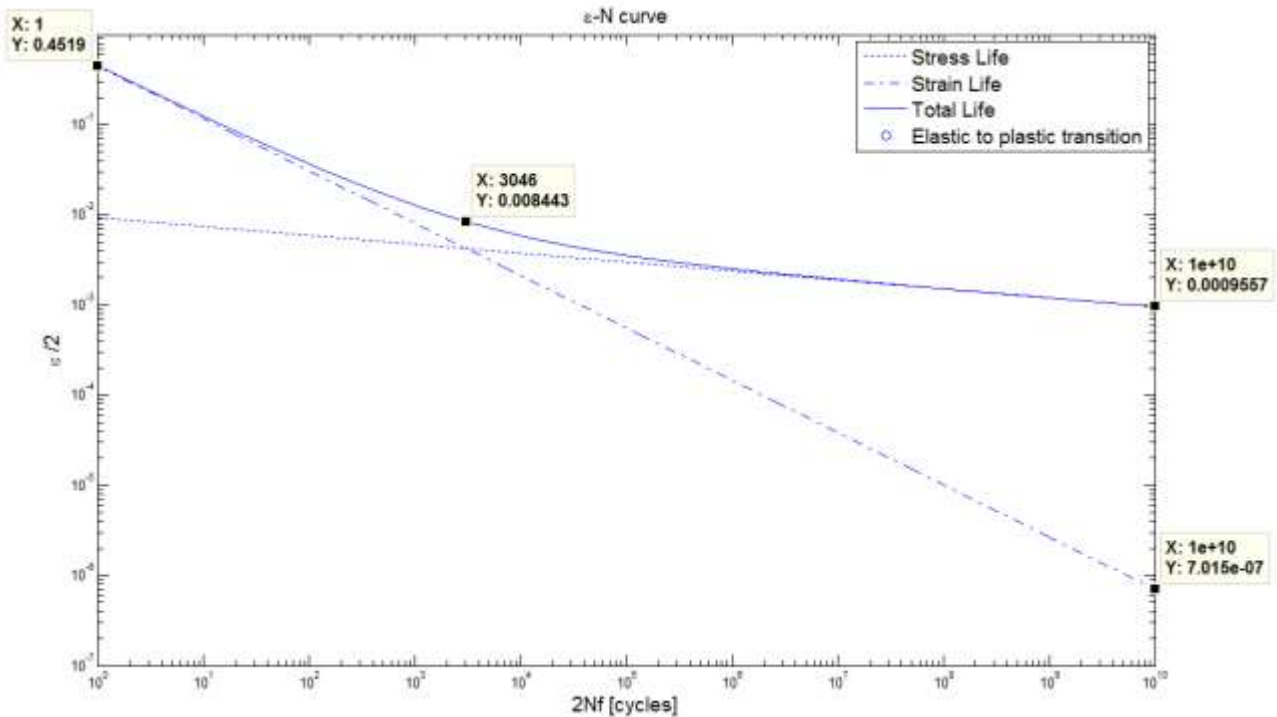
Figure 4-11: ε-N curve for the blade material at a temper condition of 600 ˚C with EUML

4.3   Fatigue analysis

The fatigue analysis was conducted using the pre-stress results with an overspeed plasticity on the model, as a mean stress input. This was calculated from a linear elastic FEA model and then corrected for plasticity based on literature in section 1.2.4.5 and work done by EPRI (2008). A dynamic load was added to the mean stress from the modal analysis, which was corrected as per the BTT data as explained in section 4.1. The fatigue analysis was done with most of the calculation being in the tension-tension cycle as explained in section 1.2.4.1, with the stress ratio being higher than 1.

The fatigue analysis was computed in MATLAB, which is good with managing and processing large data files. The fatigue analysis was implemented only on the root section of the blade and transition to the blade as shown in Figure 4-12. The main reason for only including this section in the fatigue analysis is since failures that were recorded in practice on this blade mainly occur in this region. The analysis was done on the average element results exported from the FEA.
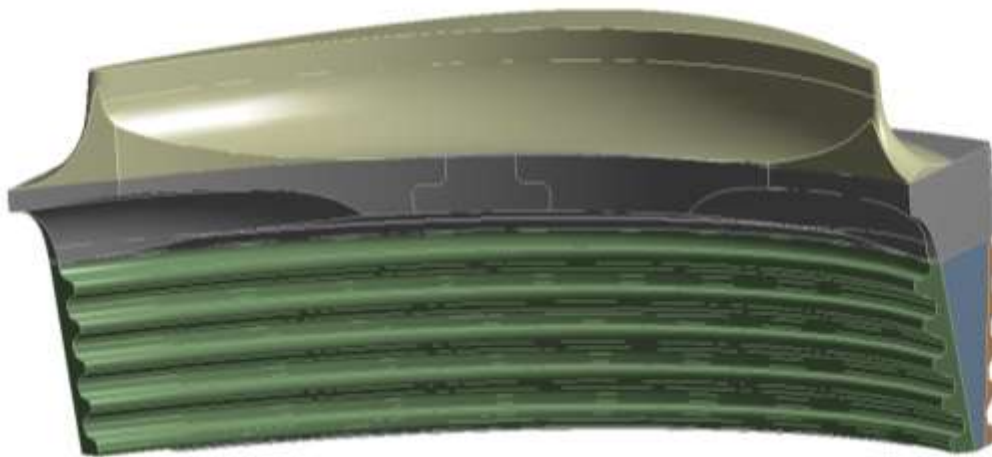
Figure 4-12: Fatigue analysis region

Option 1: Constant amplitude

Option 2: Rainflow cycle counting
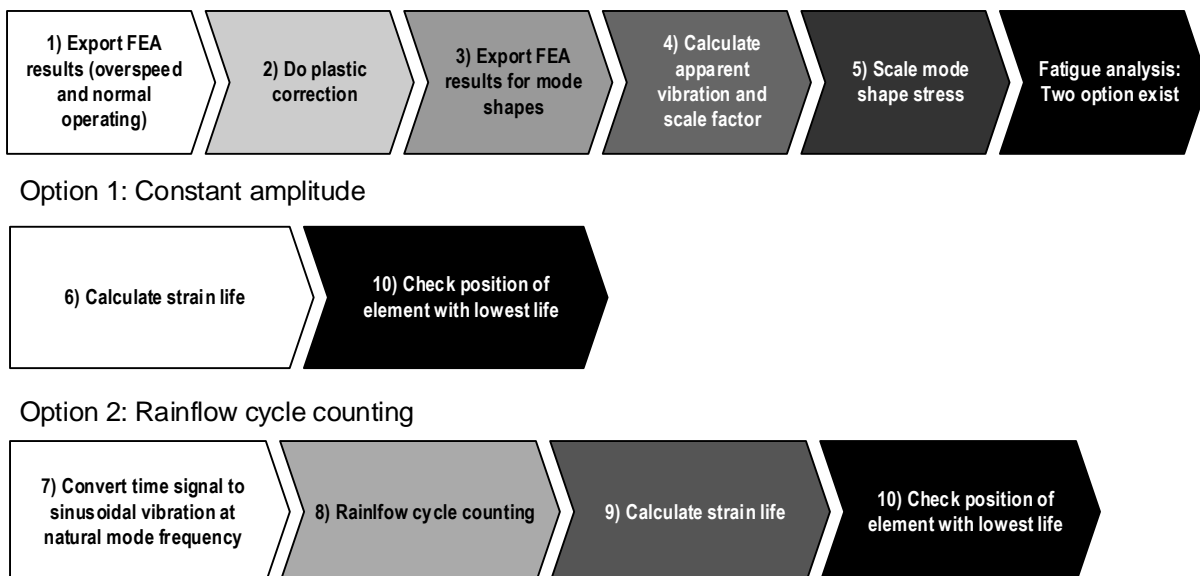
Figure 4-13: Fatigue calculation process flow

The process flow for computing the fatigue analysis is outlined in Figure 4-13, with the numbers related to the points below:

1. Export FEA result for 3600 rpm and 3000 rpm cases
2. Do plastic correction on local areas where yielding occur
3. Export FEA results for mode shapes
4. Calculate apparent vibration and calculate scale factor as per equation (4.3)
5. Scale the mode shape stress based on the scale factor
6. Calculate strain life, with mean stress correction based on constant amplitude of dynamic stress
7. Do the calculation to convert the time signal to a sinusoidal vibration as per equation (4.2)
8. Do rainflow counting and use Miner's rule for damage estimation
9. Calculate strain life, with mean stress correction based on rainflow amplitude of dynamic stress

10. Check position of element with the lowest life

$$Scale\ factor = \frac{Maximum\ displacement\ BTT}{Maximum\ displacement\ FEA} \qquad (4.3)$$

4.3.1 Rainflow cycle counting

Rainflow cycle counting was done as described in section 1.2.4.2 using a MATLAB script. The script used was the algorithm developed by (Niesłony, 2009) and using *ASTM E 1049-85 (1997)* for cycle counting in fatigue. This method does not incorporate the loading sequence effect on fatigue analysis, but purely the effected damage, due to number of cycles.

A convergence check was done on the life calculated from the rainflow cycles counting algorithm, by varying the number of bins. Convergence occurred at about 4500 bins considering only the results of the first six modes having zero nodal diameter. Figure 4-14 only shows the first mode. The result will converge at about 1000 to 1500 bins, but the gradient is slightly upwards, but only reach a near horizontal line at about 4500 bins. The fatigue analysis based on a rainflow cycle counting was analysed with 4500 bins. The life calculated with more bins resulted in a slightly longer life calculation, with a difference of 7.3% calculated from 64 bins to 4500 bins.

The data was created around a zero mean value, since the data used was generated based on the measured vibration, and then further interpolated. This is shown centred around a zero mean in Figure 4-15. Note that the number of bins used for the plot is only 64 bins to simplify the visual representation. The majority of the data lies in the small displacement amplitude region as expected, since only a few high range cycles are present. The full results for all the modes can be found in Appendix D.
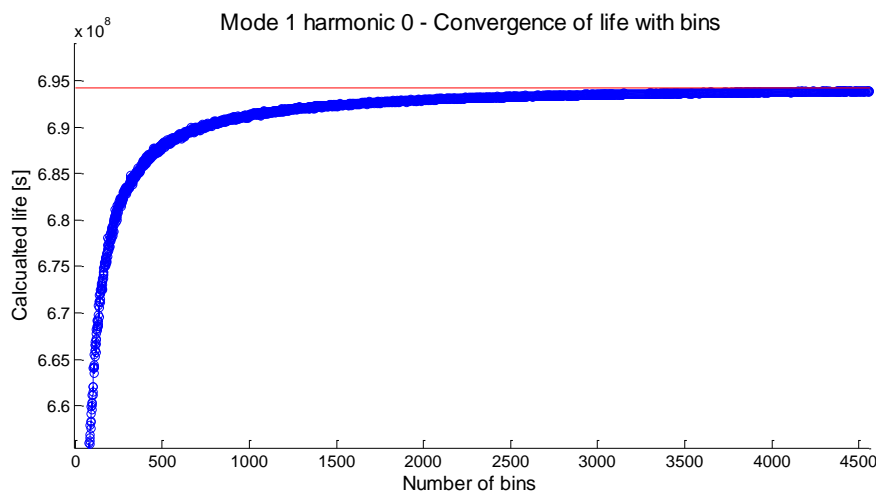
Figure 4-14: Rainflow fatigue life convergence

Blade tip timing to determine turbine blade fatigue in low vacuum conditions   75
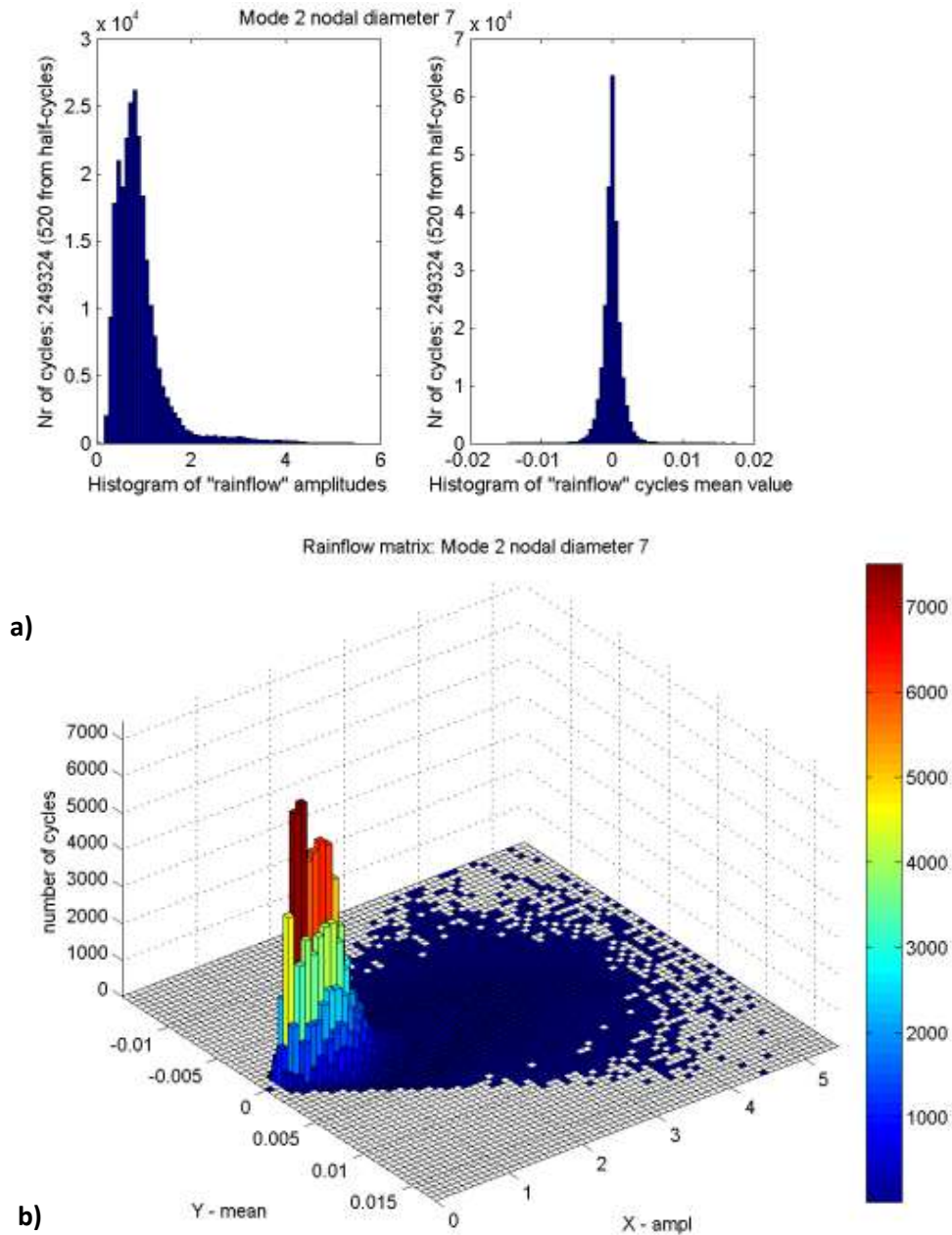
Figure 4-15: Rainflow cycle counting with a) amplitude and mean values b) rainflow matrix

4.3.2 Damage assessment

A fatigue damage assessment was executed, using the process described in section 4.3 and formulas discussed in section 1.2.4 of the literature study. This includes the mean stress results of the centrifugal loading, which were added as a static mean stress. The analysis was done in MATLAB, due to the number of elements analysed as per the FEA result for the root of the blade. Shown in Figure 4-16 is the damage fraction for the time series as per the displacement amplitude of the tip of the blade. As expected the high displacement region contribute to most of the damage, even though very few cycles are present at these high amplitudes.
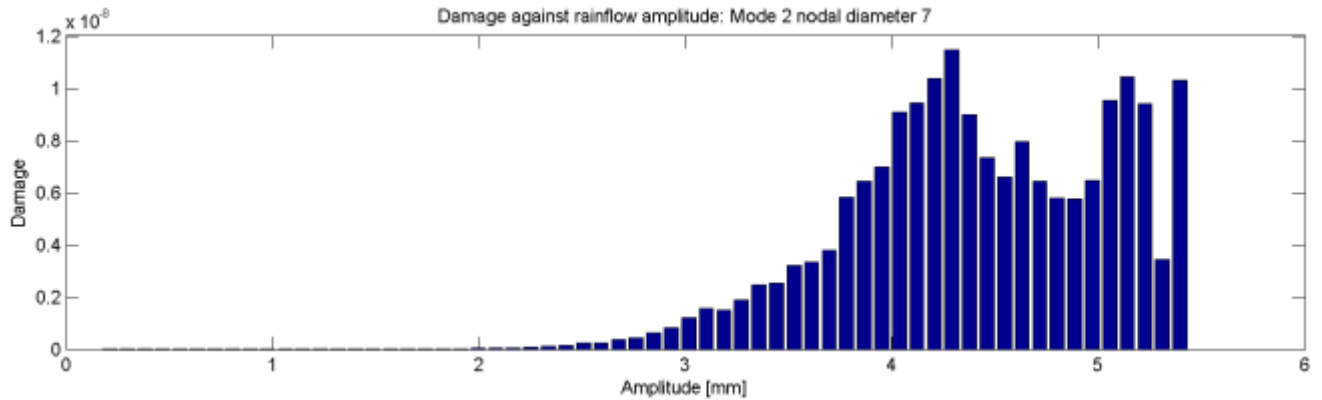
Figure 4-16: Damage fraction for time signal against displacement amplitude

Knowing that the sequence of events play an effect in fatigue analysis and ultimately the life which is calculated. While using rainflow cycle counting and Palmgren-Miner's rule, none of these methods incorporates the sequence of events and therefore the life calculated could be slightly off due to this. However the major influence of plasticity due to overspeed of 20% in the initial installation of the blades are included.

4.3.3   Fatigue results

Fatigue data can usually be presented in either damage or amount of repeats during life. For this specific analysis the results will be represented in life repeats, which is more representative for the type of analysis that is considered. To make the output more useful and applicable it was converted to hours, day and years. The fatigue analysis was only considered at the root of the blade, where most of the failures were experienced.

The blade tip timing data that was analysed by the OEM, showed that for low load conditions the mode which were excited was that of mode 2 nodal diameter 7. However a study was done on the first 3 modes, up the 10th nodal diameter of each mode. These are the modes that normally get excited, due to lower frequencies, which need a low energy input in the system to excite these. By looking at this wider spectrum, it can also be investigated which of the other frequencies are sensitive for failure. This is based on an equal displacement of the tip, measured by the BTT system. The results will not necessarily be very accurate, because different modes of vibration will result in different tip displacements, but it will give some indication.

The results for the fatigue analysis for the low load condition is shown in Table 4-3, with the detail of the position on the node on the root shown in Table 4-3 and Figure 4-17. The fatigue life is colour coded as an indication of modes. Red should be avoided (red: <60), yellow can be a potential danger zones (yellow: between 60 and 365) and lastly green, which are considered no to be safe (green: >365).

Table 4-3: Fatigue life assessment result for first 3 modes, 10 nodal diameters for low load condition

Natural Frequency [Hz]											
	Nodal diameter										
Mode	0	1	2	3	4	5	6	7	8	9	10
1	101.10	101.54	102.85	104.96	107.83	111.37	115.47	120.02	124.93	130.08	135.36
2	164.25	164.32	164.51	164.84	165.30	165.88	166.60	167.44	168.43	169.57	170.89
3	310.17	310.24	310.42	310.68	310.99	311.31	311.62	311.92	312.18	312.41	312.59

Life [days], constant amplitude											
	Nodal diameter										
Mode	0	1	2	3	4	5	6	7	8	9	10
1	471.1	451.7	403.8	330.1	245.5	164.3	97.0	48.8	20.2	6.3	1.4
2	66381.7	43.9	45.3	47.6	50.9	55.2	61.7	70.4	84.1	108.5	146.0
3	34.5	2513.9	2703.3	3030.7	3572.2	4.1	5260.3	6847.4	9150.3	12991.0	25.8

Life [days], rainflow											
	Nodal diameter										
Mode	0	1	2	3	4	5	6	7	8	9	10
1	8030.6	8314.2	7314.2	5989.3	4636.1	2811.8	1817.8	931.5	334.6	125.5	28.7
2	1533025.2	987.3	1031.9	1084.0	1189.9	1083.1	559.4	1547.7	1941.0	2511.8	3455.9
3	1790.1	130498.3	139004.2	156129.2	190535.2	221.3	274805.7	360992.6	463152.6	713761.2	1248.6

Table 4-4: Position of lowest life elements

Node number											
	Nodal diameter										
Mode	0	1	2	3	4	5	6	7	8	9	10
1	151881	151881	151881	151881	151881	151881	151881	151881	151881	151881	151881
2	151166	151881	151881	151881	151881	151881	151881	151881	151881	151881	147950
3	151881	151981	151981	151981	151981	151985	151985	151985	151985	151985	151881

Serration											
	Nodal diameter										
Mode	0	1	2	3	4	5	6	7	8	9	10
1	Top	Top	Top	Top	Top	Top	Top	Top	Top	Top	Top
2	Top	Top	Top	Top	Top	Top	Top	Top	Top	Top	2nd
3	Top	Top	Top	Top	Top	Top	Top	Top	Top	Top	Top

Concave / Convex											
	Nodal diameter										
Mode	0	1	2	3	4	5	6	7	8	9	10
1	Concave	Concave	Concave	Concave	Concave	Concave	Concave	Concave	Concave	Concave	Concave
2	Convex	Concave	Concave	Concave	Concave	Concave	Concave	Concave	Concave	Concave	Concave
3	Concave	Concave	Concave	Concave	Concave	Concave	Concave	Concave	Concave	Concave	Concave

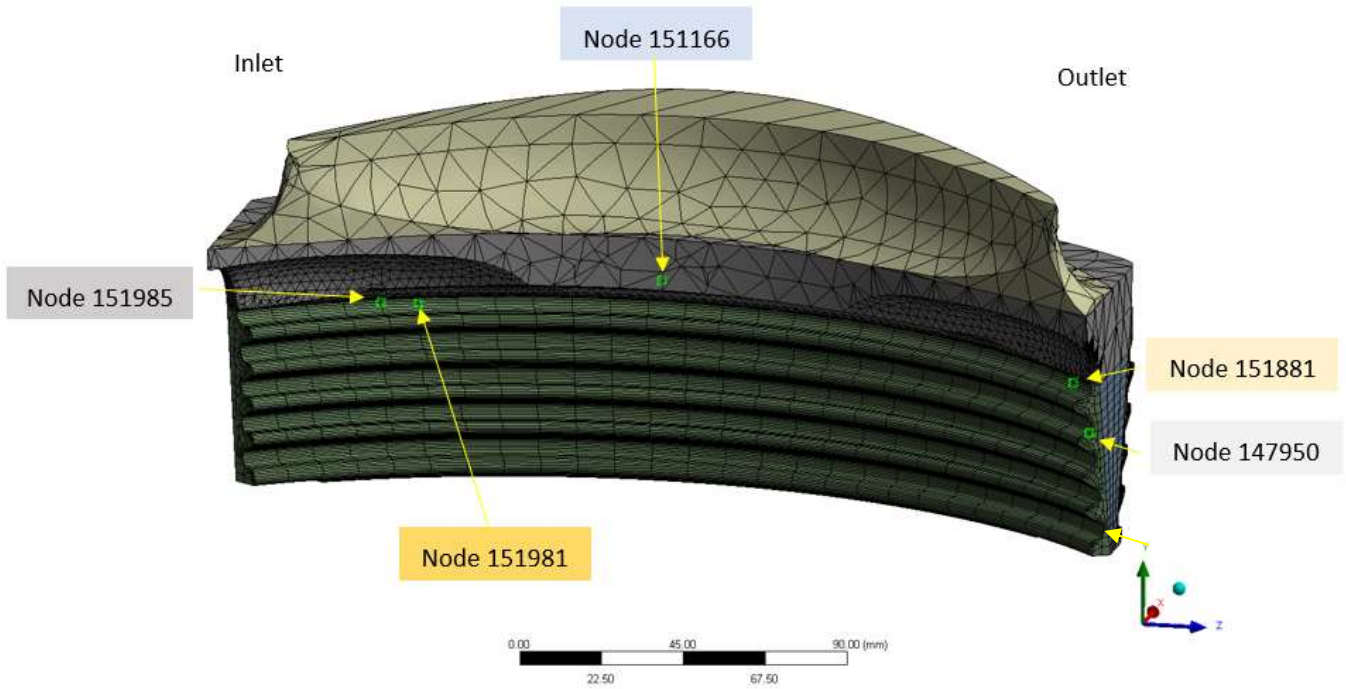| Position of blade											
	Nodal diameter										
Mode	0	1	2	3	4	5	6	7	8	9	10
1	Outlet	Outlet	Outlet	Outlet	Outlet	Outlet	Outlet	Outlet	Outlet	Outlet	Outlet
2	Centre	Outlet	Outlet	Outlet	Outlet	Outlet	Outlet	Outlet	Outlet	Outlet	Outlet
3	Outlet	Inlet / centre	Inlet / centre	Inlet / centre	Inlet / centre	Inlet / centre	Inlet / centre	Inlet / centre	Inlet / centre	Inlet / centre	Outlet

Figure 4-17: Position of nodes on mesh

The same process, which is described in section 4.3 was used to calculate the fatigue for the high load condition. The main difference between the input values for the low load and high load conditions at constant amplitude, is the maximum value for the BTT displacement. This is calculated in equation (4.4) and result to 13.459 times.

$$
\begin{aligned}
Displacement\ ratio &= \frac{low\ load\ displacement}{high\ load\ displacement} \\
&= \frac{5.4764}{0.4069} \\
&= 13.459
\end{aligned}
\tag{4.4}
$$

This change will have a direct effect on the dynamic stress, which then have an exponential effect on the stress life. If a constant blade tip displacement amplitude is considered, equation (1.14), can be used directly to calculate the life expectancy. Everything under the line stay constant between the low load and high load conditions and it is only the dynamic stress amplitude (σ_a) that changes. By replacing the dynamic stress amplitude with the displacement ratio between the low load and high load conditions the results are shown in equation (4.5).

$$
\begin{aligned}
N_{FL} &= \left(\frac{\sigma_a}{\sigma_f - \sigma_m}\right)^{\frac{1}{b}} \\
&= (13.459)^{\frac{1}{b}} \\
&= 4 \times 10^{-12}
\end{aligned}
\tag{4.5}
$$

It needs to be noted that the lower displacement result in much lower dynamic stress on the blade and is well below the dynamic stress range as explained in section 1.2.4 by EPRI, (2008) which was suggested for well designed blades. It also needs to be considered that fatigue works on a logarithmic scale and a large reduction in stress have a huge increase in expected life. In this case, for constant amplitude evaluation it lead to twelve-order decrease in life.

If the full signal recorded for the high load condition is applied and a rainflow cycle counting is conducted, the results are as shown in Table 4-5, together with the constant amplitude application for comparison. As expected a longer life is calculated for the actual BTT signal compared to the constant amplitude application. The data was then also further analyses to get a comparative result between the fatigue of the low load and high load condition. This results are shown in Table 4-6, and still show twelve-order reduction in life for the low steam flow condition, with slightly higher values.

Table 4-5: Fatigue life assessment result for first 3 modes, 10 nodal diameters for high load condition

| | Natural Frequency [Hz] | | | | | | | | | | |
| | Nodal diameter | | | | | | | | | | |
Mode	0	1	2	3	4	5	6	7	8	9	10
1	101.0957	101.5432	102.8462	104.9645	107.8343	111.3684	115.4667	120.0235	124.9312	130.081	135.362
2	164.2464	164.3204	164.5145	164.8385	165.2962	165.8837	166.5987	167.4438	168.4276	169.5671	170.8904
3	310.1663	310.2357	310.4186	310.6802	310.9856	311.3071	311.6238	311.9195	312.1833	312.4088	312.5929

| | Life [days], constant amplitude | | | | | | | | | | |
| | Nodal diameter | | | | | | | | | | |
Mode	0	1	2	3	4	5	6	7	8	9	10
1	1.18E+14	1.13E+14	1.01E+14	8.25E+13	6.14E+13	4.11E+13	2.42E+13	1.22E+13	5.05E+12	1.58E+12	3.44E+11
2	1.66E+16	1.10E+13	1.13E+13	1.19E+13	1.27E+13	1.38E+13	1.54E+13	1.76E+13	2.10E+13	2.71E+13	3.65E+13
3	8.62E+12	6.28E+14	6.76E+14	7.58E+14	8.93E+14	1.03E+12	1.32E+15	1.71E+15	2.29E+15	3.25E+15	6.45E+12

| | Life [days], rainflow | | | | | | | | | | |
| | Nodal diameter | | | | | | | | | | |
Mode	0	1	2	3	4	5	6	7	8	9	10
1	8.60E+14	8.37E+14	7.57E+14	6.18E+14	4.67E+14	2.73E+14	1.91E+14	9.38E+13	3.78E+13	1.30E+13	2.91E+12
2	1.56E+17	1.00E+14	1.06E+14	1.10E+14	1.19E+14	1.30E+14	1.16E+14	1.62E+14	2.01E+14	2.60E+14	3.50E+14
3	1.81E+14	1.31E+16	1.42E+16	1.62E+16	1.92E+16	2.23E+13	2.88E+16	3.65E+16	5.05E+16	6.72E+16	1.28E+14

Table 4-6: Fatigue life assessment results, comparing the low to high load conditions fatigue ratio

| | Low to high load conditions fatigue ratio | | | | | | | | | | |
| | Nodal diameter | | | | | | | | | | |
Mode	0	1	2	3	4	5	6	7	8	9	10
1	9.3423E-12	9.94E-12	9.66E-12	9.69E-12	9.93E-12	1.03E-11	9.54E-12	9.93E-12	8.85E-12	9.64E-12	9.86E-12
2	9.81038E-12	9.85E-12	9.71E-12	9.89E-12	9.98E-12	8.33E-12	4.82E-12	9.55E-12	9.64E-12	9.68E-12	9.87E-12
3	9.88191E-12	9.94E-12	9.8E-12	9.63E-12	9.92E-12	9.94E-12	9.53E-12	9.88E-12	9.18E-12	1.06E-11	9.77E-12

4.4 Chapter summary

Chapter 4 outlines the process used for doing the fatigue analysis, the fatigue properties and the results in order to calculate the life expectancy of a blade using BTT data. The process was established and applied to the first three modes, with their corresponding nodal diameters, up to the tenth nodal diameter. Two conditions were analysed at high backpressure, with one at low load, which is in the region of 20% load and the other at a high load, which is very close to full steam load.

The dominant vibration captured by the BTT systems for the low load condition, is the second mode, seventh nodal diameter. The OEM measure frequency was recorded round about 174 Hz compared to the FEA conducted at 167 Hz, but mode shapes was compared to ensure the same mode was used. This mode represents a fatigue life of 4.24 years (Table 4-3 results divided by 365 days), for the applied time signal in operation. It needs to be mentioned that the life calculated is not seen as an accurate finite life, but rather seen as an indication, since it only looks at a certain operating condition, based on certain assumptions. The fatigue life calculation also does not take into consideration the sequence of loading, except for the initial plastic deformation when running at 20% overspeed. The major fatigue regions are the top two serrations, on the inlet side, which is the same region where the cracks were seen and the analysis is as expected. This approached is deemed conservative because of the following assumptions:

- The BTT data that was used was the maximum for all the blades per time step, in reality a single blade will not likely see all the maximum displacements at very revolution.
- The peak stress is localised and even though the FEA mesh were refined and mesh convergence were checked there can still be a stress concentration present which result in higher localised stress.
- The material properties were chosen conservatively (cf. section 4.2) and the plastic results used were also taken as conservative. In practice, higher residual stress could be present.
- The interpolation method (cf. section 4.1) to process the BTT into a sinusoidal signal was selected due to representing less fatigue cycles.

Comparing the low load and high load conditions, the low load condition show much worse results than the high load conditions. The low load condition, show vibration levels of up to 13.5 times higher than the high load condition. It is calculated to have 12 orders lower fatigue life than the high load condition.

Chapter 5
Conclusion and further work

5.1 Conclusion

This dissertation focuses on an investigation of BTT, together with FEA as a possible procedure (cf. Figure 4-13) for calculating the fatigue life of a steam turbine LSB operating at FSNL, or low load at high backpressure conditions in the condenser. The investigation concentrates on the vibration of the LSB, which is non-synchronous in nature and vibrates at a blade resonance frequency. The procedure makes use of BTT and a method, which assumes that a dominant resonance frequency is present in the signal, and that only the mode excited by the dominant frequency contributes to the fatigue damage. The procedure does not include the participation of other modes with the dominant mode in terms of establishing life estimations. The investigation includes real life case scenarios to ensure that the method that is used is relevant and practical.

From the literature study, (cf. section 1.2) it is clear that running at off-design conditions (not recommended by OEM) largely affects LP blades, in particular the LSB. This is due to the presence of the low natural frequency of the LSB, which is dependent on the relatively long length of the blade. These blades are easily exited by the energy in the system. Excitation on the LSB is dependent on the flow angle, steam density, exhaust velocity, flow separation, and unsteadiness in the exhaust flow. High backpressure on the LSB is a result of high steam velocities going into the condenser, due to exhaust loss. BTT, otherwise known as BVM, is a modern technique, used to measure blade vibration of individual blades. Regardless of challenges in terms of obtaining accurate results and verifying vibratory responses, BTT is widely used as a vibration measurement tool and it provides good insight on blade vibration responses. The BTT data is reproduced in a vibration signal based on the assumption of a perfect sinusoidal signal of the excited mode.

This investigation includes FEA of the LSB to supplement the BTT data in order to do fatigue life calculations. The FEA was conducted on the complete LSB through a cyclic symmetric analysis of a single blade and rotor sector with two half damping pins connected to either side of the blade. A cyclic symmetric analysis simulates a perfectly tuned turbine set, because of the duplication from the single blade and where every duplicated item is exactly the same as the original. Plasticity was applied where the blade root would deform plastically at various local regions during initial overspeed testing. The initial plasticity creates a compressive stress on the surface of the blade, which reduces the mean stress during fatigue analysis and greatly influence the results. Pre-stress modal analysis was conducted to incorporate the centrifugal force and stress stiffening in the model. This also included the locking of the damping pins, which is present in the blade during this investigation under full speed conditions. Damping was added to the static model by means of friction. Thermal stresses were omitted (cf. section 1.2.3.2), due to LP blades operating at comparatively low temperatures of about 150 ˚C. The steam bending force was not simulated, due to low stress effects on the root compared to the centrifugal force. Also at low load conditions the steam load is reduced even further.

When conducting an FEA, the modal analysis and correct extraction of natural frequencies and modes are important factors to consider. Therefore, two tests were implemented to verify the FEA modal results. The first verification was a static impact test conducted by a modal hammer, to verify stationary blade natural frequencies (cf. section 3.1.2). This test showed very good correlation between all the modes below 1000 Hz. The correlation results for all the modes were below 1%, with the exception of three modes, where these modes correlation were around 2%. The second verification test was a balance pit test with strain gauges (cf. section 3.2). The test was done to verify natural frequencies at operating speed. Since centrifugal force contribute to a significant load of the blade and steam loading is relatively small, it is used as a good representation of the actual load on the turbine. This test however is not a complete comparison, but only a representative, excluding the steam loading. The test was conducted at operating speed in a balance pit, where four blades were instrumented with strain gauges at the root of the blade, including a telemetry system to transmit the signal. Data was measured at a specific operating speeds, to correlate according to a Campbell diagram. The correlation of the natural frequencies where between 2 and 3% at operating speed, with most of the FEA data slightly lower than the measured data. The FEA results does show that first mode is very close to the second harmonic of the operating speed, but spin pit tests done by the OEM showed that it is sufficiently higher than the second harmonic and by using BVM techniques it will be possible to detect the vibration of the first mode. The operation speed for this test was the same as for when the BTT data was collected.

Section 4.3 documents the fatigue life calculation, which was done with the input data from both the BTT data received from the OEM and, the input data from the FEA model. For this, the FEA results had to be exported for the operating speed, the overspeed condition and the blade modal results. Plastic correction had to be applied on the data, to compensate for overspeed yielding. The apparent vibration and scale factor was calculated and the natural modes were scaled accordingly to get the correct stresses. From these result the strain life was calculated for a constant dynamic stress amplitude. In order to do actual life estimation based on the BTT data, the BTT signal was converted to a sinusoidal vibration signal, with the dominant frequency interpolated between measurements. From there a rainflow cycle counting and the strain life analysis was conducted with Miner's rule for accumulating the damages on the LSB.

The fatigue life calculation, as documented in section 4.3.3, for the dominant frequency for mode two, nodal diameter seven was 4.24 years in operation. The deflection of the LSB tip was measured during low load conditions. This is 18.5% of the unit's design life of 40 years (200 000 operating hours). The fatigue life calculation does not include any start-up deterioration of life, neither any corrosion, erosion, impurities, defects in the blade nor load sequence. Fatigue life at high load conditions was calculated to be twelve orders higher than during low load conditions and therefore not an area of concern. Based on the data from section 4.3.3 low load conditions, with high backpressure should be avoided. Running a unit with high backpressure and low load will not necessary cause a failure immediately, but will rapidly reduce the life of the blade or enhance failure if a defect is already present. A significant change in results can be expected if a higher stress is present or, the duration of exposure to the peak stress is higher than what the test data has shown. The life calculations and

damage calculations, can however only be seen as an indication, due to slight differences between the two units; the one unit for which the BTT data was provided and the unit used for this investigation. Some differences includes, atmospheric conditions, possible transient vibration still present in signal due to the duration and stability of simulated conditions versus actual operating condition and lastly possible upstream flow conditions variations due to turbine train having minor differences. Also if accurate fatigue life predictions want to be done, one need to include the sequence of event that the blade went through in its life, to compensate for possible work hardening on the blade and accuracy of BTT technique. All of this can have an effect on the amplitude of the vibration, which have an effect on dynamic stress, which is directly responsible for the life in the component. This is due to the fatigue life that exponentially decreases, with increase in dynamic stress according to equation (1.14). The locations of the lowest fatigue life (cf. Table 4-4 & Figure 4-17), which are the top two serrations on the inlet side, corresponds to the location of failures were cracks initiated (cf. Figure 1-2).

The first three modes and ten nodal diameters was used to create a matrix (cf. Table 4-4) with which a fatigue life analysis was conducted. These modes were selected, since the first three modes are mostly effected by vibration, due to their lower frequencies. The matric can be used as a visual representation to the operator, to guide the operator when blade vibration is measured on a unit's LSB and the frequency coincides or are near a frequency to be avoided. The operator can then make slight changes to the system to try to move away from the vibration. The specific blade vibration data for mode two, nodal diameter seven was used from the BTT data to create the matrix. This is not a direct comparison, but rather an indication of fatigue life, because the vibration mode can differ from the recorded vibration for mode two, nodal diameter seven. One reason is that the direction and magnitude can be completely different. The matrix highlights the first mode with higher nodal diameters from eight to ten to be possible modes to monitor, as well as mode three nodal diameter five.

5.2 Further work

During this dissertation, areas were identified for further investigations. This includes:

- The investigation of the source of vibration and magnitude of vibration, especially in the region where more than one mode is excited or a different vibration pattern is observed. This is the case for synchronous vibration, which is not related to a mode excitation. A possible way of achieving this could be a through a structure-fluid interface model, which could also be beneficial in investigating flutter conditions. This then needs to be incorporated in the fatigue life calculations.
- A permanent BTT system installation in one of the operating units of the fleet, which runs frequently in high backpressure and low load conditions. The system could then measure and monitor the blade vibration at stable or uniform off-design conditions. This will ensure that the analysis will not rely on a simulated condition, kept at this condition for a very short time and includes, most probably transients in the analysed signal. Data that is stable or in steady state can result in more accurate results of what the blade in practise is experiencing. Therefore more informed decisions can be made to quantify the life and then ultimately the

maintenance intervals for crack inspection on the blade. With a permanent BTT system the influence of other operating parameters can also be investigated like recirculation while hood spray system is activated.

- Various different conditions of off-design can be explored with the BTT system. This can help to identify operating conditions to avoid and operating conditions still accepted to be safe operating conditions. This can then be quantified to determine RUL of the blade.

- Residual effects can be included in the model for shot peening and the degrading of the residual stress over the fatigue life. Both these can influence the range of the fatigue stress, which can highly influence the fatigue life of the LSB.

- In order to estimate time to failure, a fatigue analysis of a cracked blade could be included to simulate crack propagation.

References

Alstom (2016) *945 / 787mm Last Stage LP Blade-Customer Information Bulletin 2GBSTU00084U01A*.

Alstom Drawings (1993). GEC Alsthom.

'ANSYS Help Viewer, Theory referance' (2017). ANSYS.

ASTM E 1049-85: Standard practises for cycle counting in fatigue analysis. (1997). Philadelphia, USA: American Society for Testing and Materials.

ATOS Core (no date). Available at: http://www.atos-core.com/en/features.php#tripleScan (Accessed: 16 February 2016).

Bachschmid, N., Pesatori, E. and Bistolfi, S. (2015) 'Blade vibration measurements and excitation force evaluation', *3rd Middle East Turbomachinery Symposium (METS III)*, (February), pp. 15–18.

Bader, Q. and Kadum, E. (2014) 'Mean Stress Correction Effects On the Fatigue Life Behavior of Steel Alloys by Using Stress Life Approach Theories', *International Journal of Engineering & Technology IJET-IJENS*, 14(04).

Balda, M. (2018) 'BTT & RFBL - The optimum set for steam turbine blades monitoring', *Acta Polytechnica CTU Proceedings*, 20, pp. 5–9. doi: 10.14311/app.2018.20.0005.

Bastow, J. and Hosking, D. (1971) *12% Chromium Stainless steel turbine blade forgings*. Rugby.

Bezuidenhout, M. and Van Rooyen, G. (2004) *Heat treatment benchmarking testing of FV566 blade material*. Johannesburg.

Booysen, C. (2014) *Fatigue Life Prediction of Steam Turbine Blades during Start-up Operation Using Probabilistic Concepts*. University of Pretoria. Available at: https://repository.up.ac.za/bitstream/handle/2263/43250/Booysen_Fatigue_2014.pdf?sequence=1.

BS 7608 (1993) *Code of practice for fatigue design and assessment of steel structures*. doi: ISBN 0 580 21281 5.

Chowdhury, I. and Dasgupta, S. P. (2003) 'Computation of Rayleigh Damping Coefficients for Large Systems', *Int. J. Space Struct.. 43.*, pp. 6855–6868.

Das, G. *et al.* (2003) 'Turbine blade failure in a thermal power plant', *Engineering Failure Analysis*, 10(1), pp. 85–91. doi: 10.1016/S1350-6307(02)00022-5.

Deshpande, S. S. *et al.* (2016) 'Detailed studies on stress concentration by classical and finite element analysis', *International Journal of Mechanical Engineering and Technology*, 7(2), pp. 148–167.

Diamond, D. H. (2016) *A Probabilistic Approach to Blade Tip Timing Data Processing*. University of Pretoria.

Dowling, N. E. (2010) 'Mean Stress Effects in Stress-Life and Strain-Life Fatigue', *SAE Technical Paper Series*, 1. doi: 10.4271/2004-01-2227.

Dowling, N. E. (2013) *Mechanical Behavious or Materials*. Fourth Edi. Virgina: Pearson.

EPRI (2002) *Noncontacting Detection of Turbine Blade Vibration: Technology Assesment*, *EPRI*. Palo Alto, CA: 2002. 1004559.

EPRI (2006) *State-of-the-Art Weld Repair Technology for Rotating Components*. Palo Alto, CA: 2006 TR-107021-V1.

EPRI (2008) *Steam Turbine Blade Failure Root Cause Analysis Guide*. Palo Alto, CA: 2008: 1014137.

EPRI (2012) *Field Demonstration of Low-Pressure Turbine Blade Vibration Monitoring*. Palo Alto, CA.

EPRI (2017) *Low Pressure Steam Turbine Latter Stage Blades: Reliability Considerations and Risk Mitigation*, *EPRI*. Palo Alto, CA: 2017. 3002008574.

EPRI (2018) *Impacts of Low-Load Operation on Turbine Deposition: Risk Assesment*. Palo Alto, CA: 2018. 3002010785.

Ewins, D. J. (1995) *Model testing: Theory and practice*. Research Studies Press.

Fondjo, A. A. and Dzogbewu, T. C. (2019) 'Assessment of stress raiser factor using finite element solvers', *Universal Journal of Mechanical Engineering*, 7(6), pp. 367–379. doi: 10.13189/ujme.2019.070608.

Forbes, G. L. and Randall, R. B. (2013) 'Estimation of turbine blade natural frequencies from casing pressure and vibration measurements', *Mechanical Systems and Signal Processing*. Elsevier, 36(2), pp. 549–561. doi: 10.1016/j.ymssp.2012.11.006.

Friction and Friction Coefficients (no date). Available at: https://www.engineeringtoolbox.com/friction-coefficients-d_778.html (Accessed: 4 September 2018).

Fung, E.H.K., Yau, D. T. W. (1999) 'Effects of centrifugal stiffening on the vibration frequencies of a constrained flexible arm', *Journal of Sound and Vibration*, 224(5), pp. 809–841.

Hamidipoor, I. *et al.* (2015) 'The Impact of Blade and Material Damping in Turbine Blades', *International Journal of Science and Qualitative Analysis*, 1(3), pp. 64–68. doi: 10.11648/j.ijsqa.20150103.14.

Harish, A. B. (2016) *Finite Element Analysis: what's the difference between first order and second order elements?* Available at: https://www.quora.com/Finite-Element-Analysis-whats-the-difference-between-first-order-and-second-order-elements (Accessed: 13 September 2018).

Hultman, H. and Groth, P. (2015) 'Validation of Forced Response Methods for Turbine Blades'.

James, M. N. *et al.* (2010) 'Shot-peening of steam turbine blades: Residual stresses and their modification by fatigue cycling', *Procedia Engineering*. Elsevier, 2(1), pp. 441–451. doi: 10.1016/j.proeng.2010.03.048.

Knappett, D. and Garcia, J. (2008) 'Blade tip timing and strain gauge correlation on compressor blades', *Proceedings of the Institution of Mechanical Engineers, Part G: Journal of Aerospace Engineering*, 222(4), pp. 497–506. doi: 10.1243/09544100JAERO257.

Lee, K. S. and Song, J. H. (2006) 'Estimation methods for strain-life fatigue properties from hardness', *International Journal of Fatigue*, 28(4), pp. 386–400. doi: 10.1016/j.ijfatigue.2005.07.037.

Logan, D. L. (2007) *A First Course in the Finite Element Method*. Fourth. University of Wisconsin, Platteville: Thomson.

Logan, E. and Roy, R. (2003) *Handbook of Turbomachinery*. Second Edi. New york: Marcel Dekker Inc.

Maré, C. F. (2018) *An investigation of computational fluid dynamics simulation for estimation of turbine remaining useful life*. University of Pretoria. Available at: https://repository.up.ac.za/handle/2263/69152.

Mazur, Z. *et al.* (2006) 'Investigation of the failure of the L-0 blades', *Engineering Failure Analysis*, 13, pp. 1338–1350. doi: 10.1016/j.engfailanal.2005.10.018.

Mazur, Z., García-Illescas, R. and Porcayo-Calderón, J. (2009) 'Last stage blades failure analysis of a 28 MW geothermal turbine', *Engineering Failure Analysis*. Elsevier Ltd, 16(4), pp. 1020–1032. doi:

10.1016/j.engfailanal.2008.05.012.

Mccloskey, T. H., Dooley, R. B. and McNaughton, W. . (1999a) *Turbine Steam Path Damage : Theory and Practice Volume 1 : Turbine Fundamentals*. EPRI.

Mccloskey, T. H., Dooley, R. B. and McNaughton, W. . (1999b) *Turbine Steam Path Damage : Theory and Practice Volume 2 : Damage Mechanisms*.

Megerle, B. (2014) *Unsteady Aerodynamics of low-pressure steam turbines operating under low volume flow coniditions.* Federal Institute of Technology in Lausanne. doi: 10.5075/epfl-thesis-6096.

Ming, Z. *et al.* (2014) 'Fatigue behavior and mechanism of FV520B-I in ultrahigh cycle regime', *Procedia Materials Science*. Elsevier B.V., 3, pp. 2035–2041. doi: 10.1016/j.mspro.2014.06.328.

Modern Energetics (no date). Available at: http://mda139.net/ (Accessed: 10 January 2017).

Newby, M. (2006) 'Duvha manual excitation LP2'. Johannesburg.

Newby, M. (2013) *Optimisation of shot peeining for 12Cr steel in steam turbine blade applications*. University of Plymouth. Available at: http://hdl.handle.net/10026.1/1493.

Niesłony, A. (2009) 'Determination of fragments of multiaxial service loading strongly influencing the fatigue of machine components', *Mechanical Systems and Signal Processing*, 23(8), pp. 2712–2721. doi: 10.1016/j.ymssp.2009.05.010.

Oberholster, A. J. and Heyns, P. S. (2009) 'Online condition monitoring of axial-flow turbomachinery blades using rotor-axial Eulerian laser Doppler vibrometry', *Mechanical Systems and Signal Processing*, 23(5), pp. 1634–1643. doi: 10.1016/j.ymssp.2009.01.001.

Ostrovskii, L. I. (1969) 'Damping capacity of chromium turbine blade steels', *Strength of Materials*, 1(3), pp. 239–243. doi: 10.1007/BF01543208.

Palin-luc, T. and Jeddi, D. (2018) 'The gigacycle fatigue strength of steels : a review of structural and operating factors operating factors', *Procedia Structural Integrity*. Elsevier B.V., 13, pp. 1545–1553. doi: 10.1016/j.prostr.2018.12.316.

Perkins, K. M. and Bache, M. R. (2005) 'Corrosion fatigue of a 12%Cr low pressure turbine blade steel in simulated service environments', *International Journal of Fatigue*, 27(10–12), pp. 1499–1508. doi: 10.1016/j.ijfatigue.2005.06.031.

Quijano, C. (2018) *When Is It Just a Pretty Picture? Tips For a Better Structural Analysis*. Available at: https://www.simscale.com/blog/2016/07/tips-better-structural-analysis/ (Accessed: 3 October 2018).

Rama Rao, A. and Dutta, B. K. (2014) 'Blade vibration triggered by low load and high back pressure', *Engineering Failure Analysis*. Elsevier Ltd, 46, pp. 40–48. doi: 10.1016/j.engfailanal.2014.07.023.

Rao, J. S. (2013) 'Significance Of Damping and its Simulation in Fatigue Damage', *ASME 2013 International Mechanical Engineering Congress and Exposition*.

Rieger, N. F. and Salzman, R. N. (2005) 'Application of a Crack-Closure Model for Turbine Life Assessment', *Proceedings of the 34th Turbomachinery Symposium*, pp. 105–110.

Russhard, P. (2014) 'The Rise and Fall of the Rotor Blade Strain Gauge', in *Vibration Engineering and Technology of Machinery*. Springer.

Sabbatini, D. *et al.* (2012) 'Data acquisition and processing for tip timing and operational modal analysis of turbomachinery blades', *AIP Conference Proceedings*, 1457(June), pp. 52–60. doi: 10.1063/1.4730542.

Sanders, W. P. (1996) *Turbine Steam Path Engineering for Operations and Maintenance Staff*. First

Edit.

Scheepers, R. and Booysen, C. (2012) 'The Specification of Target Flaws in Turbine Blades', (April), pp. 16–20.

Schijve, J. (2003) 'Fatigue of structures and materials in the 20th century and the state of art', *International Journal of Fatigue*, 25, pp. 679–702.

Siewert, C. *et al.* (2017) 'Development of a Last Stage Blade Row Coupled By Damping Elements : Numerical Assessment of Its Vibrational Behavior and', *ASME Turbo Expo*, (GT2017), pp. 1–9. doi: 10.1115/GT2017-63630.

Sinan Korkmaz (2008) *Extension of the Uniform Material Law for High Strength Steels*. Bauhaus University. Available at: https://infoscience.epfl.ch/record/148269/files/Extension_of_the_Uniform_Material_Law_for_High _Strength_Steels_by_Sinan_Korkmaz.pdf (Accessed: 29 August 2017).

Singh, D. M. and Lucas, D. G. M. (2011) *Blade Design and Analysis for Steam Turbines*. McGraw Hill.

Singh, M. P. *et al.* (1988) 'SAFE Diagram-A design and reliability tool for turbine blading', *Proceedings of the 17th turbomachinery symposium*, pp. 93–101.

Srinivasan, A. V. (1997) 'Flutter and Resonant Vibration Characteristics of Engine Blades', *Journal of Engineering for Gas Turbines and Power*, p. 742. doi: 10.1115/1.2817053.

The Fundamentals of Modal Testing (1997). USA. Available at: http://www.modalshop.com/techlibrary/Fundamentals of Modal Testing.pdf.

Du Toit, R. G. (2017) 'A Stochastic Hybrid Blade Tip Timing Approach for the Identification and Classification of Turbomachine Blade Damage', p. 138.

Vyas, N. S. and Rao, J. S. (1994) 'Fatigue life estimation procedure for a turbine blade under transient loads', *Journal of Engineering for Gas Turbines & Power*, 116(1), pp. 198–206. doi: 10.1115/1.2906792.

Wang, Q., Khan, M. K. and Bathias, C. (2012) 'Current understanding of ultra-high cycle fatigue', *Theoretical and Applied Mechanics Letters*. Elsevier, 2(3), p. 031002. doi: 10.1063/2.1203102.

Wheel, M. A., Frame, J. C. and Riches, P. E. (2015) 'Is smaller always stiffer ? On size effects in supposedly generalised continua', *International Journal of Solids and Structures*. Elsevier Ltd, 67–68, pp. 84–92. doi: 10.1016/j.ijsolstr.2015.03.026.

Witos, M. (2003) 'Compressor Blade Fatigue Diagnostics and Modelling', 1, pp. 112–133.

Zakaria, K. A., Abdullah, S. and Ghazali, M. J. (2016) 'A Review of the loading sequence effects on the fatigue life behaviour of metallic materials', *Journal of Engineering Science and Technology Review*, 9(5), pp. 189–200. doi: 10.25103/jestr.095.30.

Zhang, D. and Xie, Y. H. (2008) 'Study on service life of last stage blade with damped structure in large power steam turbine', *Advanced Materials Research*, 44–46, pp. 803–808. doi: 10.4028/www.scientific.net/AMR.44-46.803.

Zhang, L. Y., He, L. and Stüer, H. (2011) 'A Numerical Investigation of the Rotating Instabilitiy in steam turbine last stage', *Proceedings of ASME Turbo Expo 2011*, pp. 1–10.

Appendix A

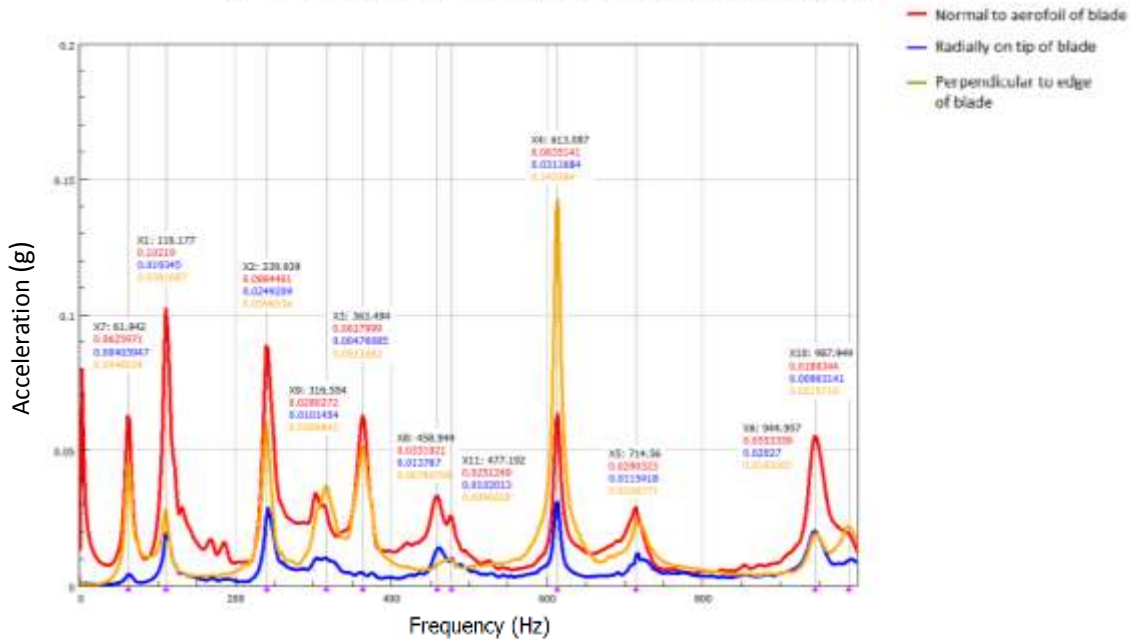# Experimental test results

FFT of blades at the 3 o'clock position

Figure A-1: FFT result of the blade at the 3 o'clock position
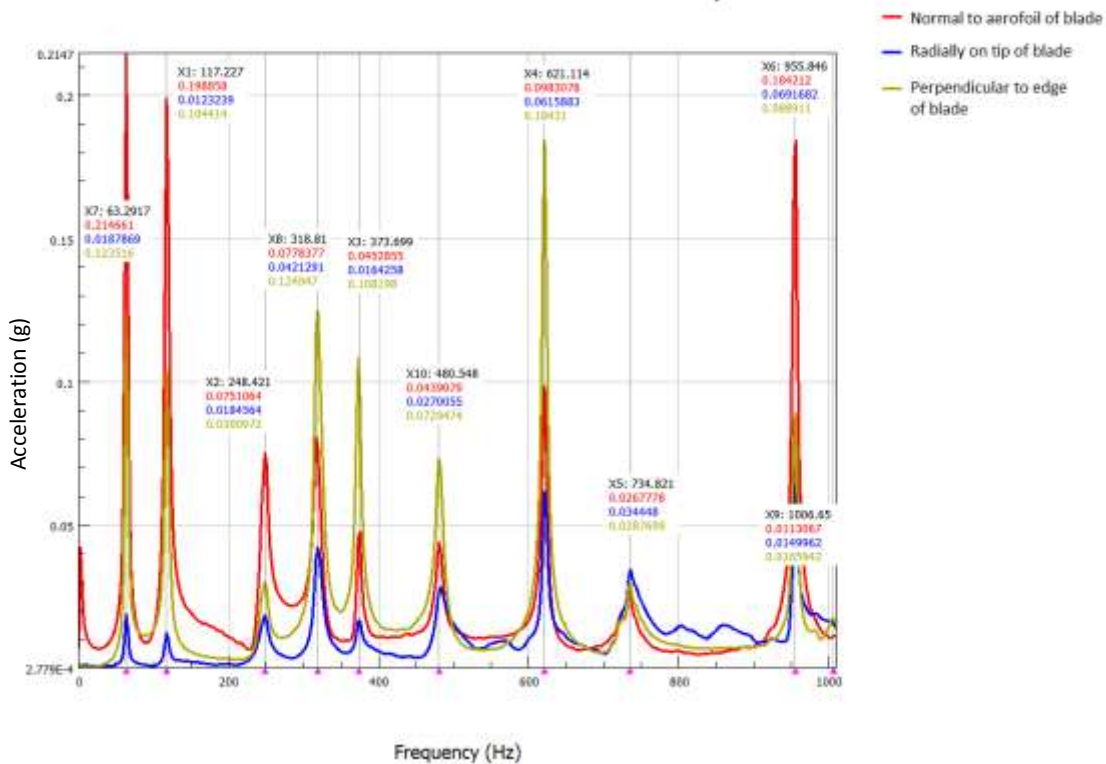
FFT of blade at the 6 o'clock position

Figure A-2: FFT result of the blade at the 6 o'clock position
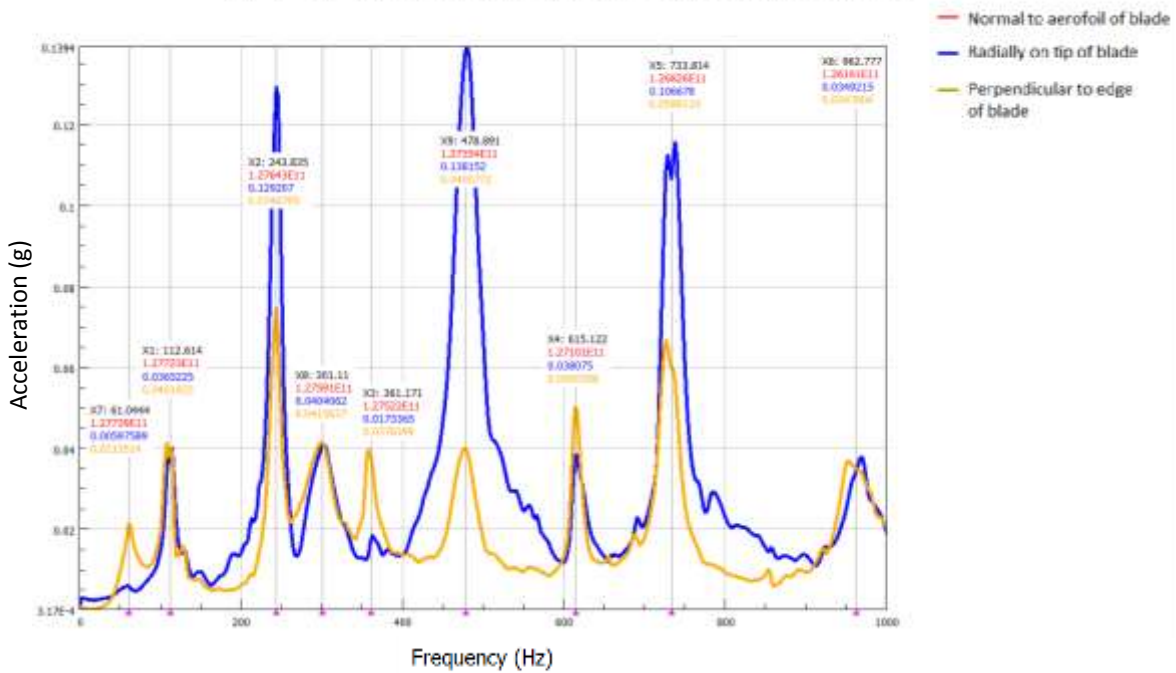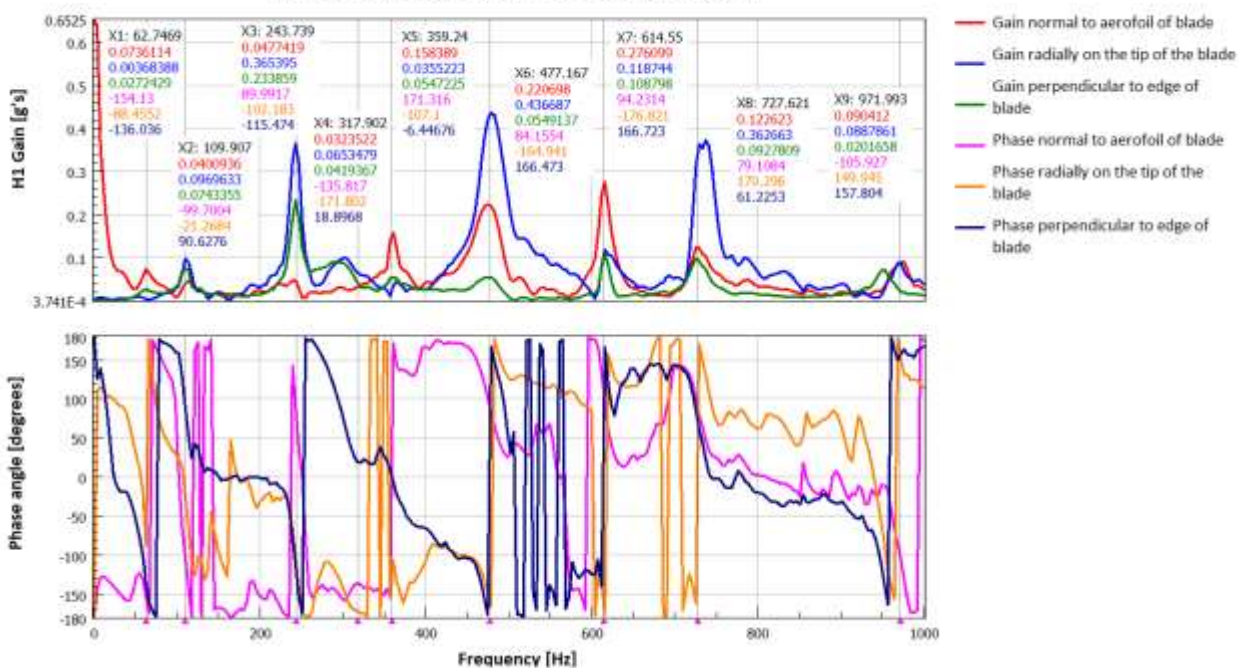
FFT of blades at the 9 o'clock position

Figure A-3: FFT result of the blade at the 9 o'clock position
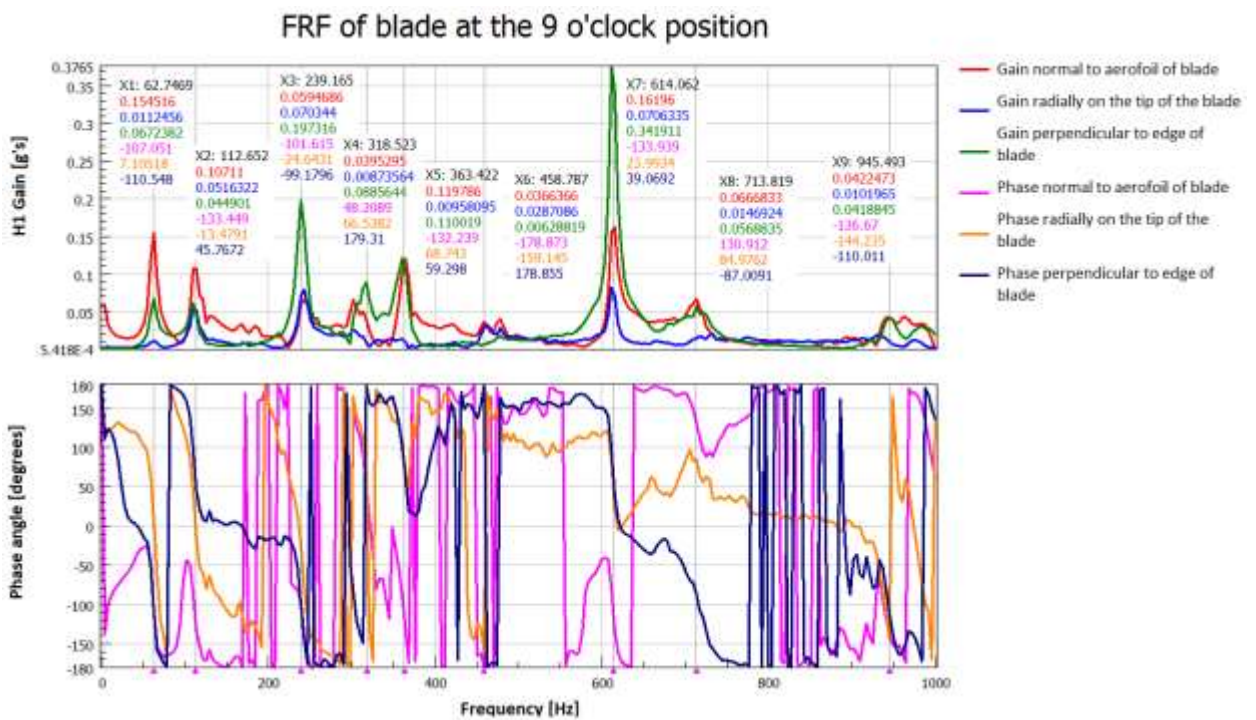
FRF of blade at the 3 o'clock position

Figure A-4: FRF results of the blade at the 3 o'clock position, with impacts perpendicular to aerofoil of blade

FRF of blade at the 3 o'clock position
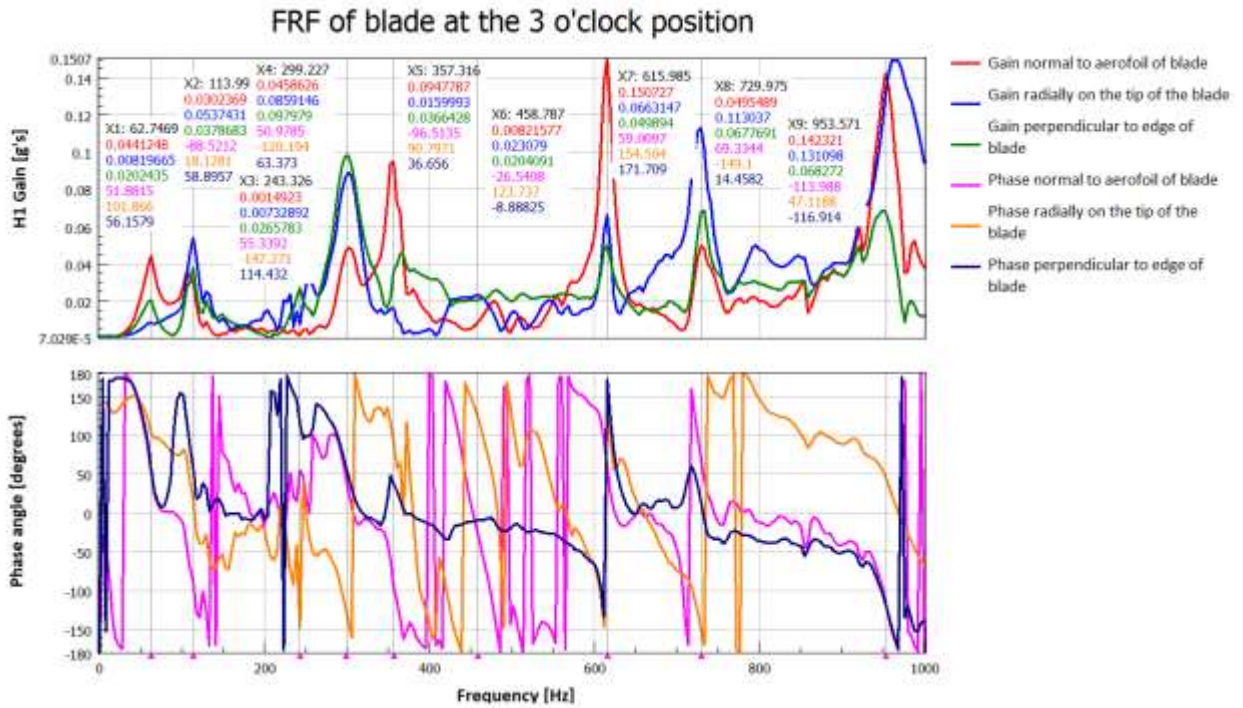
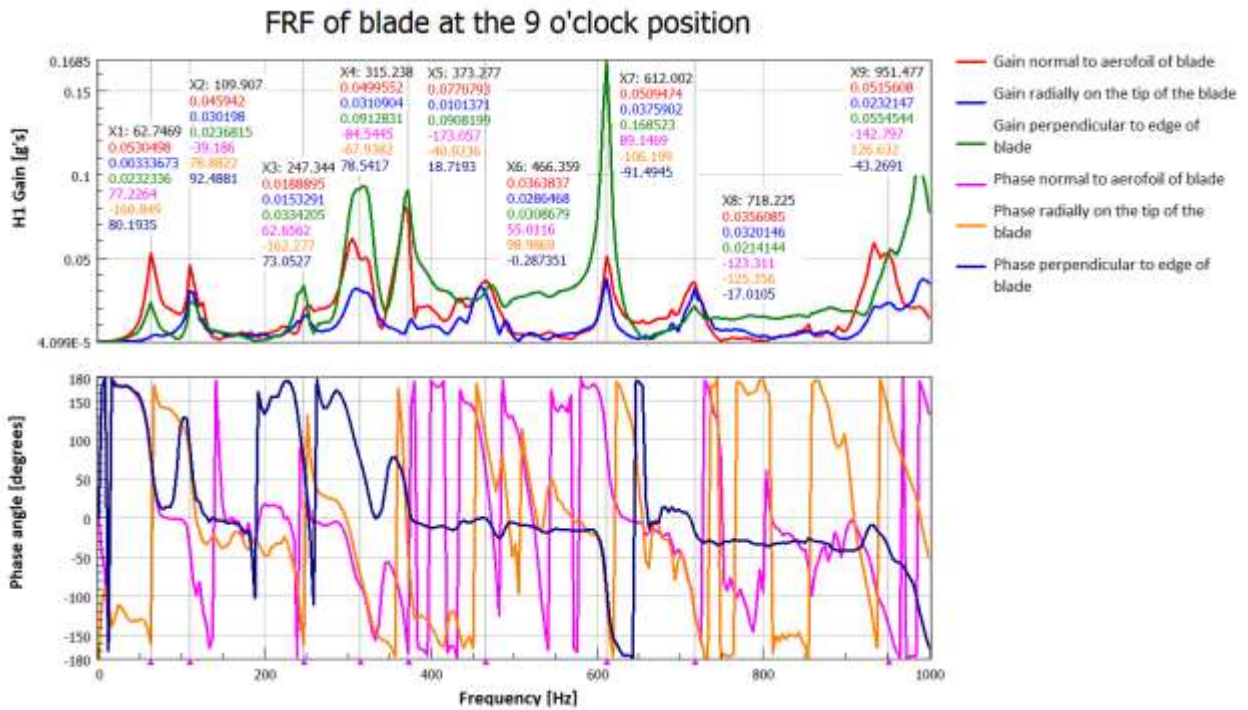**Figure A-5:** FRF results of the blade at the 3 o'clock position, with impacts perpendicular to edge of blade

FRF of blade at the 3 o'clock position
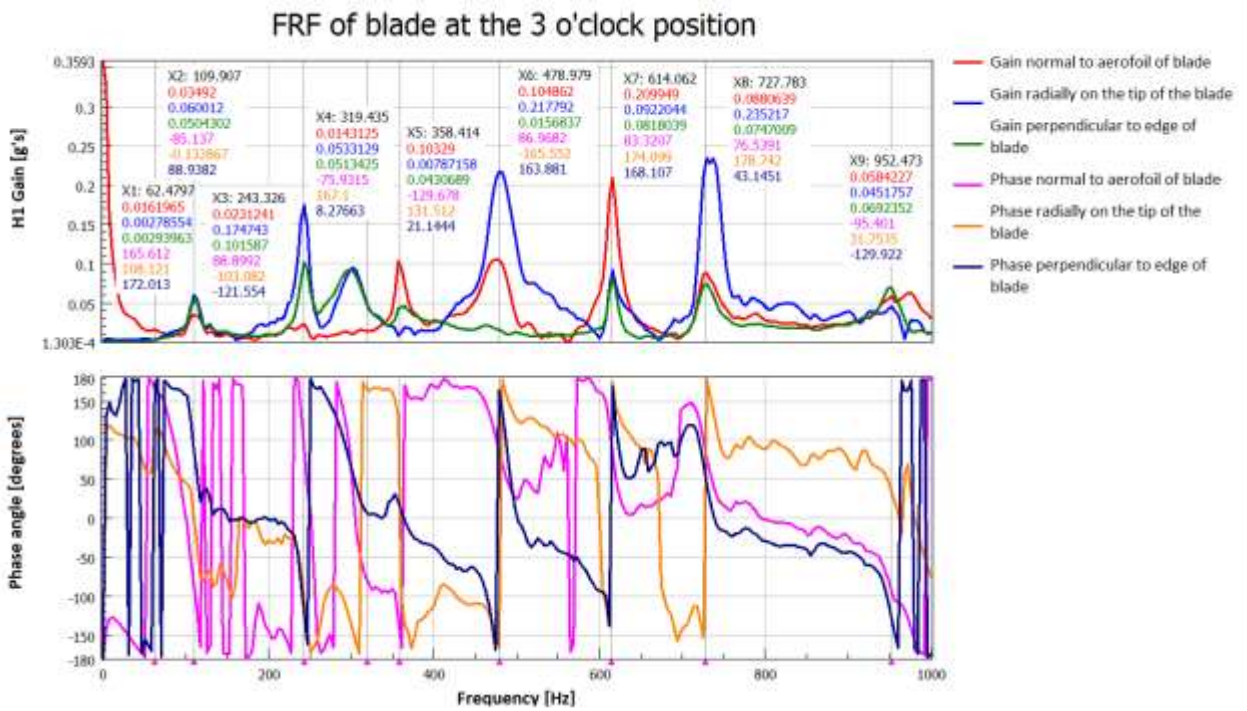
Figure A-6: FRF results of the blade at the 3 o'clock position, with all impact positions average

FRF of blade at the 6 o'clock position
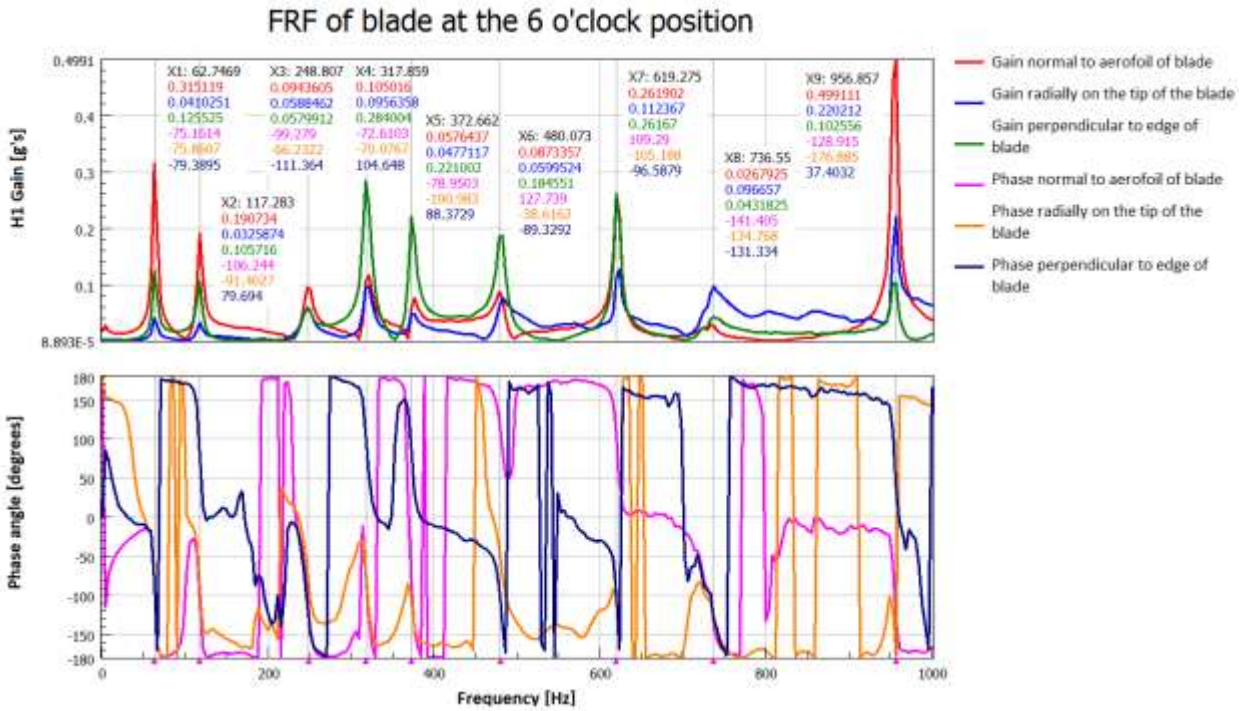
Figure A-7: FRF results of the blade at the 6 o'clock position, with impacts perpendicular to aerofoil of blade

FRF of blade at the 6 o'clock position
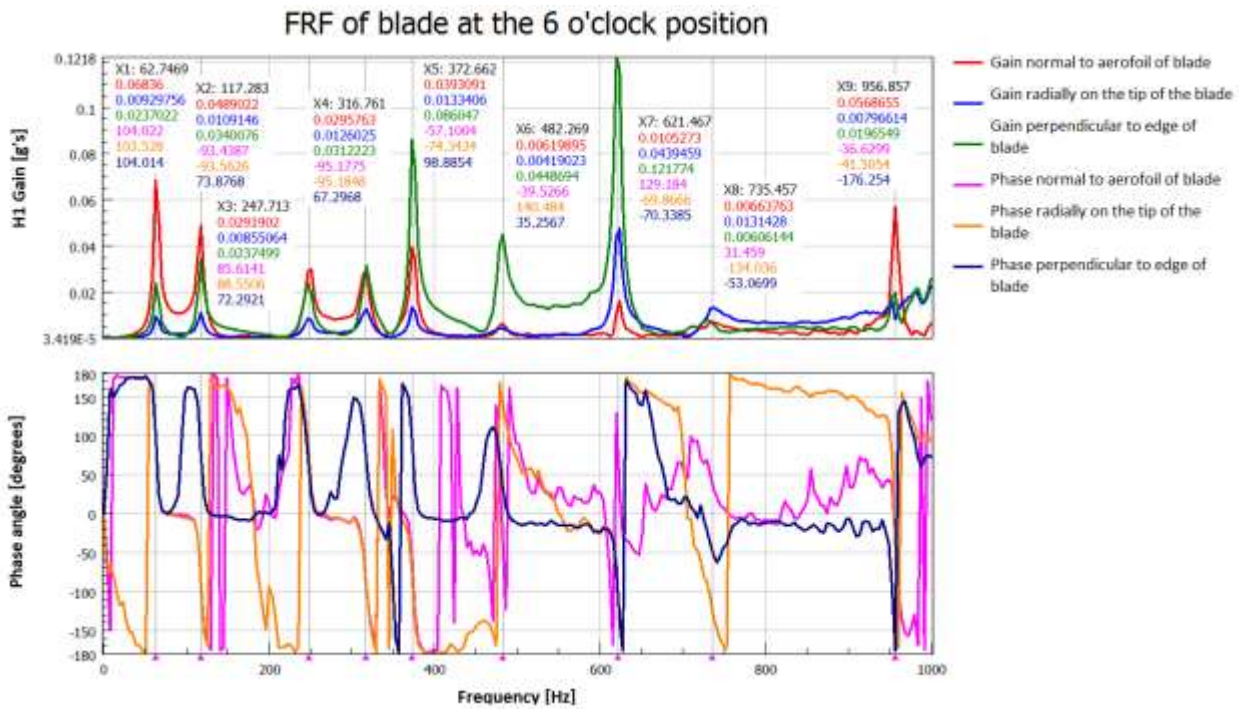
Figure A-8: FRF results of the blade at the 6 o'clock position, with impacts perpendicular to edge of blade
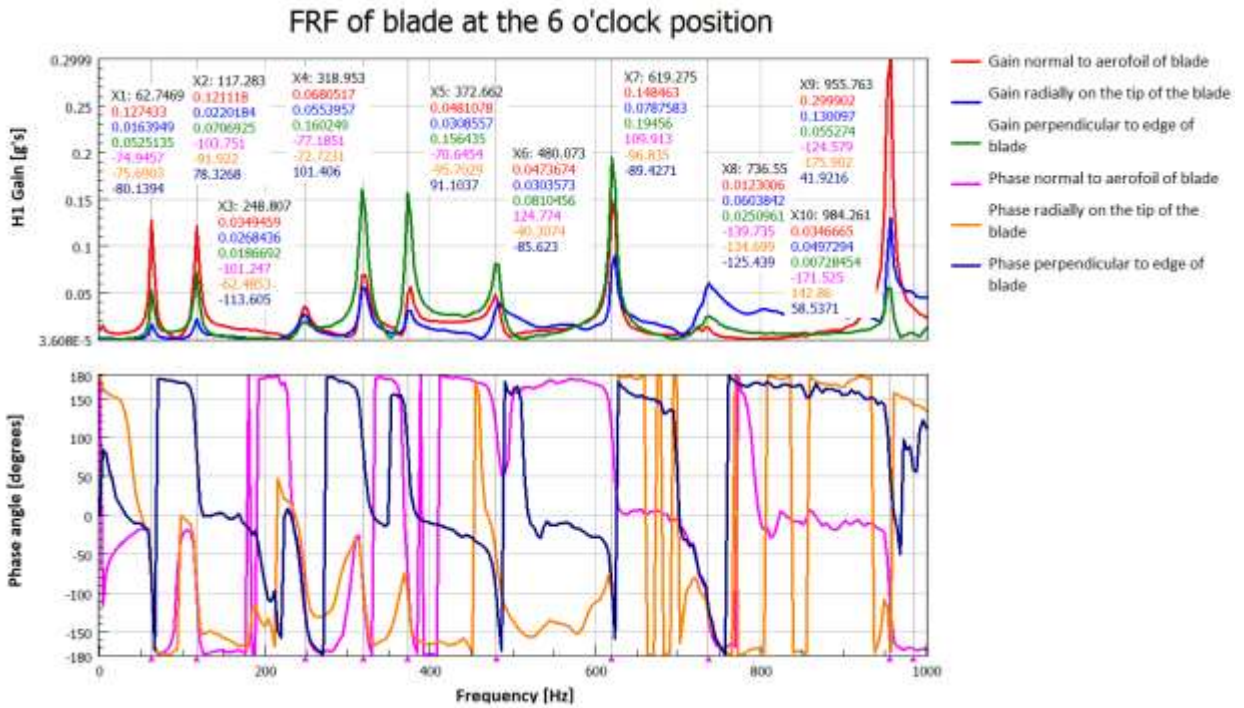
Figure A-9: FRF results of the blade at the 6 o'clock position, with all impact positions average

Figure A-10: FRF results of the blade at the 9 o'clock position, with impacts perpendicular to aerofoil of blade

Figure A-11: FRF results of the blade at the 9 o'clock position, with impacts perpendicular to edge of blade
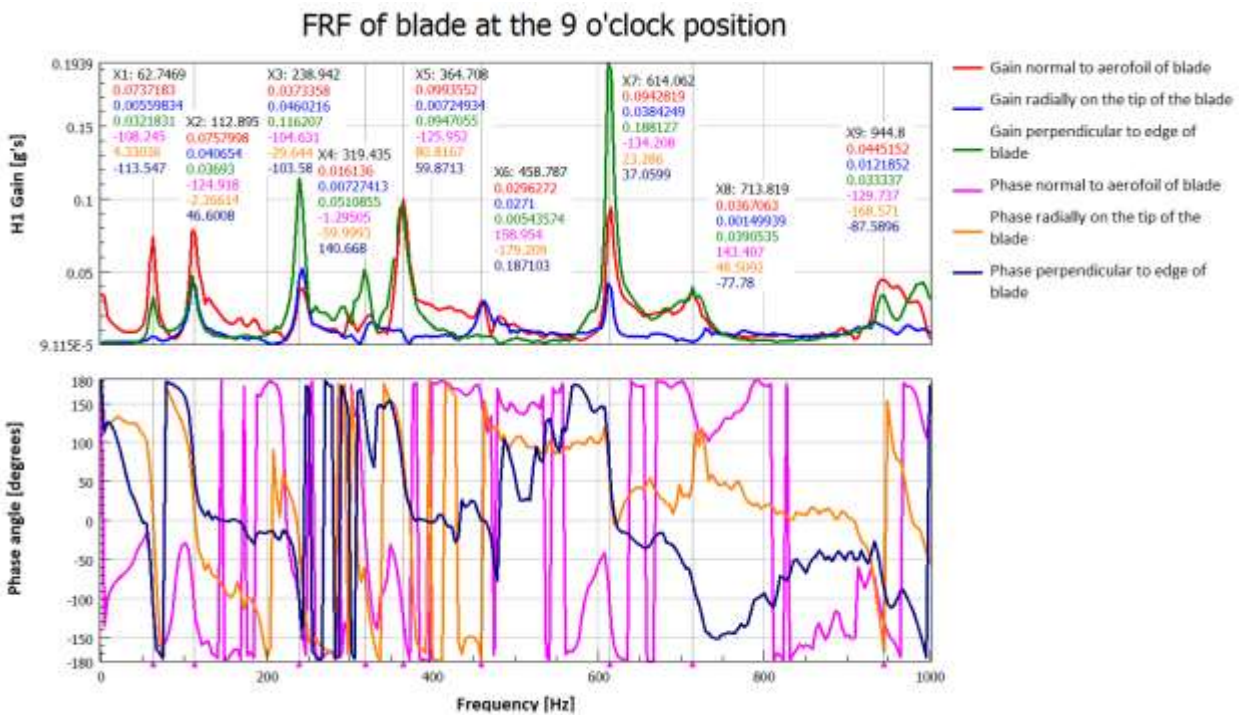
Figure A-12: FRF results of the blade at the 9 o'clock position, with all impact positions average

Appendix B

Rayleigh damping ratio

A pre-stressed modal analysis was done without any damping to obtain the natural frequencies as well as the mass participation of the frequencies as shown in Table B-1.

Table B-1: Mass participation for pre-stress modal analysis

Mode	Frequency [Hz]	x direction Participation Factor	x direction Ratio of effective mass to total mass	y direction Participation Factor	y direction Ratio of effective mass to total mass	z direction Participation Factor	z direction Ratio of effective mass to total mass	Sum Ratio of effective mass to total mass
1	101.3	0.88315E-01	0.05172	0.37101E-03	0.00000	0.31118E-01	0.00642	0.05814
2	164.4	-0.53716E-01	0.01913	0.67275E-03	0.00000	0.60272E-01	0.02409	0.04322
3	311.2	0.36983E-02	0.00009	-0.22645E-02	0.00003	-0.71856E-01	0.03424	0.03436
4	397.8	0.45219E-01	0.01356	-0.50919E-02	0.00017	0.33997E-01	0.00766	0.02139
5	434.4	0.38412E-01	0.00978	0.36695E-02	0.00009	0.17285E-01	0.00198	0.01185
6	553.9	-0.34718E-01	0.00799	0.15784E-02	0.00002	0.12609E-01	0.00105	0.00906
7	676.9	-0.33939E-01	0.00764	-0.39191E-02	0.00010	0.17154E-01	0.00195	0.00969
8	781.3	0.21720E-01	0.00313	0.48599E-02	0.00016	-0.35463E-01	0.00834	0.01162
9	1022.2	-0.10594E-01	0.00074	-0.81855E-02	0.00044	-0.47968E-01	0.01526	0.01645
10	1027.5	0.25458E-01	0.00430	-0.25588E-02	0.00004	0.14926E-01	0.00148	0.00582
11	1164.9	0.42626E-01	0.01205	0.27986E-01	0.00519	0.37067E-02	0.00009	0.01733
12	1325.5	-0.77405E-02	0.00040	0.16082	0.17149	0.90661E-02	0.00055	0.17243
13	1365.9	-0.13972E-01	0.00129	-0.15603	0.16144	-0.19532E-01	0.00253	0.16526
14	1454.6	-0.45667E-01	0.01383	0.54822E-02	0.00020	0.21246E-01	0.00299	0.01702
15	1648.2	0.79497E-02	0.00042	-0.17830E-01	0.00211	-0.11792E-01	0.00092	0.00345
16	1767.7	0.10415E-01	0.00072	0.49979E-02	0.00017	0.36648E-02	0.00009	0.00097
17	1832.0	-0.61018E-01	0.02469	-0.37571E-02	0.00009	0.15512E-01	0.00160	0.02638
18	1933.2	-0.53988E-01	0.01933	0.21445E-01	0.00305	-0.44742E-01	0.01327	0.03565
19	1984.3	0.46665E-01	0.01444	-0.13577E-01	0.00122	-0.58041E-02	0.00022	0.01588
20	2128.4	-0.70899E-01	0.03333	-0.22358E-01	0.00331	0.24999E-02	0.00004	0.03669
	sum		23.9%		34.9%		12.5%	71.3%

The damping ration for the first mode was selected as 0.006 and the significant mode was selected to be 0.0042. The selection for the damping considered the results for the tap testing and modal parameter estimation with a marginal increase due to damping pins engaging the blade at operating conditions. The analysis showed that the first four frequencies play a role due to mass participation and the fourth mode was therefore selected as the significant mode in the calculations. The calculation for the various damping ratios is shown in Table B-2.

Mode	Natural Frequency ω_n	Damping Ratio based on Linear Interpolation	Damping up to 5th Mode approximation	Damping up to 12th Mode approximation	Damping full range approximation	Damping with average values	Damping with average values
1	101.26	0.006	0.006	0.006	0.021036354	0.011012118	0.006390455
2	164.43	0.005616596	0.004335816	0.003548646	0.012637996	0.006840819	0.004182683
3	311.18	0.004725913	0.003699337	0.001553652	0.005982088	0.003745026	0.002753551
4	397.83	0.0042	0.003863187	0.000993915	0.0042	0.003019034	0.002527934
5	434.42	0.003977921	0.003977921	0.000809729	0.003628748	0.002805466	0.002484837
6	553.92	0.003252628	0.00445847	0.000329433	0.00218433	0.002324078	0.002465329
7	676.87	0.002506396	0.005052303	-5.08459E-05	0.001093884	0.002031781	0.002559141
8	781.27	0.001872752	0.005600556	-0.00032333	0.00034314	0.001873456	0.00268922
9	1022.2	0.000410453	0.006949396	-0.000856381	-0.001056637	0.001678792	0.003085186
10	1027.5	0.000378285	0.006979932	-0.000867118	-0.001083991	0.001676274	0.003094886
11	1164.9	-0.00045565	0.007780261	-0.001135484	-0.001758488	0.001628763	0.003356329
12	1325.5	-0.001430394	0.008732112	-0.001430394	-0.002481658	0.001606687	0.003680687
13	1365.9	-0.001675598	0.008973648	-0.001502185	-0.002655251	0.001605404	0.003764677
14	1454.6	-0.002213953	0.009506312	-0.001657099	-0.003026984	0.00160741	0.003951788
15	1648.2	-0.003388987	0.010677991	-0.001984835	-0.00380226	0.001630299	0.004370566
16	1767.7	-0.00411428	0.011406008	-0.002181637	-0.004261713	0.001654219	0.004634552
17	1832	-0.004504542	0.011798938	-0.002286153	-0.004504147	0.001669546	0.004777974
18	1933.2	-0.005118765	0.012418814	-0.002448984	-0.004879923	0.001696636	0.005005367
19	1984.3	-0.005428911	0.012732416	-0.002530515	-0.005067273	0.001711542	0.005120876
20	2128.4	-0.00630351	0.013618633	-0.002758286	-0.005588146	0.001757401	0.00544875

If the results from Table B-2 are plotted, with damping ratio on the y-axis and the natural frequency on the x-axis, the results are shown in Figure B-1. From these results, the average damping ratio is seen to be in the centre of the data points and are therefore used with α and β values as shown in Table B-3 for the respective scenarios.

Table B-3: Alpha and Beta values for different scenarios

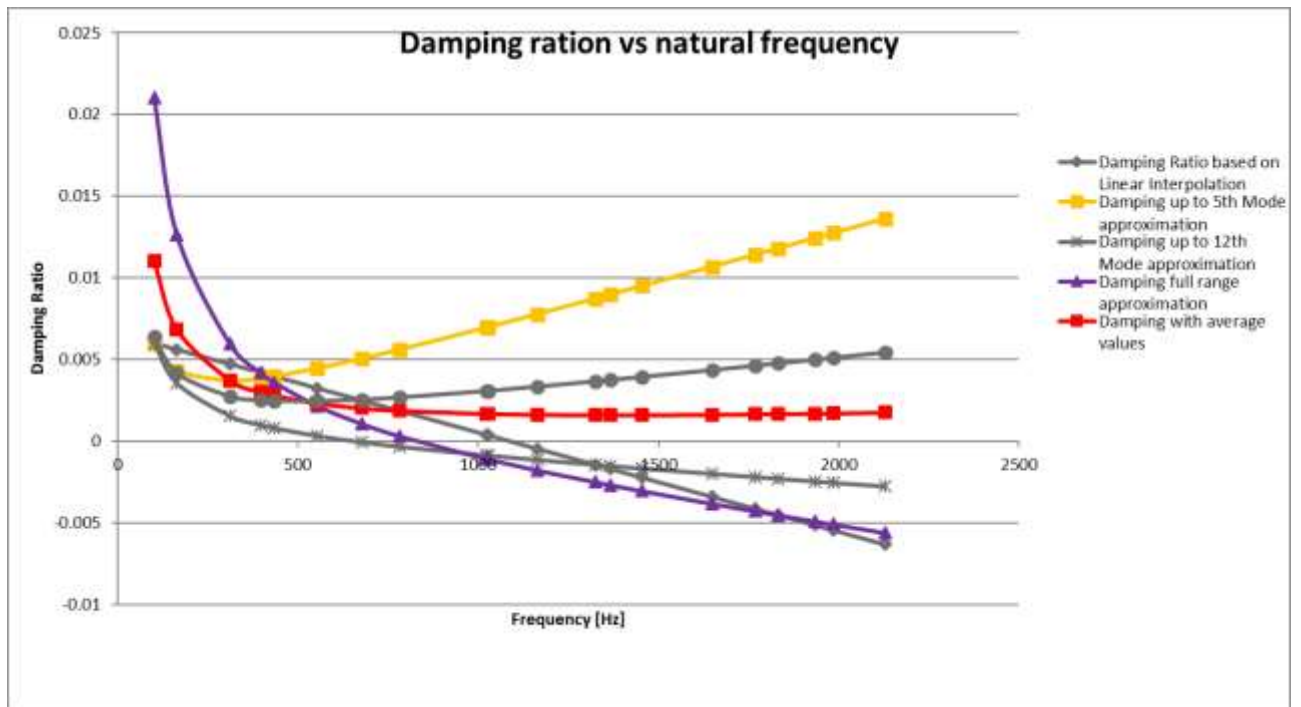|	
β_{1-5}	0.00001256
α_{1-5}	1.086363126
β_{1-12}	-0.00000287
α_{1-12}	1.24451302
β_{1-20}	-0.00000621
α_{1-20}	4.32391122
β_{ave}	0.00000116
α_{ave}	2.21826245

Figure B-1: Damping vs natural frequency

Appendix C
Apparent displacement
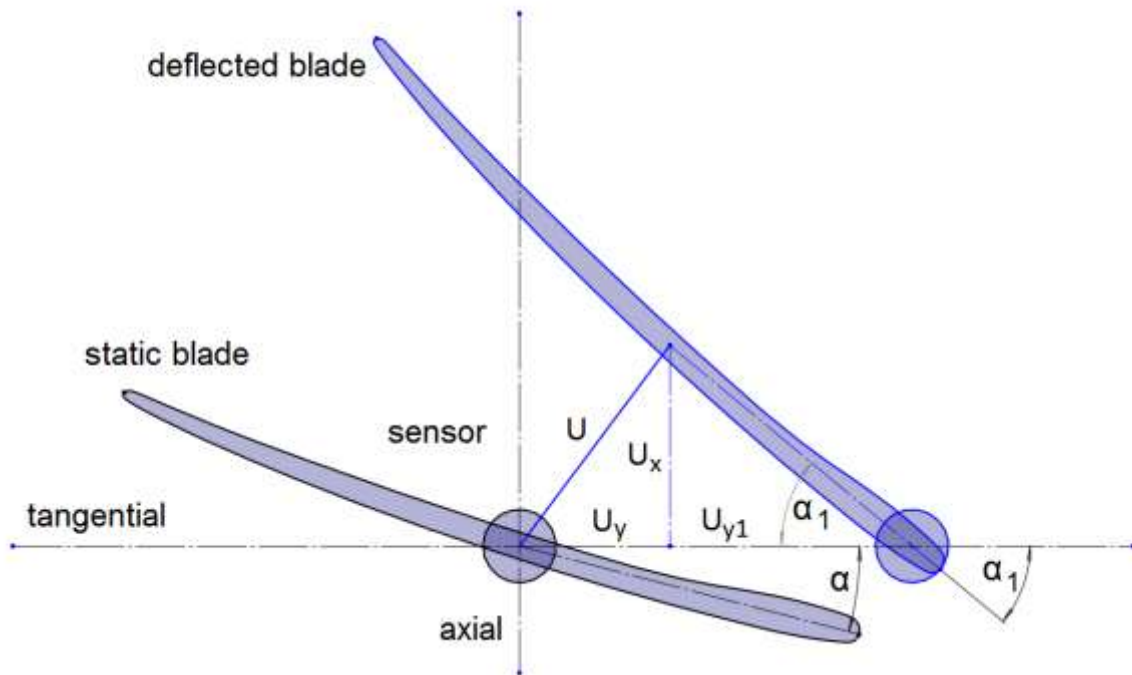
Figure C-1: Apparent vibration

$$Apparent\ vibration = U_y + U_{y1}$$
$$= U_y + \frac{U_x}{tan\alpha_1} \qquad (C.1)$$

The apparent vibration was calculated by using the sensor node, which were near the centre of the blade, and the trailing node, which were at the trailing side of the tip of the blade. The stationary position was captured and then the position of the node under model vibration conditions. The data was then used to calculate the apparent displacement as shown in Table C-1. U is usually seen as the resultant modal vibration amplitude.

Table C-1: Apparent displacement calculations for all modes

					Sensor Node (233274)				Trailing node (233256)				Apparent vibration calculations				
	Stationary Conditions				5.8154	1789.1666	-877.2251		-56.5619	1788.2817	-853.9891						
Name	Mode	Index	Freq [Hz]	Phase [deg]	Displacement Tangential (x) [mm]	Displacement longitudinal (y) [mm]	Displacement Axial (z) [mm]	Displacement Resultant [mm]	Displacement Tangential (x) [mm]	Displacement longitudinal (y) [mm]	Displacement Axial (z) [mm]	Displacement Resultant [mm]	Angle of blade irt tangential [rad]	Angle of blade [deg]	Ux/tanα	Apparent displacement [mm]	Apparent to axial displacement
M1H0	1	0	101.10	0	2.13337656	0.02449511	1.04250284	2.37459633	2.16061339	0.18306404	1.12124065	2.44109469	0.3578	20.5024	2.7879	4.9213	4.7207
M2H0	2	0	164.25	0	0.14114711	0.04669372	3.15281792	3.15632122	0.16854415	0.02116045	3.2226244	3.22709822	0.3577	20.4953	8.4347	8.5759	2.7201
M3H0	3	0	310.17	0	1.68181819	0.0414438	2.6073733	3.10300267	1.41640143	0.15558145	1.887101	2.36464559	0.3451	19.7700	7.2542	8.9360	3.4272
M4H0	4	0	390.06	0	-1.09862029	-0.10382718	0.35884354	1.16039446	-2.19298653	-0.39337655	-2.57559266	3.40552677	0.3096	17.7370	1.1219	0.0233	0.0649
M5H0	5	0	432.13	0	0.04405989	0.08707031	3.3081454	3.30958434	0.67885732	-0.09715911	4.96549661	5.01262842	0.3832	21.9583	8.2051	8.2492	2.4936
M6H0	6	0	546.69	0	1.0397909	-0.00510151	1.33753446	1.69416339	-0.90439789	0.00693888	-3.85718512	3.96180019	0.2735	15.6681	4.7686	5.8084	4.3426
M1H1	1	1	101.54	2	3.01587934	0.03460429	1.47088654	3.35562705	3.05368021	0.25865688	1.58028523	3.44806722	0.3583	20.5304	3.9277	6.9436	4.7207
M2H1	2	1	101.54	272	3.01587934	0.03460429	1.47088654	3.35562705	3.05368021	0.25865688	1.58028523	3.44806722	0.3583	20.5304	3.9277	6.9436	4.7207
M3H1	3	1	164.32	181	-0.20239757	-0.06620471	-4.46052023	4.46560058	-0.24084817	-0.03026652	-4.55844729	4.56490587	0.3550	20.3402	-12.0324	-12.2348	2.7429
M4H1	4	1	164.32	91	-0.20239757	-0.06620471	-4.46052023	4.46560058	-0.24084817	-0.03026652	-4.55844729	4.56490587	0.3550	20.3402	-12.0324	-12.2348	2.7429
M5H1	5	1	310.24	89	-2.37751771	-0.05779246	-3.68763822	4.38800707	-2.0005814	-0.21887656	-2.66476714	3.33934376	0.3730	21.3689	-9.4248	-11.8023	3.2005
M6H1	6	1	310.24	179	-2.37751771	-0.05779246	-3.68763822	4.38800707	-2.0005814	-0.21887656	-2.66476714	3.33934376	0.3730	21.3689	-9.4248	-11.8023	3.2005
M1H2	1	2	102.85	266	3.01259886	0.03430225	1.45949313	3.34769305	3.04889726	0.25777737	1.56477961	3.43667847	0.3583	20.5266	3.8981	6.9107	4.7350
M2H2	2	2	102.85	356	3.01259886	0.03430225	1.45949313	3.34769305	3.04889726	0.25777737	1.56477961	3.43667847	0.3583	20.5266	3.8981	6.9107	4.7350
M3H2	3	2	164.51	184	-0.21225375	-0.06653218	-4.46420881	4.46974702	-0.24950504	-0.03130366	-4.55891872	4.56584851	0.3551	20.3432	-12.0404	-12.2527	2.7446
M4H2	4	2	164.51	94	-0.21225375	-0.06653218	-4.46420881	4.46974702	-0.24950504	-0.03130366	-4.55891872	4.56584851	0.3551	20.3432	-12.0404	-12.2527	2.7446
M5H2	5	2	310.42	91	-2.37405632	-0.05666381	-3.68884723	4.38713439	-1.99247881	-0.21664245	-2.65348458	3.32534001	0.3732	21.3804	-9.4223	-11.7964	3.1978
M6H2	6	2	310.42	181	-2.37405632	-0.05666381	-3.68884723	4.38713439	-1.99247881	-0.21664245	-2.65348458	3.32534001	0.3732	21.3804	-9.4223	-11.7964	3.1978
M1H3	1	3	104.96	269	3.00634419	0.03379649	1.43982719	3.33351915	3.0396647	0.25621331	1.53698722	3.41577758	0.3581	20.5191	3.8471	6.8534	4.7599
M2H3	2	3	104.96	359	3.00634419	0.03379649	1.43982719	3.33351915	3.0396647	0.25621331	1.53698722	3.41577758	0.3581	20.5191	3.8471	6.8534	4.7599
M3H3	3	3	164.84	186	-0.22891035	-0.06669953	-4.47102348	4.47737643	-0.26438128	-0.03267425	-4.56095659	4.5687296	0.3551	20.3476	-12.0560	-12.2849	2.7477
M4H3	4	3	164.84	96	-0.22891035	-0.06669953	-4.47102348	4.47737643	-0.26438128	-0.03267425	-4.56095659	4.5687296	0.3551	20.3476	-12.0560	-12.2849	2.7477
M5H3	5	3	310.68	92	-2.3693993	-0.05581489	-3.69037459	4.38589021	-1.98076906	-0.2142224	-2.6360369	3.30424391	0.3735	21.3978	-9.4178	-11.7872	3.1940
M6H3	6	3	310.68	182	-2.3693993	-0.05581489	-3.69037459	4.38589021	-1.98076906	-0.2142224	-2.6360369	3.30424391	0.3735	21.3978	-9.4178	-11.7872	3.1940
M1H4	1	4	107.83	270	2.99706161	0.03304804	1.41115614	3.31282842	3.02593792	0.25394576	1.49620323	3.38517546	0.3579	20.5080	3.7727	6.7698	4.7973
M2H4	2	4	107.83	0	2.99706161	0.03304804	1.41115614	3.31282842	3.02593792	0.25394576	1.49620323	3.38517546	0.3579	20.5080	3.7727	6.7698	4.7973
M3H4	3	4	165.30	185	-0.25238904	-0.06695514	-4.48458435	4.49217988	-0.28647688	-0.03459246	-4.57079643	4.57989581	0.3552	20.3510	-12.0903	-12.3427	2.7523
M4H4	4	4	165.30	95	-0.25238904	-0.06695514	-4.48458435	4.49217988	-0.28647688	-0.03459246	-4.57079643	4.57989581	0.3552	20.3510	-12.0903	-12.3427	2.7523
M5H4	5	4	310.99	94	-2.36190669	-0.05503038	-3.68983356	4.38138143	-1.96382534	-0.21126794	-2.61008155	3.27318955	0.3739	21.4211	-9.4051	-11.7670	3.1890
M6H4	6	4	310.99	184	-2.36190669	-0.05503038	-3.68983356	4.38138143	-1.96382534	-0.21126794	-2.61008156	3.27318955	0.3739	21.4211	-9.4051	-11.7670	3.1890

Name	Mode	Index	Freq [Hz]	Phase [deg]	Displacement Tangential (x) [mm]	Displacement longitudinal (y) [mm]	Displacement Axial (z) [mm]	Displacement Resultant [mm]	Displacement Tangential (x) [mm]	Displacement longitudinal (y) [mm]	Displacement Axial (z) [mm]	Displacement Resultant [mm]	Angle of blade irt tangential [rad]	Angle of blade [deg]	Ux/tanα	Apparent displacement [mm]	Apparent to axial displacement
M1H5	1	5	111.37	270	2.98594214	0.03212375	1.37212544	3.2862761	3.0107654	0.25125983	1.44606768	3.34947034	0.3578	20.4979	3.6703	6.6563	4.8511
M2H5	2	5	111.37	0	2.98594214	0.03212375	1.37212544	3.2862761	3.0107654	0.25125983	1.44606768	3.34947034	0.3578	20.4979	3.6703	6.6563	4.8511
M3H5	3	5	165.88	198	-0.28283977	-0.06708234	-4.49807086	4.50745381	-0.31376274	-0.03680869	-4.57578281	4.5866753	0.3553	20.3588	-12.1216	-12.4045	2.7577
M4H5	4	5	165.88	108	-0.28283977	-0.06708234	-4.49807086	4.50745381	-0.31376274	-0.03680869	-4.57578281	4.5866753	0.3553	20.3588	-12.1216	-12.4045	2.7577
M5H5	5	5	311.31	95	-2.35531673	-0.05424132	-3.69030275	4.37821806	-1.94649676	-0.20826007	-2.58168144	3.23995385	0.3743	21.4477	-9.3935	-11.7489	3.1837
M6H5	6	5	311.31	185	-2.35531673	-0.05424132	-3.69030275	4.37821806	-1.94649676	-0.20826007	-2.58168144	3.23995385	0.3743	21.4477	-9.3935	-11.7489	3.1837
M1H6	1	6	115.47	270	2.97073164	0.03084607	1.31935523	3.25067627	2.98930971	0.24770905	1.37626719	3.30021873	0.3575	20.4822	3.5321	6.5028	4.9288
M2H6	2	6	115.47	0	2.97073164	0.03084607	1.31935523	3.25067627	2.98930971	0.24770905	1.37626719	3.30021873	0.3575	20.4822	3.5321	6.5028	4.9288
M3H6	3	6	166.60	197	-0.32202057	-0.06738707	-4.51849281	4.53045423	-0.35005328	-0.03976098	-4.58843155	4.6019368	0.3555	20.3659	-12.1720	-12.4940	2.7651
M4H6	4	6	166.60	107	-0.32202057	-0.06738707	-4.51849281	4.53045423	-0.35005328	-0.03976098	-4.58843155	4.6019368	0.3555	20.3659	-12.1720	-12.4940	2.7651
M5H6	5	6	311.62	96	-2.34631887	-0.05333515	-3.68893448	4.37221848	-1.92513764	-0.20467685	-2.54709176	3.1993318	0.3749	21.4782	-9.3754	-11.7217	3.1775
M6H6	6	6	311.62	186	-2.34631887	-0.05333515	-3.68893448	4.37221848	-1.92513764	-0.20467685	-2.54709176	3.1993318	0.3749	21.4782	-9.3754	-11.7217	3.1775
M1H7	1	7	120.02	274	2.94891362	0.0290073	1.24809044	3.20229023	2.95667355	0.2428287	1.27566019	3.22927131	0.3570	20.4553	3.3461	6.2950	5.0437
M2H7	2	7	120.02	4	2.94891362	0.0290073	1.24809044	3.20229023	2.95667355	0.2428287	1.27566019	3.22927131	0.3570	20.4553	3.3461	6.2950	5.0437
M3H7	3	7	167.44	191	-0.37076472	-0.06751974	-4.53722908	4.55285329	-0.39291686	-0.04308666	-4.59137816	4.60836126	0.3557	20.3804	-12.2130	-12.5838	2.7734
M4H7	4	7	167.44	101	-0.37076472	-0.06751974	-4.53722908	4.55285329	-0.39291686	-0.04308666	-4.59137816	4.60836126	0.3557	20.3804	-12.2130	-12.5838	2.7734
M5H7	5	7	311.92	98	-2.33464147	-0.05229187	-3.68544402	4.36300159	-1.89976639	-0.20050084	-2.50680795	3.15172953	0.3755	21.5119	-9.3503	-11.6850	3.1706
M6H7	6	7	311.92	188	-2.33464147	-0.05229187	-3.68544402	4.36300159	-1.89976639	-0.20050084	-2.50680795	3.15172953	0.3755	21.5119	-9.3503	-11.6850	3.1706
M1H8	1	8	124.93	272	2.92380777	0.02685449	1.15464932	3.14365839	2.92178796	0.23748482	1.15564916	3.15099491	0.3566	20.4310	3.0996	6.0234	5.2167
M2H8	2	8	124.93	2	2.92380777	0.02685449	1.15464932	3.14365839	2.92178796	0.23748482	1.15564916	3.15099491	0.3566	20.4310	3.0996	6.0234	5.2167
M3H8	3	8	168.43	191	-0.43214114	-0.06773862	-4.56100344	4.58193048	-0.44740273	-0.04726213	-4.59664917	4.61861304	0.3560	20.3974	-12.2659	-12.6980	2.7840
M4H8	4	8	168.43	101	-0.43214114	-0.06773862	-4.56100344	4.58193048	-0.44740273	-0.04726213	-4.59664916	4.61861304	0.3560	20.3974	-12.2659	-12.6980	2.7840
M5H8	5	8	312.18	98	-2.32407513	-0.05120338	-3.68350807	4.35570645	-1.87477901	-0.19630706	-2.46612986	3.10405046	0.3761	21.5475	-9.3284	-11.6525	3.1634
M6H8	6	8	312.18	188	-2.32407513	-0.05120338	-3.68350807	4.35570645	-1.87477901	-0.19630706	-2.46612986	3.10405046	0.3761	21.5475	-9.3284	-11.6525	3.1634
M1H9	1	9	130.08	272	2.88926485	0.02397099	1.0295792	3.06732119	2.87357084	0.23065173	0.99354488	3.04921974	0.3560	20.3970	2.7689	5.6582	5.4956
M2H9	2	9	130.08	2	2.88926485	0.02397099	1.0295792	3.06732119	2.87357084	0.23065173	0.99354488	3.04921974	0.3560	20.3970	2.7689	5.6582	5.4956
M3H9	3	9	169.57	198	-0.51152084	-0.06841339	-4.59994014	4.62879933	-0.52214406	-0.05305605	-4.62310564	4.65280078	0.3562	20.4089	-12.3630	-12.8745	2.7988
M4H9	4	9	169.57	108	-0.51152084	-0.06841339	-4.59994014	4.62879933	-0.52214406	-0.05305605	-4.62310564	4.65280078	0.3562	20.4089	-12.3630	-12.8745	2.7988
M5H9	5	9	312.41	101	-2.31015184	-0.04997425	-3.67884554	4.34433003	-1.84531455	-0.19146986	-2.41972544	3.04908473	0.3767	21.5858	-9.2984	-11.6086	3.1555
M6H9	6	9	312.41	191	-2.31015184	-0.04997425	-3.67884554	4.34433003	-1.84531455	-0.19146986	-2.41972544	3.04908473	0.3767	21.5858	-9.2984	-11.6086	3.1555
M1H10	1	10	135.36	273	2.84703754	0.02047893	0.86495467	2.97559888	2.81808319	0.22294158	0.79301454	2.93601224	0.3554	20.3640	2.3303	5.1773	5.9856
M2H10	2	10	135.36	3	2.84703754	0.02047893	0.86495467	2.97559888	2.81808319	0.22294158	0.79301454	2.93601224	0.3554	20.3640	2.3303	5.1773	5.9856
M3H10	3	10	170.89	197	-0.60954589	-0.06869674	-4.63225909	4.6726962	-0.60969521	-0.0594821	-4.62730559	4.66767858	0.3567	20.4347	-12.4327	-13.0423	2.8155
M4H10	4	10	170.89	107	-0.60954589	-0.06869674	-4.63225909	4.6726962	-0.60969521	-0.0594821	-4.62730559	4.66767858	0.3567	20.4347	-12.4327	-13.0423	2.8155
M5H10	5	10	312.59	274	2.33158317	0.04952782	3.69727722	4.37133754	1.85859215	0.19263028	2.41630939	3.05450852	0.3361	19.2555	10.5841	12.9157	3.4933
M6H10	6	10	312.59	4	2.33158317	0.04952782	3.69727722	4.37133754	1.85859215	0.19263028	2.41630939	3.05450852	0.3361	19.2555	10.5841	12.9157	3.4933

Blade tip timing to determine turbine blade fatigue in low vacuum conditions

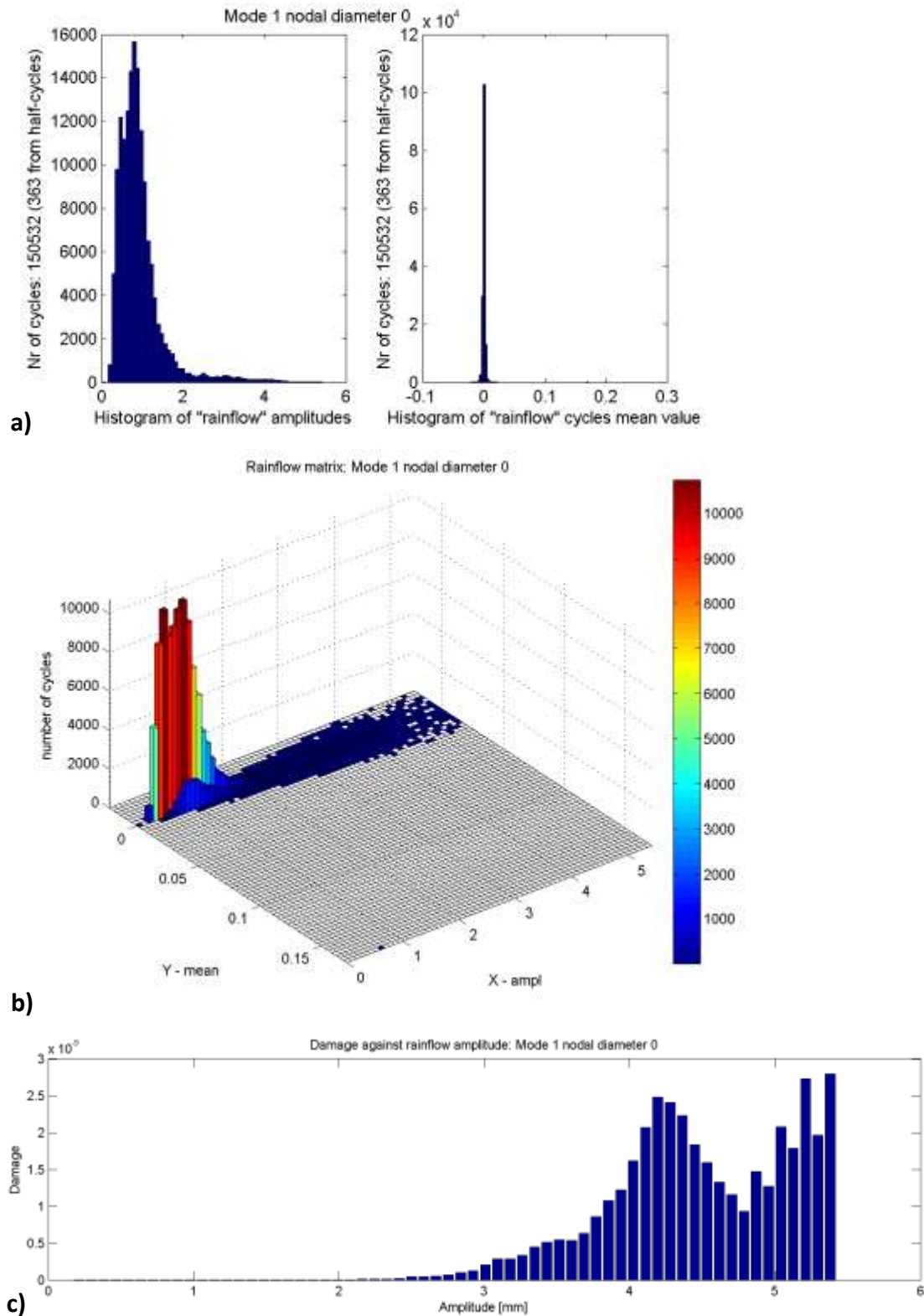# Appendix D

Fatigue results for all modes

Figure D-1: Rainflow cycle counting for mode 1 nodal diameter 0 with a) amplitude and mean values b) rainflow matrix and c) damage
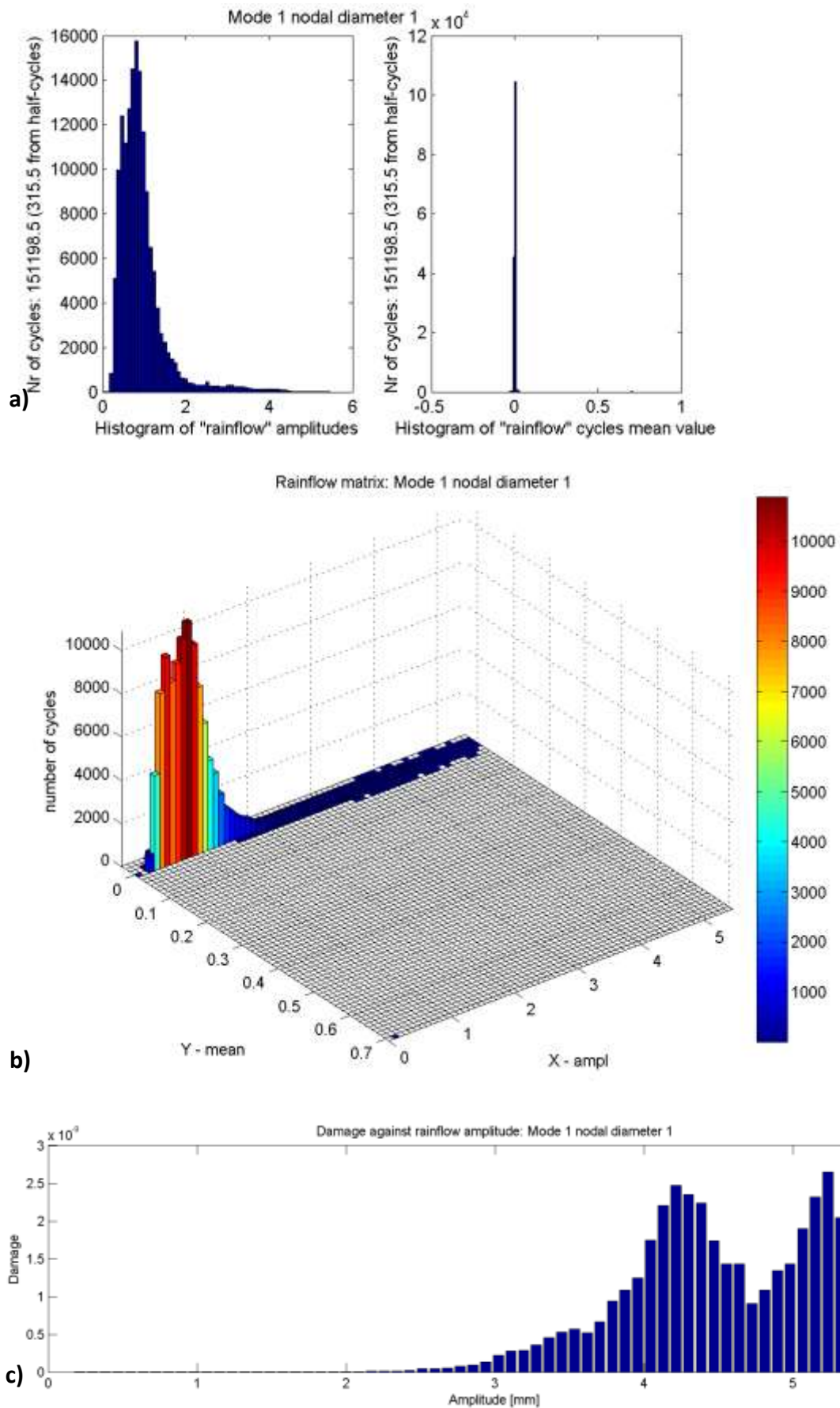
Figure D-2: Rainflow cycle counting for mode 1 nodal diameter 1 with a) amplitude and mean values b) rainflow matrix and c) damage
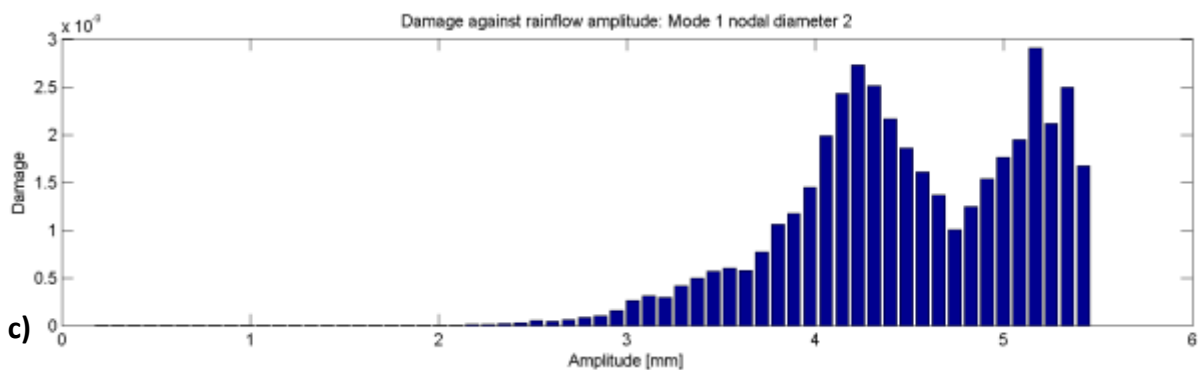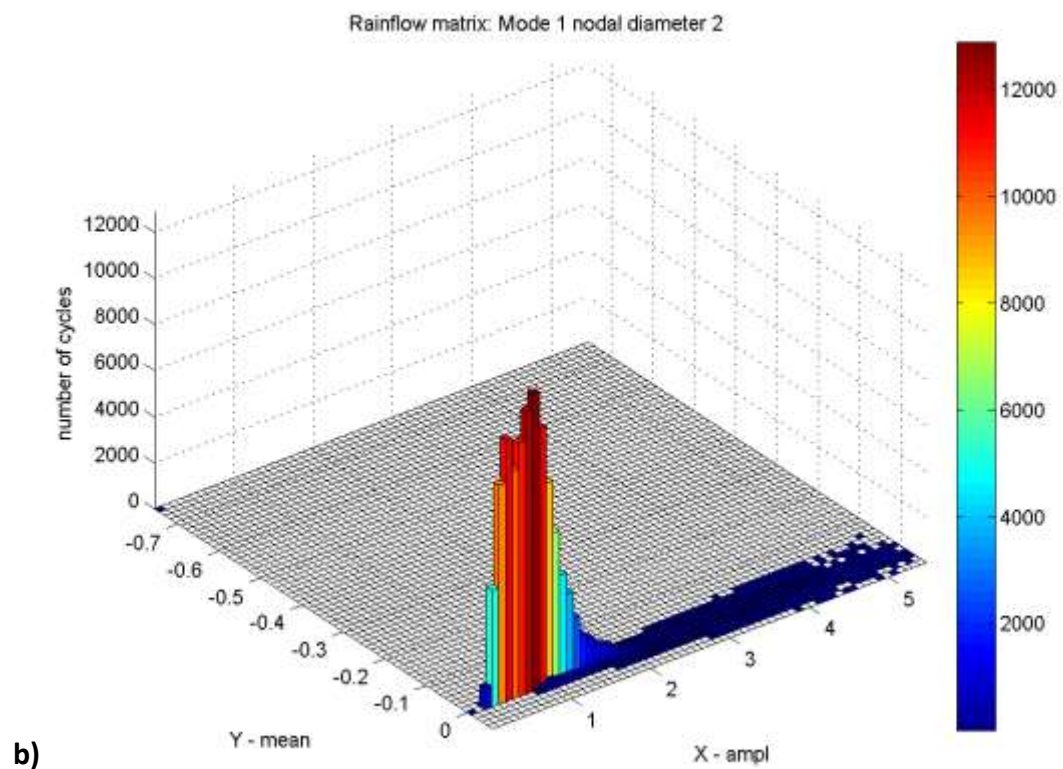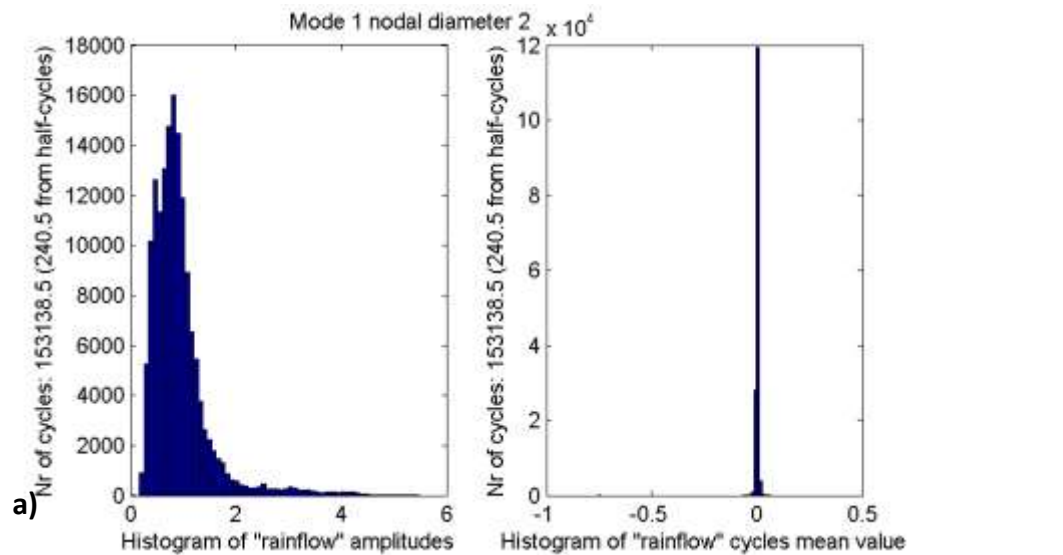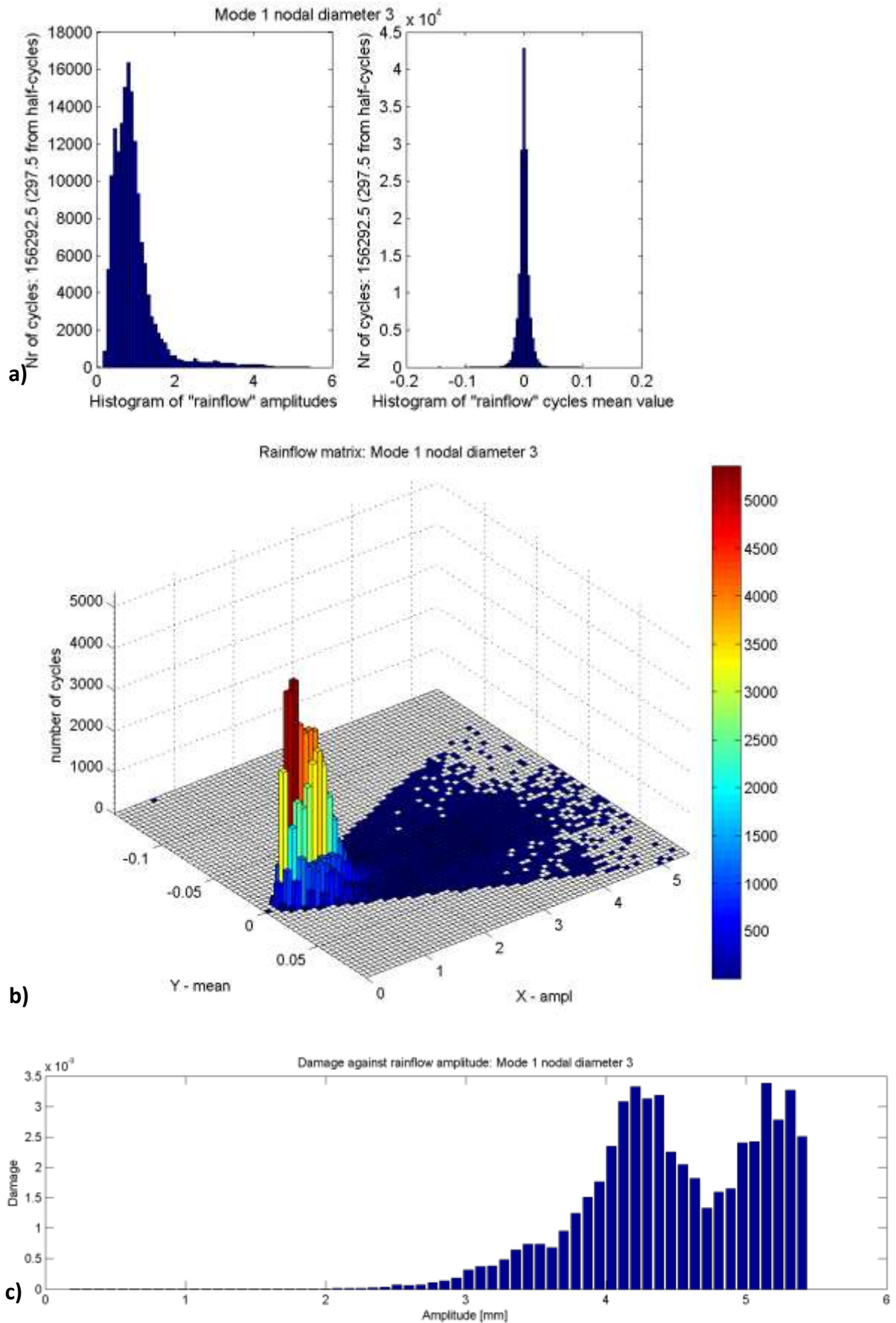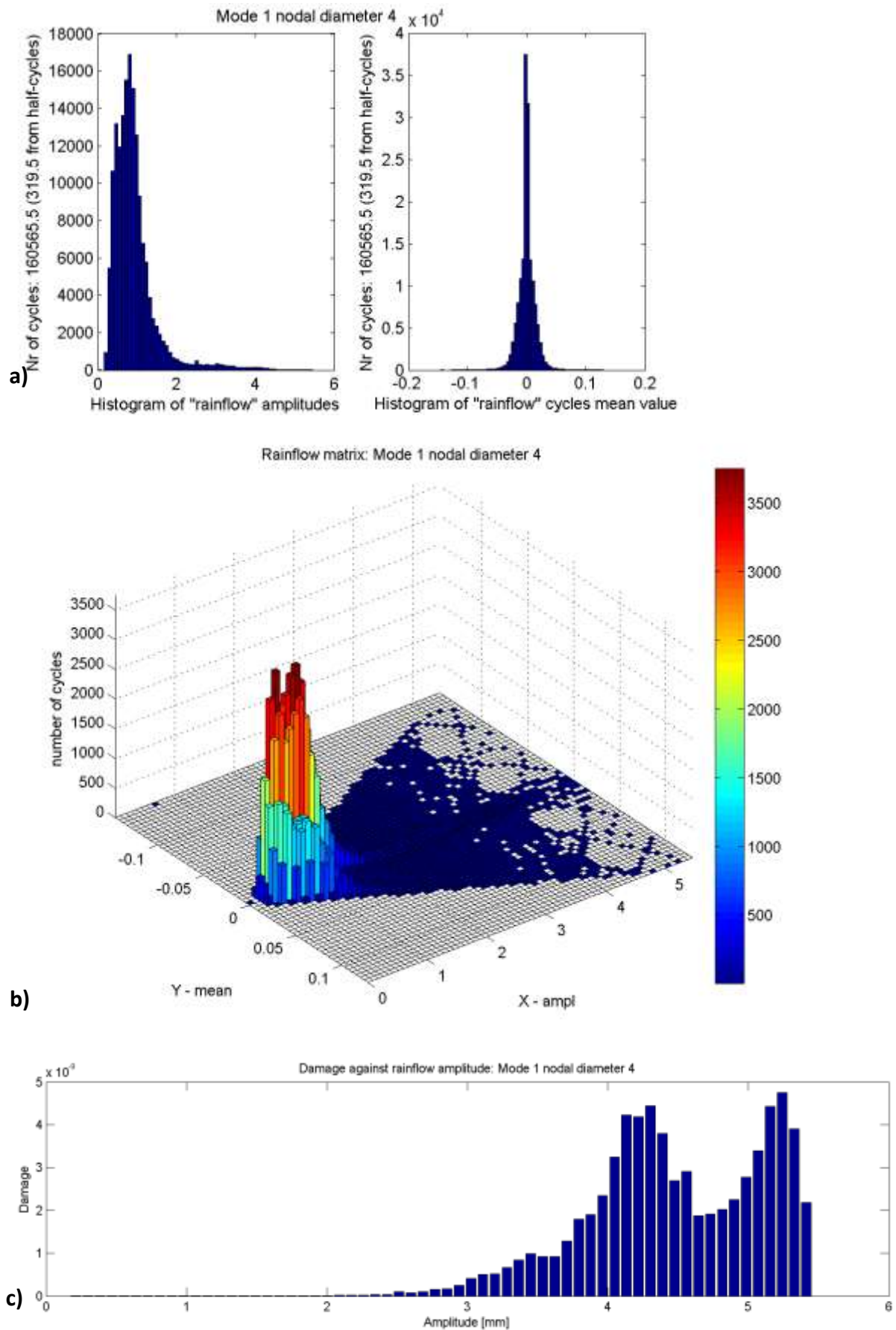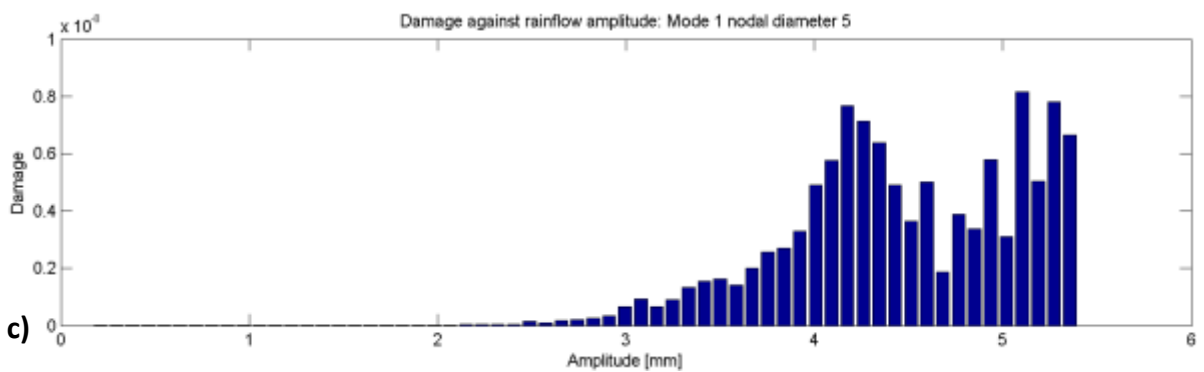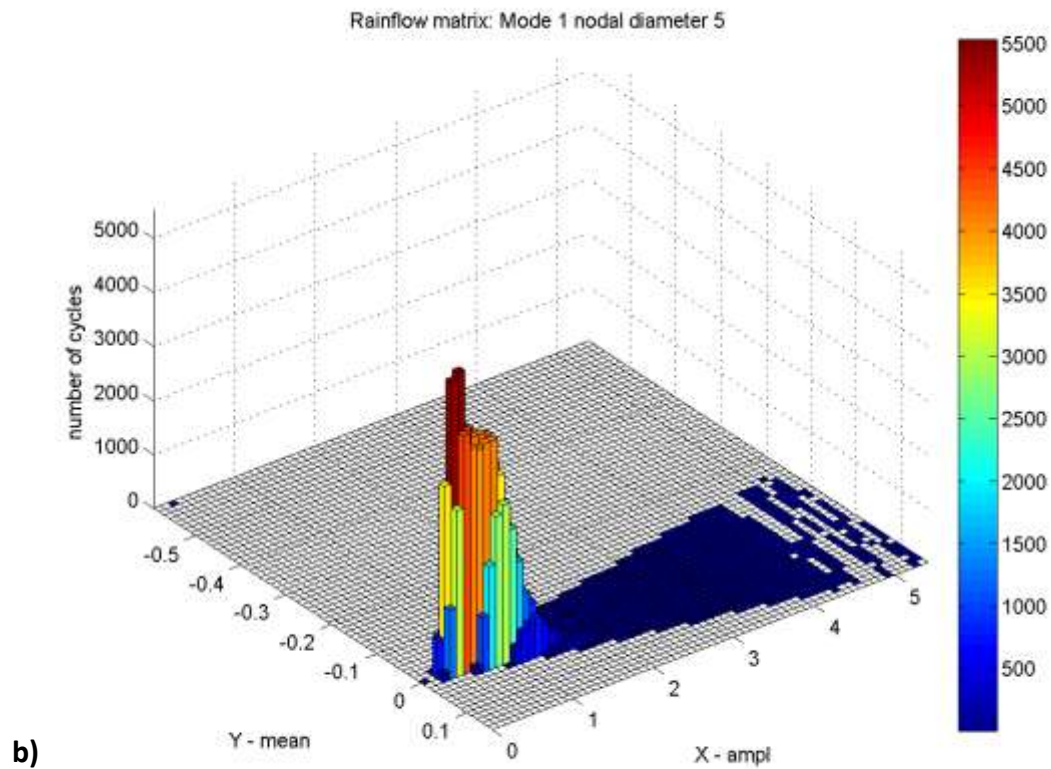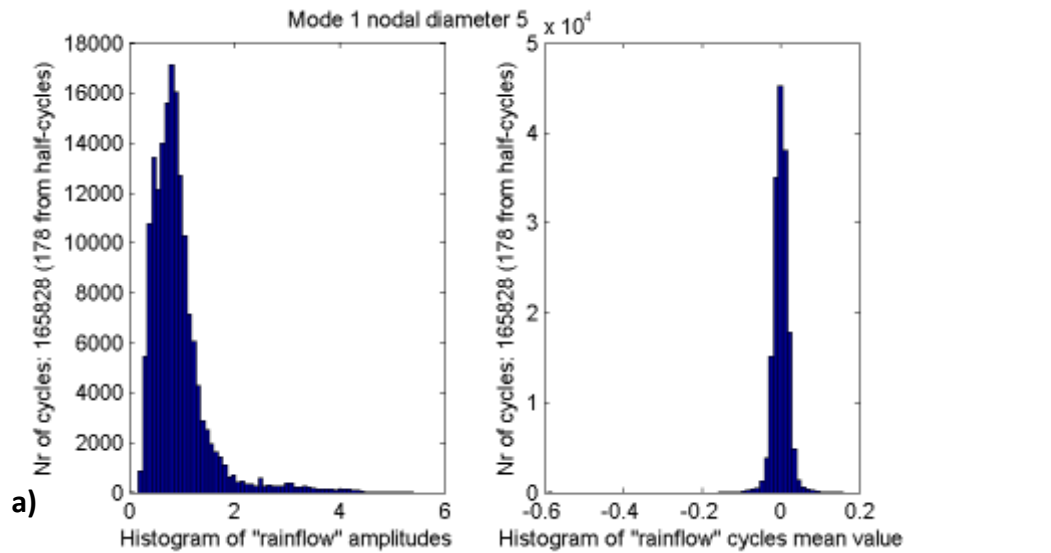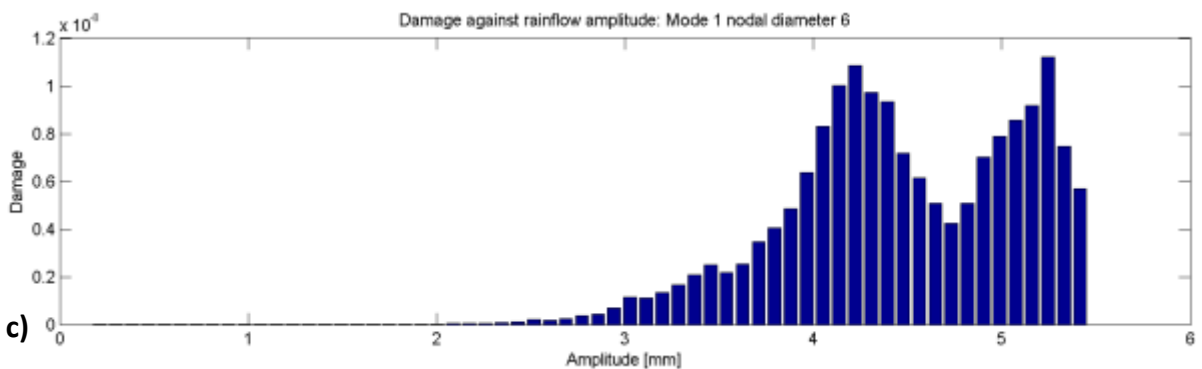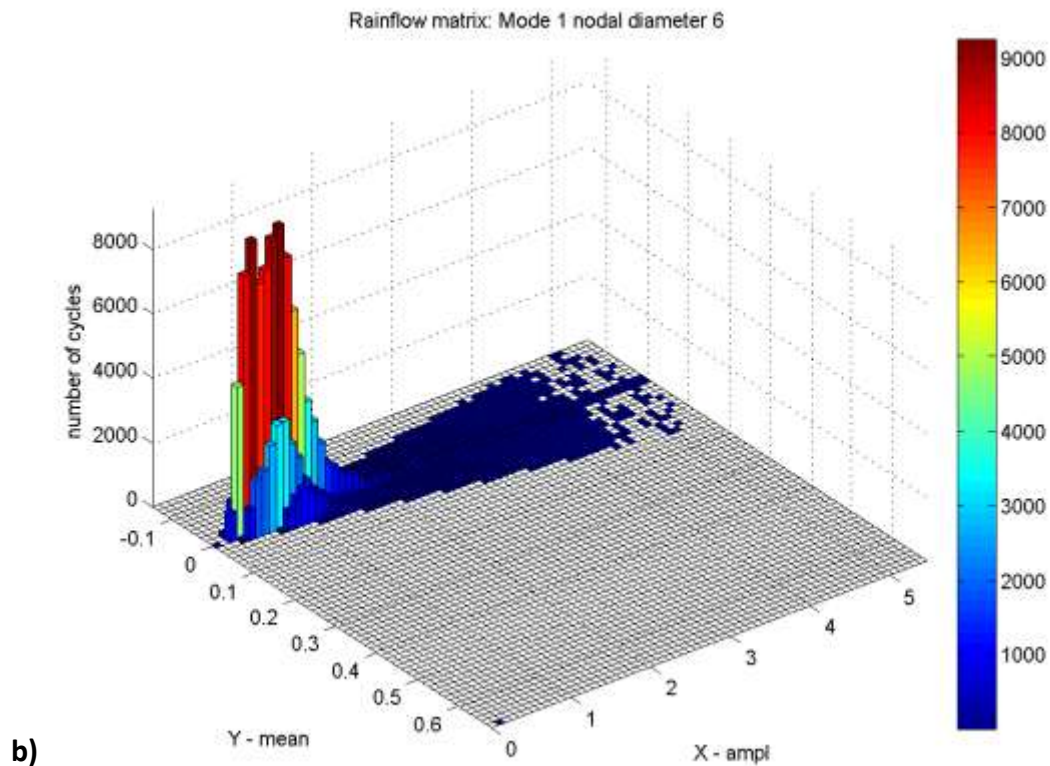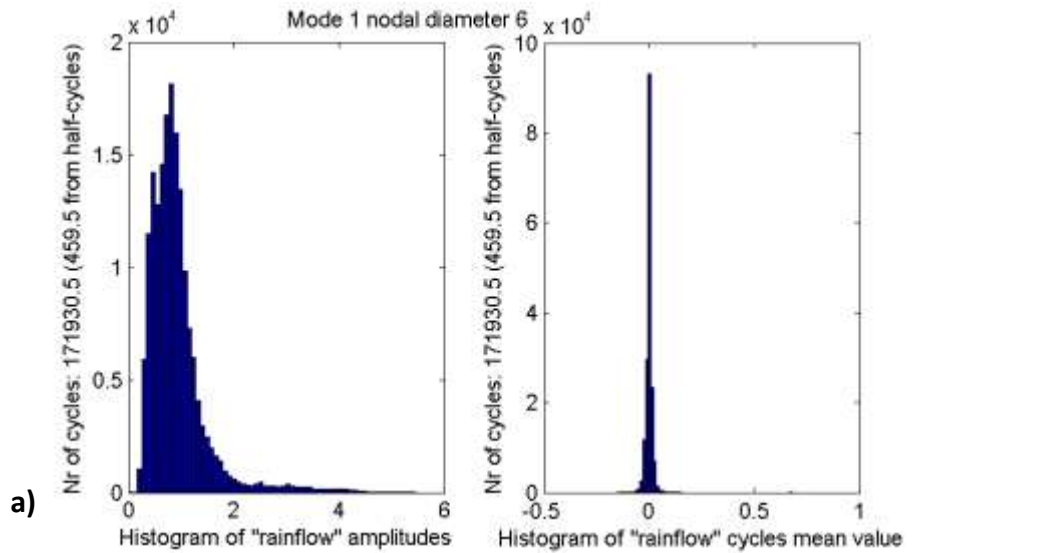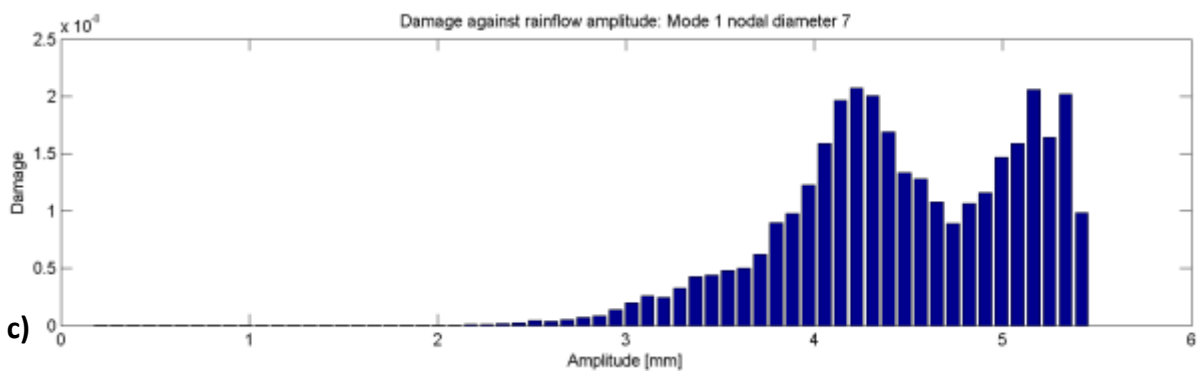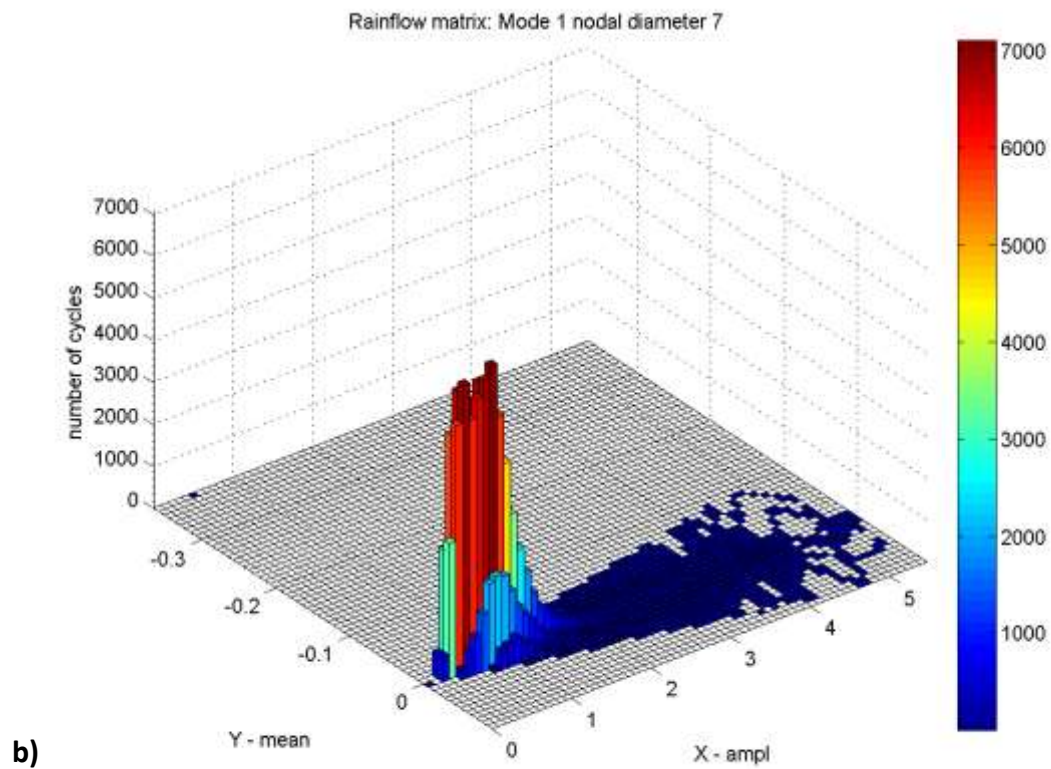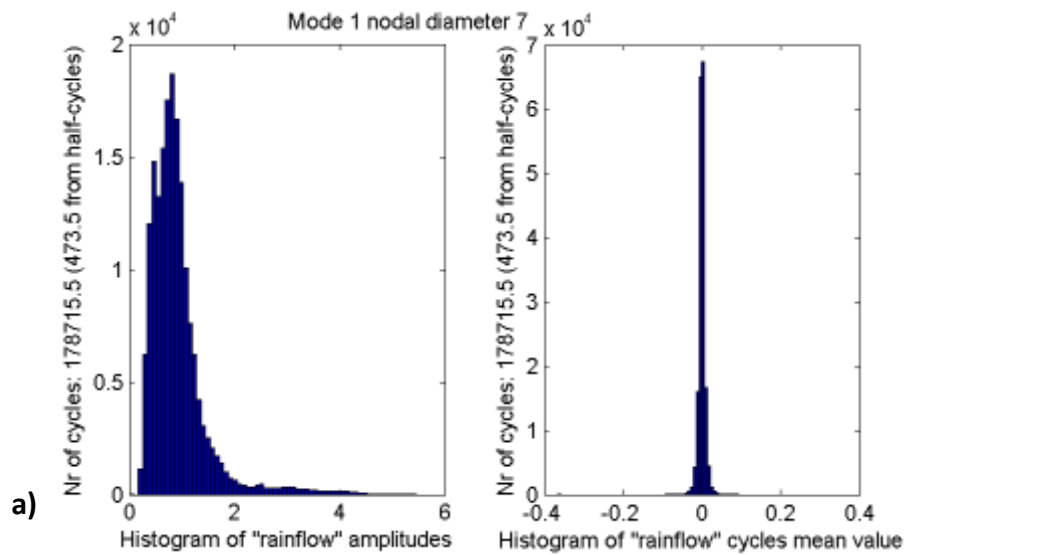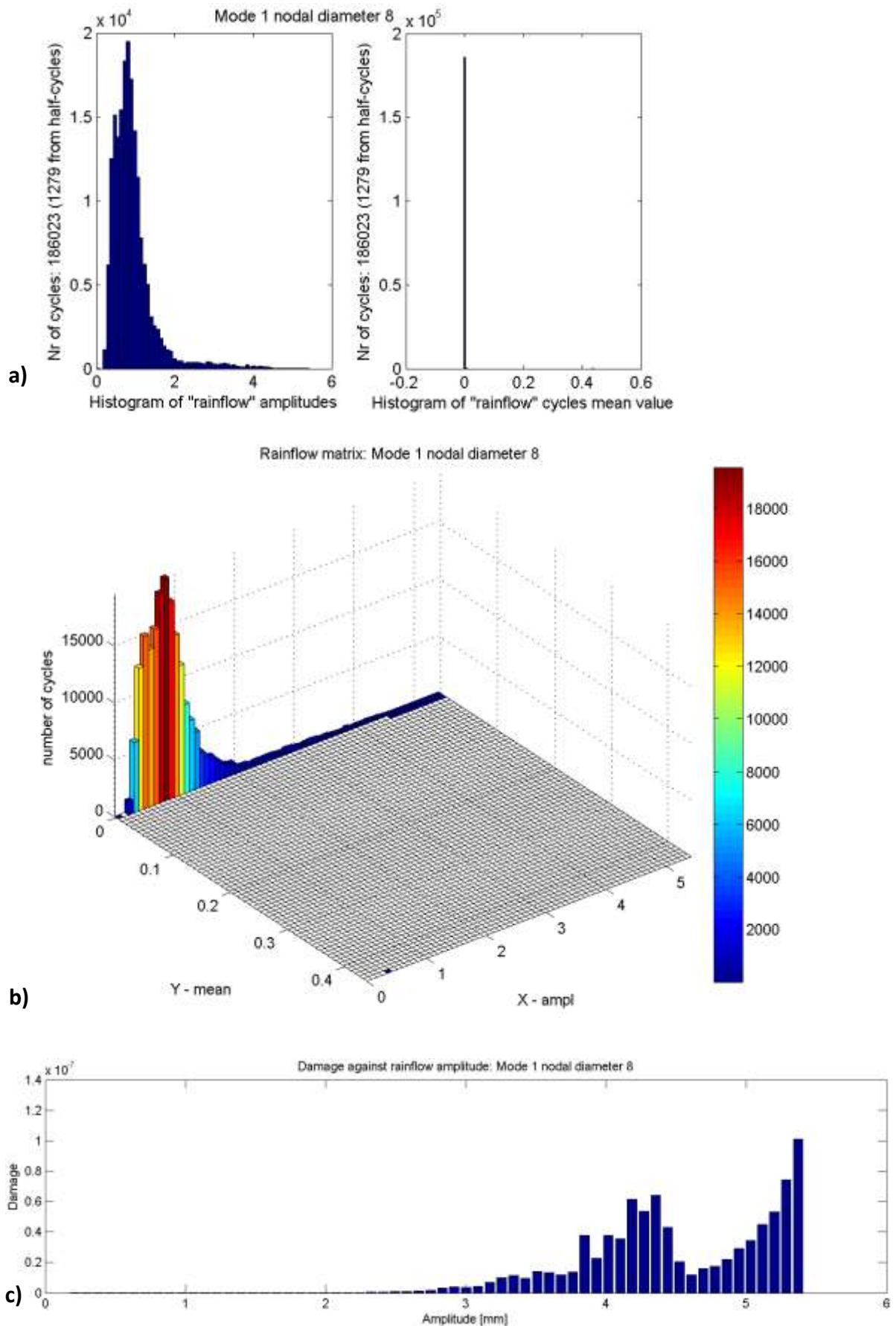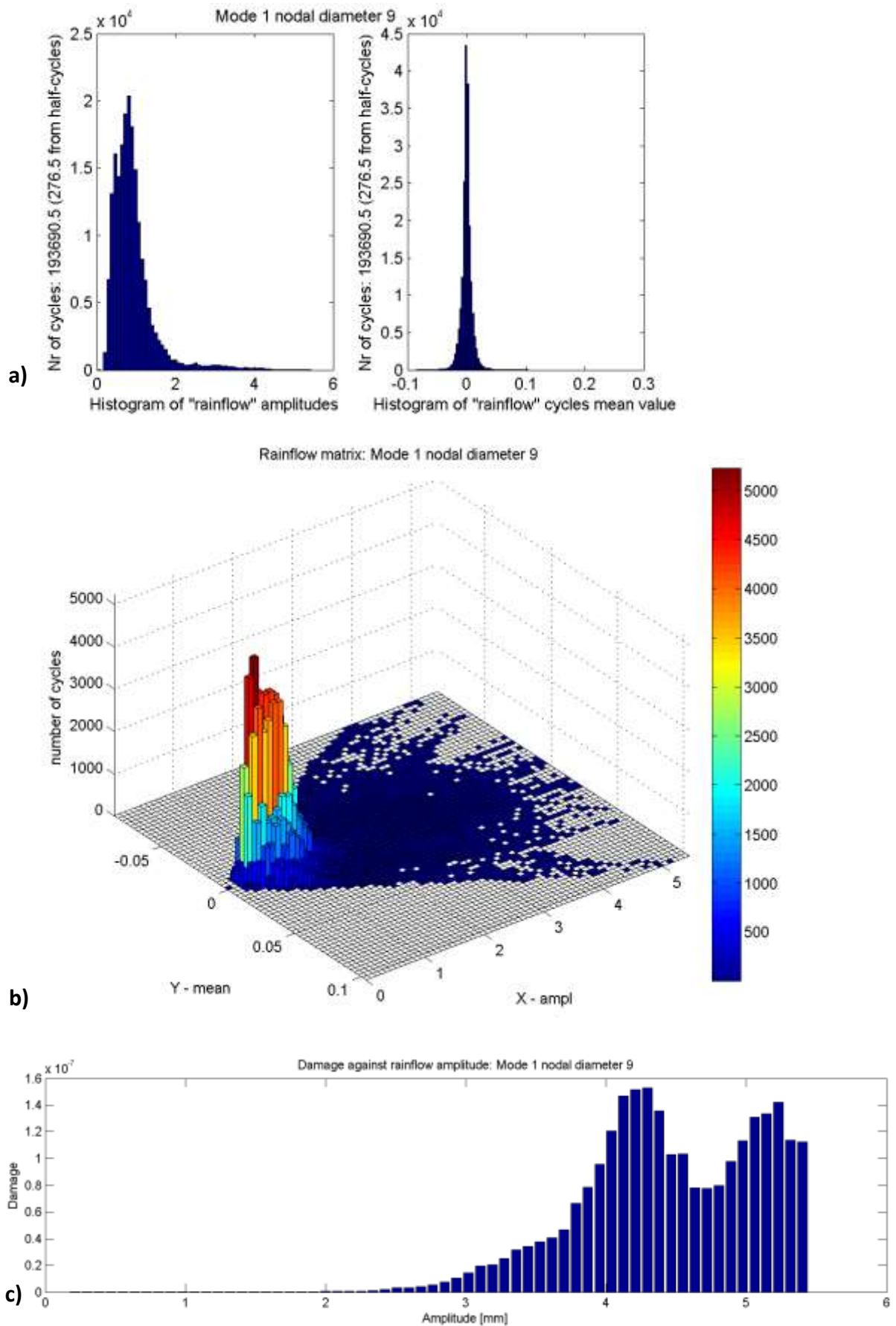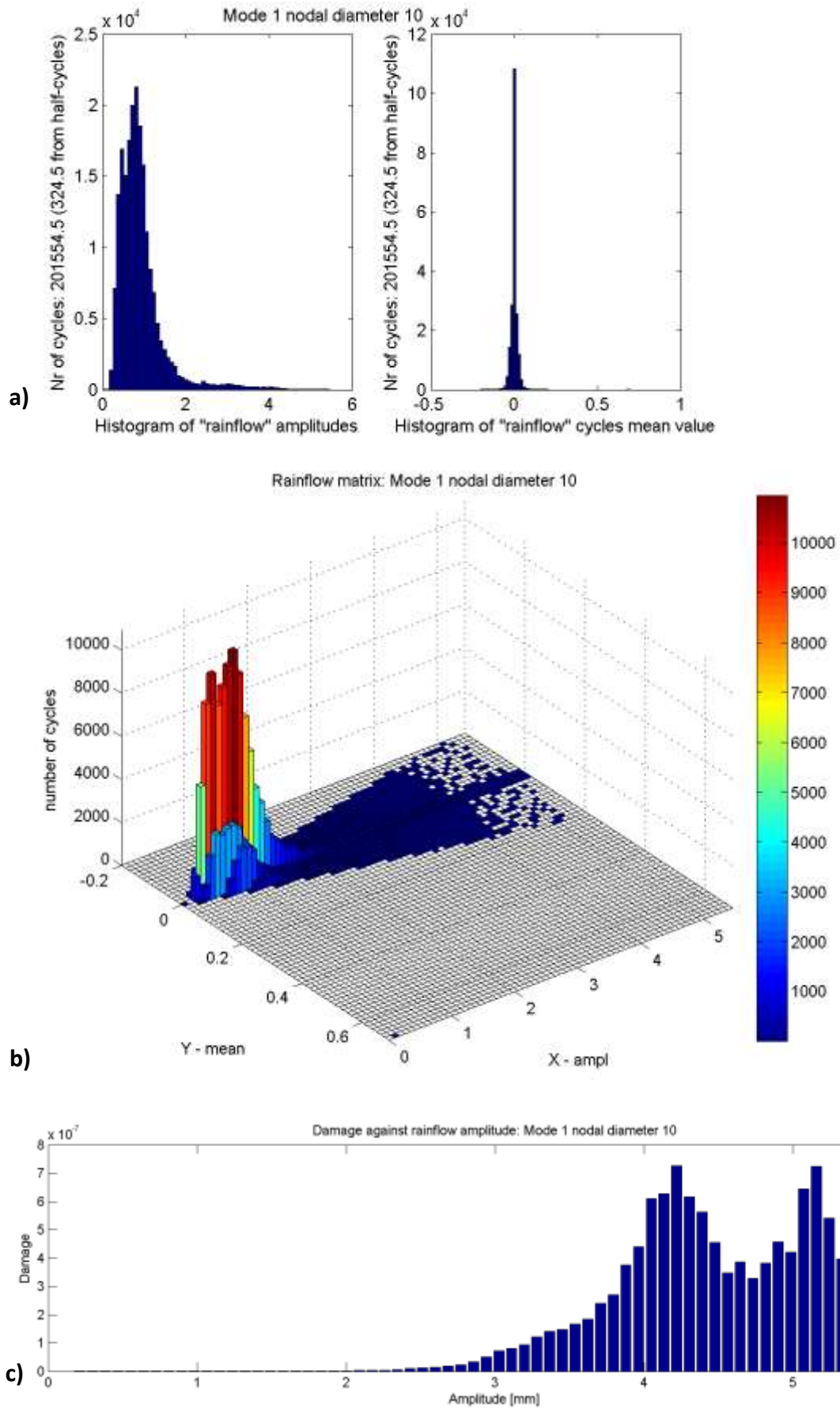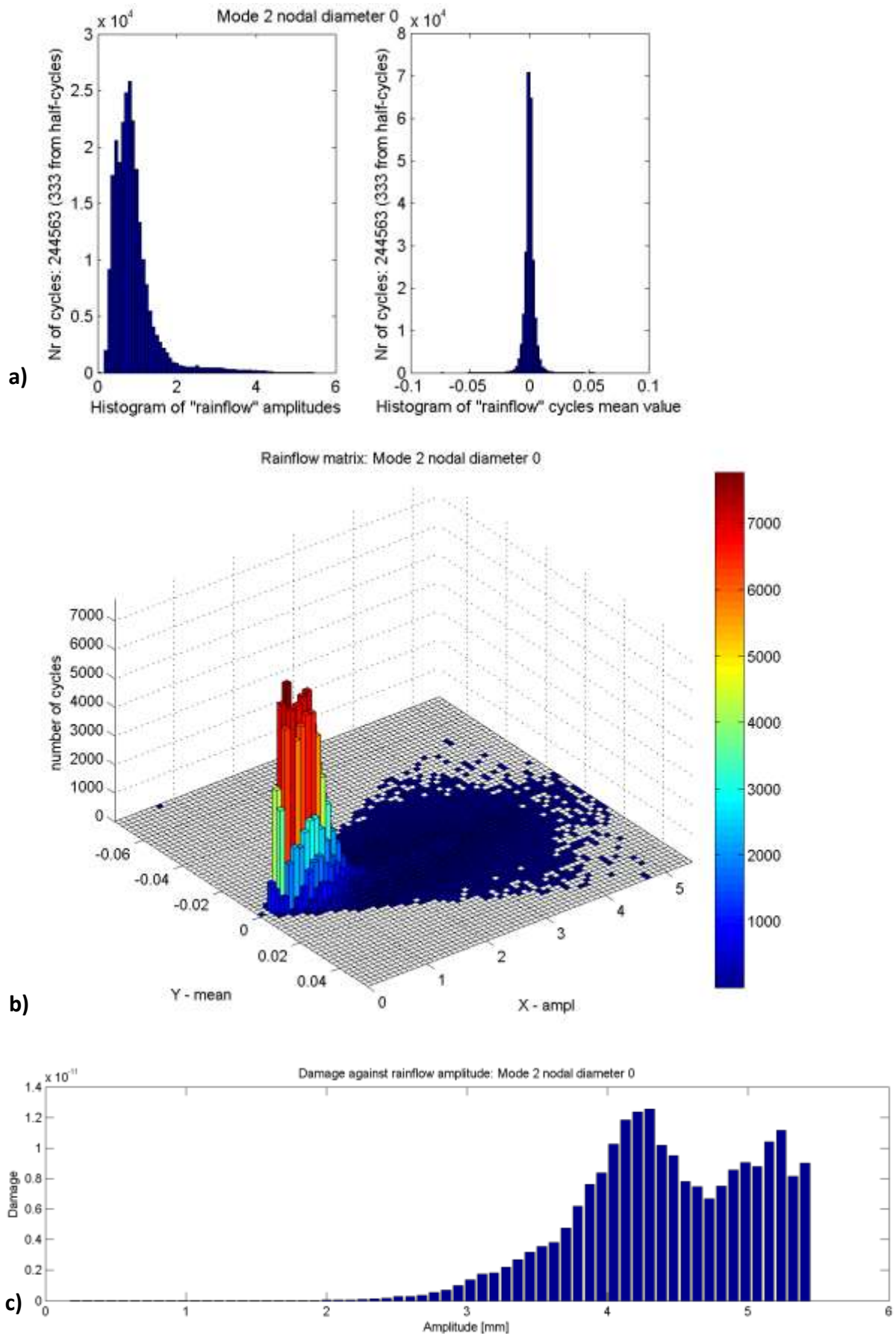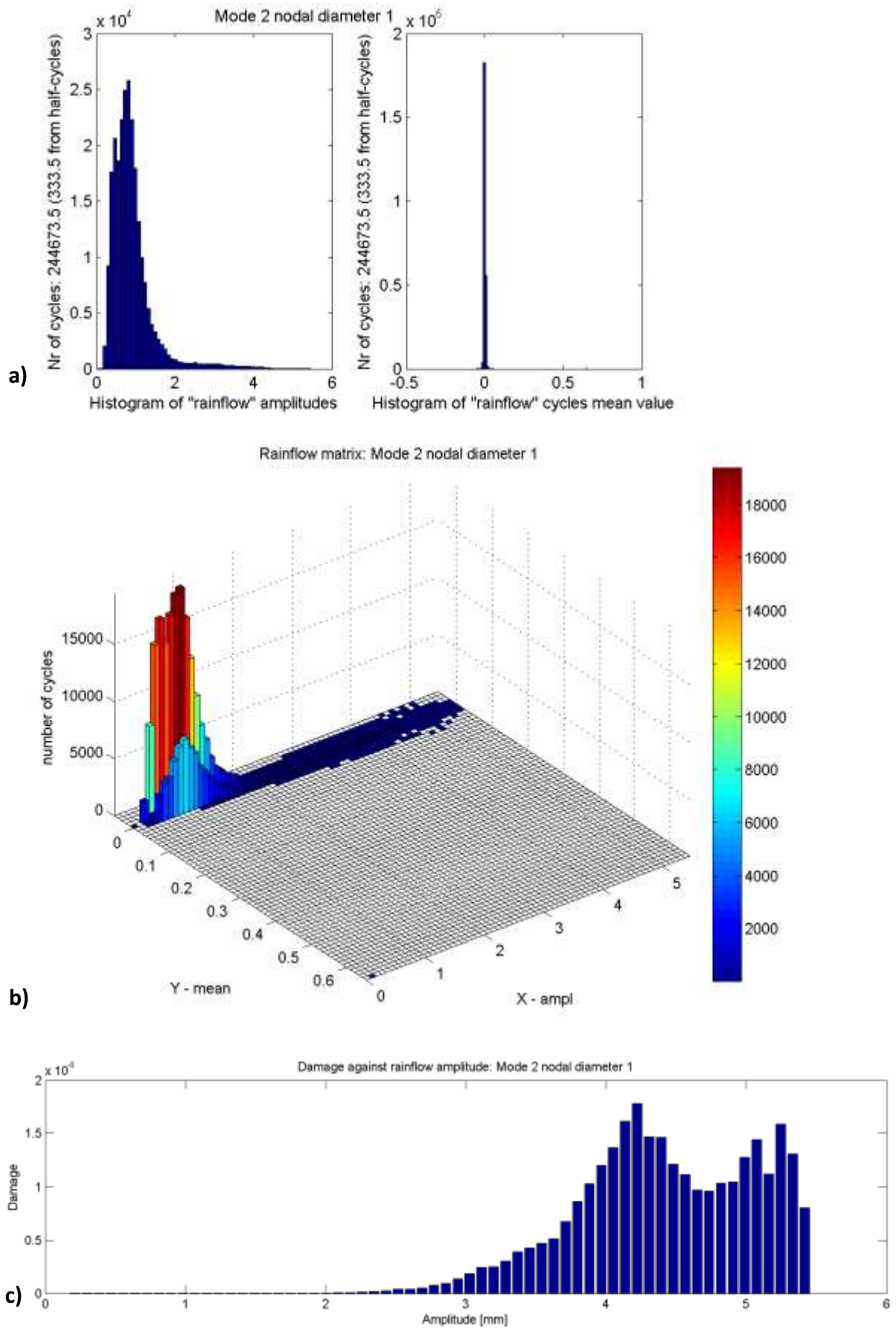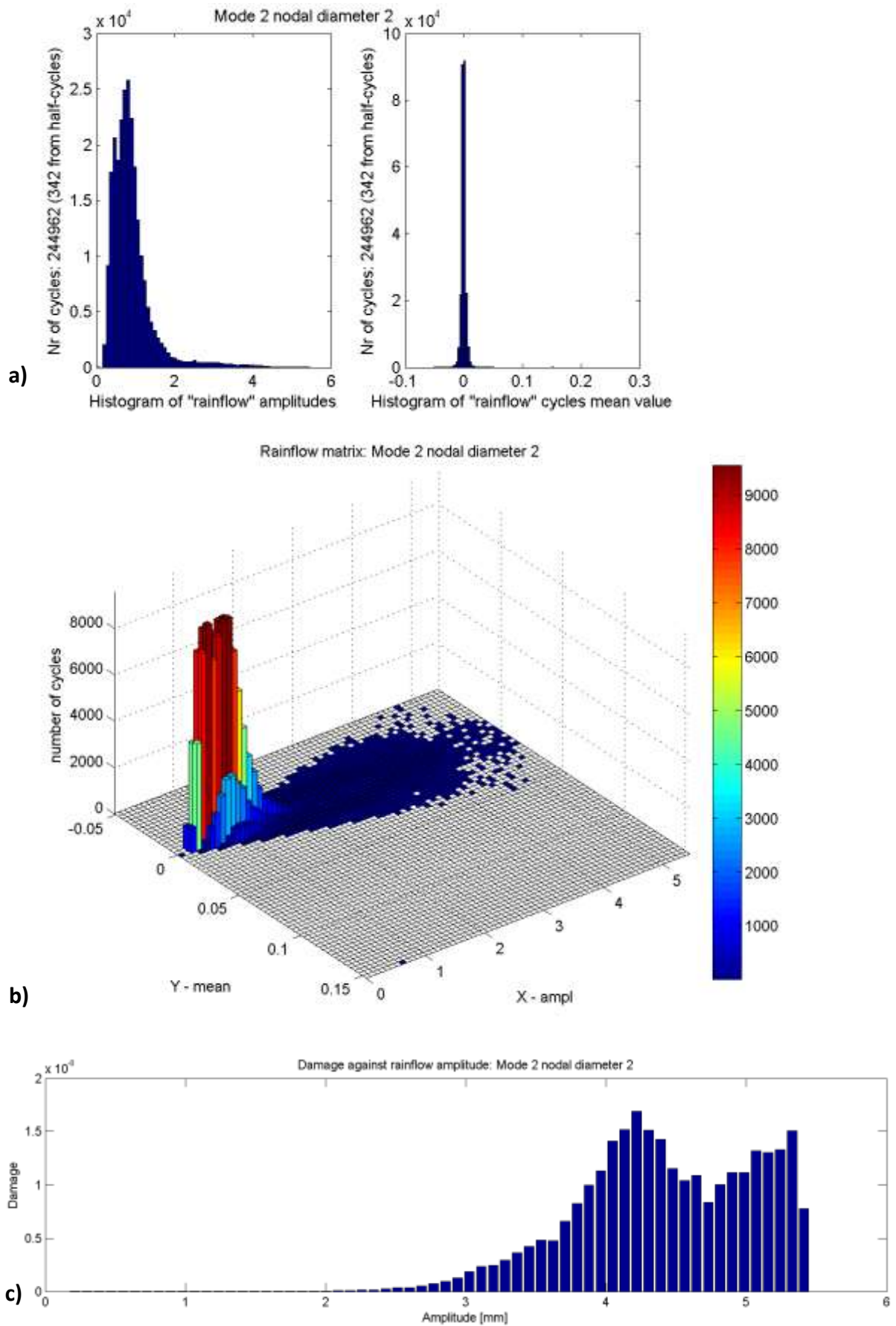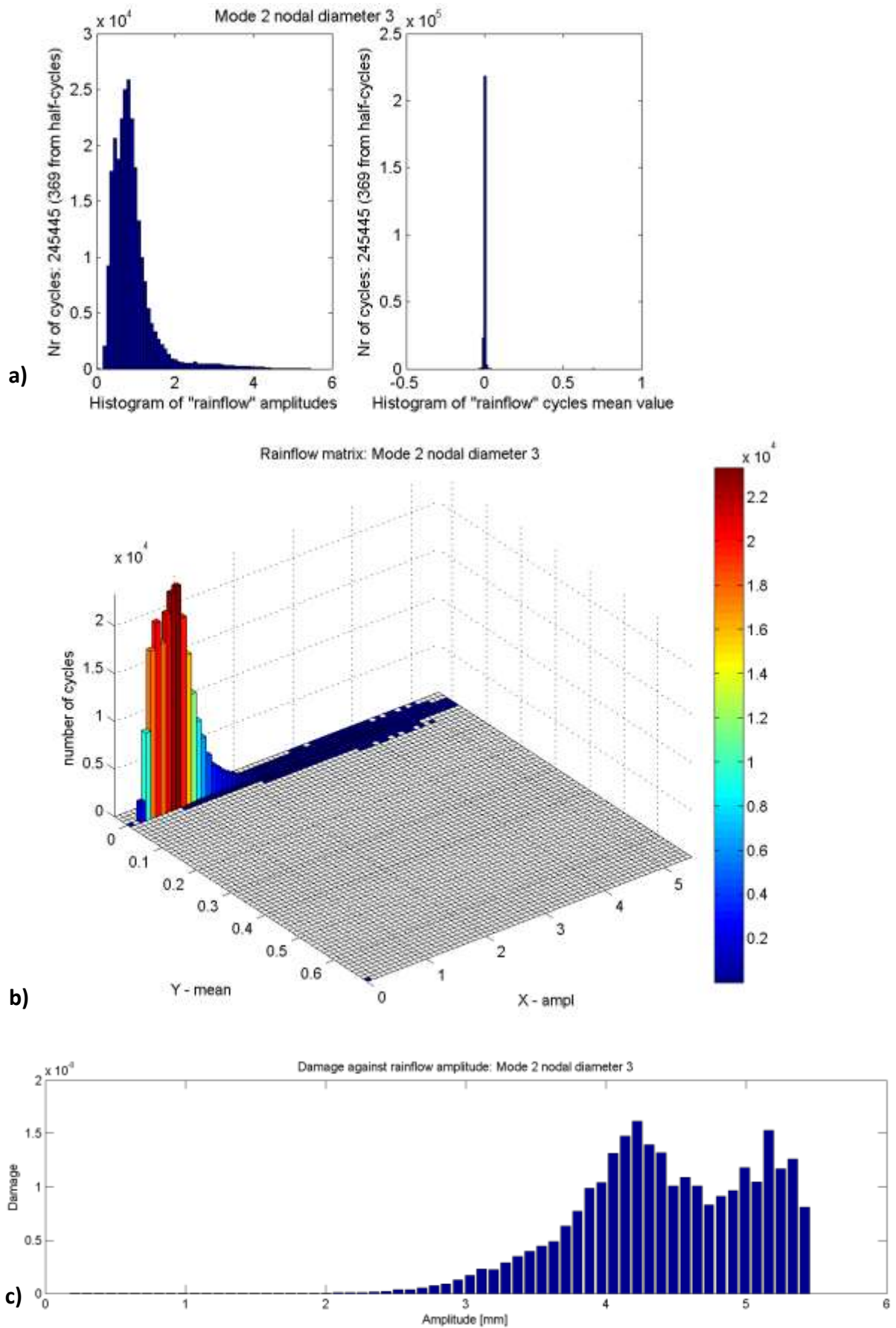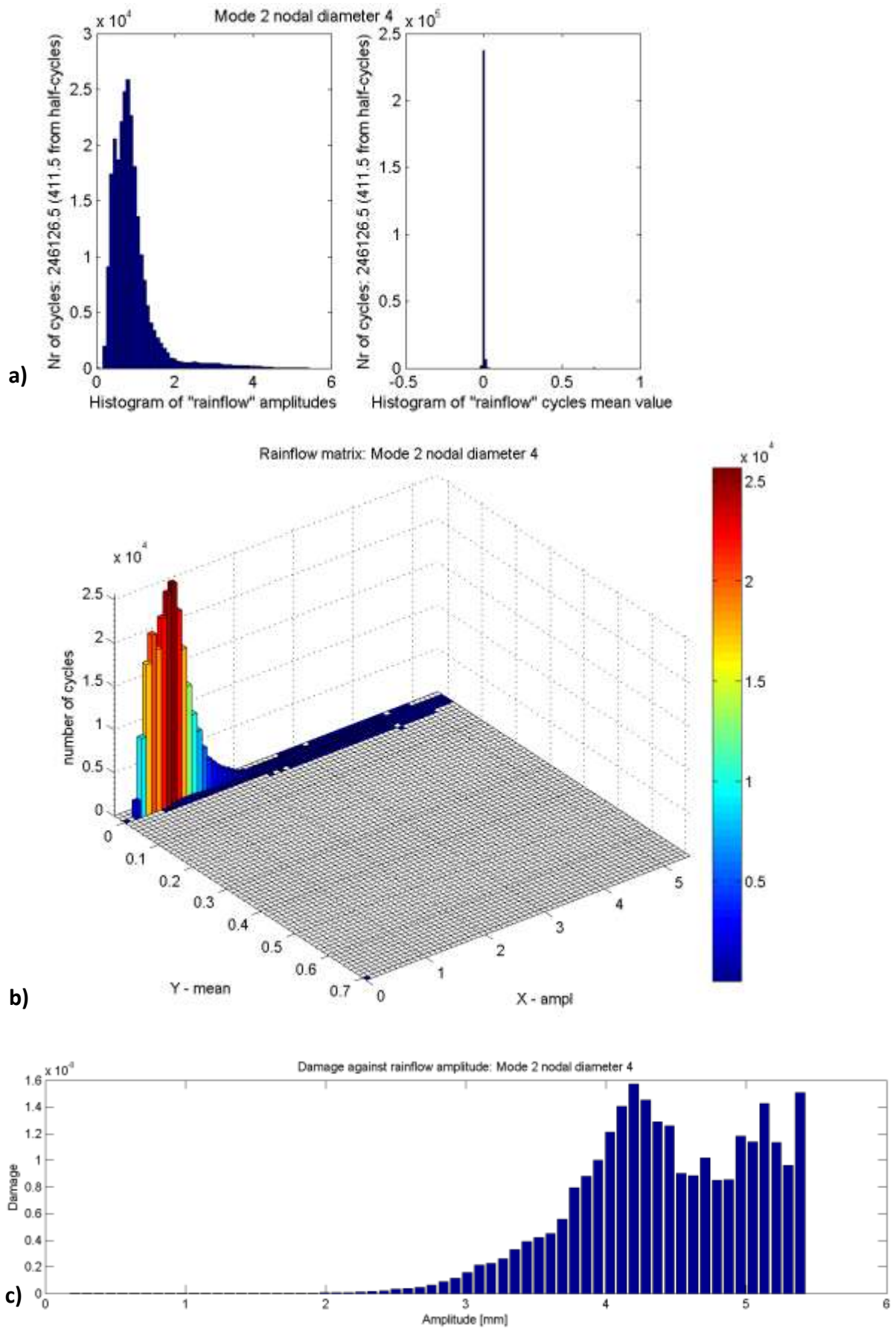
Figure D-3: Rainflow cycle counting for mode 1 nodal diameter 2 with a) amplitude and mean values b) rainflow matrix and c) damage

Figure D-4: Rainflow cycle counting for mode 1 nodal diameter 3 with a) amplitude and mean values b) rainflow matrix and c) damage

Figure D-5: Rainflow cycle counting for mode 1 nodal diameter 4 with a) amplitude and mean values b) rainflow matrix and c) damage
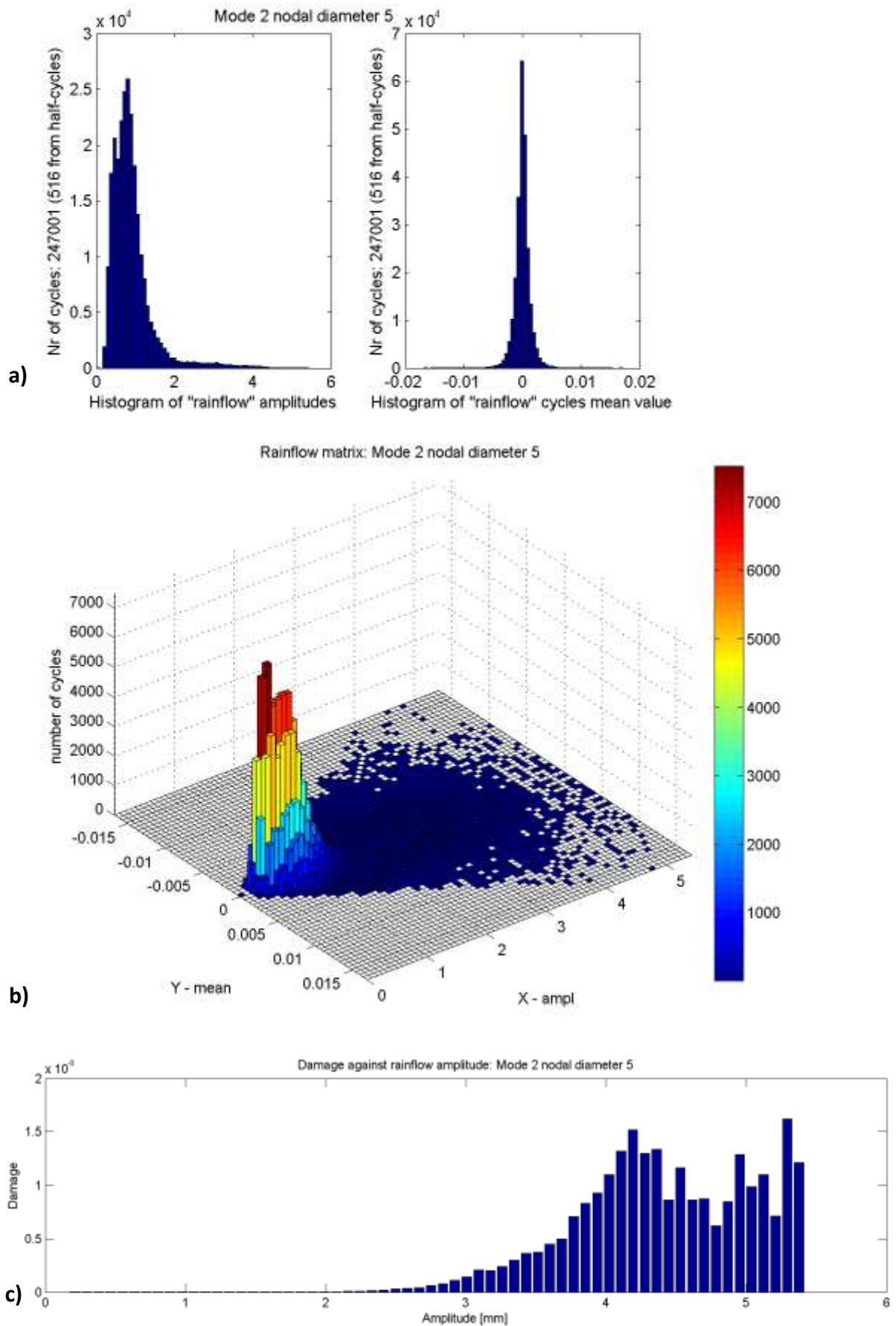
Figure D-6: Rainflow cycle counting for mode 1 nodal diameter 5 with a) amplitude and mean values b) rainflow matrix and c) damage
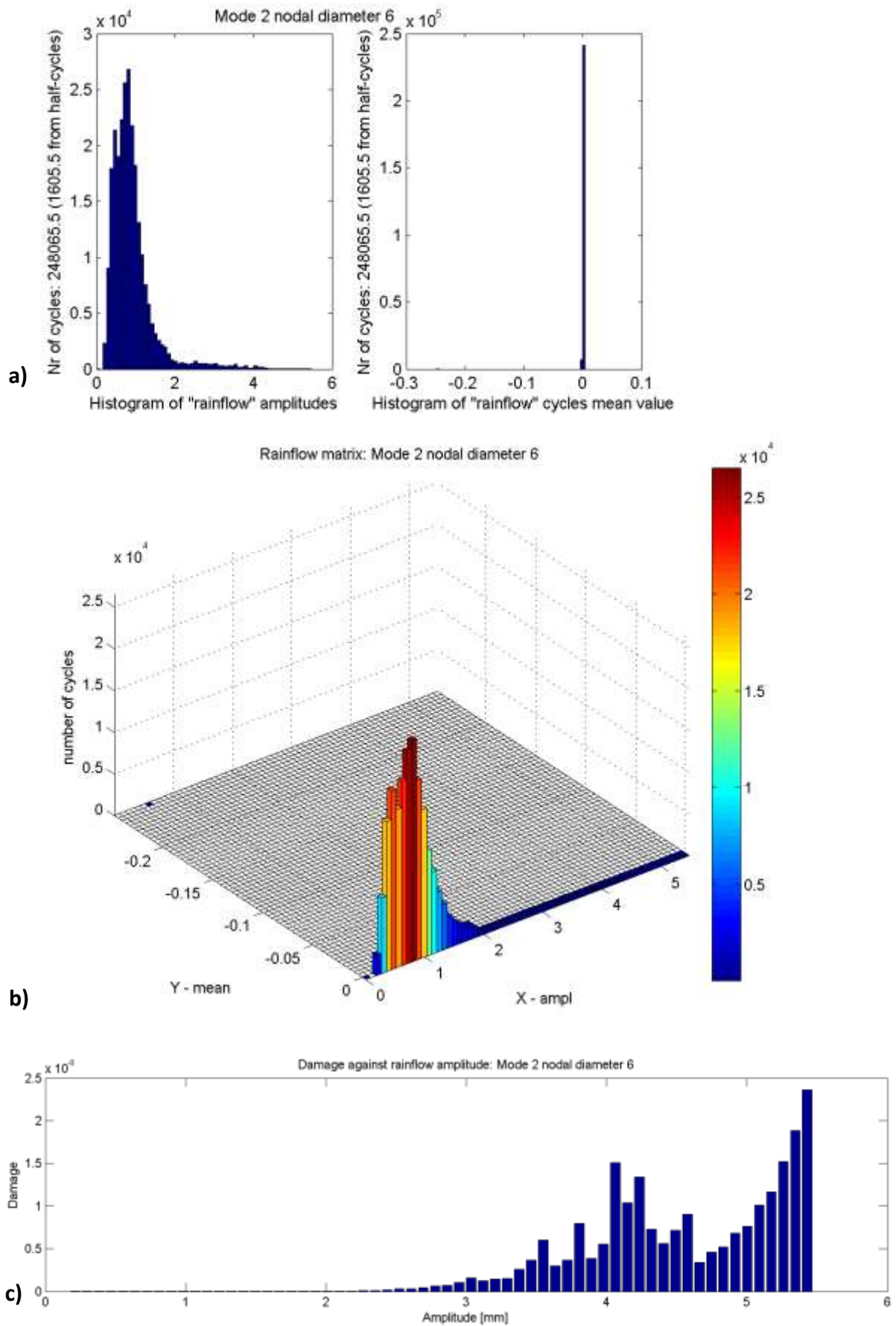
Figure D-7: Rainflow cycle counting for mode 1 nodal diameter 6 with a) amplitude and mean values b) rainflow matrix and c) damage

Figure D-8: Rainflow cycle counting for mode 1 nodal diameter 7 with a) amplitude and mean values b) rainflow matrix and c) damage

Figure D-9: Rainflow cycle counting for mode 1 nodal diameter 8 with a) amplitude and mean values b) rainflow matrix and c) damage
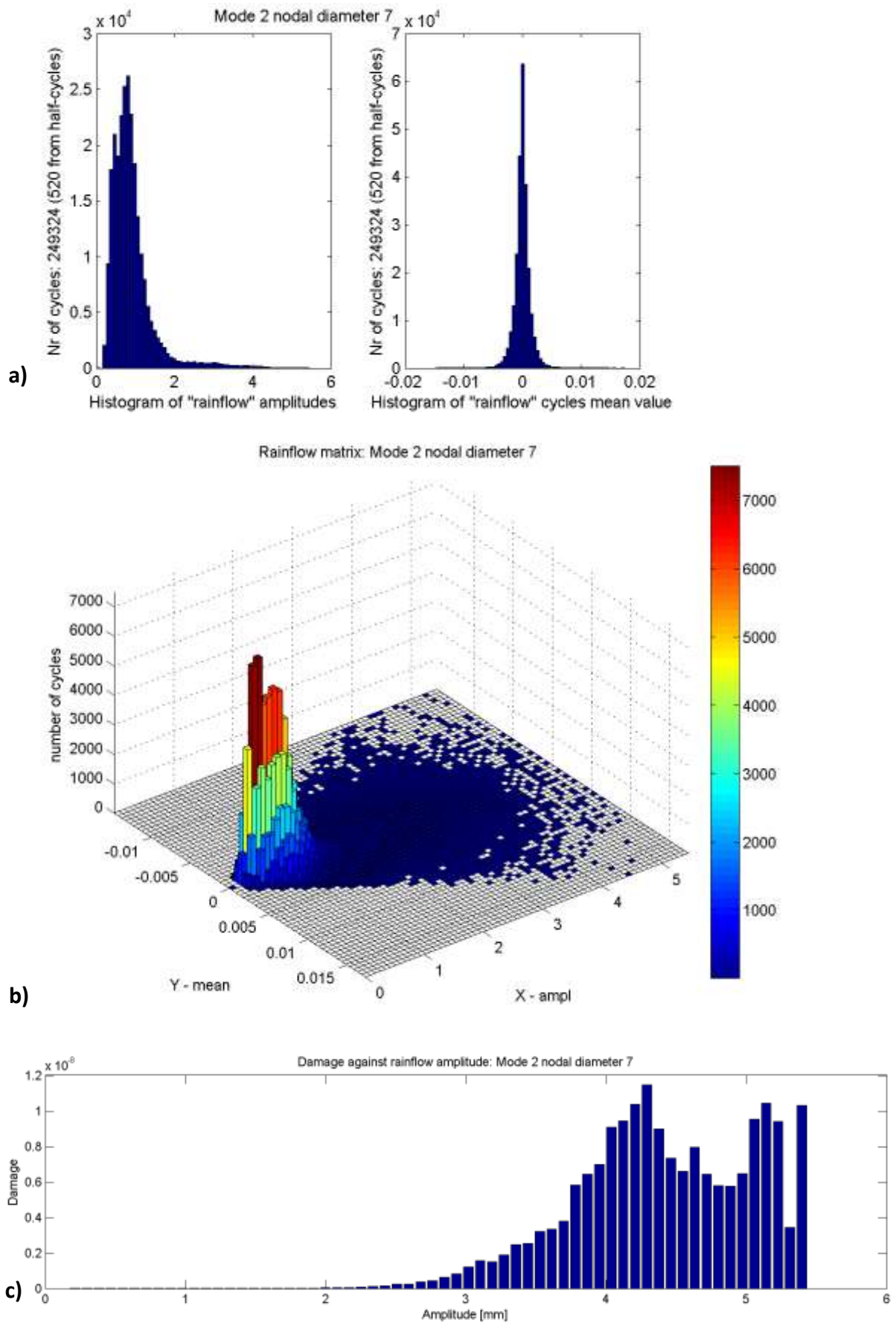
Figure D-10: Rainflow cycle counting for mode 1 nodal diameter 9 with a) amplitude and mean values b) rainflow matrix and c) damage

Figure D-11: Rainflow cycle counting for mode 1 nodal diameter 10 with a) amplitude and mean values b) rainflow matrix and c) damage
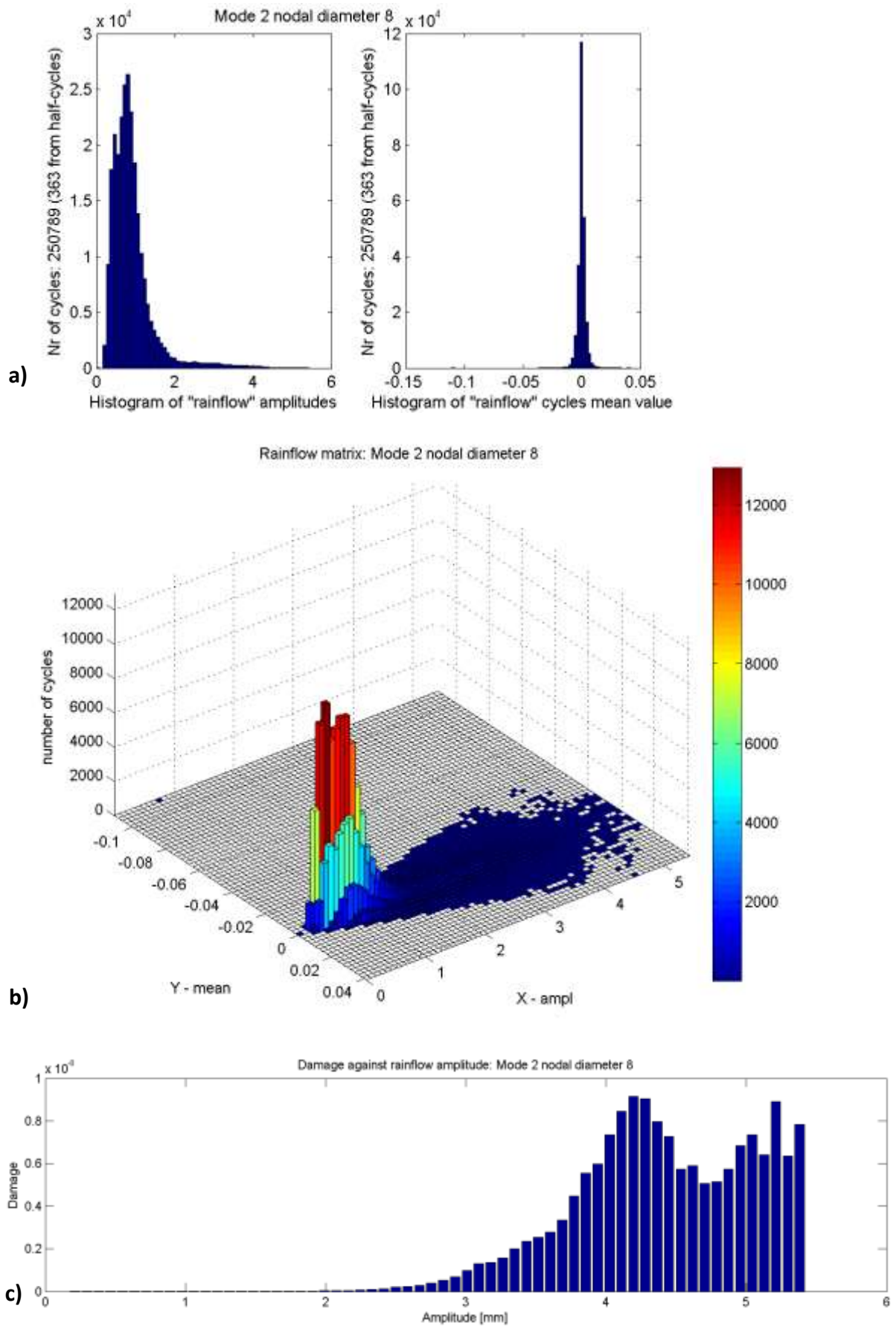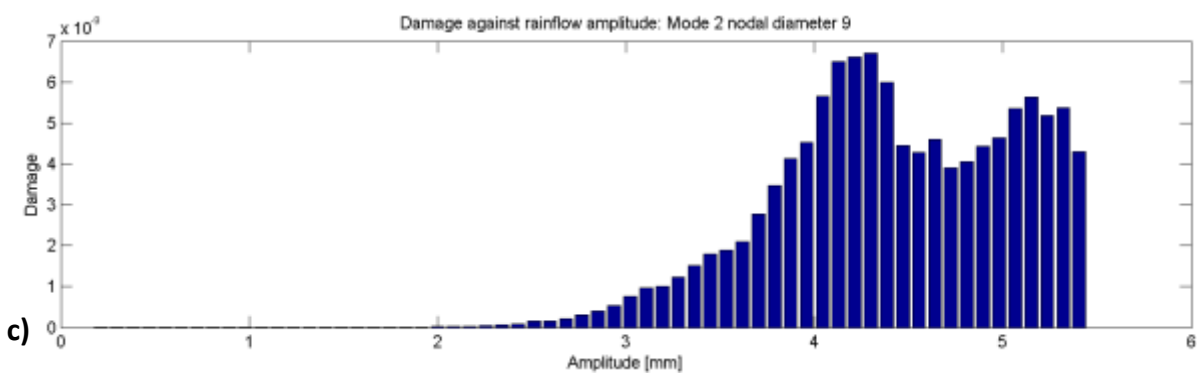
Figure D-12: Rainflow cycle counting for mode 2 nodal diameter 0 with a) amplitude and mean values b) rainflow matrix and c) damage

Figure D-13: Rainflow cycle counting for mode 2 nodal diameter 1 with a) amplitude and mean values b) rainflow matrix and c) damage

Figure D-14: Rainflow cycle counting for mode 2 nodal diameter 2 with a) amplitude and mean values b) rainflow matrix and c) damage
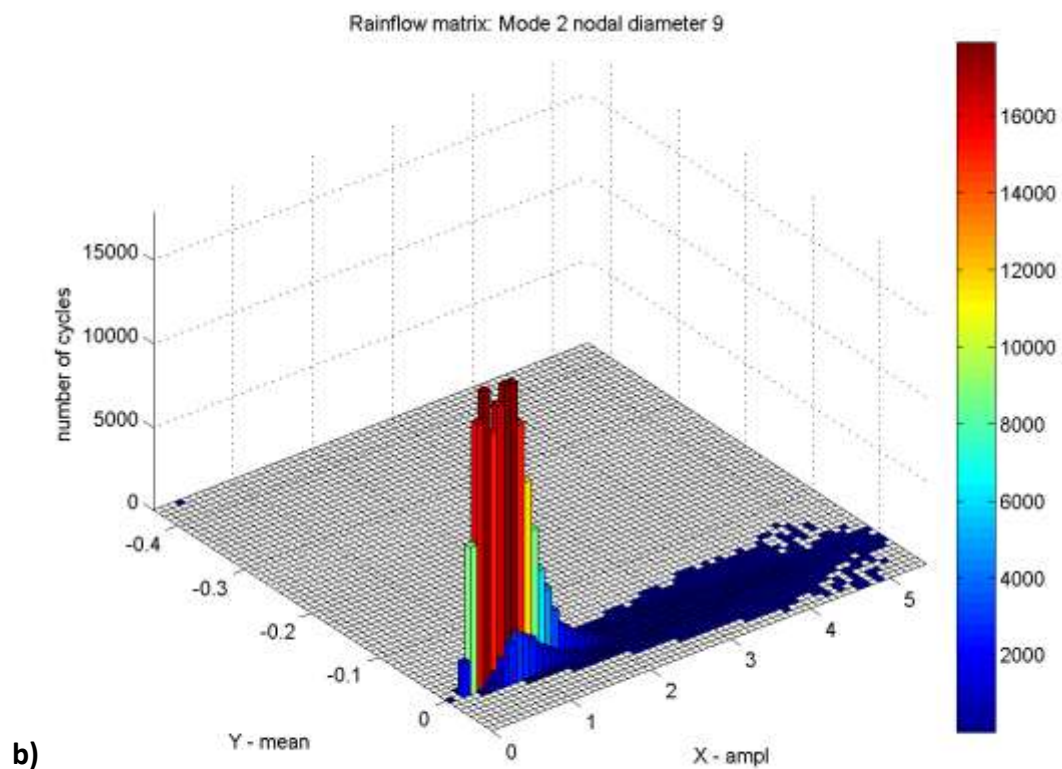
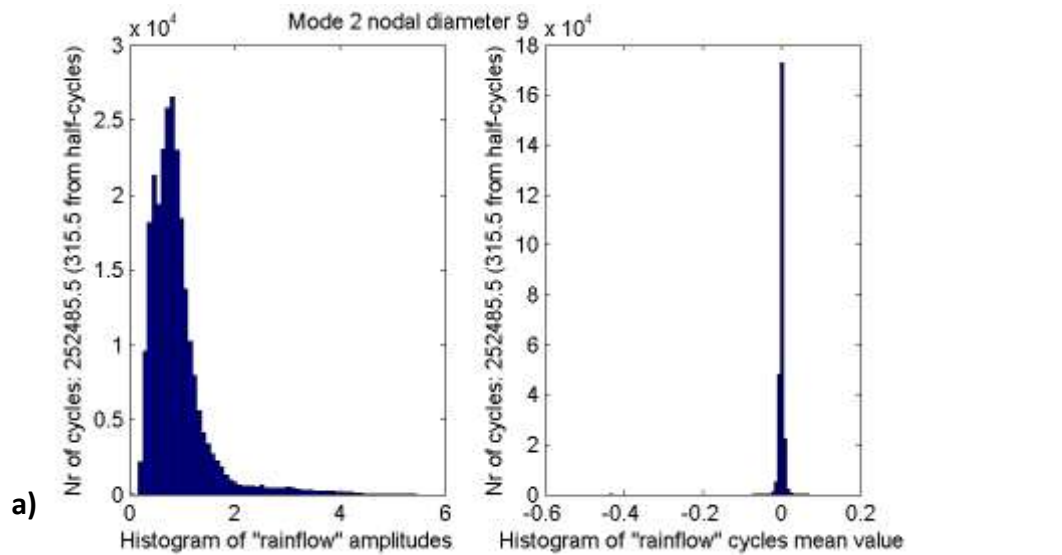**Figure D-15:** Rainflow cycle counting for mode 2 nodal diameter 3 with a) amplitude and mean values b) rainflow matrix and c) damage

Figure D-16: Rainflow cycle counting for mode 2 nodal diameter 4 with a) amplitude and mean values b) rainflow matrix and c) damage

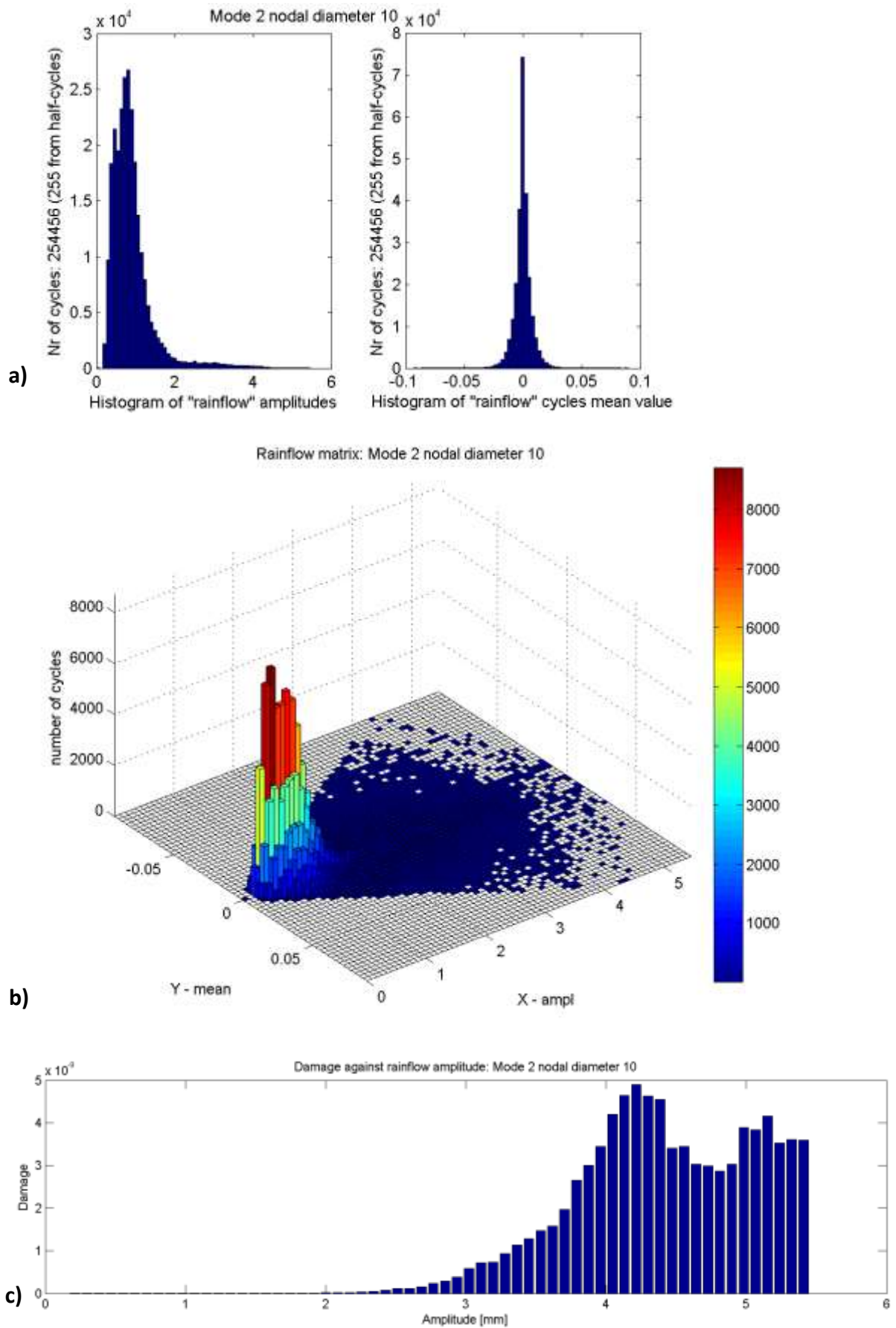**Figure D-17:** Rainflow cycle counting for mode 2 nodal diameter 5 with a) amplitude and mean values b) rainflow matrix and c) damage

Figure D-18: Rainflow cycle counting for mode 2 nodal diameter 6 with a) amplitude and mean values b) rainflow matrix and c) damage

Figure D-19: Rainflow cycle counting for mode 2 nodal diameter 7 with a) amplitude and mean values b) rainflow matrix and c) damage

Figure D-20: Rainflow cycle counting for mode 2 nodal diameter 8 with a) amplitude and mean values b) rainflow matrix and c) damage
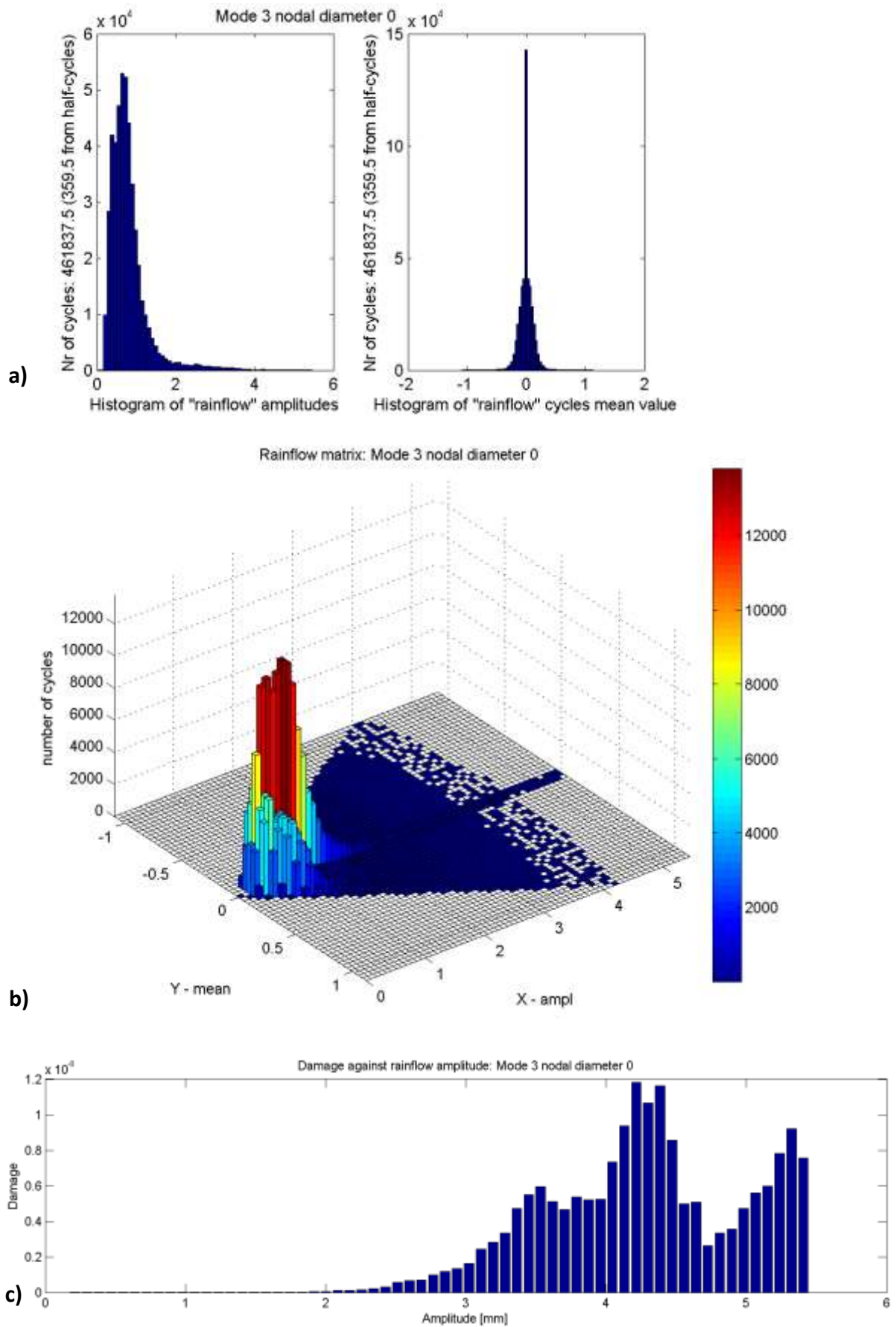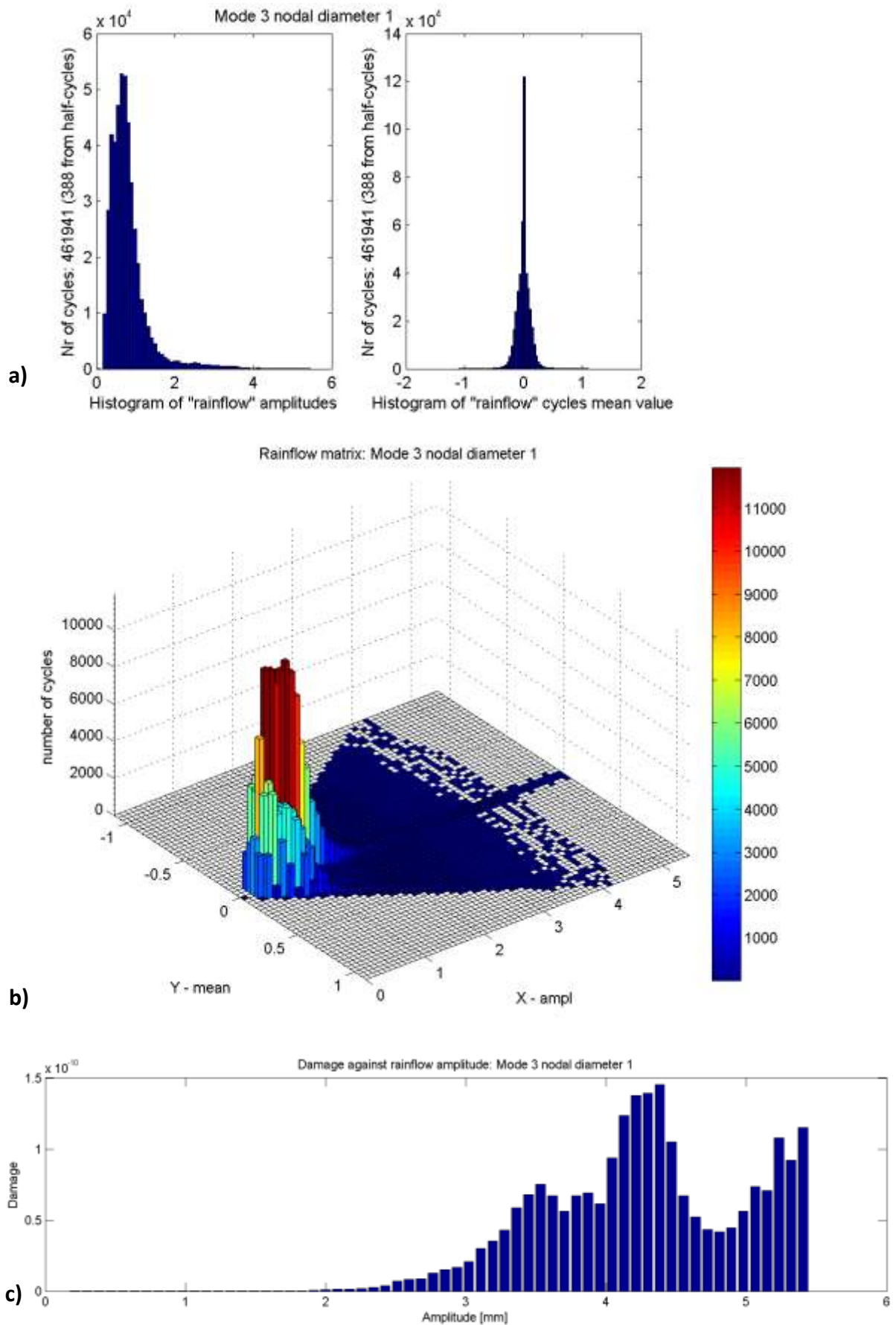
Figure D-21: Rainflow cycle counting for mode 2 nodal diameter 9 with a) amplitude and mean values b) rainflow matrix and c) damage

Figure D-22: Rainflow cycle counting for mode 2 nodal diameter 10 with a) amplitude and mean values b) rainflow matrix and c) damage

Figure D-23: Rainflow cycle counting for mode 3 nodal diameter 0 with a) amplitude and mean values b) rainflow matrix and c) damage

Figure D-24: Rainflow cycle counting for mode 3 nodal diameter 1 with a) amplitude and mean values b) rainflow matrix and c) damage
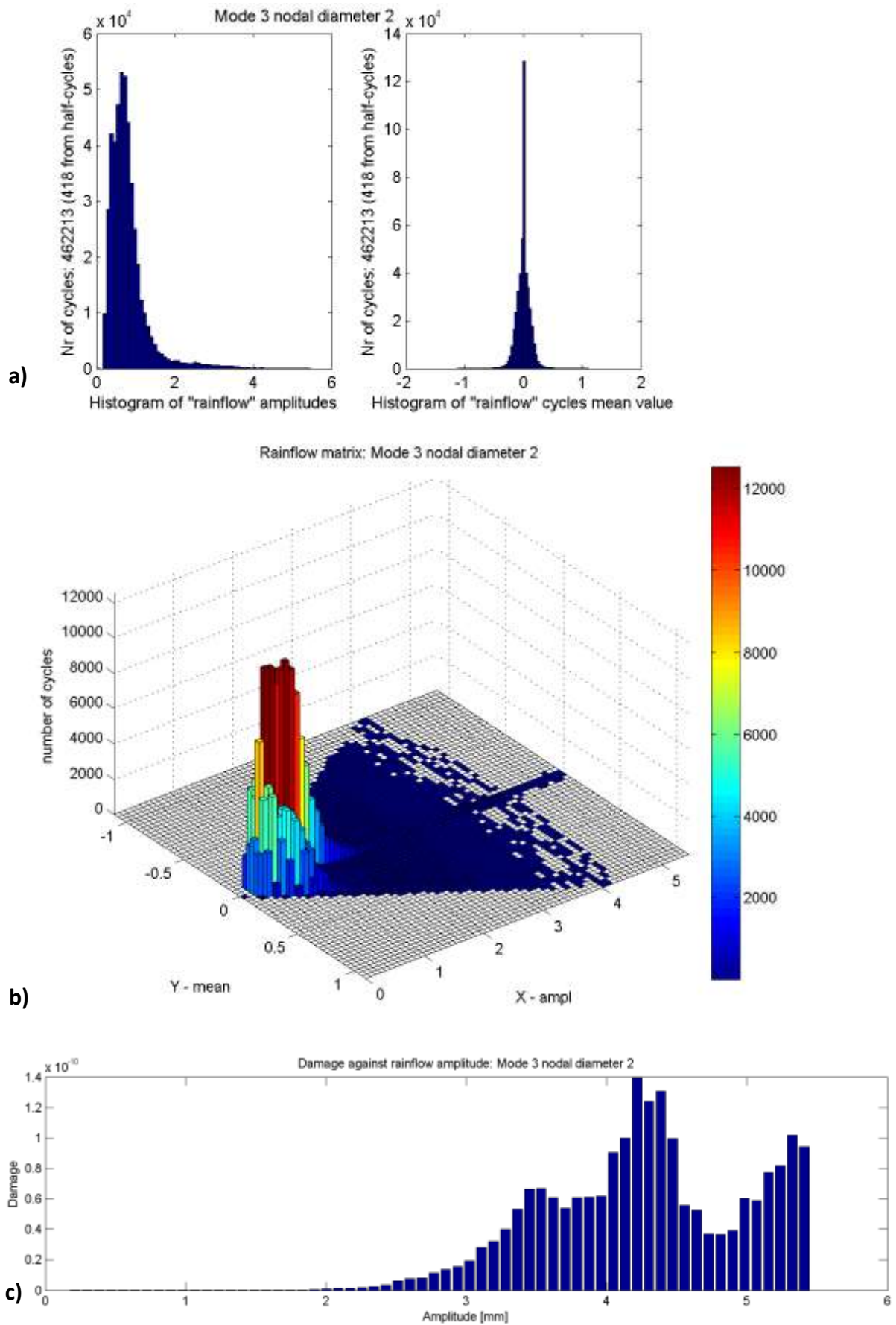
Figure D-25: Rainflow cycle counting for mode 3 nodal diameter 2 with a) amplitude and mean values b) rainflow matrix and c) damage
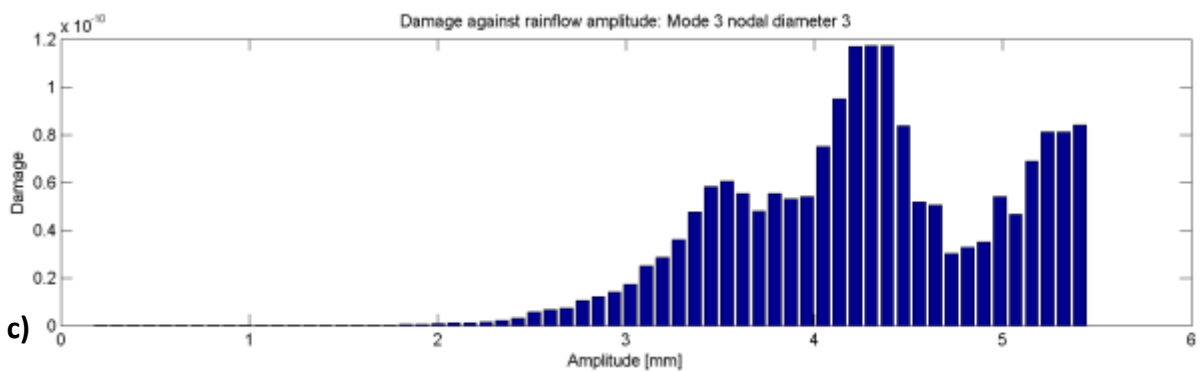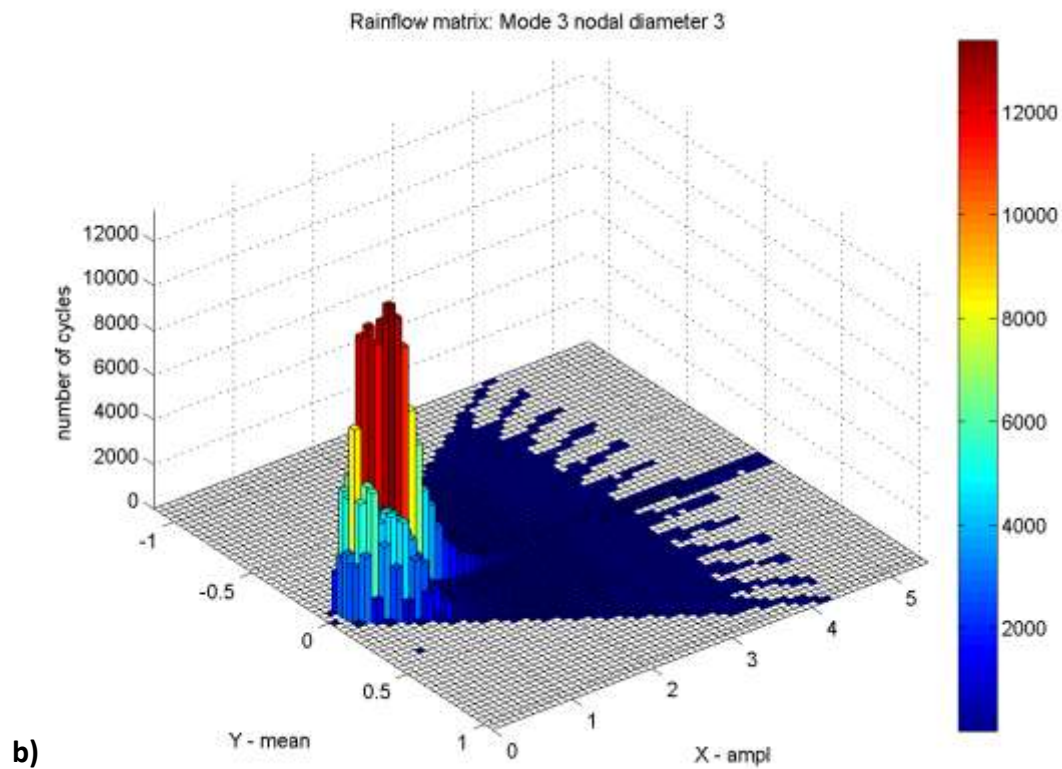
Figure D-26: Rainflow cycle counting for mode 3 nodal diameter 3 with a) amplitude and mean values b) rainflow matrix and c) damage

Figure D-27: Rainflow cycle counting for mode 3 nodal diameter 4 with a) amplitude and mean values b) rainflow matrix and c) damage

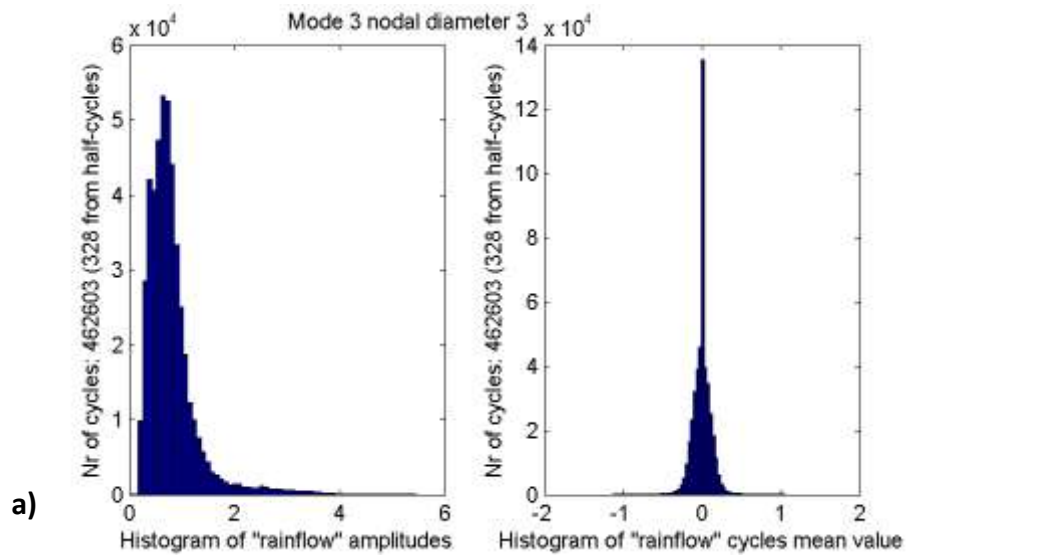**Figure D-28:** Rainflow cycle counting for mode 3 nodal diameter 5 with a) amplitude and mean values b) rainflow matrix and c) damage
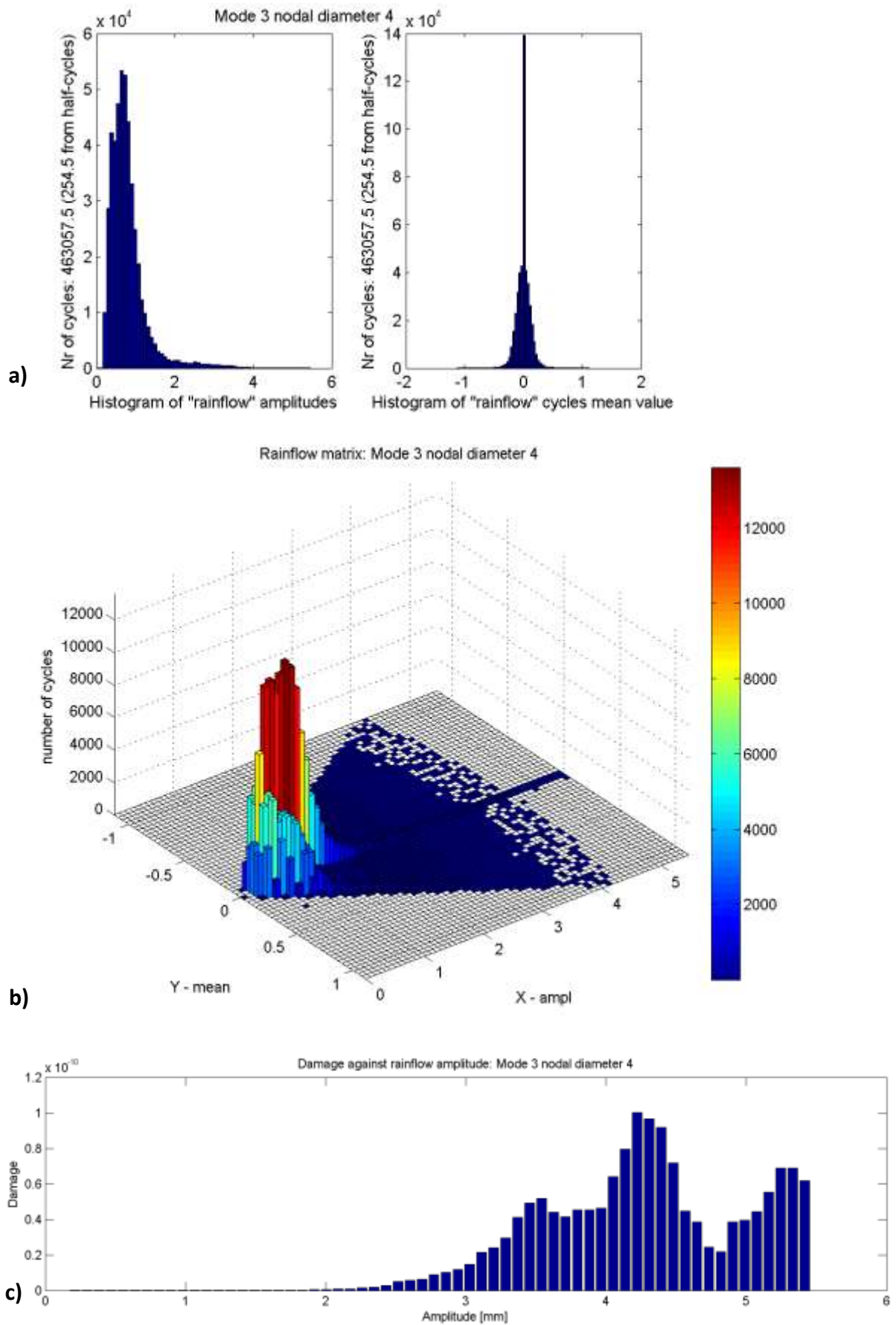
Figure D-29: Rainflow cycle counting for mode 3 nodal diameter 6 with a) amplitude and mean values b) rainflow matrix and c) damage
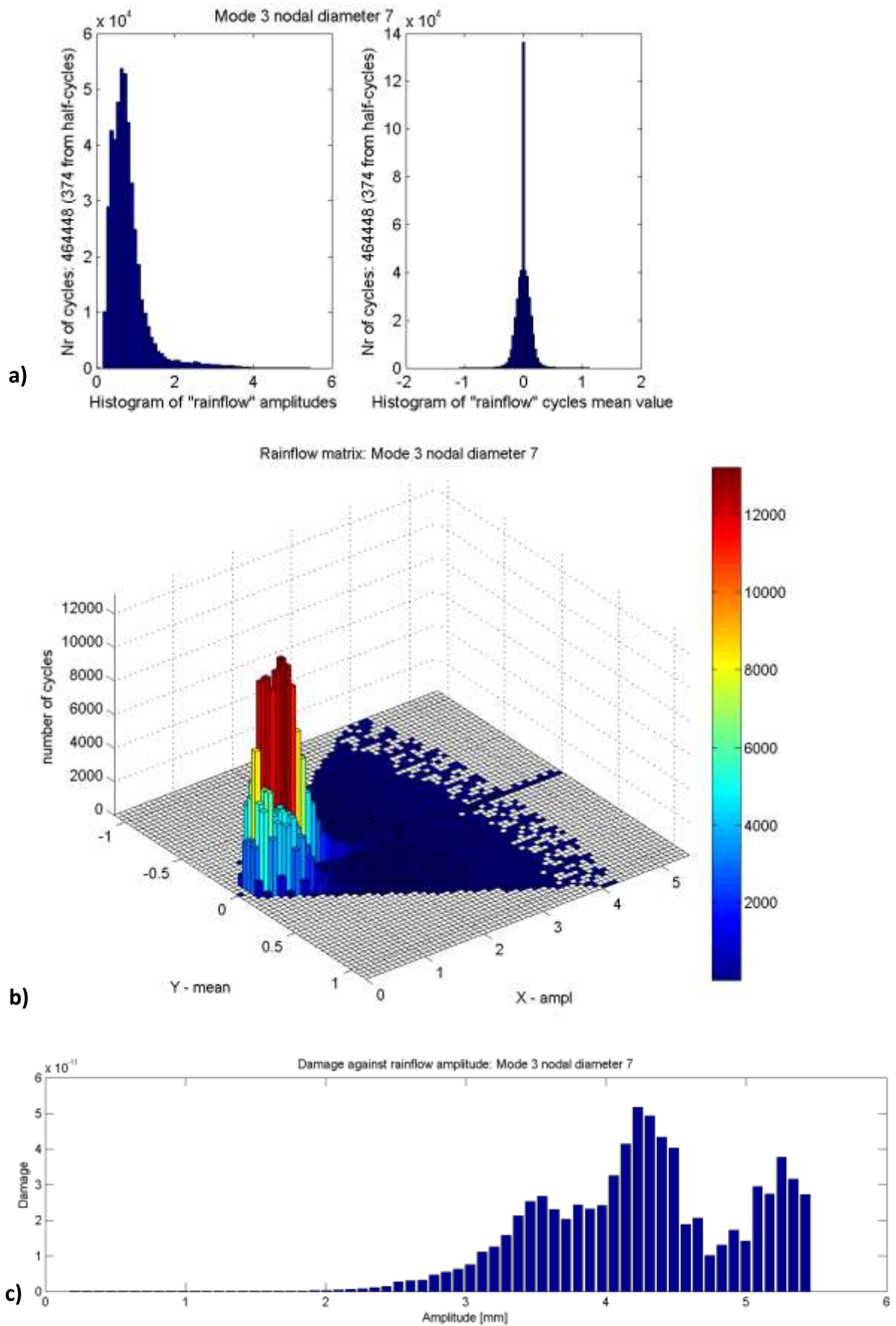
Figure D-30: Rainflow cycle counting for mode 3 nodal diameter 7 with a) amplitude and mean values b) rainflow matrix and c) damage
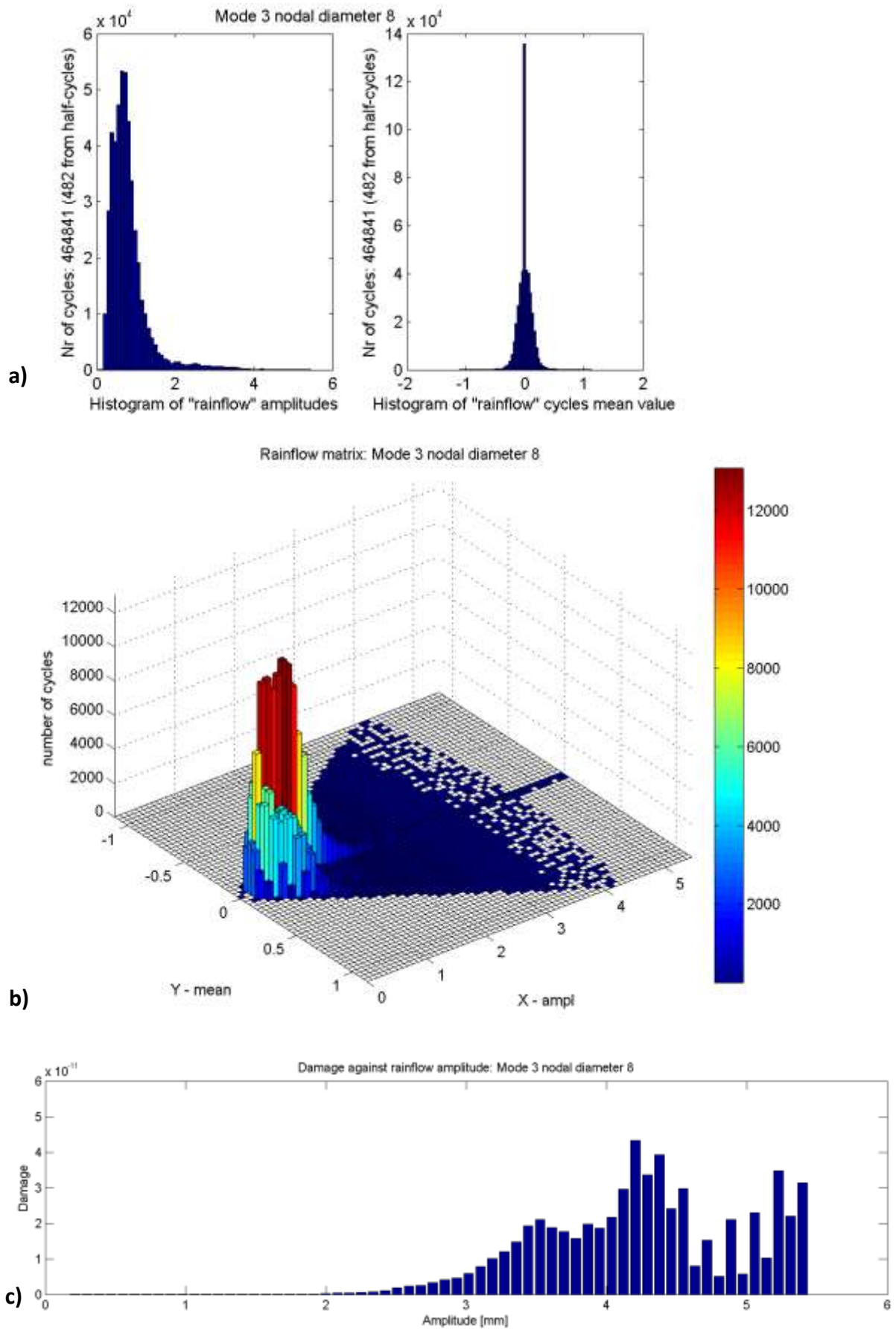
Figure D-31: Rainflow cycle counting for mode 3 nodal diameter 8 with a) amplitude and mean values b) rainflow matrix and c) damage
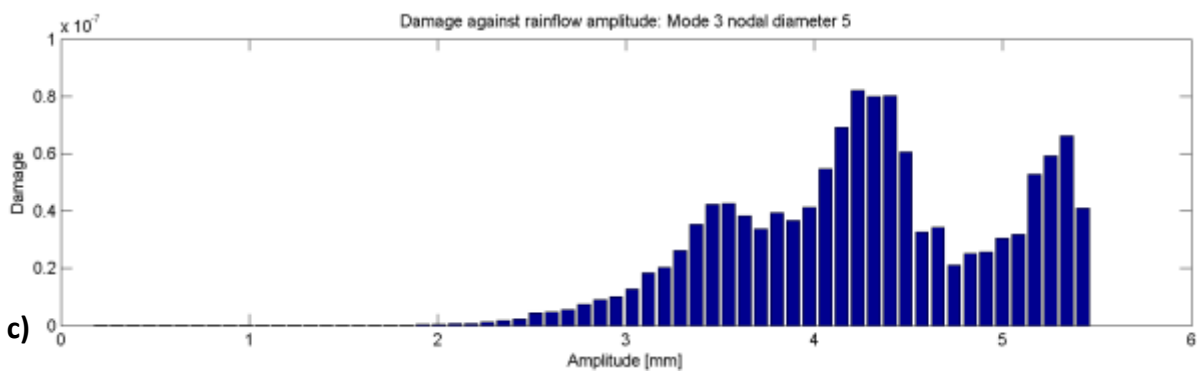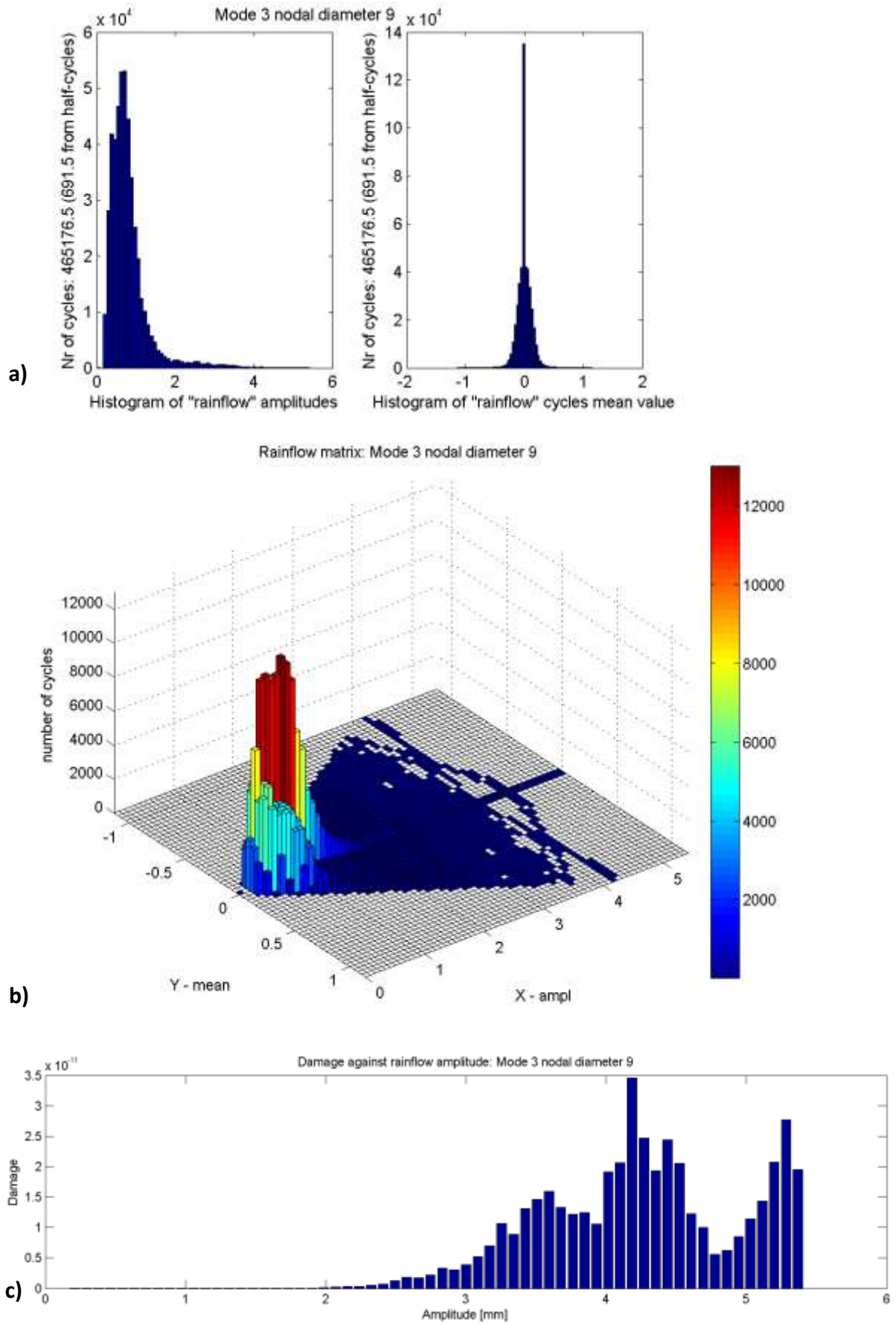
Figure D-32: Rainflow cycle counting for mode 3 nodal diameter 9 with a) amplitude and mean values b) rainflow matrix and c) damage

Figure D-33: Rainflow cycle counting for mode 3 nodal diameter 10 with a) amplitude and mean values b) rainflow matrix and c) damage

Figure D-34: Rainflow cycle counting for mode 4 nodal diameter 0 with a) amplitude and mean values b) rainflow matrix and c) damage
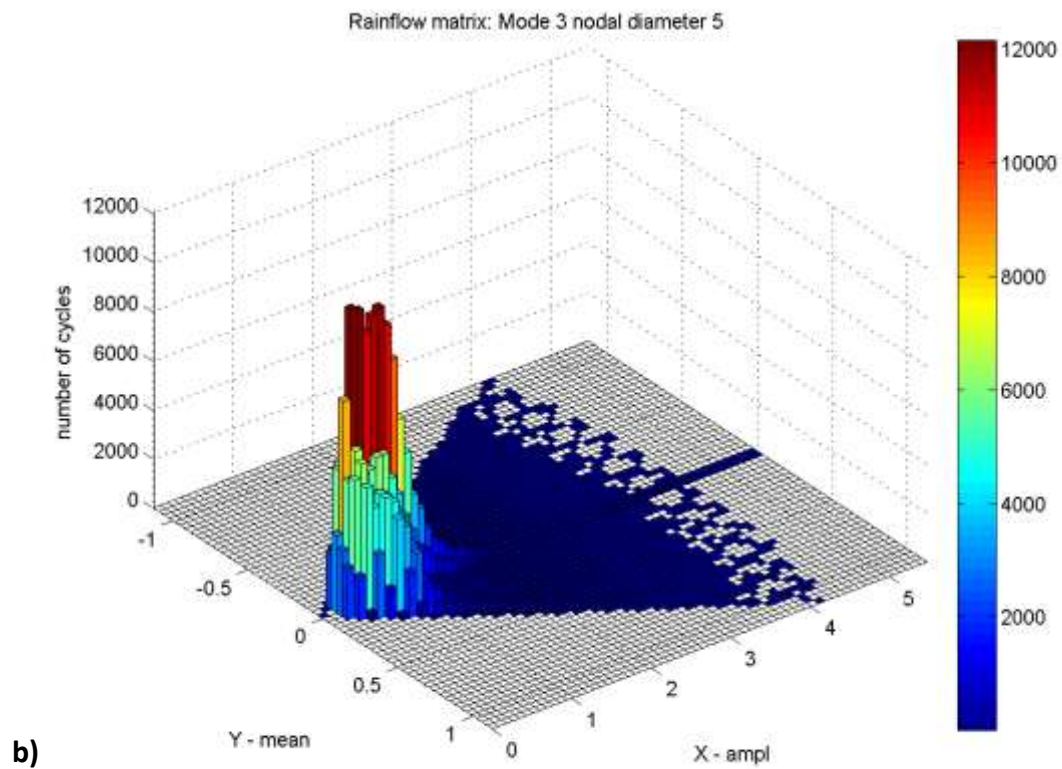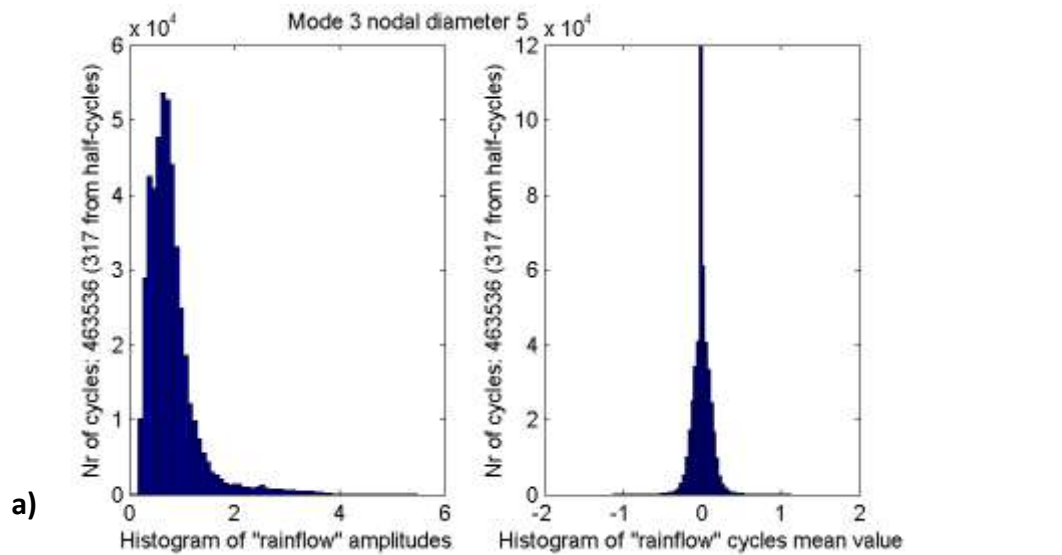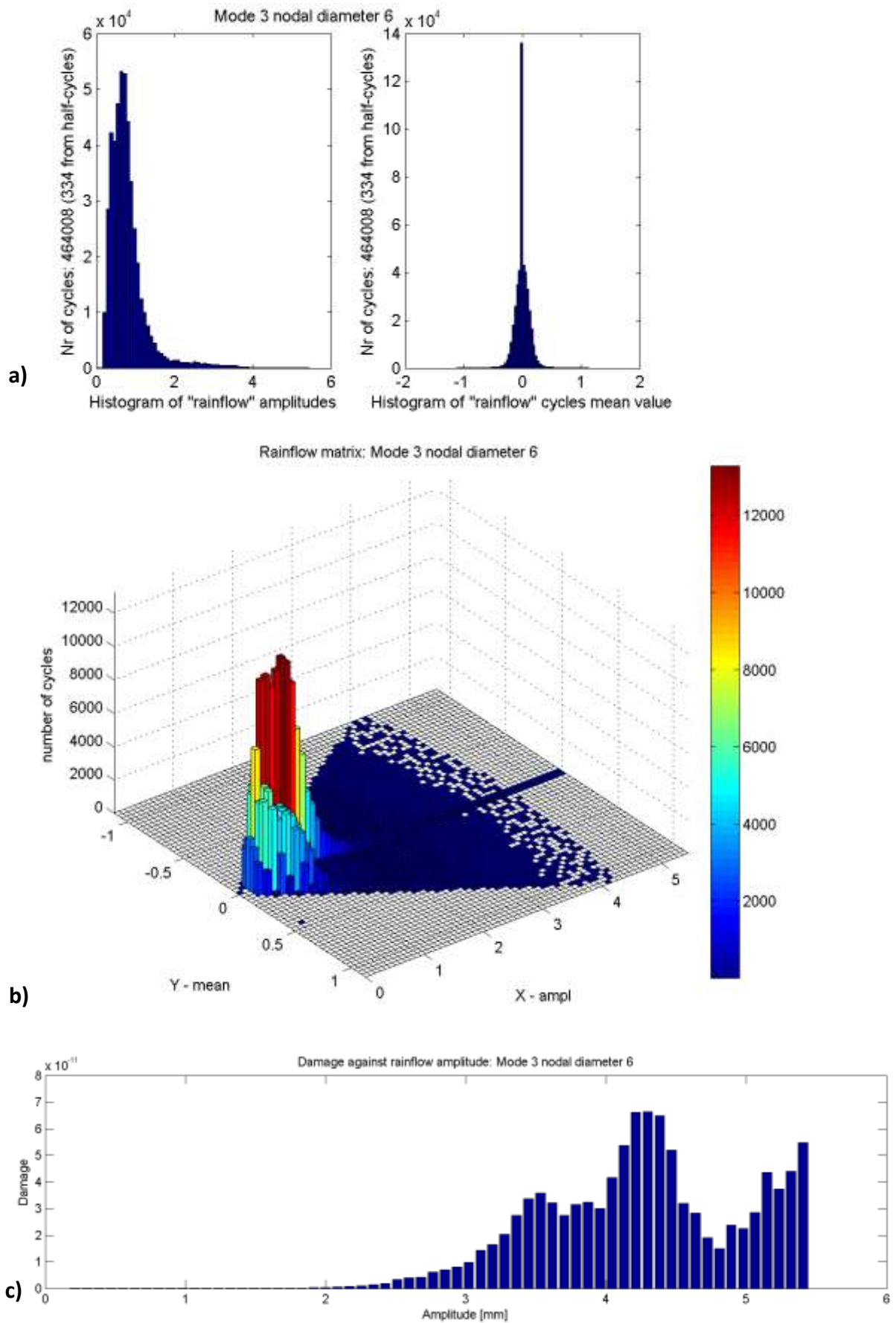
© University of Pretoria
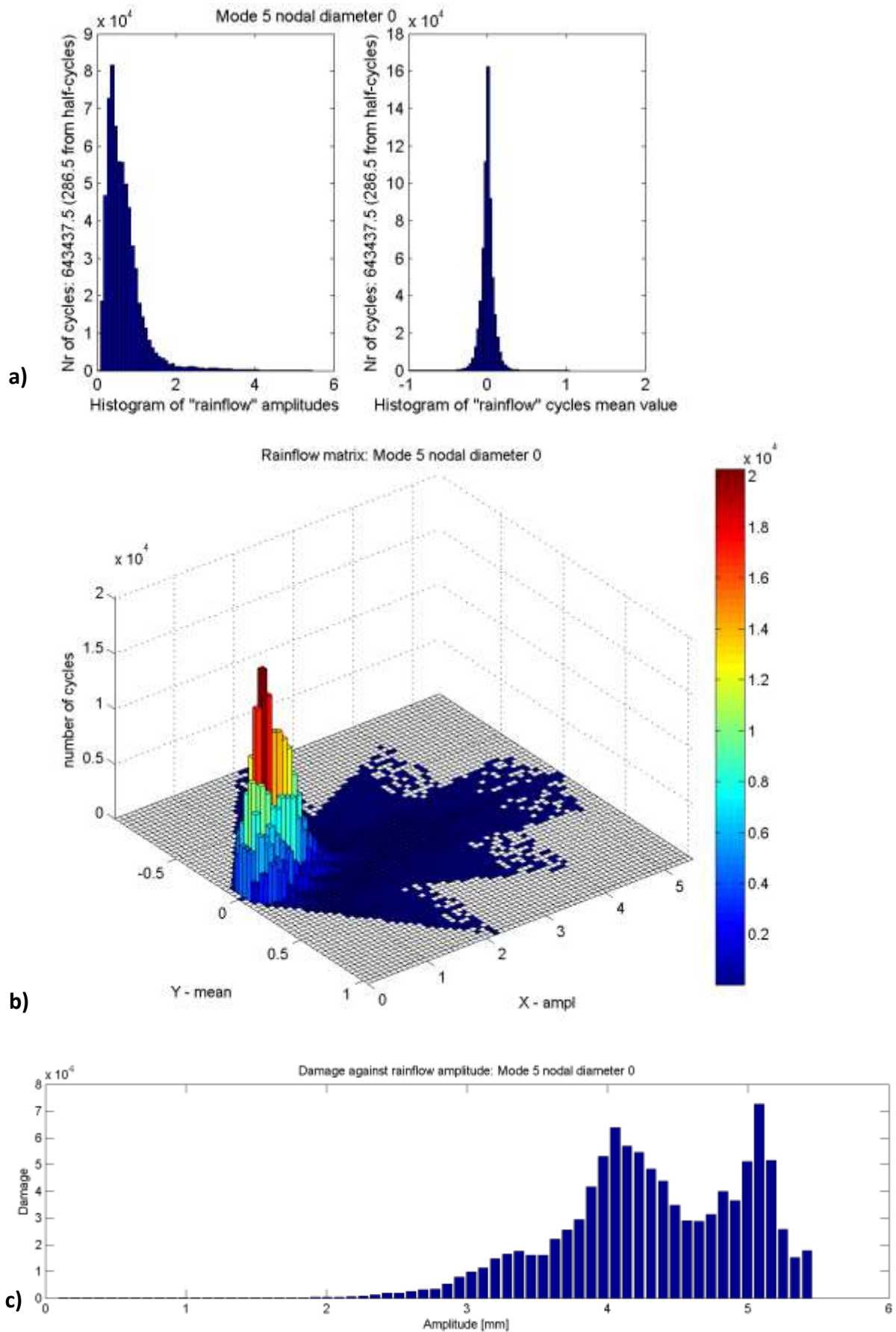
Figure D-35: Rainflow cycle counting for mode 5 nodal diameter 0 with a) amplitude and mean values b) rainflow matrix and c) damage
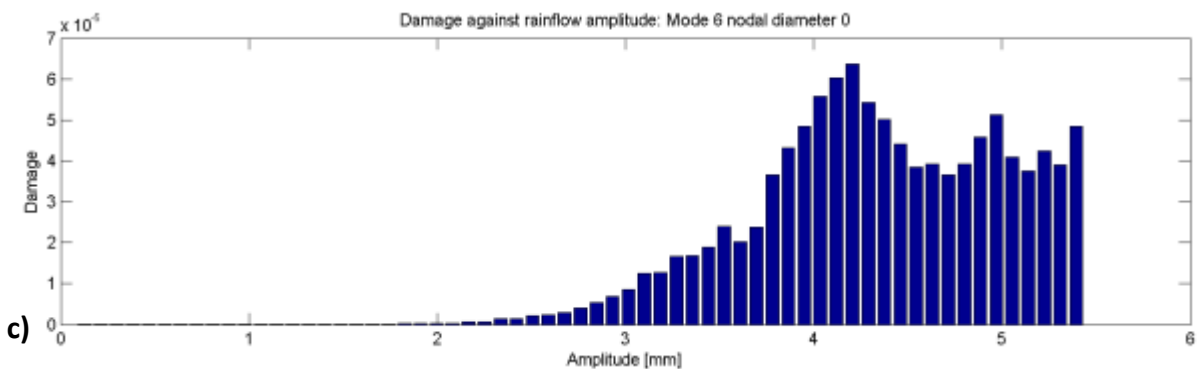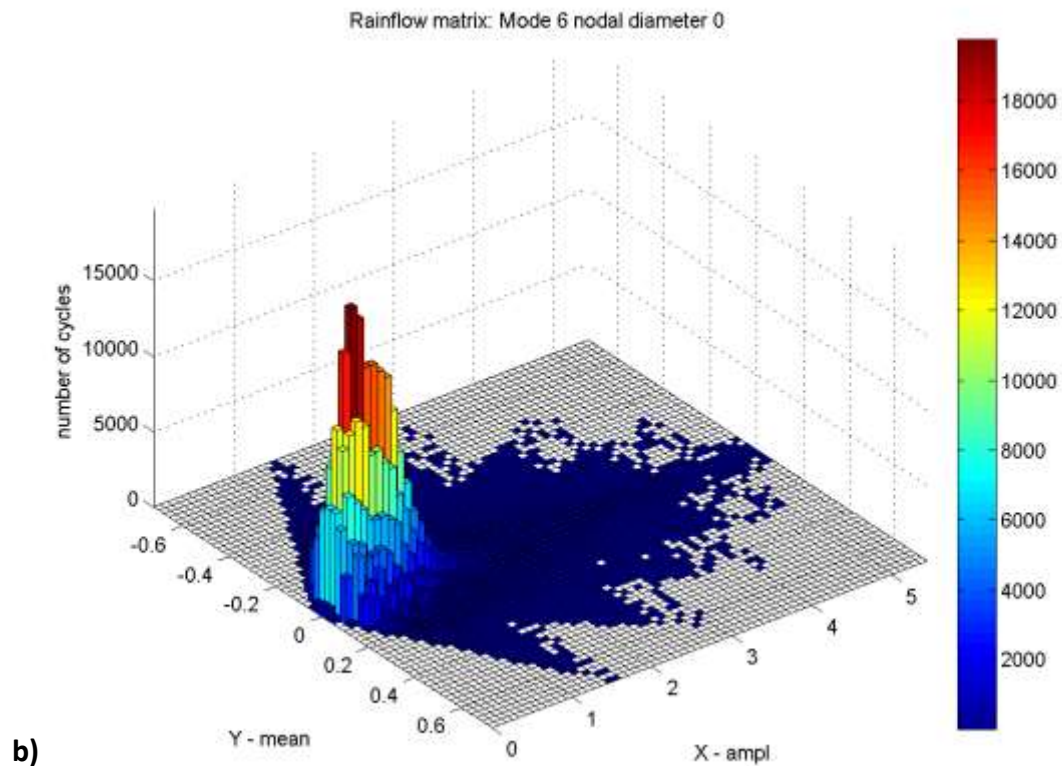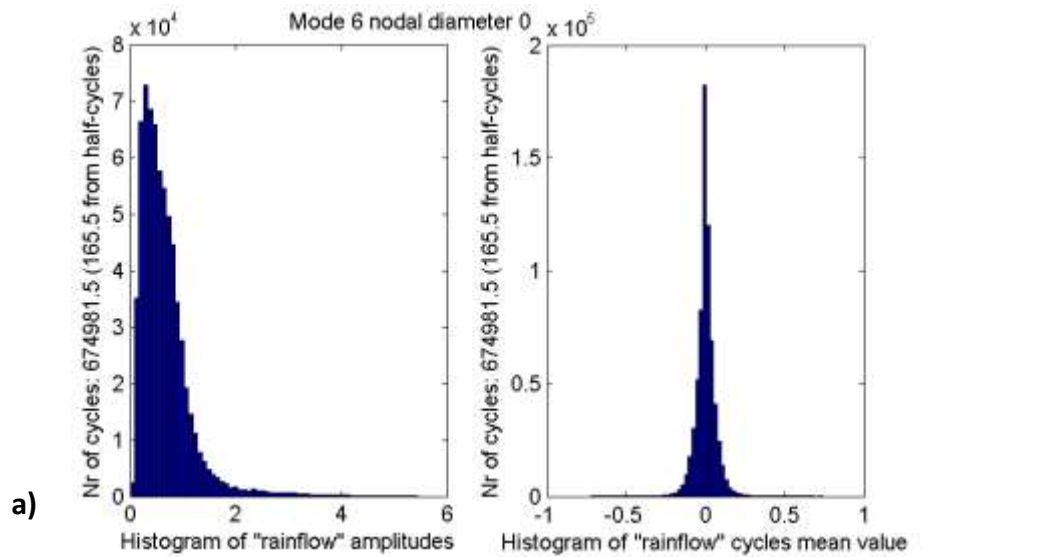
Figure D-36: Rainflow cycle counting for mode 6 nodal diameter 0 with a) amplitude and mean values b) rainflow matrix and c) damage
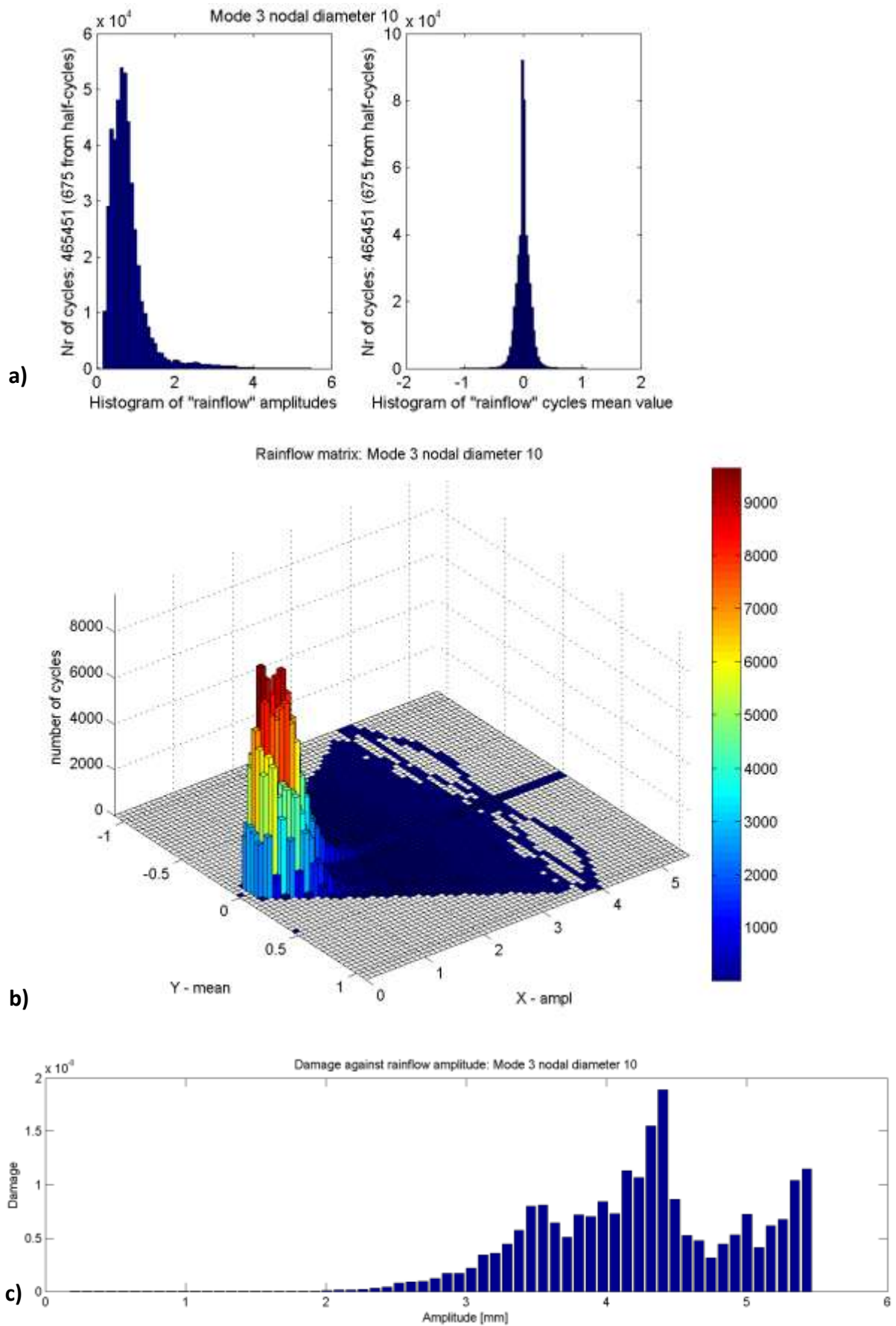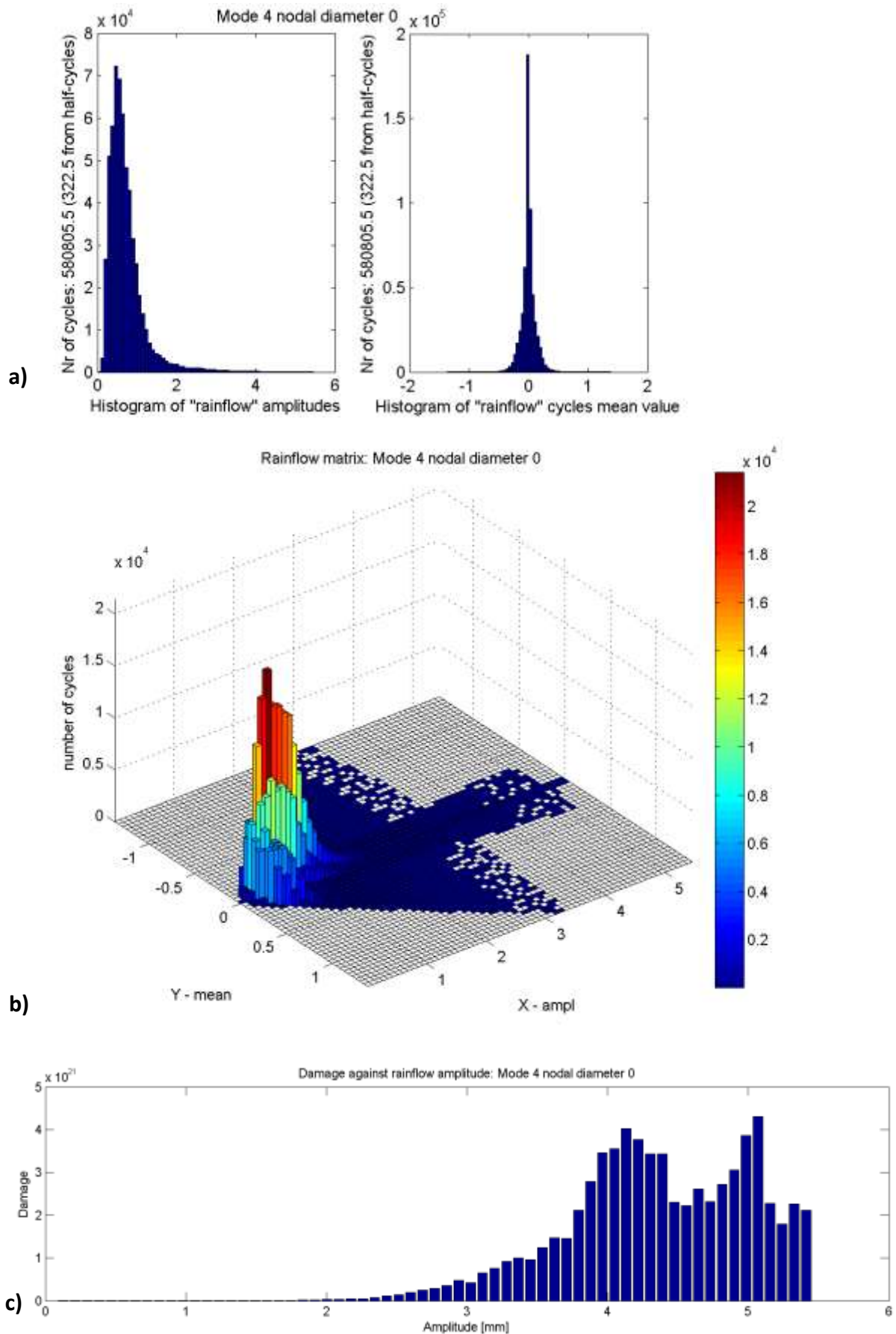
Appendix E

MATLAB Code

E.1 Hysteresis loop

```matlab
% Ramberg Osgood equitions for elastic and plastic analysis
clear all;
close all;
clc;

%FV566 UML 350 deg
E=213000;       % Young's Modulus [MPa]
SF=2070;        % Fatigeu Strenght coeficient [MPa]
b=-0.087;       % Fatigue elastic exponent
Ef=0.333433;    % Fatigue ductile coeficient
c=-0.58;        % Fatigue ductile exponent

% Sweepable 3600 600 LE
Smax=2767.5;        % Max principle from FEA @3600rpm [MPa]
Smin=-80;           % min principle from M. Newby shot peening @3600rpm [MPa]

Smaxo=1826.5;       % Max principle from FEA @3000rpm [MPa]
Smino=-80;          % min principle from M. Newby shot peening @3000rpm [MPa]

[x,y] = CalcHist(E,SF,b,c,Smax,Smin,Smaxo,Smino);

figure(10)   % Plot sigma-E curve
hold on
plot(x,y,'b','LineWidth',2)
title('Stress strain curve')
xlabel('\epsilon');
ylabel('\sigma (MPa)');
legend('UML 350','\sigma_m','(\sigma_{min},\epsilon_{min})','Overspeed','Normal Operation')
grid on
hold off

% FV566 Extended UML 350 deg
E=213000;                   % Young's Modulus [MPa]
SF=2187.66031291651;        % Fatigeu Strenght coeficient [MPa]
b=-0.097;                   % Fatigue elastic exponent
Ef=0.349451435863461;       % Fatigue ductile coeficient
c=-0.58;                    % Fatigue ductile exponent

[x,y] = CalcHist(E,SF,b,c,Smax,Smin,Smaxo,Smino);

% Plot sigma-E curve
figure(10)
hold on
plot(x,y,'b-.')
hold off

% FV566 UML 600 deg
E=213000;           % Young's Modulus [MPa]
SF=1710;            % Fatigeu Strenght coeficient [MPa]
```

```matlab
b=-0.087;           % Fatigue elastic exponent
Ef=0.4165316901;    % Fatigue ductile coeficient
c=-0.58;            % Fatigue ductile exponent

[x,y] = CalcHist(E,SF,b,c,Smax,Smin,Smaxo,Smino);

% Plot sigma-E curve
figure(10)
hold on
plot(x,y,'r','LineWidth',2)
hold off


% FV566 Extended UML 600 deg
E=213000;           % Young's Modulus [MPa]
SF=1990.287767;     % Fatigeu Strenght coeficient [MPa]
b=-0.0990539803;    % Fatigue elastic exponent
Ef=0.4426025481;    % Fatigue ductile coeficient
c=-0.58;            % Fatigue ductile exponent

[x,y] = CalcHist(E,SF,b,c,Smax,Smin,Smaxo,Smino);

% Plot sigma-E curve
figure(10)
hold on
plot(x,y,'r-.')
hold off


% FV566 UML 650 deg
E=213000;       % Young's Modulus [MPa]
SF=1523;        % Fatigeu Strenght coeficient [MPa]
b=-0.087;       % Fatigue elastic exponent
Ef=0.46;        % Fatigue ductile coeficient
c=-0.58;        % Fatigue ductile exponent

[x,y] = CalcHist(E,SF,b,c,Smax,Smin,Smaxo,Smino);

% Plot sigma-E curve
figure(10)
hold on
plot(x,y,'g','LineWidth',2)
hold off


% FV566 Extended UML 650 deg
E=213000;       % Young's Modulus [MPa]
SF=1847;        % Fatigeu Strenght coeficient [MPa]
b=-0.1000688;   % Fatigue elastic exponent
Ef=0.485;       % Fatigue ductile coeficient
c=-0.58;        % Fatigue ductile exponent

[x,y] = CalcHist(E,SF,b,c,Smax,Smin,Smaxo,Smino);

% Plot sigma-E curve
figure(10)
hold on
plot(x,y,'g-.')
hold off
```

```
legend('UML 350 \circC','Extended UML 350 \circC','UML 600 \circC','Extended UML 600
\circC','UML 650 \circC','Extended UML 650 \circC')
```

```
function [EE,S] = CalcHist(E,SF,b,c,Smax,Smin,Smaxo,Smino)

n=b/c      % Strain hardening exponent

Sa=(Smax-Smin)/2;
Sao=(Smaxo-Smino)/2;

Stress=@(sig) (sig^2+sig*E*((sig/SF)^(1/n)))^0.5;    % equation 13.61 in Dowling
Strain=@(sig) sig/E+(sig/SF)^(1/n);       % Ramberg osgood equiation 14.1 in Dowling

% Iteratively solve the maximum stress and stress amplitude for overspeed
sig_max=fsolve(@(sig) Stress(sig)-Smax,Smax-100); sig_max
sig_a=fsolve(@(sig) Stress(sig)-Sa,Smax-100); sig_a

sig_m=sig_max-sig_a        % mean stress
sig_min=sig_max-2*sig_a    % min stress

% Get corresponding strain for sig_max, sig_a, sig_m for overspeed
Ep_max=Strain(sig_max)
Ep_a=Strain(sig_a)
Ep_m=Ep_max-Ep_a
Ep_min=Ep_max-2*Ep_a

% Calculate the strain curve for overspeed
sig=linspace(0,sig_max,1000);
sigm=linspace(0,sig_a*2,1000);

for k=1:length(sig)
    Ep(k)=Strain(sig(k));
    Epm(k)=2*Strain(sigm(k)/2); % fig 12.14 in Dowling
end

% Calculate relaxaton from overspeed
Ep_down=Ep_max-Epm;
Sig_down=sig_max-sigm;

% Iteratively solve the maximum stress and stress amplitude for normal
% operation without residual correction
sig_maxo=fsolve(@(sig) Stress(sig)-Smaxo,Smaxo-100); sig_maxo
sig_ao=fsolve(@(sig) Stress(sig)-Sao,Smaxo-100); sig_ao

sig_mo=sig_maxo-sig_ao        % mean stress
sig_mino=sig_maxo-2*sig_ao    % min stress

% Get corresponding strain for sig_maxo, sig_ao, sig_mo form normal
% operation
Ep_maxo=Strain(sig_maxo)
Ep_ao=Strain(sig_ao)
Ep_mo=Ep_maxo-Ep_ao
Ep_mino=Ep_maxo-2*Ep_ao

% Calculate the strain curve for normal operation
```

```
sigo=linspace(0,sig_maxo,1000);
sigmo=linspace(0,sig_ao*2,1000);

for k=1:length(sig)
    Epo(k)=Strain(sigo(k));
    Epmo(k)=2*Strain(sigmo(k)/2); % fig 12.14 in Dowling
end

% Do residual stress correction
Ep_upo=Ep_min+Epmo;
Sig_upo=sig_min+sigmo;
Ep_maxo=Ep_upo(length(Ep_upo))
sig_maxo=Sig_upo(length(Sig_upo))
sig_ao=(sig_maxo-sig_min)/2
sig_mo=sig_maxo-sig_ao          % mean stress
sig_mino=sig_maxo-2*sig_ao      % min stress
Ep_ao=Strain(sig_ao)
Ep_mo=Ep_maxo-Ep_ao
Ep_mino=Ep_maxo-2*Ep_ao

% Calculate relaxaton from normal operation
Ep_downo=Ep_maxo-Epmo;
Sig_downo=sig_maxo-sigmo;

EE=[Ep,Ep_down,Ep_upo,Ep_downo]
S=[sig,Sig_down,Sig_upo,Sig_downo]

end
```


Stress strain curve
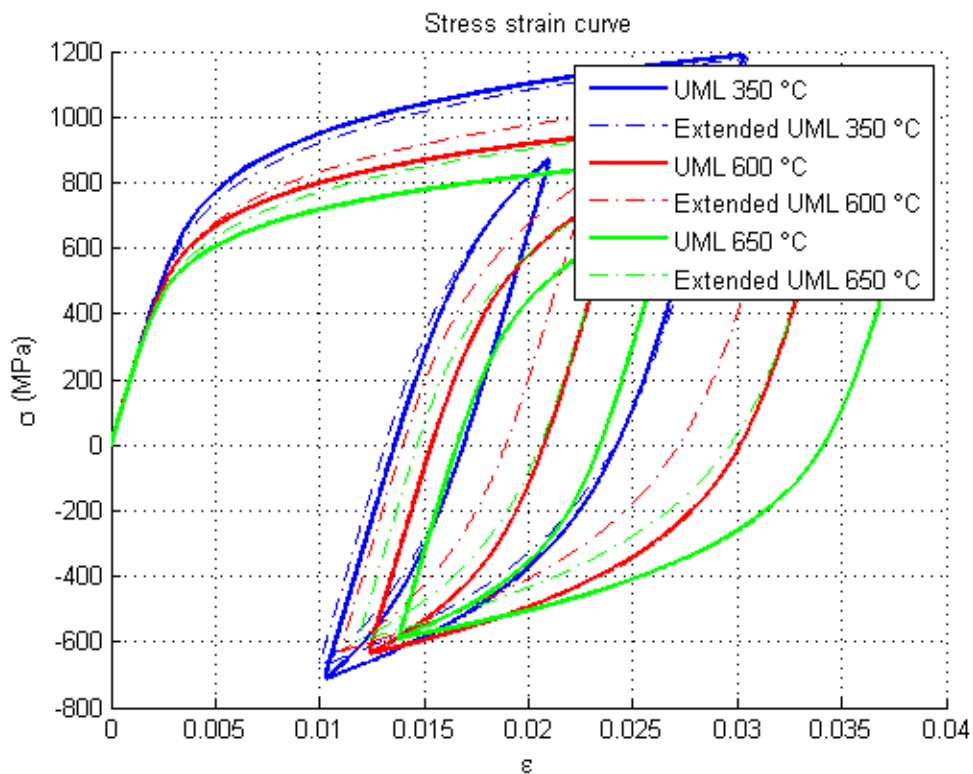
Published with MATLAB® R2013a

E.2 SN and εN Curves

```matlab
% Plot elastic, plastic and total SN curves
clear all;
close all;
clc;

%FV566 UML 350 deg
E=213000;      % Young's Modulus [MPa]
Sf=2070;       % Fatigeu Strenght coeficient [MPa]
b=-0.087;      % Fatigue elastic exponent
Ef=0.333433;   % Fatigue ductile coeficient
c=-0.58;       % Fatigue ductile exponent

[Ee,Ep,ET,Nt,Et,Nf] = SN( E,Sf,b,Ef,c );

figure(1)
loglog(Nf,Ee,'b:',Nf,Ep,'b-.',Nf,ET,'b-',Nt,Et,'bo')
title('\epsilon-N curve')
ylabel('\epsilon /2');
xlabel('2Nf [cycles]');
legend('Stress Life','Strain Life','Total Life','Elastic to plastic transition')

%FV566 Extended UML 350 deg
E=213000;                  % Young's Modulus [MPa]
Sf=2187.66031291651;       % Fatigeu Strenght coeficient [MPa]
b=-0.097;                  % Fatigue elastic exponent
Ef=0.349451435863461;      % Fatigue ductile coeficient
c=-0.58;                   % Fatigue ductile exponent

[Ee,Ep,ET,Nt,Et,Nf] = SN( E,Sf,b,Ef,c );

figure(1)
hold on
loglog(Nf,Ee,'r:',Nf,Ep,'r-.',Nf,ET,'r-',Nt,Et,'ro')
hold off

%FV566 UML 600 deg
E=213000;          % Young's Modulus [MPa]
Sf=1710;           % Fatigeu Strenght coeficient [MPa]
b=-0.087;          % Fatigue elastic exponent
Ef=0.4165316901;   % Fatigue ductile coeficient
c=-0.58;           % Fatigue ductile exponent

[Ee,Ep,ET,Nt,Et,Nf] = SN( E,Sf,b,Ef,c );

figure(1)
hold on
loglog(Nf,Ee,'g:',Nf,Ep,'g-.',Nf,ET,'g-',Nt,Et,'go')
hold off

%FV566 Extended UML 600 deg
E=213000;          % Young's Modulus [MPa]
Sf=1990.287767;    % Fatigeu Strenght coeficient [MPa]
b=-0.0990539803;   % Fatigue elastic exponent
Ef=0.4426025481;   % Fatigue ductile coeficient
c=-0.58;           % Fatigue ductile exponent
```

```matlab
[Ee,Ep,ET,Nt,Et,Nf] = SN( E,Sf,b,Ef,c );

figure(1)
hold on
loglog(Nf,Ee,'k:',Nf,Ep,'k-.',Nf,ET,'k-',Nt,Et,'ko')
hold off

%FV566 UML 650 deg
E=213000;          % Young's Modulus [MPa]
Sf=1523;           % Fatigeu Strenght coeficient [MPa]
b=-0.087;          % Fatigue elastic exponent
Ef=0.46;           % Fatigue ductile coeficient
c=-0.58;           % Fatigue ductile exponent

[Ee,Ep,ET,Nt,Et,Nf] = SN( E,Sf,b,Ef,c );

figure(1)
hold on
loglog(Nf,Ee,'c:',Nf,Ep,'c-.',Nf,ET,'c-',Nt,Et,'co')
hold off

%FV566 Extended UML 650 deg
E=213000;          % Young's Modulus [MPa]
Sf=1847;           % Fatigeu Strenght coeficient [MPa]
b=-0.1000688;      % Fatigue elastic exponent
Ef=0.485;          % Fatigue ductile coeficient
c=-0.58;           % Fatigue ductile exponent

[Ee,Ep,ET,Nt,Et,Nf] = SN( E,Sf,b,Ef,c );

figure(1)
hold on
loglog(Nf,Ee,'m:',Nf,Ep,'m-.',Nf,ET,'m-',Nt,Et,'mo')
hold off

figure(2)
plot(Nf,Ee,'b',Nf,Ep,'r',Nf,ET,'g',Nt,Et,'k',Nf,Ee,'c',Nf,Ep,'m')
legend('UML 350 \circC','Extended UML 350 \circC','UML 600 \circC','Extended UML 600
\circC','UML 650 \circC','Extended UML 650 \circC')
```

```matlab
function [Ee,Ep,ET,Nt,Et,Nf] = SN( E,Sf,b,Ef,c )
%UNTITLED Summary of this function goes here
%   Detailed explanation goes here

Nf = logspace(0,10,1000);

for i=1:length(Nf)
    Ee(i)=Sf/E*(Nf(i))^b;      % Stress life
    Ep(i)=Ef*(Nf(i))^c;        % Strain life
    ET(i)=Ee(i)+Ep(i);         % Total life
end

Nt = (Ef*E/Sf)^(1/(b-c))
Et=Sf/E*(Nt)^b + Ef*(Nt)^c
```
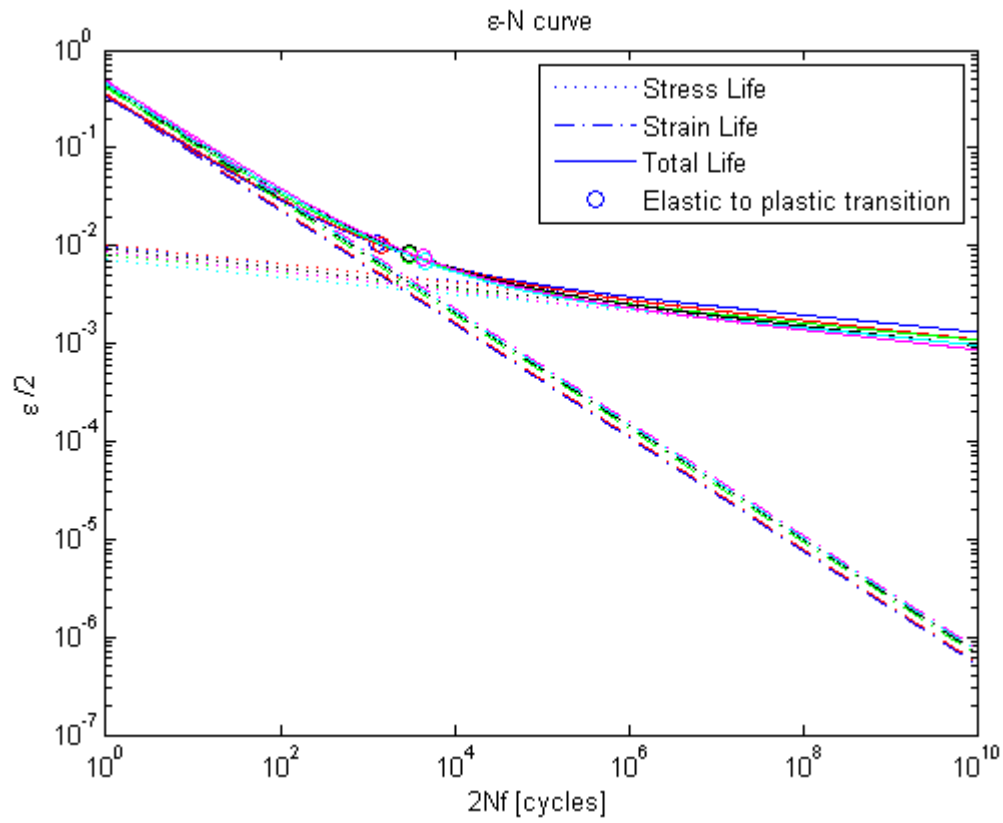
ε-N curve

Published with MATLAB® R2013a

© University of Pretoria

E.3 Ramberg Oswald for plastic correction

```matlab
clc
clear all
close all

%% Set up General Properties

delimiter = '\t';
formatSpec = '%f%f%[^\n\r]';
startRow = 2;

%% Set up Fatigue Properties

%  UML 600 degrees
E=213000;          % Young's Modulus [MPa]
Sf=1710;           % Fatigeu Strenght coeficient [MPa]
b=-0.087;          % Fatigue elastic exponent
Ef=0.4165316901;   % Fatigue ductile coeficient
c=-0.58;           % Fatigue ductile exponent
n=b/c;             % Strain hardening exponent
H=Sf/(Ef)^n;       % cyclic strenght coeficient

%FV566 Extended UML 600 deg
E=213000;          % Young's Modulus [MPa]
Sf=1990.287767;    % Fatigeu Strenght coeficient [MPa]
b=-0.0990539803;   % Fatigue elastic exponent
Ef=0.4426025481;   % Fatigue ductile coeficient
c=-0.58;           % Fatigue ductile exponent
n=b/c;             % Strain hardening exponent
H=Sf/(Ef)^n;       % cyclic strenght coeficient

%% Import Data

% Import data from Fatique3600_600   Worksheet: Sweepable   For a fixed number of rows

[~, ~, raw0_0] = xlsread('Fatigue3600_600deg_LE_EUML.xlsx','Sweepable','A4:A76');
[~, ~, raw0_1] = xlsread('Fatigue3600_600deg_LE_EUML.xlsx','Sweepable','D4:D76');
[~, ~, raw0_2] = xlsread('Fatigue3600_600deg_LE_EUML.xlsx','Sweepable','U4:U76');
raw = [raw0_0,raw0_1,raw0_2];
raw(cellfun(@(x) ~isempty(x) && isnumeric(x) && isnan(x),raw)) = {''};
cellVectors = raw(:,1);
raw = raw(:,[2,3]);

% Replace non-numeric cells with NaN and create dataset array
R = cellfun(@(x) ~isnumeric(x) && ~islogical(x),raw);   % Find non-numeric cells
raw(R) = {NaN};      % Replace non-numeric cells
data = reshape([raw{:}],size(raw));           % Create output variable
fatqData = dataset;      % Create dataset array

% Allocate imported array to column variable names
fatqData.Name = cellVectors(:,1);
fatqData.FreqHz = data(:,1);
fatqData.CorrectionFactor = data(:,2);

% Clear temporary variables
clearvars data raw raw0_0 raw0_1 raw0_2 cellVectors R;
```

```matlab
dataArray=xlsread('Corrected_LE_3600_600deg_EUML.xlsx');
filename = 'Corrected_LE_3600_600deg_UML.xlsx';
fileID = fopen(filename,'r');
dataArray = textscan(fileID, formatSpec, 'Delimiter', delimiter, 'EmptyValue'
,NaN,'HeaderLines' ,startRow-1, 'ReturnOnError', false);
NodeMean = dataArray{:, 1};
Mean = dataArray{:, 4};
NodeMean = dataArray(:, 1);
Mean = dataArray(:, 4);

%% Fatigue Calculations

numFatq = numel(fatqData.Name);
for fatqCalcI = 1:numFatq

    % Import Stress Data
    filename = [fatqData.Name{fatqCalcI},'.txt'];  % filename = 'M1H0.txt';
    fileID = fopen(filename,'r');
    if fileID ~= -1
        dataArray = textscan(fileID, formatSpec, 'Delimiter', delimiter, 'EmptyValue'
,NaN,'HeaderLines' ,startRow-1, 'ReturnOnError', false);
        fclose(fileID);
        Node = dataArray{:, 1};
        maxPrinciple = dataArray{:, 2};

        % Calculations
        corFact = fatqData.CorrectionFactor(fatqCalcI);
        freq = fatqData.FreqHz(fatqCalcI);
        CorrectedDynamic = maxPrinciple*corFact;
        StressLife = 0.5*(CorrectedDynamic/Sf).^(1/b);
        MeanStressCorrection = (1-Mean/Sf).^-(1/b);
        StressLifeCor = StressLife.*MeanStressCorrection/freq;
        LifeHr = StressLifeCor/3600;
        LifeDays = LifeHr/24;
        LifeYears = LifeDays/365;

        % Write Results back to Fatigue Workbook
        resultNames =
{'NodeMean','Mean','NodeM1H0','M1H0','CorrectedDynamic','StressLife','MeanStressCorrection','
StressLifeCor','LifeHr','LifeDays','LifeYears'};
        result =
[NodeMean,Mean,Node,maxPrinciple,CorrectedDynamic,StressLife,MeanStressCorrection,StressLifeC
or,LifeHr,LifeDays,LifeYears];
        lastCol = numel(result(1,:));
        resultSorted = sortrows(result,lastCol);
        resultCell = [resultNames;num2cell(resultSorted)];

xlswrite('Fatigue3600_600deg_LE_EUML.xlsx',resultCell(1:100,:),fatqData.Name{fatqCalcI})
    end
end
```

Published with MATLAB® R2013a

E.4 Rainflow cycle counting

```
clc
clear all
close all

%FV566 Extended UML 600 deg
E=213000;           % Young's Modulus [MPa]
Sf=1990.287767;     % Fatigue Strenght coeficient [MPa]
b=-0.0990539803;    % Fatigue elastic exponent
Ef=0.4426025481;    % Fatigue ductile coeficient
c=-0.58;            % Fatigue ductile exponent
n=b/c;              % Strain hardening exponent
H=Sf/(Ef)^n;        % cyclic strenght coeficient

%% Import GE Supplied Data

dataArray = xlsread('D:\MyDocuments\MEng\Duvha\8_Measurements\LD66 LSB vibration data
2010_original.xlsx','Data');
x = length(dataArray(:,1));
GE_time = linspace(0,x,x)';
GE_displacement = dataArray(:,4);
Peak = GE_displacement*sqrt(2);    % convert from rms to peak
t = linspace(0,x,x*1000)';          % resample time
ts = timeseries(Peak,GE_time);
ds = resample(ts,t);      % resamble peak interpolate

d = ds.data;

%% Import Stress measurements

[~, ~, raw0_0] =
xlsread('D:\MyDocuments\MEng\Duvha\4_Analysis\Fatigue\3600_600_LE\Fatigue3600_600deg_LE_EUML.
xlsx','Sweepable','A4:A69');
[~, ~, raw0_1] =
xlsread('D:\MyDocuments\MEng\Duvha\4_Analysis\Fatigue\3600_600_LE\Fatigue3600_600deg_LE_EUML.
xlsx','Sweepable','D4:D69');
[~, ~, raw0_2] =
xlsread('D:\MyDocuments\MEng\Duvha\4_Analysis\Fatigue\3600_600_LE\Fatigue3600_600deg_LE_EUML.
xlsx','Sweepable','Z4:Z69');
[~, ~, raw0_3] =
xlsread('D:\MyDocuments\MEng\Duvha\4_Analysis\Fatigue\3600_600_LE\Fatigue3600_600deg_LE_EUML.
xlsx','Sweepable','AB4:AB69');
raw = [raw0_0,raw0_1,raw0_2,raw0_3];
raw(cellfun(@(x) ~isempty(x) && isnumeric(x) && isnan(x),raw)) = {''};
cellVectors = raw(:,1);
raw = raw(:,[2,3,4]);

% Replace non-numeric cells with NaN and create dataset array
R = cellfun(@(x) ~isnumeric(x) && ~islogical(x),raw); % Find non-numeric cells
raw(R) = {NaN}; % Replace non-numeric cells
data = reshape([raw{:}],size(raw)); % Create output variable
fatqData = dataset; % Create dataset array

% Allocate imported array to column variable names
fatqData.Name = cellVectors(:,1);
fatqData.FreqHz = data(:,1);
```

```matlab
fatqData.CorrectedDynamic = data(:,2);
fatqData.MeanStressCorrection = data(:,3);
fatqData.Mode = [1;2;3;4;5;6;1;1;2;2;3;3;1;1;2;2;3;3;1;1;2;2;3;3;1;1;2;2;...
    3;3;1;1;2;2;3;3;1;1;2;2;3;3;1;1;2;2;3;3;1;1;2;2;3;3;1;1;2;2;3;3;...
    1;1;2;2;3;3;];
fatqData.Harmonic = [0;0;0;0;0;0;1;1;1;1;1;1;2;2;2;2;2;2;3;3;3;3;3;3;...
    4;4;4;4;4;4;5;5;5;5;5;5;6;6;6;6;6;6;7;7;7;7;7;7;8;8;8;8;8;8;9;9;9;...
    9;9;9;10;10;10;10;10;10;];

% Clear temporary variables
clearvars data raw raw0_0 raw0_1 raw0_2 cellVectors R;

%% Rainflow

bin = 64;

numFatq = numel(fatqData.Name);
for fatqCalcI = 1:numFatq
    a = isnan(fatqData.CorrectedDynamic(fatqCalcI));    % only do for fatigue calcualted
    if a == 1
        ;
    else
        CorrectedDynamic = fatqData.CorrectedDynamic(fatqCalcI);
        f = fatqData.FreqHz(fatqCalcI);
        MeanStressCorrection = fatqData.MeanStressCorrection(fatqCalcI);
        S=d.*sin(2*pi*f*t);

        %plot(t,S)
        Se=sig2ext(S);
        rf=rainflow(Se);
        [no,xo]=rfhist(rf,bin,'ampl');
        [m,mx,my]=rfmatrix(rf,bin,bin);
        figure(fatqCalcI)
        subplot(1,2,1), rfhist(rf,bin,'ampl')
        subplot(1,2,2), rfhist(rf,bin,'mean')
        annotation('textbox', [0 0.9 1 0.1],...
            'String', ['Mode ' num2str(fatqData.Mode(fatqCalcI)) ' nodal diameter '
num2str(fatqData.Harmonic(fatqCalcI))], ...
            'EdgeColor', 'none', ...
            'HorizontalAlignment', 'center','Position',[0 0.9 0.85 0.1])
        set(fatqCalcI,'Position',[0 0 600 350])
        set(figure(fatqCalcI),'PaperPositionMode','auto')
        print(fatqCalcI,'-dpng',['D:\MyDocuments\MEng\Duvha\4_Analysis\Fatigue\3600_600_LE\M'
num2str(fatqData.Mode(fatqCalcI)) 'H' num2str(fatqData.Harmonic(fatqCalcI)) '_Mean.png'])
        figure(fatqCalcI+100)
        rfmatrix(rf,bin,bin), colorbar
        title(['Rainflow matrix: Mode ' num2str(fatqData.Mode(fatqCalcI)) ' nodal diameter '
num2str(fatqData.Harmonic(fatqCalcI))])
        saveas(fatqCalcI+100,['D:\MyDocuments\MEng\Duvha\4_Analysis\Fatigue\3600_600_LE\M'
num2str(fatqData.Mode(fatqCalcI)) 'H' num2str(fatqData.Harmonic(fatqCalcI)) '_Rain.png'])

        Max = max(xo);
        StressLife = 0.5*((CorrectedDynamic*xo/Max)/Sf).^(1/b);
        StressLifeCor=StressLife*MeanStressCorrection;
        D = no./StressLifeCor;
        Ds= sum(D)        % damage done in 25 minutes
        Life = 1/Ds;      % Cylces of 25 Minutes it can take
        Life = Life*25    % Total amount of cycles it can take
```

```
        LifeHr = Life / 3600;    % Hours
        LifeDay = LifeHr/24;     % Days
        LifeYears = LifeDay/365  % Years

        figure(fatqCalcI+200)
        axes('Parent',figure(fatqCalcI+200),'Position',[0.045 0.125 0.94 0.795])
        bar(mx',D)
        ylabel('Damage')
        xlabel('Amplitude [mm]')
        title(['Damage against rainflow amplitude: Mode ' num2str(fatqData.Mode(fatqCalcI)) '
n ' num2str(fatqData.Harmonic(fatqCalcI))])
        set(fatqCalcI+200,'Position',[0 0 1000 300])
        set(figure(fatqCalcI+200),'PaperPositionMode','auto')
        print(fatqCalcI+200,'-
dpng',['D:\MyDocuments\MEng\Duvha\4_Analysis\Fatigue\3600_600_LE\M'
num2str(fatqData.Mode(fatqCalcI)) 'H' num2str(fatqData.Harmonic(fatqCalcI)) '_ZDamage.png'])

%% Export data
    % Write Results back to Fatigue Workbook
    result = [Ds,LifeHr,LifeDay,LifeYears];
    range = ['AG',num2str(fatqCalcI+3)]

xlswrite('D:\MyDocuments\MEng\Duvha\4_Analysis\Fatigue\3600_600_LE\Fatigue3600_600deg_LE_EUML
.xlsx',result,'Sweepable',range)

end
end
```

```
% RAINFLOW cycle counting.
%   RAINFLOW counting function allows you to extract
%   cycle from random loading.
%
% SYNTAX
%   rf = RAINFLOW(ext)
%   rf = RAINFLOW(ext, dt)
%   rf = RAINFLOW(ext, extt)
%
% OUTPUT
%   rf - rainflow cycles: matrix 3xn or 5xn dependend on input,
%     rf(1,:) Cycles amplitude,
%     rf(2,:) Cycles mean value,
%     rf(3,:) Number of cycles (0.5 or 1.0),
%     rf(4,:) Begining time (when input includes dt or extt data),
%     rf(5,:) Cycle period (when input includes dt or extt data),
%
% INPUT
%   ext  - signal points, vector nx1, ONLY TURNING POINTS!,
%   dt   - sampling time, positive number, when the turning points
%          spaced equally,
%   extt - signal time, vector nx1, exact time of occurrence of turning points.
%
%
%   See also SIG2EXT, RFHIST, RFMATRIX, RFPDF3D.
```

```
%    RAINFLOW
%    Copyright (c) 1999-2002 by Adam Nieslony,
%    MEX function.
```

```
function [ext, exttime] = sig2ext(sig, dt, clsn)
% SIG2EXT - search for local extrema in the time history (signal),
%
% function [ext, exttime] = sig2ext(sig, dt, clsn)
%
% SYNTAX
%   sig2ext(sig)
%   [ext]=sig2ext(sig)
%   [ext,exttime]=sig2ext(sig)
%   [ext,exttime]=sig2ext(sig, dt)
%   [ext,exttime]=sig2ext(sig, dt, clsn)
%
% OUTPUT
%   EXT     - found extrema (turning points of the min and max type)
%             in time history SIG,
%   EXTTIME - option, time of extremum occurrence counted from
%             sampling time DT (in seconds) or time vector DT.
%             If no sampling time present, DT = 1 is assumed.
%
% INPUT
%   SIG     - required, time history of loading,
%   DT      - option, descripion as above, scalar or vector of
%             the same length as SIG,
%   CLSN    - option, a number of classes of SIG (division is performed
%             before searching of extrema), no CLSN means no division
%             into classes.
%
% The function caused without an output draws a course graph with
% the searched extrema.
%

% By Adam Nies³ony
% Revised, 10-Nov-2009
% Visit the MATLAB Central File Exchange for latest version

error(nargchk(1,3,nargin))

% Is the time analysed?
TimeAnalize=(nargout==0)|(nargout==2);

% Sprawdzam czy przyrost dt jest podany prawid³owo
if nargin==1,
    dt=1;
else
    dt=dt(:);
end

% Zamieniam dane sig na jedn¹ kolumnê
sig=sig(:);
```

```matlab
% Dzielimy na klasy je¿eli jest podane CLSN
if nargin==3,
    if nargout==0,
        oldsig=sig;
    end
    clsn=round(clsn);
    smax=max(sig);
    smin=min(sig);
    sig=clsn*((sig-smin)./(smax-smin));
    sig=fix(sig);
    sig(sig==clsn)=clsn-1;
    sig=(smax-smin)/(clsn-1)*sig+smin;
end

% Tworzê wektor binarny w gdzie 1 oznacza ekstremum lub równoœæ,
% Uznajê ¿e pierwszy i ostatni punkt to ekstremum
w1=diff(sig);
w=logical([1;(w1(1:end-1).*w1(2:end))<=0;1]);
ext=sig(w);
if TimeAnalize,
    if length(dt)==1,
        exttime=(find(w==1)-1).*dt;
    else
        exttime=dt(w);
    end
end

% Usuwam potrójne wartoœci
w1=diff(ext);
w=~logical([0; w1(1:end-1)==0 & w1(2:end)==0; 0]);
ext=ext(w);
if TimeAnalize,
    exttime=exttime(w);
end

% Usuwam podwójne wartoœci i przesuwam czas na œrodek
w=~logical([0; ext(1:end-1)==ext(2:end)]);
ext=ext(w);
if TimeAnalize,
    w1=(exttime(2:end)-exttime(1:end-1))./2;
    exttime=[exttime(1:end-1)+w1.*~w(2:end); exttime(end)];
    exttime=exttime(w);
end

% Jeszcze raz sprawdzam ekstrema
if length(ext)>2,  % warunek: w tym momencie mo¿e ju¿ byæ ma³o punktów
    w1=diff(ext);
    w=logical([1; w1(1:end-1).*w1(2:end)<0; 1]);
    ext=ext(w);
    if TimeAnalize,
        exttime=exttime(w);
    end
end

if nargout==0,
    if length(dt)==1,
        dt=(0:length(sig)-1).*dt;
    end
```

```matlab
    if nargin==3,
        plot(dt,oldsig,'b-',dt,sig,'g-',exttime,ext,'ro')
        legend('signal','singal divided in classes','extrema')
    else
        plot(dt,sig,'b-',exttime,ext,'ro')
        legend('signal','extrema')
    end
    xlabel('time')
    ylabel('signal & extrema')
    clear ext exttime
end
```

```matlab
function [no,xo] = rfhist(rf,x,rfflag)
% rfhist - histogram for use with rainflow data.
%
% function [no,xo] = rfhist(rf,x,rfflag)
%
% Syntax: rfhist(rf)
%         rfhist(rf,30)
%         rfhist(rf,-55:10:55,'mean')
%         [no,xo]=rfhist(rf,30);
%
% Input: rf    - rainflow data from rainflow function,
%                see RAINFLOW for more details,
%        x     - when x is a scalar, uses x bins or when
%                x is a vector, returns the distribution of rf
%                among bins with centers specified by x, like in hist(),
%        rfflag - string, data type flag,
%                'ampl' for amplitude,
%                'mean' for mean value,
%                'freq' for frequency and 'period' for time period of
%                extracted cycles.
%
% Output: no - vector, number of extracted cycles,
%         xo - vector, bin locations.
%
% See also: HIST, RAINFLOW, RFMATRIX.

% By Adam Nieslony, 10-Aug-2003
% Revised, 10-Nov-2009
% Visit the MATLAB Central File Exchange for latest version

error(nargchk(1,3,nargin))

if nargin<3,
   rfflag='ampl';
   if nargin<2,
      x=10;
   end
end

% description and data definition
if rfflag(1)=='m',
   r=2;
```

```
    xl='Histogram of "rainflow" cycles mean value';
elseif rfflag(1)=='f',
    r=5;
    rf(5,:)=rf(5,:).^-1;
    xl='Histogram of "rainflow" cycles frequency';
elseif rfflag(1)=='p',
    r=5;
    xl='Histogram of "rainflow" cycles period';
else
    r=1;
    xl='Histogram of "rainflow" amplitudes';
end

% histogram
halfc=find(rf(3,:)==0.5);      % find half-cycle
[N1 x]=hist(rf(r,:),x);        % for all data
if ~isempty(halfc),
    [N2 x]=hist(rf(r,halfc),x); % only for half-cycle
    N1=N1-0.5*N2;
end

% set the output or plot the results
if nargout == 0,
    bar(x,N1,1);
    xlabel(xl)
    ylabel(['Nr of cycles: ' num2str(sum(N1)) ...
          ' (' num2str(sum(N2)/2) ' from half-cycles)']);
elseif nargout == 1,
    no = N1;
else
    no = N1;
    xo = x;
end
```

```
function [m,mx,my]=rfmatrix(rf,x,y,flagx,flagy)
% rfmatrix - rain flow matrix estimation
%
% function [m,mx,my] = rfmatrix(rf,x,y,flagx,flagy)
%
% Syntax: rfmatrix(rf)
%         rfmatrix(rf,x,y)
%         rfmatrix(rf,x,y,flagx,flagy)
%         [m,mx,my] = rfmatrix(...)
%
% Input: rf          - rainflow data - output from rainflow function,
%        x,y         - numbers of bins in x and y direction,
%        flagx,flagy - strings,
%                      'ampl' for amplitude,
%                      'mean' for mean value,
%                      'freq' for frequency and 'period' for
%                      time period of extracted cycles.
%
% Output: m     - rainflow matrix,
%         mx,my - the bin locations respectively to x and y.
```

```matlab
% By Adam Nieslony, 16-Aug-2003
% Revised, 10-Nov-2009
% Visit the MATLAB Central File Exchange for latest version.

error(nargchk(1,5,nargin))
if nargin<5,
    flagy='mean';
    if nargin<4,
        flagx='ampl';
        if nargin<3,
            y=10;
            if nargin<2,
                x=10;
            end
        end
    end
end

% rainflow data
if flagx(1)=='m',
    xdata=rf(2,:);
elseif flagx(1)=='f',
    xdata=rf(5,:).^-1;
elseif flagx(1)=='p',
    xdata=rf(5,:);
else
    xdata=rf(1,:);
end

if flagy(1)=='m',
    ydata=rf(2,:);
elseif flagy(1)=='f',
    ydata=rf(5,:).^-1;
elseif flagy(1)=='p',
    ydata=rf(5,:);
else
    ydata=rf(1,:);
end
cdata=rf(3,:);

x=x(:)';
y=y(:)';

if length(x) == 1
    minx = min(xdata);
    maxx = max(xdata);
    binwidth = (maxx - minx) ./ x;
    xx = minx + binwidth*(0:x);
    xx(length(xx)) = maxx;
    x = xx(1:length(xx)-1) + binwidth/2;
else
    xx = x;
    minx = min(xdata);
    maxx = max(xdata);
    binwidth = [diff(xx) 0];
    xx = [xx(1)-binwidth(1)/2 xx+binwidth/2];
end
```

```matlab
if length(y) == 1
    miny = min(ydata);
    maxy = max(ydata);
    binwidth = (maxy - miny) ./ y;
    yy = miny + binwidth*(0:y);
    yy(length(yy)) = maxy;
    y = yy(1:length(yy)-1) + binwidth/2;
else
    yy = y;
    miny = min(ydata);
    maxy = max(ydata);
    binwidth = [diff(yy) 0];
    yy = [yy(1)-binwidth(1)/2 yy+binwidth/2];
end
% x, y - center of the intervals in xx and yy, respectively

srf=zeros(length(y),length(x));
rf=[xdata; ydata; cdata];

rfk=find(ydata>=yy(1) & ydata<=yy(2));
if ~isempty(rfk),
    srf(1,:)=rfhist(rf(:,rfk),x,'ampl');
end

for k=2:length(y),
    rfk=find(ydata>yy(k) & ydata<=yy(k+1));
    if ~isempty(rfk),
        srf(k,:)=rfhist(rf(:,rfk),x,'ampl');
    end
end

% plot if no output exist
if nargout==0,
    h=bar3(y,srf,1);
    for i=1:length(h)
        c=repmat(srf(:,i)',4*6,1);
        c=reshape(c,4,6*length(y))';
        c(c==0)=NaN;
        set(h(i),'CData',c)
        c=get(h(i),'XData');
        set(h(i),'XData',(max(x)-min(x))/(length(x)-1)*(c-1)+min(x))
    end
    set(gca,'XTickMode','auto')
    grid on
    xlabel(['X - ' flagx])
    ylabel(['Y - ' flagy])
    zlabel('number of cycles')
    title('rainflow matrix')
    axis tight
elseif nargout==1
    m=srf;
elseif nargout==2
    m=srf;
    mx=x;
elseif nargout==3
    m=srf;
    mx=x;
```

```
        my=y;
end
```